Towards a Design Method for Bamboo Geodesic Domes

Geometrically Non-Linear Structural Analysis and Stability Consideration of Geodesic Domes
Experimental Investigation of the Influence of Nodes on Bolted Connections in Bamboo Structures

Version of January 30, 2015

Lisa-Mareike Ottenhaus

Towards a Design Method for Bamboo Geodesic Domes

THESIS

submitted in partial fulfillment of the
requirements for the degree of

MASTER OF SCIENCE

in

CIVIL ENGINEERING

by

Lisa-Mareike Ottenhaus

Department of Structural Mechanics
Faculty CEG, Delft University of Technology
Delft, the Netherlands
www.ceg.tudelft.nl

© 2015 Lisa-Mareike Ottenhaus.

Towards a Design Method for Bamboo Geodesic Domes

Author: Lisa-Mareike Ottenhaus
Student ID: 4254597
E-mail: lisa@ottenhaus.de

Abstract

This Master of Science thesis depicts the research done on geodesic dome structures and tensile bolted bamboo connections. The report includes a parametric structural analysis of bamboo geodesic domes assessing the influence of openings, local and global stability, geometrical non-linearity, and the maximum possible dome diameters for domes constructed with *Guadua angustifolia* and *Phyllostachys pubescens*. The considered load cases are self-weight and a point load on top of the dome; the latter includes the option of incremental load application and geometrically non-linear analysis. Rules of thumb are derived indicating boundary conditions under which global buckling of half-spherical icosahedron-based geodesic domes does not occur. Furthermore, a comparison of geodesic domes and half-spherical shells is conducted with respect to stability. One of the main challenges in bamboo structures is the design of tensile connectors that exploit bamboo's tensile strength, avoid splitting, and provide a predictable, ductile failure. In the context of the design and strength prediction of a bolted axial bamboo connector, experiments assessing the dynamic Modulus of Elasticity and compression strength of *Guadua angustifolia* and *Phyllostachys pubescens* were conducted. For both properties a significant correlation with density was found. Additionally, the behaviour of bolted connections was simulated by testing the bolt bearing and splitting strength of *Phyllostachys pubescens* in a single bolt test with square and round bolts. It was found that square bolts result in ductile embedment failure with large displacements. Special focus was paid to the influence of nodes on strength and stiffness; a 3D scan (ESEM) and electron microscopy of the nodes of *Guadua angustifolia* and *Phyllostachys pubescens* were made. Findings from microscopic investigation matched findings from experimental testing: Nodes had a positive influence on embedment and splitting strength and an overall negative effect on full-culm compression strength and compressive Modulus of Elasticity. Last but not least, the insights gained in this research were combined in a case study of a bamboo geodesic dome with elliptical door opening. The case study adopts a probabilistic safety concept and partial safety factors in the style of the Eurocodes.

Thesis Committee:

Chairman:	Prof. Dr. Ir. Jan G. Rots, Faculty CEG, TU Delft
Main Supervisor:	Dr. Ir. Pierre C.J. Hoogenboom, Faculty CEG, TU Delft
Committee Member:	Ir. Geert J.P. Ravenshorst, Faculty CEG, TU Delft
Committee Member:	Ir. Andrew Borgart, Faculty BK, TU Delft

Preface

First of all, I would like to thank my committee members, who provided valuable feedback and encouraged this self-devised project: Pierre, who was able and willing to give helpful feedback and advice at every hour of the day. Geert, who gave good, critical feedback and knew the right people to help me with the experiments. Andrew, who followed the development of the research project and made new suggestions. And of course professor Jan Rots, whose feedback was always well-disposed and encouraging, and who inspired me to pursue earthquake engineering in my PhD research.
The lab staff was very helpful. My thanks goes to Ruben, John and Fred.
Bamboe Bouw Nederland was so kind to provide abundant material for experimental testing. Thank you very much!
The following people helped me a lot with software problems and deserve special credits: Jon Mirtschin, who did not only help me with *Grasshopper* problems but even programmed a *Geometry Gym* component that extracts the global buckling factor from GSA. Tim Chen, who truly deserves the nickname "walking Wikipedia" as he is able to assist with no matter what software problem and seems to have an answer to literally any engineering question. He is certainly one of the smartest and kindest people I have ever met! Arend van Waart, whose MSc thesis was great inspiration for the *Grasshopper* script and who helped me with modelling problems.
Special thanks go to the "timber people": Wolfgang Gard, who became interested in the topic and suggested to examine the microstructure of bamboo nodes. Vielen Dank! And Peter de Vries, whose timber connector was inspiration for the new bamboo connector and who helped setting up the bolt test.
The greatest help was received from Stefan Bernardi, who helped preparing the angles for the bolt test over night, even though both of us had a bad cold. Vielen Dank!
I would also like to thank the heart and soul of the 6th floor: Anneke Meijer, who is always helpful with everything. She has an open ear for all study-related (and other) problems and tries to fix them (e.g. a key box next to the door of the graduate room!). Hartelijk dank!
Special thanks goes to Andrei Metrikine, who is one of the most inspiring teachers I know and finally let me see the beauty of dynamics.
Last but not least, I would like to thank the best roommate I ever had, Carolin Briele!

Lisa-Mareike Ottenhaus
Delft, the Netherlands
January 30, 2015

Contents

List of Figures

List of Symbols

Symbol	Units	Definition
A	mm^2	Surface area of bamboo culm
A_b	mm^2	Bolt bearing surface
A_{cr}	mm^2	Surface of tensile crack
A_{net}	mm^2	Net surface area of bamboo culm
A_v	mm^2	Shear surface
a	-	Robertson constant (as indicated)
a	$[m]$	Radius of spherical shell
B	-	Average number of vascular bundles per unit area
C_i	-	Coefficient as indicated
D	m	Dome diameter
D_0	mm	Outer diameter of bamboo culm
D_i	mm	Inner diameter of bamboo culm
D_{max}	m	Limit dome diameter
D_{true}	m	True dome diameter, obtained by measuring the greatest distance of the dome's base points
d	mm	Dowel or bolt diameter
d_1	mm	Diameter of bolt hole
E	MPa	Modulus of Elasticity (Young's Modulus) (in bending)
E_c	MPa	Compressive Modulus of Elasticity
E_d	MPa	Design value of Modulus of Elasticity
E_{dyn}	MPa	Dynamic Modulus of Elasticity
E_f	MPa	Modulus of Elasticity of fibres
E_{global}	MPa	Global Modulus of Elasticity
E_{local}	MPa	Local Modulus of Elasticity
E_m	MPa	Modulus of Elasticity of matrix
F	kN	Point load on top of geodesic dome (as indicated)
F	kN	Force (as indicated)
$F_{b,max}$	kN	Maximum force in bolt (also denoted as $F_{bolt,max}$)
F_c	kN	Compressive force
F_{cr}	kN	Force that leads to tensile splitting failure
F_{Ed}	kN	Design value of force caused by action
F_{Rd}	kN	Design value of resistance force
F_s	kN	Strut force

$\mathfrak{f}$	-	Dome frequency, number of subdivisions of polyhedron surface
$\mathfrak{f}_{max}$	-	Maximum dome frequency (utilization of global and local buckling are 1.0)
f_b	MPa	Bearing or embedment strength (parallel to the grain)
f_c	MPa	Compressive strength (parallel to the grain)
f_{cr}	MPa	Euler buckling strength
f_{cc}	MPa	Compressive buckling strength interaction of Euler buckling and compression
$f_{c,\parallel}$	MPa	Compressive strength parallel to the grain
$f_{c,\perp}$	MPa	Compressive strength perpendicular to the grain
f_d	MPa	Design strength
f_k	MPa	Characteristic strength (5%-percentile)
f_{LB}	MPa	Local buckling resistance (Euler buckling strength)
f_m	MPa	Bending strength
f_t	MPa	Tensile strength (parallel to the grain)
$f_{t,\parallel}$	MPa	Tensile strength parallel to the grain
$f_{t,\perp}$	MPa	Tensile strength perpendicular to the grain
f_s	MPa	Tensile splitting capacity (perpendicular to the grain)
f_v	MPa	Shear strength
g	N/kg	Gravity (9.81)
h	mm	Height of bamboo specimen
I	mm^4	Inertia
k_{def}	-	Creep factor
k_{mod}	-	Modification factor for load duration and exposure
L	m	Length of (longest) strut
l_{culm}	cm	Length of culms in dynamic Modulus of Elasticity test
l_{edge}	mm	Edge distance of fastener
l_i	m	Influence of edge disturbance in shell
N	kN	Normal force
n	kN/m	Normal force flow in shell membrane (as indicated)
n	$-$	Number of cracks (as indicated)
P	-	Probability
p	-	p-value
p_{cr}	kN/m^2	Shell buckling load
p_z	kN/m^2	Distributed self-weight of shell or geodesic dome
R^2	-	Coefficient of determination
r	-	Distance from inner culm surface $r \in [0;1]$
T	m	Position of trimming plane in relation to dome diameter: $T \in [-0.5;0.5]D$
t	mm	Culm wall thickness
t_cr	mm	Thickness of culm wall at location of tensile crack
t_s	mm	Shell thickness
V_f	%	Fibre volume fraction
$\overline{x}$	-	Sample mean
$x_{5\%}$	-	Characteristic value
x_k	-	Characteristic value
z	m	z-position of opening $z \in [0;1]D$
α	-	Significance level
$\alpha_{i\to k}$	-	Strut stress increase factor for increased frequency $\mathfrak{f} = i$ to $\mathfrak{f} = k$

α_R	-	FORM sensitivity factor resistance
α_S	-	FORM sensitivity factor load
β	-	Desired reliability index
$\gamma_{G,1}$	-	Partial safety factor (self-weight)
γ_m	-	Partial safety factor (material)
δ	mm	Deflection
η	-	Perry factor
θ	$^\circ$	Load grain angle
λ_0	$^\circ$	Limiting slenderness
λ_1	$^\circ$	Slenderness ratio
μ	-	Population mean (as indicated)
μ	-	Utilization factor (as indicated)
ν	-	Poisson's ratio
ξ	-	Spring stiffness
ρ	kg/m^3	Density
σ	MPa	Stress (as indicated)
σ	-	Standard deviation (as indicated)
σ_{max}	MPa	Maximum strut stress
ϕ	$^\circ$	Angle from z-axis in a shell

List of Terms and Abbreviations

Abb.	Definition
bearing	used as a synonym of embedment
BSc	Bachelor of Science
CAD	Computer Aided Design
CHS	Circular hollow section
DIP	Digital Image Processing
EC	Eurocode
Elephant	Export tools for *Grasshopper* developed by Arend van Waart
embedment	used as a synonym of bearing
ESEM	Environmental Scanning Electron Microscope
EWB	Engineers without Borders
FE	Finite element
FEA	Finite element analysis
FEM	Finite element model
FGM	Functionally graded material
FORM	First Order Reliability Method
FRP	Fibre reinforced polymer
GB	Global buckling
Geometry Gym	Provides utilities and plug-ins for *Rhinoceros* and *Grasshopper*. Enables exchange of *Grasshopper* models with *Oasys GSA*. Developed by Jon Mirtschin
GNL	Geometrically non-linear
Grasshopper	Graphical algorithm editor linked with *Rhinoceros*
GSA	Used short for *Oasys GSA*
Guadua	Used short for *Guadua angustifolia*
Hoopsnake	Component that enables feedback loops within *Grasshopper* developed by Yiannis Chatzikonstantino
INBAR	International Network for Bamboo and Rattan
ISO	International Organization for Standardization
ISO 2004b	Used as synonym for ISO 22157-1
LB	Local buckling
LC	Load case
LCA	Life cycle assessment
LEED	Leadership in Energy and Environmental Design, US rating system for the design, construction, operation, and maintenance of environmentally friendly buildings and neighbourhoods

LF	Load factor
MC	Moisture content
MOE	Modulus of Elasticity (Young's Modulus)
Moso	Chinese name and synonym for *Phyllostachys pubescens*
MSc	Master of Science
NDT	Non-destructive testing
Oasys GSA	Non-linear structural analysis software developed and owned by ARUP
PhD	Doctor of Philosophy
Platonic Solid	Convex regular polyhedron that tries to approximate a sphere: tetrahedron, cube, octahedron, icosahedron and dodecahedron
Polyhedron	three dimensional solid that is characterized by flat faces, straight edges and sharp corners (vertices)
RH	Relative humidity
Rhinoceros	(abbreviated Rhino) 3D CAD software developed by Robert McNeel & Associates
strut	bar element that can transfer axial stresses - no distinction between compressive struts and tensile ties is made
S235	Structural steel with yield strength of 235 MPa
UDHR	Universal Declaration of Human Rights
UN	United Nations
US	United States (of America)
vertex	corner of a polyhedron

Chapter 1

Introduction

1.1 Background and Motivation

1.1.1 The Global Need for Housing and Sustainable Building Materials

In article 25.1 of the Universal Declaration of Human Rights it is stated that "*everyone has the right to a standard of living adequate for the health and well-being of himself and of his family, including food, clothing, housing and medical care* [...]" [1]

Still as of today nearly one billion people around the world are living in urban slums – informal settlements that lack structural safety and durability – therefore being exposed to natural disasters such as earthquakes, flooding, storms, etc. [90]. The current trends indicate an ongoing urbanization in developing and emerging countries, resulting in even larger and more densely populated slums [85]. As an example, in Brazil alone, about 6% of the population lived in 'favelas'[2] in 2010 which equals 11.4 million people [13]. As houses in favelas are self-made, construction takes several years. One of the major problems is the availability and affordability of construction materials combined with the lack of knowledge and skills that resulted in repeated collapse of buildings in the past[71][40]. While many low-income families are hardly able to afford construction materials such as brick and concrete, bamboo is theoretically readily and cheaply available as Brazil has the greatest bamboo diversity and the highest percentage of woody bamboos of all countries in Latin America [76]. Woody bamboo (in the following simply referred to as 'bamboo') is an excellent building material, lightweight, easy to handle, fast-growing, and could substantially aid in meeting the increasing demand for safe, cheap and sustainable housing, not only in Brazil but all over the world.

Comparing a map of the world's urban population living in slums to the distribution of bamboo, a remarking resemblance can be found (figure 1.1). Still people living in slums as well as building authorities of developing and emerging countries strive for houses made out of concrete which – if to be realized cheaply – would be disastrous in terms of carbon dioxide emissions and water consumption [69]. A bamboo load bearing structure for medium sized residential buildings can be equally strong as a concrete structure while being cheaper and much more sustainable [69][47][5].

The enduring preference for concrete as a building material has two main reasons:

1. The bamboo ISO codes were only released in 2004, and engineered bamboo structures are still the exception rather than the rule. The design of traditional bamboo structures is usually experience based, believing that "tradition is proof enough" [4]. This leads to

[1] http://www.un.org/en/documents/udhr/
[2] Brazilian term for slum

inadequate preservation and jointing techniques; in the worst case resulting in the collapse of a structure. Repeated failure of bamboo structures is the main reason why bamboo is still perceived as an 'unsafe' material by many local building authorities [60].

2. Another important aspect is the social status associated with the use of natural building materials. As mainly rich people can afford concrete houses, bamboo is stigmatised as a "poor man's material" [4] [99].

In order for bamboo to be applied more often, the image of bamboo as a building material needs to be improved, e.g. through application by pioneer architects, education of local contractors, and active promotion by governments and building authorities [5]. A precondition for this to happen is continued research on material properties, jointing techniques, and preservation methods.

(a) Distribution of woody bamboos (www.eeob.iastate.edu [12])

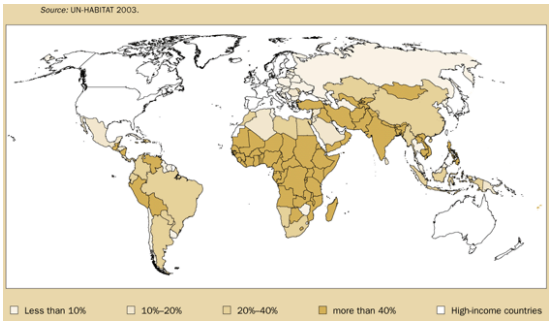

(b) Urban population living in slums (www.unmillenniumproject.org[89])

Figure 1.1: Maps of bamboo and slums

1.1.2 Bamboo as a Structural Material

General Features Bamboo is a fast growing wood-like grass which is found in many parts of the world, mainly East Asia, Northern Australia, India, sub-Saharan Africa and parts of South America (figure 1.1). It is lightweight, easy to handle and has good mechanical properties. Bamboo is harvested after 3 – 5 years, and after few weeks of drying ready for construction application. As natural durability is rather low [98], special attention needs to be paid to moisture control and structural detailing [50]. The individual culm can easily reach a diameter of 30 cm, a length up to 20 m and bamboo fibres can reach the specific tensile strength of mild steel [47][72]. When harvested in a controlled manner, the plant itself does not die and is suitable for growth in plantations [4]. Bamboo application mitigates deforestation when used as a timber substitute [99][11][39][50] and substantially reduces carbon dioxide emission when used as a steel substitute[3][32][2][53].

Sustainability Similar to timber, bamboo works as a carbon trap as long as in use [99]. Local application of bamboo as a building material makes sense as natural materials are already adapted to their surrounding climate. Additionally, local application results in short transportation distances and thus lower carbon dioxide emission. For longer transportation distances, the material's high relative strength accounts for increased CO_2 emissions [81] without suffering from the production related carbon footprint of other lightweight materials, such as steel or fibre reinforced polymers (FRP). Several researches have tried to quantify the ecological benefits

[3]Due to its high tensile strength, bamboo is suitable as a structural steel substitute in lightweight structures and as a reinforcement substitute in reinforced concrete.

of bamboo application: Janssen was one of the first who assessed ecological aspects of bamboo and bamboo plantations in his book of 2000, naming for example the potential positive effects on erosion and ground water level [47]. Trujillo reports a life cycle assessment (LCA) conducted on Colombian 'Bambusa' houses in 2002, resulting in half the environmental impact of an identically sized reinforced masonry house [85]. Another illustrative LCA for the Columbian 'Bohio' bamboo house is provided by Archila-Santos et al., who also considered architectural and mechanical aspects of the design [5]. Yu et al. conducted an LCA on a residential bamboo building in comparison to a typical brick-concrete building, using three different scenarios according to the LEED standard. They found that the bamboo building requires less energy and emits less carbon dioxide while meeting identical functional requirements. They suggested to establish a nationwide database for different types of residential buildings in China in order to asses building life cycle related carbon dioxide emissions [100]. Richard conducted a comparative LCA as part of his PhD thesis of 2013, in order to assess the environmental impacts of structural bamboo, boxed timber, solid timber and steel. He found that the positive impact of bamboo is highest, if applied locally [69]. Summarizing it can be stated that bamboo is a fast regrowing, natural building material, able to compete with other building materials in terms of structural performance, and very sustainable if applied locally.

Standards and Norms The use of bamboo has been promoted by the International Network for Bamboo and Rattan (INBAR) since the late 1980s, and reached its peak in the release of the bamboo ISO codes in 2004. National adaptations of the ISO codes were developed in Columbia and China and serve as bamboo building codes.

One of the major challenges in bamboo engineering is the lack of a material property database, mainly due to a lack of standardized test methods prior to the release of the ISO standards [81][69]. Another problem is the reliability and comparability of test results, which has been addressed by several researchers [80][75][38][47][62]. Therefore, it is not only important to conduct material tests according to the ISO codes, but also to report entire sets of results, including mean values, standard deviation, etc.; in lack of globally accepted material properties, this still enables engineers to base their structures on probabilistic design conforming to (inter)national building standards.

1.1.3 Solutions for Seismic Areas: Bamboo Geodesic Dome Structures

Seismic Resistance of Geodesic Domes Geodesic domes are material cost and energy efficient, provide a column free interior space and have low wind drag coefficients [8]. In his MSc Thesis of 2009, Kubik states that the *"degree of compactness in a building correlates with its resistance against seismic shock"* [52]. Geodesic domes approximate hemispheres, maximizing volume while minimizing surface area, therefore being very compact. Kubik suggests a geodesic dome variant called "Pabal dome" for seismic areas in India. The design is made of steel, chicken wire and concrete, and was realized in an initiative of Engineers Without Borders (EWB). In 2010, Drake et al. suggested an adapted Pabal dome making use of locally available bamboo. The main objective of this EWB project was to *"enable low-skilled low-resourced people to build their own structure using a 'kit' that includes pre-fabricated connections, tools and instructions or guidelines"*. According to Drake et al., one of the major challenges was to design an easy-to-assemble joint that provided sufficient stiffness [20].

Seismic Resistance of Bamboo Structures The severity of earthquake damage and casualties is correlated with the advancement of building techniques in the affected area. Unfortunately, areas affected by seismic activity also involve the majority of areas with low socio-economic development, including large parts of Asia and Latin America [75]. In turn, most of these areas also

have natural bamboo resources which could easily be used to construct earthquake-safe houses. Examples from history show that even low-tech bamboo houses are able to provide great earthquake resistance. During a typhoon in the Philippines in 1987, several bamboo houses collapsed due to splitting of nailed connections. Still, more bamboo houses than concrete houses stayed intact which the author relates to the low-quality concrete and poor workmanship that was used [1]. Apparently, low-tech bamboo houses are still safer than low-tech concrete houses, which can be partially attributed to the light weight of bamboo. Similar observations are reported by Sharma in his PhD thesis of 2010 [81]: In the Sikkim region (India), poorly constructed concrete houses collapsed due to an earthquake in 2006, while bamboo houses stayed intact. Another example is reported by Archila-Santos et al. and Luna et al.: During an earthquake in Columbia in 1999, most of the bamboo buildings survived with minor structural damage, whereas conventional concrete buildings collapsed, and almost 60% of all buildings collapsed [5][59]. Paudel even claims, that the seismic performance of bamboo is better than the one of timber [65].

Besides these examples from history, the seismic performance of bamboo structures was also assessed by experimental testing [81] and finite element modelling (FEM) [22]. Several authors relate the excellent seismic performance to bamboo's high axial strength, lightweight and flexibility [22][47][53][75]. Remaining challenges are the development of stronger and stiffer joints that provide sufficient deformation capacity, the implementation of seismic design in bamboo building codes, and the training of high-skilled workers who can cope with the natural variability and low durability of full-culm bamboo. Subsequently, bamboo's structural capacity can be fully exploited, providing safe and sustainable housing solutions for seismic areas.

Bamboo Geodesic Domes In terms of structural resistance to earthquakes, it is only logical to combine the structural advantages of geodesic domes and the mechanical advantages of bamboo. Bamboo performs especially well under axial loading – the predominant load direction in geodesic dome struts. Bamboo geodesic domes could be applied for medium sized public buildings, or housing in rural areas in South America or South East Asia. The modular character of a geodesic dome allows for replacement of single members, which facilitates maintenance of structures employing natural materials such as bamboo[4]. In more densely populated areas, the shape of geodesic domes is impractical. However, research on bamboo tensile connectors is independent of the overall structural design. It can even be claimed that any bamboo research, adding to the general knowledge of bamboo properties, enables architects and structural engineers to apply bamboo more easily, thereby leading to the promotion of the use of bamboo, and finally providing cheap, safe, and sustainable housing for the world's growing population [4][48][5].

[4]As durability of untreated bamboo is limited, preservative treatment and structural detailing are advised to enhance durability [85]. After events like heavy rain, seismic damage, etc., it is favourable if affected members can be replaced easily. This should also be considered in bamboo connector design.

1.2 Problem Statement

Bamboo geodesic domes are able to provide sustainable, aesthetic, and structurally safe buildings in seismic areas with natural bamboo resources. However, neither geodesic domes as a structural system, nor bamboo as an engineered building material, are frequently applied yet. In the following, the main challenges in designing bamboo geodesic dome structures are presented.

1.2.1 Parametric Stability Analysis of Bamboo Geodesic Domes

When designing geodesic domes, individual solutions can easily be obtained by application of FEA (finite element analysis). However, no standardized solutions or rules of thumb are available that indicate whether a design is feasible and structurally sound. In this context, the predictability of global buckling is considered crucial for three main reasons:

1. Global buckling is a sudden failure mode and needs to be absolutely avoided.
2. It is almost impossible to check global buckling by hand, especially for large structures.
3. The global buckling mode and load factor depend on the magnitude and kind of load or load case combination. Linear superposition of global buckling load factors of individual load cases is not possible.

It is expected that depending on the dome frequency, a change from local strut buckling to global dome buckling will occur. The aim of the FE implementation is the derivation of boundary conditions that determine this transition point. Subsequently, limit parameters can be derived under which global buckling does not occur, which is the precondition for linear superposition of geometrically linear load cases. The remaining challenge is the evaluation of the influence of geometrical non-linearity.

Furthermore, practice application requires the insertion of openings in domes. Location and size of elliptical door openings determines the magnitude of maximum strut stresses. The FE model is used to derive stress patterns resulting from the location of opening insertion. This model feature is also employed in a case study.

1.2.2 Bamboo Material Properties and Tensile Connector Design

By the introduction of the ISO standards for bamboo, a great step was made in the acceptance and standardization of bamboo as a structural material. However, calculation rules are still far from being well established and material properties are not known to an extend that allows for a strength prediction of structural components, let alone bamboo joints. Therefore, several essential mechanical properties are determined including Modulus of Elasticity, compression strength, bolt bearing (embedment) strength and splitting strength.

Another challenge is the connection of full-culm bamboo members, especially in tension. One aim of this research is to propose a tensile bolted connector that is able to cope with the natural variation of culm geometry and mechanical properties, while avoiding tensile splitting. The design needs to be attachable to a dome hub, cheap, efficient, easy to assemble, permit ductile failure[5], and allow for accurate strength prediction. Assembly and destructive testing of the connector is beyond the scope of this research.

[5]Ductility and deformation capacity of joints is important for several reasons: (a) it reduces scatter of test results and increases strength predictability (b) large deformations provide a warning for the user instead of sudden, unexpected failure

1.3 Scope of Research

The aim of this research is to work towards a parametric design method for bamboo geodesic dome structures, including rules of thumb that predict maximum dome dimensions. An additional goal is to propose a bolted tensile connector that avoids splitting. One main research question is posed to guide the course of the research:

1. **What are the limiting parameters in the design of bamboo geodesic domes and can a maximum diameter be derived?**

Regarding geodesic dome design, the following research questions are posed:

2. Does a limiting diameter exist for bamboo geodesic domes made of *Guadua angustifolia* and *Phyllostachys pubescens* (if connector strength is not taken into account) and what parameters are decisive?
3. Is it possible to determine boundary conditions under which global buckling does not occur and is linear superposition then possible?
4. What is the effect of opening size and position on the maximum strut stresses in bamboo geodesic dome struts?

In terms of connector design and experimental determination of material properties of *Guadua angustifolia* and *Phyllostachys pubescens*, the following aspects will be investigated:

5. What is the effect of nodes on compression capacity?
6. What is the effect of nodes on bearing and splitting capacity of bolted connections?
7. What influence does the shape of the bolt (round or square) have?
8. Is it possible to suggest a bolted tensile connector that avoids splitting and provides sufficient strength and ductility for geodesic dome application?

Finally, real life application is simulated in a case study to give a qualitative answer to the following question:

9. What are the main limiting parameters in real life application (including limited tensile connector strength) and how can bamboo geodesic dome performance be generally improved?

1.3.1 Limitations

Three different materials are implemented into the geodesic dome FE model: S235, *Guadua angustifolia* and *Phyllostachys pubescens*[6]. Strength properties and geometry of bamboo are derived from literature and experiments.

Two load cases (self-weight, point load) are analysed in detail to illustrate the concept of FE stability analysis and geometrical non-linearity. The case study illustrates probabilistic design and superposition of the analysed load cases. It should be seen as an example of use rather than a design case or structural verification. Dead load of cladding, wind, and snow are implemented into the model, but analysis is beyond the scope of this research.

[6]These species were supplied by *Bamboe Bouw Nederland* and were used in experiments as part of this research

1.4 Methodology

First, a bipartide literature review literature is presented. Chapter 2 discusses bamboo as a structural material. Geodesic domes in general and bamboo geodesic domes in particular are discussed in chapter 3.

The experimental program consists of three experimental cycles and a microscopic examination whose results are discussed in chapter 4. The experiments assess the dynamic Modulus of Elasticity, compressive strength and compressive Modulus of Elasticity of *Guadua angustifolia* and *Phyllostachys pubescens*, and bolt bearing and splitting strength of *Phyllostachys pubescens*. Additionally, a 3D nano scan (ESEM) and electron microscopy are conducted for both species.

Chapter 5 reports the results of a FE dome model analysis conducted in *Grasshopper*[7] and *Oasys GSA* (GSA)[7]. The model input is based on mean strength values of *Guadua angustifolia* and *Phyllostachys pubescens*, derived from literature and experiments. The exchange of model data between *Grasshopper* and GSA is enabled by the plug-in *Geometry Gym* provided by Jon Mirtschin. The model analysis investigates stability, non-linearity, insertion of openings and theoretical limit dome diameters. Two load cases are analysed in detail: self-weight and point load on top of the dome. Tensile connector strength is neglected. Probabilistic design is neither applied on the load nor the material side as magnitude of loads, as load safety factors and relevant load combinations are end-use dependent. Linear superposition is applicable for both SLS and ULS for linear static load, provided that global buckling is not governing. Global buckling and non-linear results are load dependent, i.e. the final load combination must be applied in the structural analysis! Therefore, boundary conditions are derived under which global buckling does not occur, and the impact of non-linearity is quantified.

In chapter 6, probabilistic design is discussed, which is the underlying safety concept of the tensile connector design and case study.

In chapter 7, a tensile connector is proposed. Strength is predicted in a component based approach, applying knowledge gained from literature research and experiments. The actual assembly and experimental investigation of stiffness and strength of the full-sized joint are beyond the scope of this research.

A case study in chapter 8 is used to illustrate the concept of probabilistic design and load case superposition. Knowledge gained from literature, experiments, and FEA is applied and combined. The case study includes design strength values and tensile strength of the proposed connector.

Chapter 9 summarizes the results, answers the posed research questions and draws conclusions.

The overall outcome is a working *Grasshopper* model for bamboo geodesic domes, rules of thumb indicating the transition from local to global buckling, and the maximum possible dome diameter for two different load cases. Material tests provide insight into the effect of nodes on compressive, splitting and bearing strength of bolted connections. This allows for the proposal of a new bolted bamboo tensile connector which – after sufficient testing – can be applied in axially loaded full-culm bamboo structural components.

[7] more information regarding *Grasshopper* and *Oasys GSA* is provided in chapter 5

Chapter 2

Literature Research Bamboo

In 2000, Janssen published the book "Designing and Building with Bamboo" in cooperation with the International Network for Bamboo and Rattan (INBAR), summarizing his knowledge and research done on bamboo. In the following, a brief summary of the most important features of bamboo as a structural material is given, with focus on material properties of the species *Phyllostachys pubescens* (Moso) and *Guadua angustifolia*, which were subject of this research. If the reader wants to gain more general knowledge about the subject, it is recommended to study the works of Janssen or the INBAR Technical Reports.

Chapter 2.1 provides general information, including natural distribution and harvesting of bamboo. In chapter 2.2, an extensive literature review presents material properties of *Phyllostachys pubescens* (Moso) and *Guadua angustifolia*. As this research aims to understand and exploit the special features of the full culm, special attention is paid to the macroscopic and microscopic functionally graded structure of bamboo, including fibre distribution in the radial direction and along the height of the culm. Different methods are available to obtain fibre distribution; therefore the advantages and disadvantages of Digital Image Processing (DIP) and fibre extraction techniques are discussed. Additionally, relationships between mechanical and physical properties are presented and discussed. The importance of research advancements in non-destructive testing (NDT) is emphasized and suggestions are made, how future research can contribute to further standardization and facilitated bamboo application. Note that more detailed information on experiment-related literature is given in the respective sections of chapter 4.

In chapter 2.3, different bamboo tensile connectors are presented and their performance is assessed with respect to geodesic dome application. Detailed information on the proposed connector, including a strength prediction, is presented in chapter 7.1.

2.1 General Information

Bamboo is a fast growing wood-like grass found in many parts of the world, mainly East Asia, Northern Australia, India, sub-Saharan Africa and parts of South America (figure 2.1). It is lightweight, easy to handle and has good mechanical properties. Bamboo is harvested after 3 – 5 years as it reaches its maximum strength. After few weeks of drying, the culms are ready for construction application. The individual culm can easily reach a diameter of 30 cm, a length up to 20 m and the fibres can reach the specific tensile strength of mild steel [47][72]. Natural durability is limited but can be enhanced by preservative treatment and adequate detailing [85][50].

Figure 2.1: Distribution of woody bamboos (www.eeob.iastate.edu [12])

2.2 Material Properties

Bamboo's material properties are governed by its functionally graded macro- and microstructure. In the following, a brief overview of the macro structure is given. Subsequently, the microstructure of the internode and the resulting axial mechanical properties are discussed more deeply. Relationships between mechanical and physical properties are presented and the need of NDT is emphasized. As nodes were of special importance in this research, chapter 2.2.3 focusses on the microscopic structure of nodes and influence on material properties.

2.2.1 Bamboo as a Functionally Graded Material

The functionally graded macro and microstructure of *Phyllostachys pubescens* (Moso) and *Guadua angustifolia* are discussed, focussing especially on axial mechanical properties.

2.2.1.1 Macrostructure

The bamboo culm is characterized by nodes and internodes. As part of a node, a transverse diaphragm interrupts the hollow round cross-section of the culm. An internode is the section between two nodes (figure 2.2).

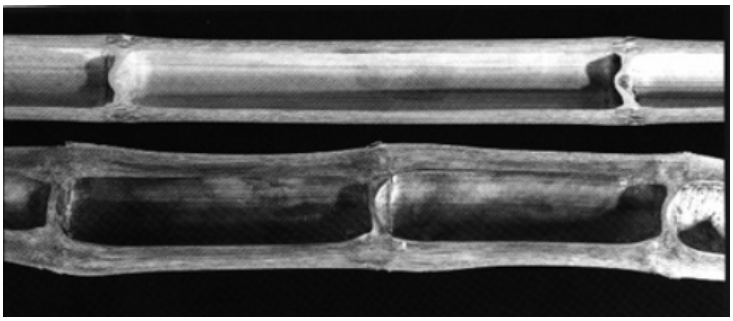

Figure 2.2: Longitudinal cross-section of bamboo culm (Liese, 1971 [55])

Unlike timber, bamboo does not experience radial growth. New culms emerge from an underground rhizome system with their final diameter and final amount of nodes [69]. In general, geometry changes along the height of the culm: While culm diameter stays constant for some species and decreases for others, wall thickness is found to decrease for most bamboos leading

to a reduction in cross-sectional area [11] [32]. Mechanical properties generally improve with age and reach their peak between three to five years, depending on the species. After five to seven years, strength starts to decrease again, explaining the age at which bamboo is usually harvested [69][44]. Moisture content for green condition and air dried condition is species dependent [11]. The decrease of moisture content from green to dry is higher for bamboo than for timber, leading to radial cracking and longitudinal splitting if drying is not carried out carefully [69]. Change of moisture content also needs to be considered when bamboo is transported to a different climate.

2.2.1.2 Microstructure

Bamboo is a composite material with strong cellulose fibres embedded in a soft parenchyma matrix. The culm wall composition can roughly be described as 40% fibres, 50% matrix and 10% vessels in the internode [47]. The fibres are part of a vascular bundle which also contains vessels for water and nutrient transport [64]. The vascular bundle can be structured into fibres, metaxylem and phloem vessels, and sclerenchyma sheaths (figure 2.3). Similar to other fibre matrix composites, bamboo's strength and stiffness are directly correlated with the fibre content; an indirect measure for the fibre content is the amount of vascular bundles. In the internode, the cellulose fibres are axially orientated, resulting in orthotropic properties. In the nodal diaphragm, the fibres are short and randomly orientated, resulting in an isotropic structure that transversely connects the culm wall [68][55][1] Fibre content increases radially and along the height of the culm; the latter mitigates the effect of the decreased cross-sectional area.

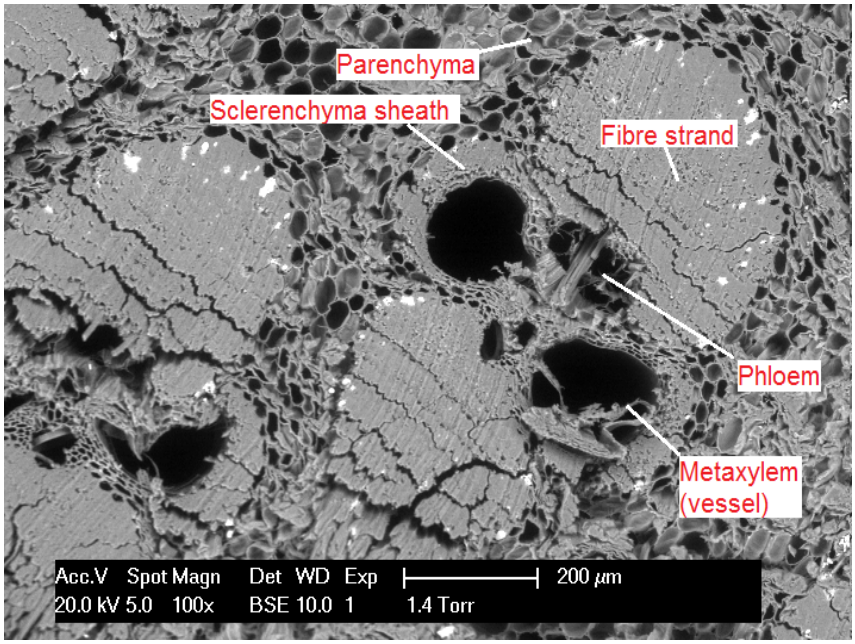

Figure 2.3: Transverse cross-section of *Guadua angustifolia* vascular bundle (from electron microscopy at TU Delft, part of this research)

Mechanical Properties and Fibre Distribution In 1995, Nogata and Takahashi published an article describing bamboo as a Functionally Graded Material (FGM) [64]. They investigated the fibre distribution in Moso culms, concluding that fibre density increases longitudinally from the bottom to the top of the culm and non-linearly from the inside to the outside surface of the culm cross-section. They found similar results for the distribution of tensile strength and

[1]For more detailed information on the macro and microstructure of nodes see chapter 2.2.3.

Modulus of Elasticity (MOE). The radial increase of MOE was described by a power law with r=0...1 (distance from inner culm surface). They concluded that bamboo fibres have high specific tensile strength but low specific rigidity (figure 2.4).

$$\text{bottom: MOE} = 2.5e^{(2.2r/t)}; \quad \text{top: MOE} = 3.75e^{(2.2r/t)}$$

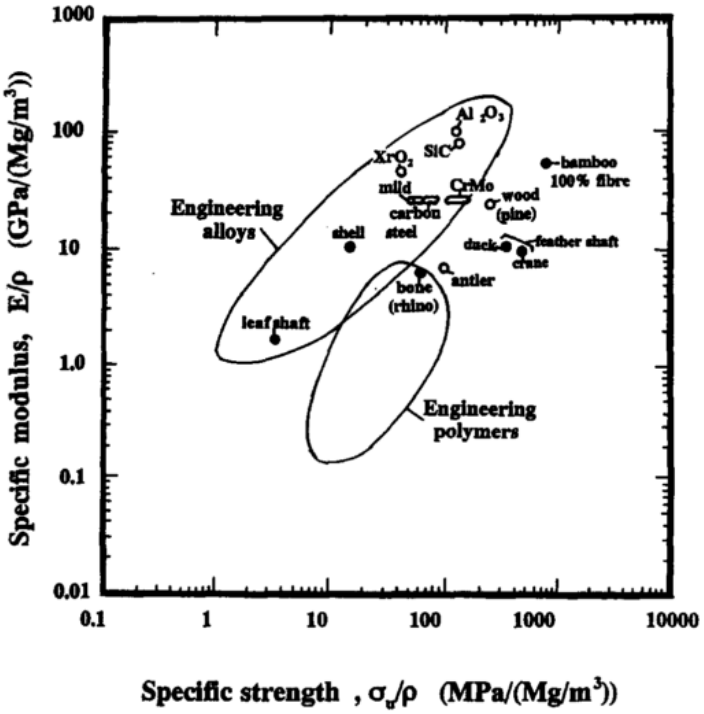

Figure 2.4: Specific MOE vs. specific strength, hard tissues (Nogata and Takahashi, 1995)

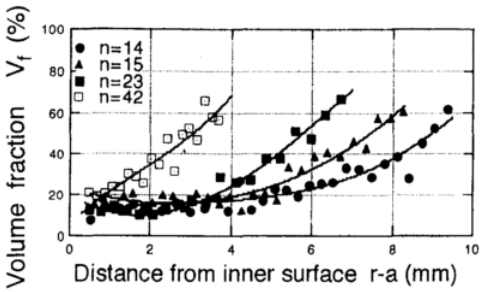

Figure 2.5: Radial fibre distribution at different heights of the Moso culm (Amada et al., 1997)

Amada et al. examined Moso bamboo on a macroscopic and microscopic level in 1996 [3]. They concluded that bamboo is a *"unidirectional fibre-reinforced composite with many nodes along its length"*, which has a functionally graded and hierarchical structure. They attributed diameter, thickness and node distance to the macroscopically graded structure and the fibre distribution within the culm wall to the microscopically graded structure. The measured fibre distribution along the thickness of the culm for different location along the height of the culm is displayed in figure 2.5. All volume fractions ranged between 10 and 70% which Amada et al. related to strength properties. The tensile fibre strength was found to be 600 MPa, matrix strength was found to be 12 times lower. Additionally, Amada et al. investigated the microstructure of nodes, finding that fibres deviate from the culm into the node, to reinforce the node and connect it to

the culm. They concluded that the entangled fibre structure in the nodes results in isotropic properties, so that the nodes can act as "reinforcement" for the culm.

In his book of 2000, Janssen states that fibre content varies from 10% on the inside wall to 60% at the outside wall independent of the species. Assuming that the MOE of a single fibre is 35 000 MPa, he derives the following rule of thumb for the radial distribution of MOE, neglecting the contribution of the matrix [47]:

$$\text{MOE} = 35\ 000\ V_f\ [\text{MPa}] \quad V_f ...\text{fibre volume fraction}$$

Yu et al. sliced the culm wall of Moso bamboo into several layers, investigating the tensile strength, MOE, shrinkage and relative density along the thickness and height of the culm. They concluded that the layer position had a significant effect on all properties while height had an effect on all properties except tensile strength. Relative density, tangential shrinkage, tensile MOE and tensile strength showed a strong increase from the inside to the outside. Longitudinal shrinkage decreased strongly from inside to outside layer. Relative density, tangential shrinkage and tensile MOE increased along the height of the culm whereas tensile strength remained constant [101]. This illustrates the effect how increased relative fibre content mitigates the effect of a decreased cross-sectional area at the top of the culm. It also shows, that Janssen's assumption of a species independent average MOE of 35 GPa is a gross simplification.

Shao et al. derived linear formulas for the correlation of tensile strength and MOE, and fibre volume fraction V_f of Moso [78]. A more detailed report of research on tensile properties can be found in appendix B.1.

$$f_t = 562.69\ V_f + 19.04\ [\text{MPa}] \qquad \text{MOE} = 40.13\ V_f + 0.22\ [\text{MPa}]$$

Chen and Long performed linear and curvilinear regression analyses for tensile properties and fibre volume fraction of Moso, using models with different amounts of layers in the radial direction. They concluded that mechanical properties are strongly related to the fibre volume fraction. Models with averaged properties and less layers overestimate resulting deformation and axial stresses and are conservative as they don't take the positive effects of the gradient fibre distribution into account. The findings from the linear regression analysis for tensile strength and MOE were [10]

$$f_t = 6.936 + 617.789\ V_f\ [\text{MPa}] \qquad \text{MOE} = 0.871 + 41.202\ V_f\ [\text{GPa}]$$

Sutanun et al. found that for *Dendrocalamus Asper* (Petung) among other tropical species, the fibre volume fraction increases linearly from the inside to the outside surface, whereas for Moso, the fibre distribution is non-linear[84].

Ghavami used DIP to derive a non-linear formulation of the fibre volume fraction V_f and MOE of *Dendrocalamus giganteus* using the rule of mixture [32]. A similar approach can be used for any bamboo species.

$$\left.\begin{aligned} \text{MOE}(r) &= E_f V_f(r) + E_m(1 - V_f(r)) \\ V_f(r) &= 49.8r^2 - 0.49r + 20.01 \end{aligned}\right\} \quad \begin{aligned} &E_f ...\text{MOE of fibre;} \quad E_m ...\text{MOE of matrix} \\ &r \in [0;1] ...\text{distance from inner culm surface} \end{aligned}$$

Silva et al. modelled the continuous radial change of Moso's MOE using graded FEM. They used different MOE distributions: One according to Nogata's power law, one with an average MOE using the integration of Nogata's power law, and a model using a homogenization method to obtain an elastic stiffness matrix. They concluded that an averaged MOE obtained from a rule of mixture provides enough accuracy to capture the global deflection of a bamboo structure. In order to estimate local features such as stresses near supports, bolted connections, etc., it is necessary to employ a more accurate FE model [82].

Mechanical Properties and Distribution of Vascular Bundles The amount of vascular bundles B is an indirect measure for the amount of fibres in the bamboo cross-section.

Lo et al. examined the compressive strength of Moso bamboo in relation to the number of vascular bundles, position along the culm, thickness, age and outside diameter. They found that compressive strength for Moso bamboo ranges between 45 and 65 MPa and can be related linearly to average number of vascular bundles and outside culm diameter [57][58]:

$$f_c(B) = 2.63\ B + 36\ \text{[MPa]} \qquad B \ldots \text{average number of vascular bundles per unit area;}$$
$$f_c(D_0) = -0.28\ D_0 + 71.5\ \text{[MPa]} \qquad D_0 \ldots \text{average outside diameter [mm]}$$

Huang et al. derived two linear formulas for MOE and tensile strength of Moso bamboo based on the distribution of vascular bundles B and rule of mixture[43].

$$\text{MOE}(B) = 0.389 + 28.998\ B\ \text{[GPa]}; \qquad f_t(B) = 10 + 475\ B\ \text{[MPa]}$$

Li and Shen extracted vascular bundles from different heights of Moso culms, deriving non linear formulas for the MOE and tensile strength of vascular bundles at different heights of the culm. The values they found were slightly lower than those of Nogata and Takahashi which they explained by different age and origin (Japan and China respectively) [54].

$$\text{MOE}(r) = a_1 r^3 + a_2 r^2 + a_3 r + a_4; \quad f_t(r) = a_1 r + a_2;$$
$r \in [0;1]$ distance from inner culm surface; $a_{1\ldots4}$ coefficients for position along the culm

Influence of Sample Size and Extraction Technique Ge at al investigated the effect of specimen size and extraction technique on the measured tensile strength and MOE of single fibres, fibre bundles and bamboo strips. [31]. They found that single fibres reach the highest capacity whereas bamboo strips result in the lowest capacities. Fracture occurred in the tissue (parenchyma matrix) between the single fibres. Therefore, rule of mixture should be considered only as a guideline for tensile strength and larger specimens need to be tested to obtain reliable strength values. Other factors that had an influence on measured strength were the extraction method of the fibres and the location of the bamboo strips (inside or outside surface of the culm). Chemical extraction resulted in higher strength than mechanical extraction.

2.2.1.3 Conclusions

It can be concluded that bamboo is a natural FGM. The fibre volume fraction increases from the inside surface to the outside surface of the culm and generally increases from the bottom to the top of the culm. The shape of the distribution curve is species dependent. For Moso, a non-linear distribution seems to fit best. Several material properties such as MOE, tensile strength and compressive strength are directly correlated to fibre content. Applying the rule of mixture, linear relationships for a mechanical property X and fibre volume fraction V_f can be derived:

$$X(r,z) = X_f V_f(r,z) + X_m(1 - V_f(r,z));$$
$V_f(r,z)$... fibre volume fraction along the thickness r and height z of the culm
X_f... property of the fibre; X_m... property of the matrix

The exact fibre distribution is hard to determine. Alternatively, the distribution of vascular bundles can be determined, which can easily be done by DIP. Subsequently, the volume fraction of vascular bundles can be related to fibre volume fraction or directly to mechanical properties.

Note that vascular bundles change shape across the culm wall thickness and that their composition of vessels and fibres is generally not constant. DIP therefore generally results in less accuracy than manual microscopic determination of the fibre distribution. The measurement of properties of the fibre X_f is also connected to some difficulties, as measurement of mechanical properties of a single fibre or fibre bundle depends on sample size and extraction technique. Therefore, the researcher has to make a compromise between experimental effort and accuracy of the results.

For overall culm strength and stiffness, average properties provide conservative model input values. In order to obtain local stress and deformation peaks, e.g. close to a bolted connector, the functionally graded microstructure needs to be modelled accurately. Alternatively, full scale experiments can be conducted.

2.2.2 Relationships between Mechanical and Physical Properties

Several attempts were made to relate mechanical properties directly to physical or mechanical properties that can be measured non-destructively (e.g. density, moisture content or dynamic MOE), avoiding destructive testing and exact determination of fibre distribution in the future.

2.2.2.1 Mechanical Properties and Density

In his PhD thesis of 1981, Janssen made the first attempt to derive species independent "rules of thumb" for mean strength of air-dried bamboo, relating compression and shear strength of the full-culm internode and bending strength of 5 m culms directly to density [kg/m^3] [46].

$$\text{compression: } f_c = 0.091\ \rho \quad \text{bending: } f_m = 0.14\ \rho \quad \text{shear: } f_v = 0.021\ \rho$$

Yu et al. related tensile strength and MOE of Moso bamboo dog-bone specimens directly to air-dried density [g/cm^3] producing the two linear relationships below [102]. A more detailed report of research on tensile properties can be found in appendix B.1.

$$\text{MOE} = 41.956\ \rho - 18.431; \quad f_t = 334.941\ \rho - 93.866$$

Mechanical Properties and Age Correal et al. tried to quantify the effect of age and position along the culm on density, compression, bending and shear strength of *Guadua angustifolia*. They concluded that for ages between 2 to 5 years, regardless of age, the top portion of the culm shows maximum strength (compression, shear and bending) and MOE. Regardless of culm position, the optimal age for harvesting seems to be between 3 and 4 years as mechanical properties were highest and remained almost constant at that age. For culms older than 5 years, mechanical properties started to decrease due to ageing effects and dying of fibres [14].

2.2.2.2 Mechanical Properties and Moisture Content

Chung and Yu investigated the influence of the moisture content, wall thickness and position along the culm on the characteristic bending and compression strength of *Bambusa Pervariabilis* and *Phyllostachys pubescens* (Moso). They concluded that increase in moisture content leads to a significant decrease in compression and bending strength until fibre saturation is reached. Additionally, they found that physical and mechanical properties are broadly constant along the culm length for *Bambusa Pervariabilis* but vary significantly for *Phyllostachys pubescens*[2]. While

[2]Nevertheless it can be assumed that samples of same diameter, thickness and moisture content should produce similar strength results – provided that their fibre content is approximately the same, which brings us back to the need of microscopic investigation.

cross-sectional area stayed almost constant for *Bambusa Pervariabilis*, it decreased significantly for *Phyllostachys pubescens* bamboo. The same observation was made for moisture content [11].

The effects of moisture content on mechanical properties were explicitly examined by Gonzalez et al. [35], Jiang et al. [24] and Wang et al. [97][96]. Gonzalez et al. found that tensile strength of Guadua dog-bone specimens increases with moisture content up to the equilibrium moisture content and decreases above the fibre saturation point [35]. Jiang at al investigated the effect of change of moisture content below the fibre saturation point on several mechanical properties of small Moso specimens. They found that compressive and shear strength are most sensitive to change in moisture content leading to a decrease in strength for an increase of moisture content [24]. Wang et al. conducted simple mechanical experiments on bamboo strips to derive the compressive MOE of Moso bamboo. They also carried out nano indentation tests to determine the indentation Modulus of Elasticity and hardness. They found that all properties were negatively correlated to moisture content and that MOE was most sensitive [97]. In a later study, Wang et al. conducted a regression analysis on compressive strength, moisture content and density of Moso bamboo, producing the following relationship [96]:

$$f_c/\rho = 76.62 + \frac{739.90 - 76.62}{1 + e^{(MC+13.46)/7.6296}}$$

2.2.2.3 Mechanical Properties and Dynamic Modulus of Elasticity

The dynamic Modulus of Elasticity (E_{dyn}) is determined by vibration measurements and can be related to the static Modulus of Elasticity (E_{static}). While common practice in timber engineering, NDT i.e. use of E_{dyn} to determine E_{static} is a relatively new approach in bamboo engineering. To the present date, only Lin et al. found significant positive relationships between density, drilling resistance, E_{dyn}, E_{static} from three point bending and Modulus of Rupture, although coefficients of determination (R^2) were small in most cases [56]. Two interesting relations that relate E_{static} to density, and E_{static} to E_{dyn} are presented in the following (note that MOE from three-point bending contains a shear contribution, which cannot be neglected for bending of bamboo culms [30]!):

$$E_{static} = 10.3\ \rho + 2767.3; \qquad R^2 = 0.54$$
$$E_{static} = 0.6\ E_{dyn} + 1284.4; \quad R^2 = 0.75$$

Trujillo presented a research proposal in which he refers to several previous studies that related physical and mechanical properties. As factors that affect the strength of bamboo he names species, maturity, position along the culm, node or internode material. position within the culm wall, density, load duration, geometric deviations, and splitting[3]. He states that in principle it is possible to derive the strength of an individual bamboo element from NDT, which is the basis to machine strength grading and a strength classification system which is common practice in timber engineering. However, this requires hundreds of tests results from destructive tests. Therefore, Trujillo calls for an international concerted effort to complete this task [86].

2.2.2.4 Conclusions

It can be concluded that correlations of density and strength and stiffness exist, although their significance needs to be addressed in detail. Increase of moisture content clearly has a negative effect on strength and stiffness below fibre saturation point. Yet, more research needs to be done to derive relationships between physical and mechanical properties that can be obtained by means of NDT and those that require destructive testing.

[3]He states that splitting reduces bending, shear and compression resistance, though it could be argued that splitting is merely a failure mechanism for those strength properties

2.2.3 Influence of Nodes

Ray et al. state that the fibres in the nodes are randomly oriented instead of unidirectional which imparts isotropic properties [68]. They emphasize the need to examine both microscopic and macroscopic structure of bamboo, as bamboo is a "*both macroscopically and microscopically functionally graded biomaterial*" and both "*macroscopic and microscopic structure of bamboo* [are] *quite complicated*". Following this approach, first the microscopic structure of nodes in presented and then linked to the macroscopic influence of nodes on mechanical properties.

2.2.3.1 Microscopic Nodal Structure

Liese et al. studied the anatomy of nodes of different species in 1971 [37]. They found that *"most of the bundles inside the diaphragm originate from the inner part of the culm but some bundles from the periphery bend also radially and pass into the diaphragm"* (figure 2.6). In the node itself, the fibre bundles form an *"irregular interwoven texture"*. In the INBAR Technical

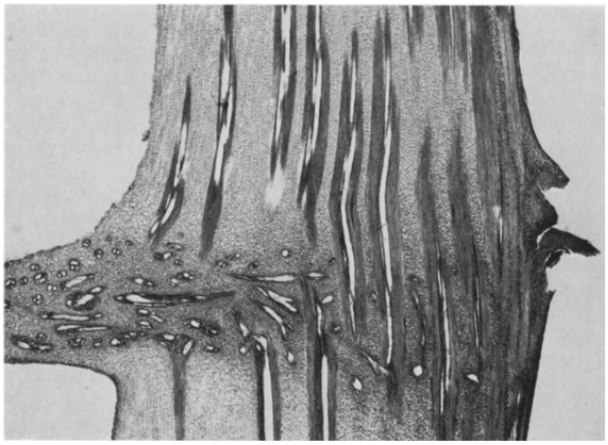

(a) Vascular bundles in node (Liese, 1971)

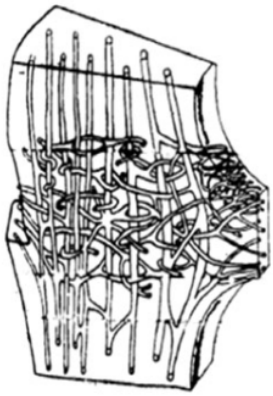

(b) Model of vascular bundles (Liese, 1998 [55])

Figure 2.6: Node Liese et al.

Report No. 18, Liese provides more information on the fibre structure in the node [55]. He states that *"most of the vascular bundles pass directly from an internode through the node into the next internode"*. Additionally he found, that close to the outside culm wall, fibres bend outwards and some branch into the sheath[4]. Close to the inside culm wall, fibres connect to those in the diaphragm. At the upper part of the diaphragm, *"small bundles turn horizontally and twist repeatedly"* which can be seen in figure 2.6b. Although the morphology of culm nodes is different for different species and the diaphragms can be plane, concave or convex, all studied species seemed to have common features regarding fibre orientation.

Amada et al. studied the microscopic structure of Moso nodes in 1997 [3]. They found that the reinforcing fibres are axially oriented in the internode, whereas in the nodes the fibres become *"entangled in a complicated manner"*, thereby producing *"nodes with isotropic properties that provide additional reinforcement for the culm"*. They found that the fibres enter the node from the lower part of the culm. Here they become entangled and randomly oriented. Eventually, the fibres continue into the upper part of the culm (figure 2.7a). The isotropic behaviour was tested by tensile tests of specimens at various radial locations in the node. They found a tensile strength of 29 ± 4.5MPa and a tensile MOE of 2.22 ± 0.3GPa with little variation at the different locations. They concluded that the fibres have no reinforcing effect, as tensile strength of the

[4]Part of the node at the outside culm wall where leaves emerge

node material was only half the strength of the internode material. However, this conclusion only holds for tensile capacity.

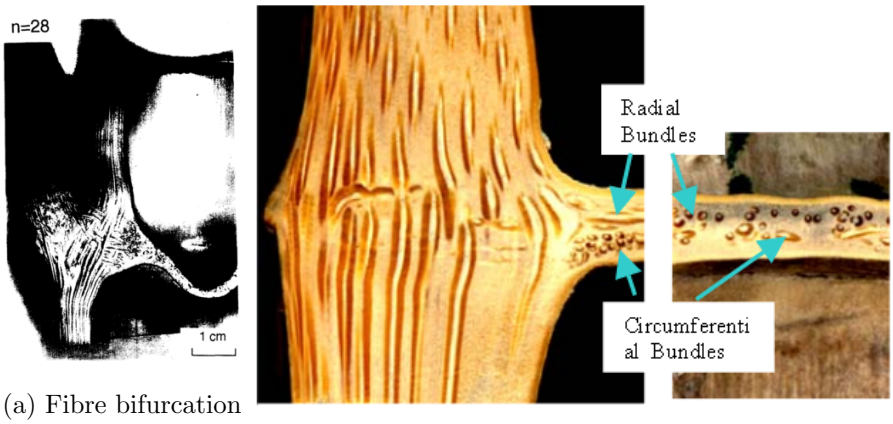

(a) Fibre bifurcation (Amada et al., 1997) (b) Fibre orientation in Moso node (Ghavami et al., 2003)

Figure 2.7: Cross-sections of Moso nodes

Ghavami et al. studied nodes of Moso in 2003 [33]. He observed that the fibres run *"along the length of the culm with interruptions at the node"*. Similar to Liese's observations, fibres closer to the outside culm wall were found to bend at the node. While fibre bundles in the upper part of the diaphragm were found to run along the circumferential direction, fibres in the bottom were oriented in radial direction. It seems that Ghavami's figure is placed upside down.

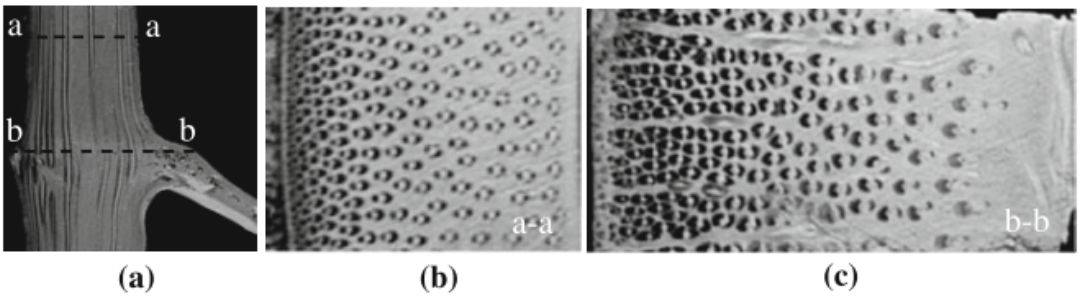

Figure 2.8: Vascular bundles in Moso node (Wang et al., 2013)

Wang et al. investigated the toughness contribution of the bamboo node to the Mode I fracture toughness of Moso [95]. They found that Mode I toughness is low along the grain of the bamboo internode, but that the node can hinder the interlaminar crack propagation. They explained this by the differences in the microstructure. In the internode, the fracture resistance comes from three interfaces: matrix to matrix, matrix to vascular bundle, and vascular bundle to vascular bundle. In the nodes, additional resistance is provided by transverse vascular bundles (figure 2.8). They found that the Mode I interlaminar fracture toughness of bamboo node specimens was 1.87 times higher than that of the internode specimens.

2.2.3.2 Macroscopic Influence of Nodes

There is general consensus that nodes cause the tensile capacity to decrease [77][99]) [32]. But what effect do nodes have on splitting, shear and compression capacity and can they serve as natural reinforcement in bolted connections?

In his PhD thesis of 2010, Sharma states that tensile splitting is often the governing failure mode of bamboo members as well as bamboo joints [81]. Mitch's split pin test of 2009 indicates that the tensile splitting capacity of clear samples is much smaller than the shear capacity of a similar sample [62]. This agrees with the finding of Shao et al. [79] and Wang et al. [94] who found a Mode I interlaminar fracture toughness of $G_{IC} = 358\text{J/m}^2$ and a Mode II interlaminar fracture toughness of $G_{IIC} = 1303\text{J/m}^2$ of clear Moso samples. Wang et al. also reported an increased Mode I interlaminar fracture toughness of the node of $G_{IC,node} = 1431\ \text{J/m}^2$ and $G_{IC,clear} = 498\ \text{J/m}^2$ for the internode [95]. These findings explain, why splitting is the prevailing failure mode and that nodes can increase splitting capacity.

Controversial opinions exist on the influence of nodes on shear capacity. Moreira et al. report that shear planes can freely develop in the parenchyma cells of the nodes while propagation of tensile splitting is hindered by radially and circumferentially oriented nodal fibres [63]. However, this statement is contradicted by Shao et al. [77] who found increased shear strength in Moso nodes.

Another strength property that is influenced by nodes is the compressive strength of full bamboo culms. In 2008, Ghavami conducted tensile and compressive tests according to the ISO 2004b standard on *Guadua angustifolia* specimens with and without nodes (table B.2) [32]. The findings suggest that nodes decrease tensile as well as compressive strength. Shao et al. [77] conducted experiments on small samples of *Phyllostachys pubescens*. They found decreased tensile strength but slightly increased compressive strength (table B.4). These findings seem to contradict each other, but as sample size and species were different, it is impossible to make a direct comparison.

Due to the changed fibre orientation, it seems logical to expect a natural reinforcing effect of the node in connections. Widyowijatnoko meant to exploit this property in his tensile lashing joint (figure 2.9) [99]. However, the connector makes use of full-culm radial compression strength rather than the reinforcing nature of the node. Widyowijatnoko assumed that this configuration would result in the highest strength without specifically exploring the benefit of placing his connector behind a node. The connector was only tested as a whole and the observations can thus not be extrapolated to bolted joints.

Figure 2.9: Multi-knot lashing joint (Widyowijatnoko, 2012)

2.2.3.3 Conclusions

The microstructure of nodes is substantially different from the internode, with fibres deviating from the axial orientation. Nodes seem to decrease overall tensile capacity and increase splitting capacity. Controversial opinions exist on the influence on full-culm shear and compression capacity and it is not clear whether nodes can be used to reinforce bolted connections.

2.2.4 Material Properties and Probabilistic Design

In the past, several attempts were made to establish design strength values for Moso and Guadua bamboo. Chung and Yu conducted tests in compression and bending establishing design values of both the strength and the MOE for Moso [11]. Yu et al. proposed a method to derive design values for the column buckling strength of Moso comparing EC3, EC5 and the British

Steel Code BS5950 [103]. Luna et al. derived design stresses and a characteristic MOE as an addition to the Colombian building code for Guadua[59]. An extensive study on the reliability of strength values was conducted by Sharma[81]: In his PhD report of 2010, a broad overview of geometrical, physical and mechanical properties of various common bamboo species is given[5]. The values are filtered based on the amount of data sources, range of results compared to other data, and up-to-dateness of the applied test method. The standard deviation of the remaining sources is computed (fitting a Gauss or Weibull distribution) which allows for the derivation of characteristic strength values. Sharma concluded that the reliability of data is strongly dependent on the source (operator, testing parameter and conditions) and that standardization of test methods is essential for comparability of test results. He further stated that more research needs to be done in order to establish a material database.

2.2.5 Discussion and Conclusion

The present literature review summarizes findings from previous research concerning material properties of *Phyllostachys pubescens* and *Guadua angustifolia*. Bamboo is a FGM that is able to perform well under axial loading and there are indications that nodes can reduce susceptibility to splitting. Several relationships between mechanical properties and fibre content have been established. However, the challenge remains to generally predict mechanical properties and relate them to other material properties, i.e. the ones that can be obtained by NDT. Many factors affect mechanical properties of bamboo: Already a different origin can have effects on strength as shown in the example of Nogata and Silva. Additionally, strength is strongly dependent on culm geometry, age, moisture content, etc., which makes it hard to compare and extrapolate results from one research to another. According to Sharma, the empirical relationships between geometrical, physical and mechanical properties are not applicable beyond a tested species [81]. While for one species, correlation of two properties might be significant, for another species, the same properties might lack correlation all together. Therefore, one has to be careful when applying the "rules of thumb" derived by Janssen in his PhD thesis of 1981 [46]. Instead, the author of this thesis advises to obtain material properties individually for a certain species according to the ISO 2004b standard and reporting the given boundary conditions. This way, different results from literature can be compared and funnelled into a bamboo design code.

In terms of structural safety, decisions have to be made on how to establish material safety factors to implement in building codes. Janssen argues, that the wide spread of bamboo strength values results in higher structural safety in case of extreme events (e.g. earthquakes), as characteristic strength values are low[47]. However, this is a very inefficient approach for all other limit states and the goal should be to reduce scatter of test results and increase reliability. Subsequently, partial safety factors should be derived that reflect the scatter of test results and loads, and the desired reliability of a structure.

[5]Sharma refers to the database GNOCMAT which provides a collection of test results

2.3 Bamboo Tensile Connectors

One of the most challenging parts of designing bamboo structures is the joint design, especially for joints that need to transfer tensile loads. While bamboo fibres can reach the specific tensile strength of mild steel, its shear and splitting capacity are very low. Especially bolted connections are susceptible to tensile splitting, which is a brittle and potentially dangerous failure mode[6] [62][63]. Glueing or mortar injection can be problematic as the bond is only established with the stiff cellulose fibres that tend to get ripped out of the soft matrix, especially when adhesives are applied at the inside culm wall where fibre density is low [4]. The goal is thus to design a joint that makes it possible to exploit the full tensile strength of the bamboo culm without splitting or crushing it [99]. Additional challenges are the smooth outer surface of the culm, its round geometry and variation in culm diameter and wall thickness.

Several connector types have been suggested in literature but only few are suitable for the multi-way tensile joints employed in geodesic domes. In the following, different tensile connectors will be presented and their performance will be discussed. Also potentially suitable connectors for round timber logs are included, as the geometry and physical structure of timber logs is very close to full-culm bamboo. Patented connectors are excluded as they are not affordable for the target group of this research.

The following performance criteria are used to assess the suitability of a connector:

- tensile strength of entire connector
- stiffness (relative slip, displacement)
- failure mode (brittle, ductile)
- availability of components and material costs
- ease of connector assembly (required workmanship and labour intensity)
- weight

Additional criteria for geodesic dome application:

- modular design: ease of initial assembly and maintenance / strut replacement[7]
- suitability for dome hub connection without (large) eccentricities
- transfer of compressive forces by contact

[6] Certain applications require ductility and plastic deformation capacity that allows for redistribution of stresses. Examples are statically undetermined structures or dynamic actions including earthquakes.

[7] The limited durability or bamboo calls for the ability to replace single members if necessary.

2.3.1 Gutierrez Joint

The Gutierrez joint is not a bamboo tensile connector as such, as it transfers tensile forces employing steel elements and only makes use of the bamboo culm in compression and bending (figure 2.10) [49]. Transmission of shear or tensile forces by the bamboo element is fully avoided. A steel bar passes through the culm (which requires drilling of the diaphragms) and an end plate is welded to the bar at each end of the culm. The joint can be adapted by using a threaded bar and nuts that pre-tighten the end plates to the culm. This avoids the stiff and labour intensive weld and allows for a connection to a geodesic dome hub. Generally, the tensile capacity of bamboo culms is much higher than the compressive capacity and it seems somewhat strange not to make use of this material property. The goal of this study is the development of a connector that employs the tensile strength of bamboo itself. Therefore, the Gutierrez joint will not be considered any further.

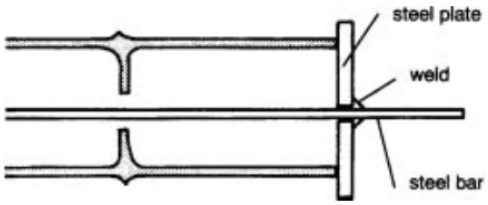

Figure 2.10: Gutierrez Joint (INBAR Technical Report No 16 [49])

2.3.2 Wood-Plug Joint by Arce-Villalobos 1993 TU Eindhoven

Arce-Villalobos proposed a wood-plug joint that is able to adapt to variation of the culm diameter while distributing axial loads to the fibres [4]. A round wood plug is glued to the inside wall of the bamboo culm (figure 2.11). The other end of the plug can be connected in a standard timber connection and verified according to timber codes, e.g. Eurocode 5.

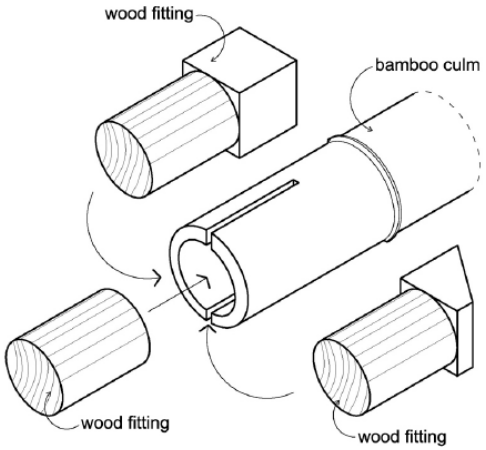

Figure 2.11: Wood-Plug joint by Arce-Villalobos (Arce-Villalobos, 1993)

Arce-Villalobos discovered that only the innermost layer of the bamboo culm takes the stresses from the glue and that shear failure in the matrix between the fibres prevails. Even when strong adhesives are used, the maximum joint capacity is quickly reached as fibres get ripped out of the matrix long before the tensile capacity of bamboo is exploited. Under compression the joint behaviour is favourable as crushing of the culm is prevented by the wood-plug. As this connector requires grinding of the inner culm surface and individual fitting of the wood plug, work intensity is high, especially if many joints need to be manufactured.

2.3.3 Cement Injection Joint and Bolted Joints studied by Fu et al. 2012

Fu et al. studied three different joints [29]: a cement injection joint, a bolted joint and groove-plate joint (figure 2.12). They concluded that both bolted connections failed in brittle tensile splitting (figure 2.13b) while the cement plug failed in more ductile relative slip between the plug and the culm (figure 2.13a).

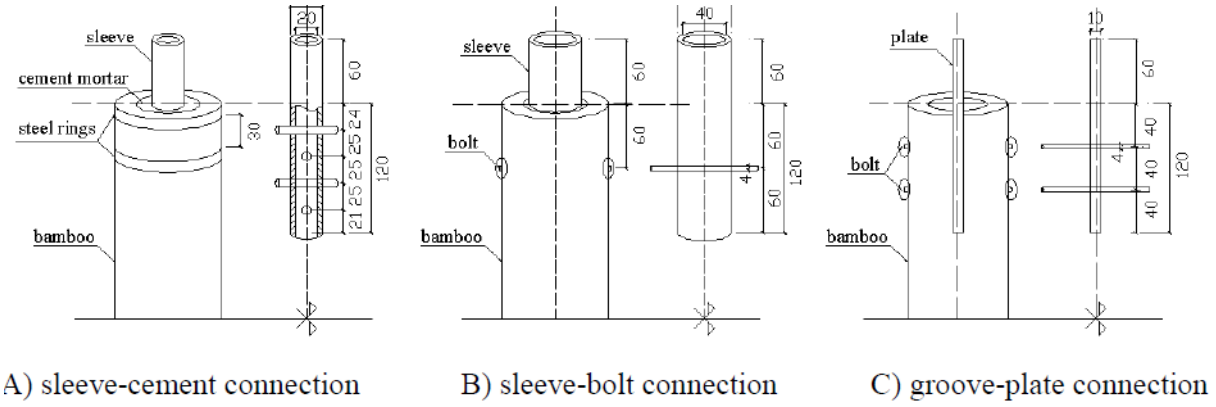

Figure 2.12: Connections studied by Fu et al. (Fu et al., 2012)

Similar to the wood-plug joint of Arce-Villalobos, the adhesive bond of the cement to the bamboo inside wall is limited at the cement-to-fibre and fibre-to-matrix interfaces. Cement injection introduces the additional disadvantage of cement paste shrinkage during drying which can cause premature joint failure. An improved version of the cement joint makes use of a cement injection behind the first node using the diaphragm as a natural cast (figure 2.13c). While cement joints are less labour intensive than the wood-plug joints, accuracy is much harder to achieve. Finally, added weight is the major disadvantage of this connector type, especially for high frequency geodesic domes that contain short struts and a high number of joints.

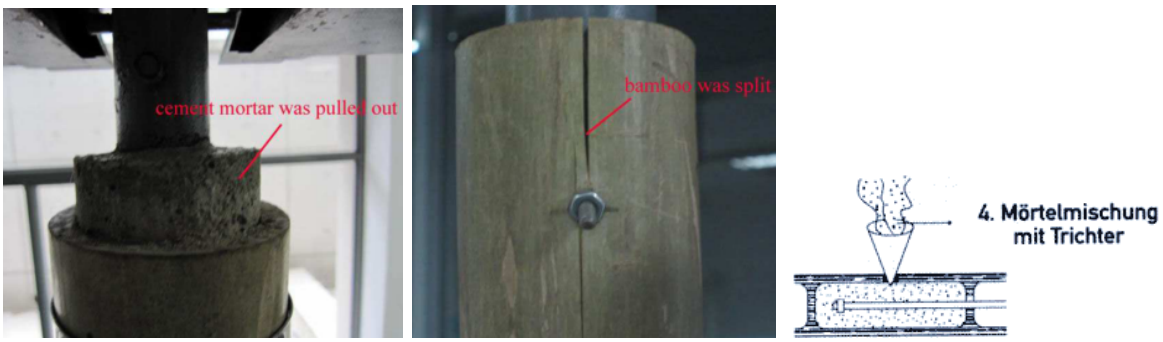

(a) Cement plug is pulled out (b) Splitting of bolted joint (c) Mortar injection in internode

Figure 2.13: (a) and (b): Failure modes of cement joint and bolted joint (Fu et al., 2012)
(c): Mortar injection joint employed in ZERI pavillon, EXPO 2000, designed by Simon Veléz [73]

2.3.4 Lashing Joint by Widyowijatnoko 2012 RWTH Aachen

Widyowijatnoko studied various existing joints and pointed out their advantages and disadvantages [99]. He proposed a new joint employing steel wire lashing which transforms axial tensile forces into a radial compression force (figure 2.14). The force is applied on the outer wall of the culm which is the strongest part of the culm due to its high fibre content. The wire is attached to a ring on the inside of the culm that connects to a threaded rod. A steel cap at the end of the culm makes it possible to introduce compression forces by contact.

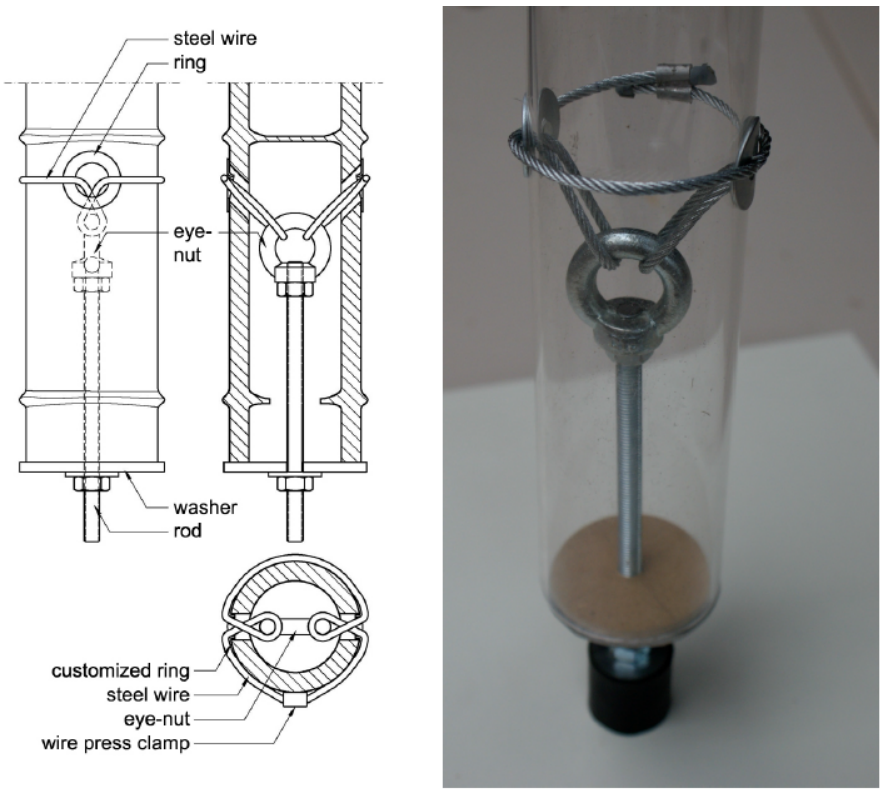

Figure 2.14: Lashing Joint with Eye-Bolt by Widyowijatnoko (Widyowijatnoko, 2012)

The main advantage of this join is its self tightening nature — as tensile forces get higher, radial compression is increased without introducing the risk of tensile splitting that comes with bolted connections. While being able to adapt to different culm diameters and non perfectly round shapes, the proposed joint avoids all problems related to adhesive based joints, such as cement injected or glued joints. Additionally, the joint is light and makes use of readily available components, providing a low-tech solution while maintaining adequate structural safety. The typical failure mechanism consisted of ovalization of the culm, the washers slipping into the holes and subsequent wires slicing through the culm (figure 2.15).

In practice, the connection should be designed in such a way that steel components are undermatched compared to the anticipated bamboo strength. For example, the threaded rod diameter could be decreased such that the rod fails in ductile yielding prior to bamboo culm ovalization. This results in higher joint strength predictability [8] and provides plastic deformation capacity. Additionally, slip needs to be limited to provide sufficient stiffness. Another difficulty lies in the determination of the force flow as it is less straight forward than e.g. a bolted connection. Last

[8] Bamboo is a natural material, therefore test results show great scatter, leading to lower 5% values and higher material safety factors than for steel. If steel yielding in decisive, the maximum joint strength can be predicted rather accurately.

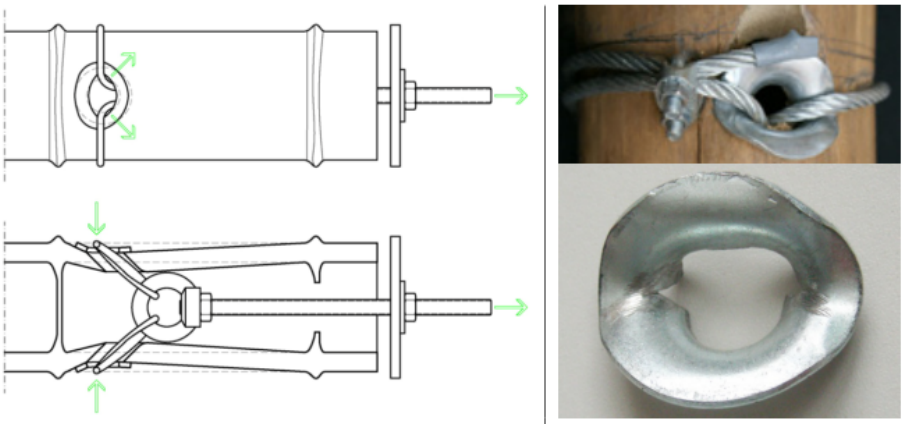

Figure 2.15: Lashing Joint with Eye-Bolt by Widyowijatnoko (Widyowijatnoko, 2012)

but not least, assembly becomes difficult especially when multi-knots are used to reach a higher joint capacity (figure 2.16). Still, this joint provides a high tensile capacity while using simple components. With small adaptations it is suitable for geodesic dome application.

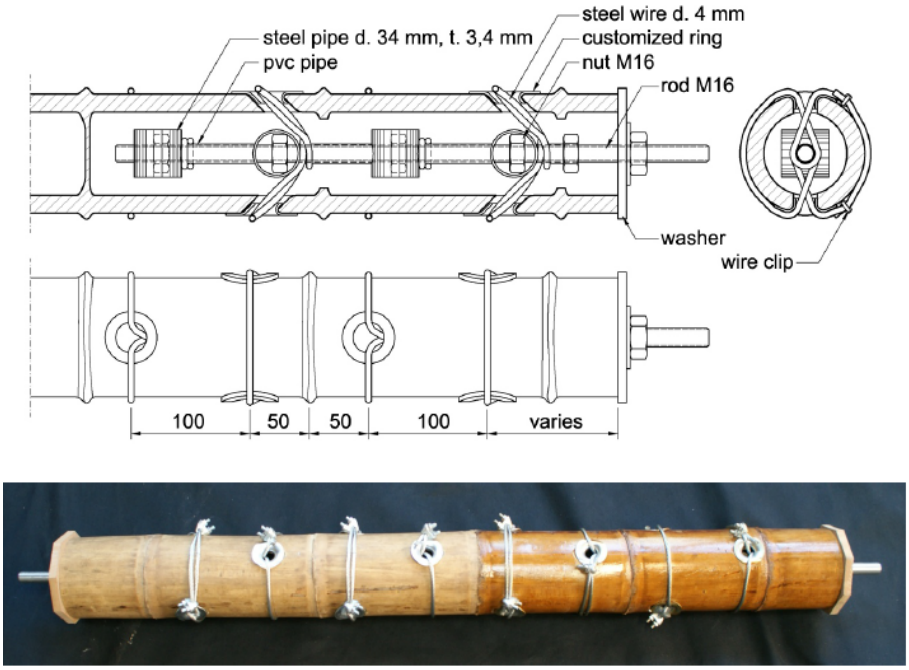

Figure 2.16: Multi-Knot Lashing Joint by Widyowijatnoko (Widyowijatnoko, 2012)

2.3.5 Timber Wire Lacing Joint by Huybers 1997 TU Delft

The wire lacing tool developed by Huybers [45] was employed in a timber log geodesic dome located in the botanical garden in Delft, the Netherlands (figure 2.17a). At both ends of each log, a steel strip is inserted and fastened with the wire (figure 2.17c). The strips are attached to flat steel discs with bolts making an easy assembly of 5-way and 6-way joints possible. The wire lacing was applied in order to provide a more ductile failure when splitting occurs. Almost all logs indeed show splitting at the ends (figure 2.17b).

(a) Timber log geodesic dome in Delft

(b) Severe splitting at log ends

(c) Wire lacing (Huybers, 1997)

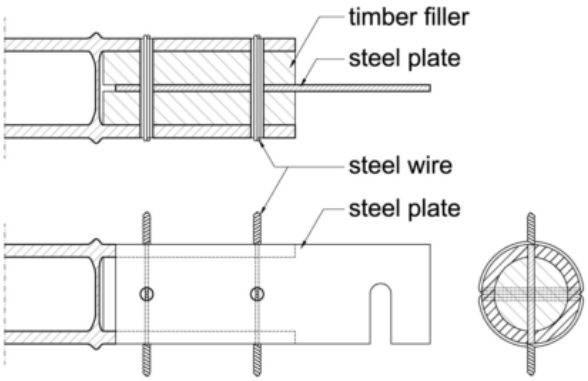

(d) Bamboo lacing joint (Widyowijatnoko 2012)

Figure 2.17: Applications of the wire lacing tool

In his PhD thesis of 2012, Widyowijatnoko proposes a joint configuration suitable for bamboo, employing a timber filler to prevent crushing (figure 2.17d). As the timber filler needs to be fitted to the culm geometry, this configuration becomes labour intensive.

Sonti reports the application of the wire lacing tool in the construction of a bamboo geodesic dome in India, spanning a diameter of 18 metres and a height of 9 metres [1]. He advertises the system to be *"simple and inexpensive"* and claims that all tendencies to splitting are avoided. This stands in contradiction to the observations made in the application in Delft (figure 2.17b). As information dates back to more than 35 years ago and pictures were not available, it was not possible to verify Sonti's statement.

Applying enough pre-stress in the lacing to prevent splitting and achieve stiffness of the connector seems to be extremely difficult as mentioned by TU Delft staff that worked with the wire lacing tool previously. The lacing does not have a self-tightening effect like lashing and is prone to corrosion unless expensive stainless steel or coating is applied. Last but not least, applying lacing is labour intensive, especially when a timber filler is inserted.

2.3.6 Timber Cross Dowel Joint by de Vries 2000 TU Delft

This bolted round wood connector was designed by Peter de Vries as part of his graduation thesis of 2000 at TU Delft [91]. The joint was developed for thin timber logs in order to build outlook posts up to 25 m height. An anchor rod is fastened by square cross dowels that penetrate the log transversely (figure 2.18a). An end plate is pre-tightened to the end of the log to prevent slip. Similar to the lashing joint of Widyowijatnoko, the cross dowel joint is very suitable for dome hub connection. Furthermore, it is easy to assemble and the force flow is straight forward.

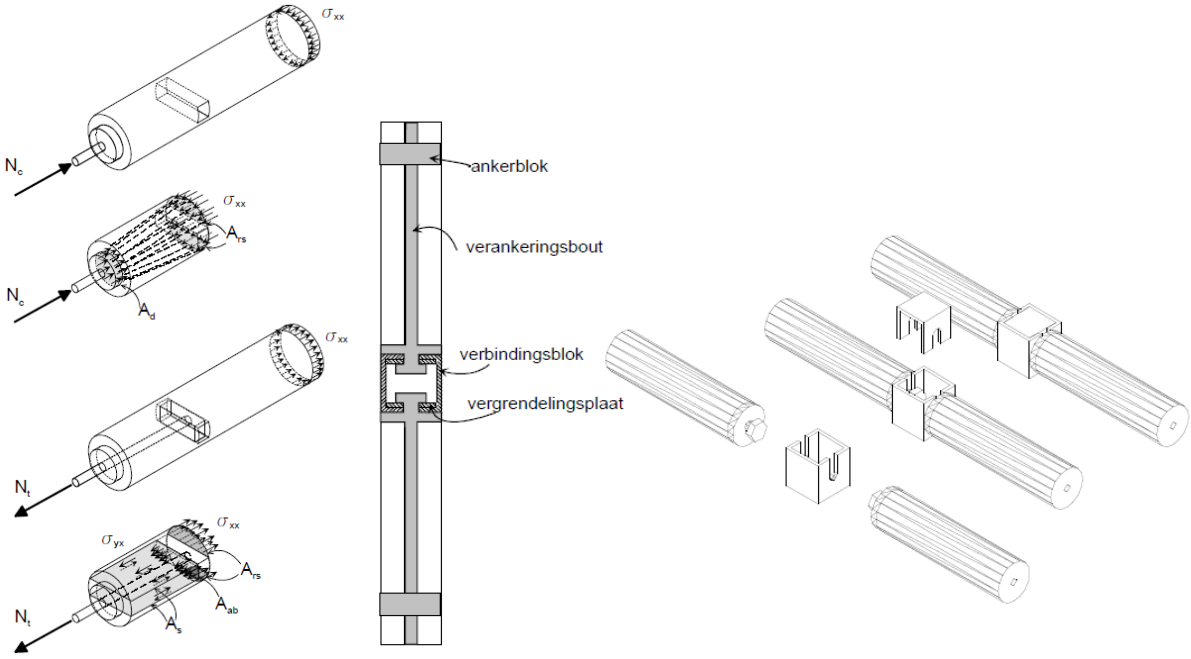

(a) Force flow in connector

(b) Axial connection of two logs

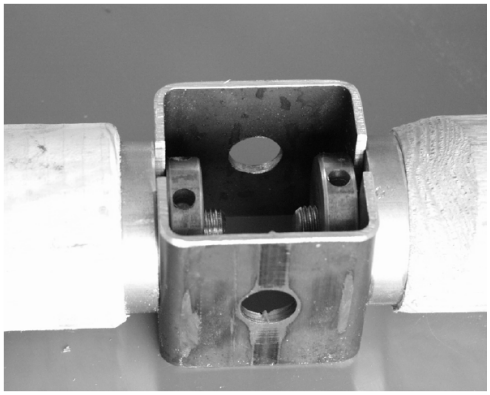

(c) Photograph of assembled connection

Figure 2.18: Round wood connector by de Vries (de Vries,2000) [91]

2.3.7 Summary and Conclusions

Designing tensile joints is challenging. The outer layer of the bamboo culm wall has the highest fibre content and is therefore the ideal location to introduce axial forces. However, the outer culm surface is smooth and hard, making adhesive bond difficult. Any form of bolted connection is susceptible to shear and splitting failure [62], both of which are brittle and thus dangerous failure modes. Additionally, connectors need to be adaptable to variation in culm diameter and wall thickness. The load application should avoid eccentricities and the force flow should be clear so that components can be verified individually. For geodesic dome application, the connector needs to be able to connect to a dome hub, transmitting both tensile and compressive forces.

Table 2.1 summarizes the advantages and disadvantages of the connectors presented above.

Table 2.1: Comparison of different connectors

Type	advantages	disadvantages
Guiterrez Joint	easy to make	doesn't use bamboo tensile strength
Wood-Plug Joint	prevents compressive crushing	work intensive (expensive) fibres get ripped out few fibres at inside culm wall: small bond surface
Cement injection	easy to make cheap	shrinkage of concrete reduces bond added weight
Lashing joint	radial compression avoids bolts	difficult to assemble force flow not straight forward
Lacing joint	cheap components	difficult to tighten work intensive
Bolted joints	well known from timber engineering	tendency to splitting

In the final decision, geodesic dome application becomes decisive: All work intensive joints are excluded as even low frequency domes require a large amount of connectors. The same argument holds for added weight. This results only in two suitable joints: The lacing joint and the bolted joint. As the lacing joint was already explored in detail by Widyowijatnoko, it is more interesting to propose a new bolted connector.

Bolted joints are common practice in timber engineering; they have proven to be safe, and strength can be predicted rather accurately. A connector similar to de Vries' round wood joint is much easier to assemble than a lashing or lacing joint and the force flow is straight forward. Splitting and shear are two failure mechanisms that are brittle and potentially dangerous and should be further explored in experiments. In the final joint design, it is favourable if embedment is the governing failure mode for bamboo as this reduces scatter. While square cross dowel proved very suitable for round wood, square holes introduce stress concentrations in the corners. These stress concentrations could cause tensile splitting. On the other hand, the embedment surface of square holes is predefined which is not the case for round boles. It is not possible to predict the behaviour of round and square bolts *a priori*. Therefore, bolt shear tests with both square and round bolts should be conducted.

Nodes are often used as a natural cast for mortar injection joints. A logical step is the application of nodes as natural reinforcement in bolted connections which was also suggested by Widyowijatnoko [99]. However, there is little knowledge on the influence of nodes on full-culm mechanical properties. Therefore, it is proposed to investigate the effect of nodes on full-culm compressive strength, and bolt embedment and splitting strength. Additionally, the nodal microstructure of nodes should be examined in order to understand findings from full-culm tests.

Chapter 3

Literature Research Geodesic Domes

First, the historical background of geodesic domes is presented in chapter 3.1. The general concept and geometry of geodesic domes is explained in chapter 3.2. In chapter 3.3, research on bamboo geodesic domes is presented, which was used as inspiration for the geodesic dome model.

3.1 History of Geodesic Domes

Buckminster Fuller is often mistaken to be the inventor of geodesic domes. Despite of his impressive work on tensegrity structures and geodesic domes, Buckminster Fuller only named the structure "geodesic" and thus invented the name "geodesic dome". Walther Bauersfeld is known to be the first architect to construct a geodesic dome in 1926. It was constructed in Jena, Germany and served as a planetarium. More information regarding the history of geodesic domes can be found on `https://simplydifferently.org/`[1] and `http://mathworld.wolfram.com/GeodesicDome.html`[1]. The Buckminster Fuller Institute provides more information on Buckminster Fuller's lifework `https://bfi.org/`[1].

3.2 Geodesic Dome Geometry

An introduction to the geometry of geodesic domes by Tom Davis [17] can be found on `http://www.geometer.org/mathcircles`[1]. For those interested in the underlying Geodesic Math, it is suggested to study the excerpt of an article by Joe Clinton provided by Jay Salsburg [74].

Geodesic domes are based on triangular platonic solids – objects that try to approximate the shape of a sphere while their surfaces consist of equilateral triangles (figure 3.1). If a principle side of one such triangle is subdivided, more vertices (corners) are introduced which are then projected onto the surface of the initial sphere and connected by new segments (struts) to form new triangles. Those new triangles are not equilateral any more, but some struts will be a bit longer and some will be a bit shorter. The number of subdivisions of the initial triangle is called frequency ƒ and is often indicated in textbooks as $V1$ (initial triangle), $V2$ (three smaller triangles where a principle side is subdivided into two segments), etc. (figure 3.2).

[1] last accessed January 30, 2015

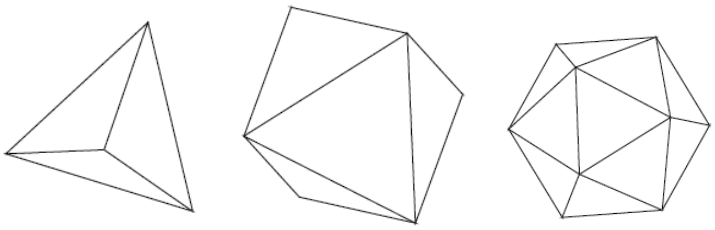

(a) Tetrahedron (b) Octahedron (c) Icosahedron

Figure 3.1: Platonic Solids (Tom Davis, 2011)

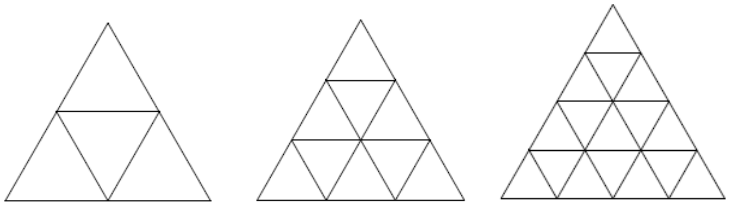

(a) $\mathfrak{f} = 2$ (V2) (b) $\mathfrak{f} = 3$ (V3) (c) $\mathfrak{f} = 4$ (V4)

Figure 3.2: Dome frequencies (Tom Davis, 2011)

Icosahedron-based geodesic domes provide a smooth approximation of the sphere as the strut length doesn‘t vary too much. However, also a tetrahedron or octahedron can be used as initial Platonic solid. Often icosahedron-based geodesic polyhedra are truncated at their equator to create a dome. However, only even frequencies provide horizontal struts at the equator and create some sort of base edge beam (figure 3.3a). For odd frequencies, a perimeter above or below the equator has to be chosen or new struts need to be inserted at the equator (figure 3.3b).

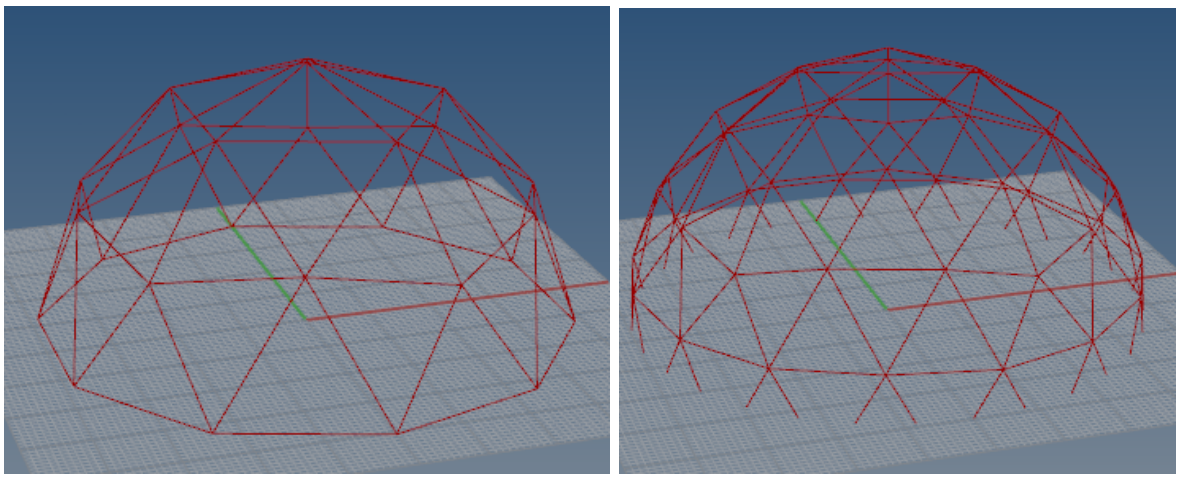

(a) $\mathfrak{f} = 2$: Horizontal struts at the equator (b) $\mathfrak{f} = 3$: Struts are cut into half at the equator

Figure 3.3: Icosahedron-based geodesic domes

3.3 Bamboo Geodesic Domes

This chapter provides an overview of bamboo geodesic domes and domes that could theoretically be made out of bamboo.

3.3.1 Bamboo Geodesic Dome Employing Wire Lacing Tool 1988

Sonti reports the construction of a bamboo geodesic dome in India, spanning a diameter of 18 metres and a height of 9 metres [1]. Unfortunately, it was not possible to find more information or pictures of this dome (see also chapter 2.3).

3.3.2 EWB Pabal Dome: Steel (2009) and Bamboo (2010)

In his MSc thesis of 2009, Kubik suggests a geodesic dome variant called "Pabal dome" for earthquake prone areas in India which was realized in an initiative of Engineers Without Borders (EWB). Kubik proposes a design made of steel, chicken wire and concrete (figure 3.4a)[52]. In 2010, Drake et al. suggested a Pabal dome variant made out of locally available bamboo and constructed a prototype. The design deviates from the classical geodesic dome, using a Hexagon as a base plan, providing straight walls (figure 3.4b). Their goal was to provide a low-tech construction kit, including pre-fabricated connectors, tools and an instruction manual, enabling unskilled locals to build their own home. According to Drake et al., one of the major challenges was to design an easy-to-assemble joint that provided sufficient stiffness [20]. Though not strictly a geodesic dome, this hut is a good example of the do-it-yourself characteristics that many small-scale geodesic domes have. An improved version of the hut provides a promising solution for low-skilled and low-income people of the Pabal region.

(a) Steel and concrete Pabal dome (Kubik, 2009)

(b) Bamboo Pabal dome variant (Drake et al. 2010)

Figure 3.4: Pabal dome variants

3.3.3 BSc Project: Dismountable Bamboo Geodesic Dome 2012

Kushwaha designed, verified and constructed a dismountable bamboo geodesic dome in Delhi, India [53]. His BSc project report does not provide a complete structural analysis of the dome. Joints are verified for wind load acting normal on the struts (hydrostatic pressure). Verification for self-weight or added weight is not given. The dome is assembled and tested with sandbags representing the wind load as a vertical load. Additionally, Kushwaha designed and tested a tensile bolted dome connector (figure 3.5). The connector was tested under tensile load, trying to

assess shear capacity. However, only two of four samples failed by shear failure. Additionally a compression test resembling the ISO compression test[2] was carried out. Obviously, the proposed connector design is not able to transfer compressive forces as two hinges are introduced at each hub (one by the bolts and one by the rings). Subsequently, unacceptably large deformations occurred when the dome was assembled and loaded with sandbags (figure 3.6).

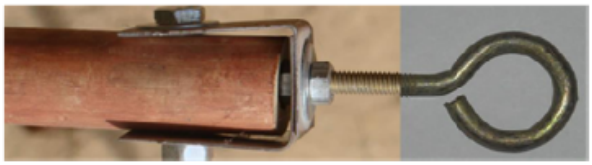

Figure 3.5: Dome connector (Kushwaha, 2012)

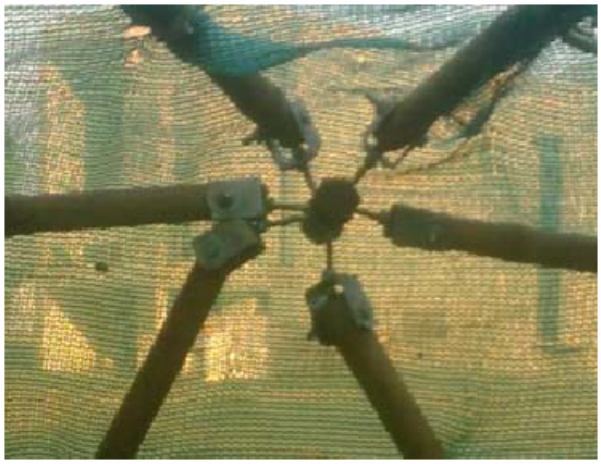

Figure 3.6: Strut displacement at dome hub (Kushwaha, 2012)

3.3.4 BSc Project: Structural Analysis of a Bamboo Dome 2013

Kraft designed and analysed a bamboo geodesic dome as part of his BSc project at the University of Stuttgart [51]. For the structural analysis he used the FE software *RStab* employing strength and stiffness values retrieved from literature. The applied load cases were self-weight, added weight, snow, wind, settlement and snow drift. Unity checks for bamboo members were conducted for tension and compression (including a reduction for slenderness representing buckling capacity) for several load combinations. Joint capacity of cement injected joints was taken from literature. The analysed dome spanned a diameter of 32 metres for *Guadua angustifolia* with a culm diameter of 17cm and a wall thickness of 1.7mm. As all unity checks were easily met, the given dimensions can serve as a guideline for the order of magnitude of the subsequent parametric study in chapter 5 and the case study in chapter 8.

[2]For more information on ISO tests see chapter 4.2

3.3.5 Geodesic Dome Hubs

Different hubs can be employed for bamboo geodesic domes. A possible configuration are metal strips that are connected to a round plate by bolts similar to figure 3.7. This dome hub does not provide much out-of-plane stability and requires exact fit of the struts.

Figure 3.7: Dome hub employed in Geodesic Timber Dome in Botanical Garden Delft

Another configuration is a thick steel ring similar to figure 3.8. This allows connecting the joints proposed by Widyowijatnoko and de Vries. Pre-tensioning of the threaded rods is possible, compression forces are transferred by contact. The last strut is fitted into the dome with the rod entirely screwed into the culm. By inserting a align-key fitting hole into the end of the threaded rods, these can be extracted from the bamboo culms and fastened by nuts. The dome hub itself should be made of a steel grade and thickness that will result in plastic deformation if the load bearing capacity of the structure is exceeded. This gives early signs of overloading and after removal of the excess load, the hub can be exchanged without damage done to the rest of the structure. More information regarding the connection of the proposed joint to such a dome hub can be found in chapter 7.3.

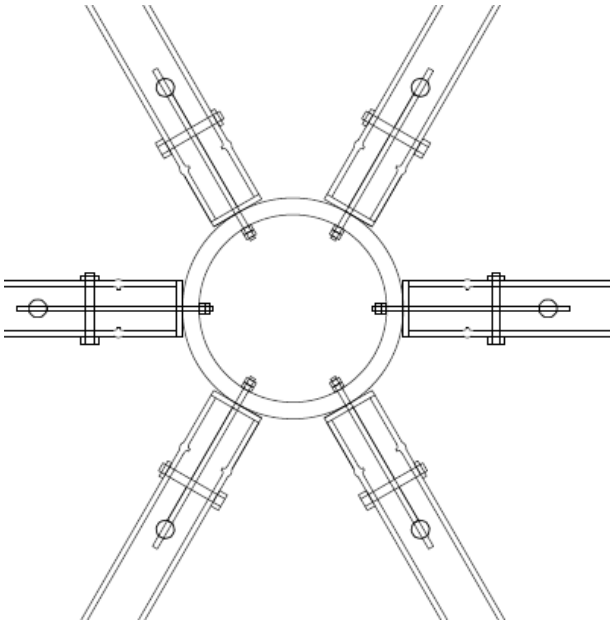

Figure 3.8: Bamboo round cross dowel joints connected to dome hub

Chapter 4

Material Properties and Experimental Program

A basic engineering principle is component-based design, i.e. predicting the strength of an entire structure by knowing the strength of the individual components. In the given case, rather than assembling and testing a connector as a whole, it makes sense to assess the strength of the individual components and determine the weakest link. For a bolted tensile connector, knowledge of mechanical properties such as tensile strength, compressive strength and bolt embedment strength is required. As this was not the case for the given bamboo species, it was necessary to conduct an experimental programme with focus on determination of material properties, rather than assembly and testing of an entire connector.

Three different bamboo species were available for experiments: *Guadua angustifolia*, *Phyllostachys pubescens* and *Dendrocalamus asper*; the latter was rejected due to lack of comparative data. Information by the supplier on the two remaining species is given in chapter 4.1.

An experimental program according to the ISO 2004b standards is suggested in chapter 4.2. Necessary experiments are identified with focus on mechanical properties that can be obtained by NDT or using a compression cylinder bank. The experimental results are presented in individual chapters; each of them is structured as follows:

1. A short review of results from related previous research is given. Related research served as inspiration for the experimental set-up.
2. The experiments conducted as part of this MSc project are presented.
    a) The employed test set-up is described.
    b) The results are presented.
    c) The results are discussed and compared to values from literature. Subsequently, conclusions are drawn.

Special attention is paid to the influence of nodes on mechanical properties. Specimens with and without nodes were included in all experiments. Additionally, the microstructure of nodes was examined in a 3D nano scan and by electron microscopy. The findings are discussed in chapter 4.2.5 and compared to related literature of chapter 2.2.3.

All results from experiments and literature are mean values unless stated differently!

4.1 Bamboo Species

The following information was provided by the supplier *Bamboe Bouw Nederland* who was so kind to provide free samples for testing.

4.1.1 *Guadua angustifolia* from Colombia

Colombia is the natural habitat of *Guadua angustifolia* and harvesting is strictly regulated by the Ministry of Forestry. The matured culm is selected at an age of $5 - 7$ years and cut at a height of approximately 1.6 metres above the ground. Bamboo at this age is at the peak of its hardness, the most resistant against insect attack and splitting of the culm. Cutting at a lower height and cutting of culms close to rivers is avoided as this reduces the strength.

All culms are subsequently cleaned with water under high pressure. The outermost layer of the culm is hard and dense and doesn't allow absorption of preservatives. Therefore the nodes (diaphragms) are perforated with a long drill to allow preservative treatment from inside of the culm. The culms are soaked in a preservatives for five days to make the culms resistant against insect and fungus attack. Afterwards, the culms are bleached vertically in the sun to remove the chlorophyll from the outermost layer of the culm wall in order to achieve a homogeneous colour and higher porosity which facilitates painting later on.

Initial drying from 30% to 20% moisture content occurs in an solar oven[1]. Afterwards drying is computer-operated until a moisture content of 13% is reached.

4.1.2 *Phyllostachys pubescens* (Moso) from China

The Moso culms quickly reduce diameter along the length and therefore large diameter culms are sparse. The culms are cut and sun-dried. Afterwards they are boiled out for about one hour. Preservatives are added to this bath to prevent insect and fungus attack. Finally, the culms are dried in a drying chamber to reduce moisture content to approximately 14%.

4.1.3 Material and Geometry

In total, 14 culms of *Phyllostachys pubescens* and 7 culms of *Guadua angustifolia* were available for tests. Table 4.1 provides and overview of the material that was used in experimental testing.

Table 4.1: Geometrical properties of *Phyllostachys pubescens* (Moso) and *Guadua angustifolia* used in experiments

Species	D_0 [cm]	t [cm]	m [kg]	l_{culm} [cm]
Moso $\overline{x}$	10.29	1.0	2.34	117.3
Moso σ	0.65	0.14	0.43	12.7
Guadua $\overline{x}$	12.91	1.4	5.82	158.2
Guadua σ	1.73	0.16	0.62	23.3

[1] trough with high reflectivity walls using solar energy to produce heat

4.2 ISO Standards and Material Property Testing

Several mechanical properties need to be known in order to design and verify a bamboo tensile connector. Unlike for timber, there is no reliable database or non-destructive strength grading method available for bamboo. Additionally, mechanical properties are dependent on origin, geometry, moisture content, etc., and the exact correlation of these parameters is not known yet. Therefore, it is generally advised to obtain mechanical properties by experimental testing according to the ISO 2004b standards, prior to structural application of a certain bamboo species. Obtained strength values served as geodesic dome model input in chapter 5 and for strength prediction of the tensile connector in chapter 7. Note that assembly and testing of the connector as a whole was beyond the scope of this research.

The following properties were obtained either from extensive literature research or experiments:

Tensile capacity (literature): The full-culm tensile strength is hard to determine by experiments. Therefore, smaller dog-bone shaped specimens are commonly used, which is also suggested in the ISO 2004b standard. Yet, the test set-up for tensile experiments is more difficult than for compression tests. Due to time limitation it was decided to only conduct experiments that could be executed in a compression cylinder bank. Therefore, tensile capacity is conservatively derived from literature.

Dynamic Modulus of Elasticity (experiments): It is generally desirable to establish a relationship between the dynamic Modulus of Elasticity and the static Modulus of Elasticity. The dynamic Modulus of Elasticity is obtained by NDT. The relationship of the static and dynamic Modulus of Elasticity is discussed and a conservative assumption is made for the model input.

Compressive capacity (experiments): This material property is obtained by experiments for both specimens with and without nodes according to the ISO 2004b standard. Values are compared to literature.

"Bolt shear test" (experiments): This test assesses the embedment and shear or splitting strength of a bolted connection. Depending on the bottom load plate configuration, the bolt shear specimens can fail either in block shear or in splitting. The name of the test is somewhat misleading, as bolt bearing (embedment) always occurs first and is thus the material property that is mainly determined! However, the experiment is known in literature by this name. The influence of nodes is investigated by testing both clear specimens and specimens with nodes. Additionally, different bold shapes (round and square) are compared. Test results are evaluated with a fracture mechanics approach.

Nodal Structure (experiments): Nodes are known to have a negative influence on tensile and compressive strength and possibly positive influence on both bolt bearing and splitting strength. The microstructure of nodes is investigated in order to find explanations for the macroscopic influence of nodes.

Comparability of Test Results of Functionally Graded Materials In chapter 2 it was concluded, that overall culm strength and stiffness can be predicted conservatively by using average material properties. In order to model local stress concentrations in a FGM, e.g. close to a bolted connector, the microstructure needs to be modelled accurately or full scale experiments need to be conducted; the latter was done to obtain bolt embedment strength and full-culm compressive strength. For tensile strength, a conservative assumption is made based on literature with consideration of the functionally-graded macro and microstructure.

4.2.1 Tensile Capacity (literature)

4.2.1.1 Tension Parallel to Fibre (ISO 2004b)

Tensile capacity parallel to the fibre is determined by using dog-bone shaped specimens taken from different radial positions (figure 4.1). The coupon thickness t is chosen equal to the culm wall thickness, the coupon width b is a circumferential chord of the culm. The length of the reduced cross-section is typically 50 to 100 mm. The ends of the specimen are wider to provide enough area for clamping. The tensile strength is calculated as:

$$f_t = \frac{F_t}{A_t} = \frac{F_t}{bt}$$

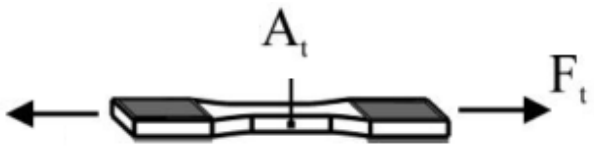

Figure 4.1: dog-bone shaped tensile test specimen (Sharma, 2010)

This test is more difficult to carry out as it requires adequate clamps and a tensile test machine. Therefore, conservative values from literature are used as a model input and to estimate tensile connector capacity (table 4.2). The literature that is used to arrive at these values is discussed in appendix B.1. Next to test method and sample size, external factors such as moisture content, age, position along the height of the culm and position in a node versus internode affect the measured tensile strength. Based on this knowledge, conservative assumptions can be made.

Table 4.2: Mean tensile strength of *Guadua angustifolia* and *Phyllostachys pubescens (Moso)*, conservative values taken from literature (see appendix B.1)

Guadua angustifolia	37 MPa
Phyllostachys pubescens (Moso)	100 MPa

4.2.2 Dynamic Modulus of Elasticity (experiments)

The Modulus of Elasticity (MOE) is needed to determine the bending stiffness (EI) of bamboo culms. Traditionally, the MOE is measured statically in 4-point or 3-point bending. Lately, the measurement of the dynamic Modulus of Elasticity E_{dyn} has become more popular, as it can be measured cheaply and non-destructively. However, this requires knowledge about the relationship between the static and dynamic MOE.

First, the relationship of local, global and dynamic Modulus of Elasticity is explained. Second, related literature is presented. Subsequently, the experimental program is described and results are discussed.

4.2.2.1 Relationships of Local, Global and Dynamic Modulus of Elasticity

There are three different properties, that are commonly referred to as static MOE: E_{3pt} from 3-point bending (figure 4.2b), E_{global} from w_{global} in 4-point bending, and E_{local} from w_{local} in 4-point bending (figure 4.2a). The latter is free from shear deflection, as the local deflection w_{local} is measured between the two loads in the zone of pure bending. As w_{local} is very small, accuracy in E_{local} is hard to achieve. But which property represents the static MOE most accurately?

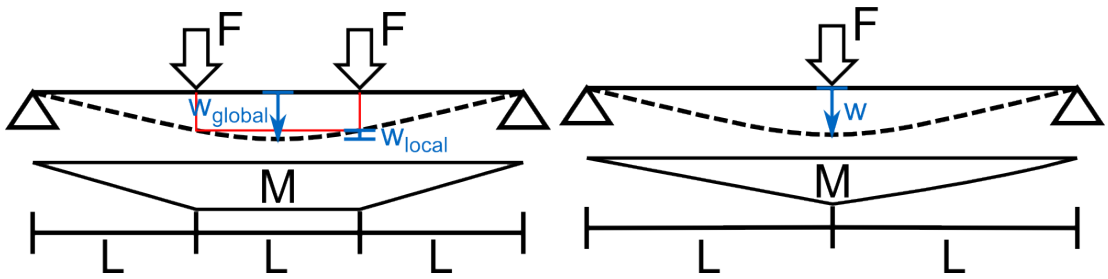

(a) E_{local} and E_{global} 4-point bending (b) E_{3pt} 3-point bending

Figure 4.2: Test set-up for measurements of global and local MOE 3-point and 4-point bending

Shear Deflection and E_{local} In practice, the impact of shear can often be neglected for two main reasons:

1. From a mechanical point of view, Euler-Bernoulli beam theory can often be used instead of Timoshenko beam theory, e.g. for slender structures including geodesic dome struts.
2. In isotropic materials the difference of the shear Modulus G and the Modulus of Elasticity E is small enough that shear deflection becomes negligible.

Timber is – similar to bamboo – characterized by it's anisotropy. Ravenshorst et al. established relationships between E_{local} and E_{global} as well as E_{dyn}[2] for several timber species [67]. They found an average relationship of $E_{local}/E_{global} = 1.16$ and $E_{local}/E_{dyn} = 0.92$ and $E_{global}/E_{dyn} = 0.79$. These results suggest that shear contributes significantly to the bending deflection in timber. Considering the difficulties of accurate measurement of E_{local}, Solli [83] and Ridley-Ellis et al. [70] question whether E_{local} is a good measure for the stiffness of timber.

A similar observation was made by Garcia-Aladin et al. [30] for bamboo. They eloquently addressed the importance of shear deflection of bamboo beams in the measurement of the bending deformation: *"According to the traditional theory of elasticity, the total deflection of a beam*

[2] from longitudinal stress wave measurements

occurs due to the combined effect of both the bending moment and the shear force. In isotropic materials such as steel and concrete, the deflection due to shear is usually not taken into account since it represents only 1% of the total deformation approximately. However, in anisotropic materials such as bamboo, the deflection due to shear should be taken into account because it may represent more than 20% of the total deformation of the beam." They found that for *Guadua angustifolia*, the longitudinal Modulus of Elasticity obtained from whole culms and prismatic specimens in three point bending was equal to 23.5 GPa, whereas the shear Modulus (G) was only 0.298GPa! **Therefore, shear deformation cannot be neglected when calculating deflections of bamboo structures!**

Difference between E_{global} and E_{3pt} Subsequently, it makes sense to use either E_{global} or E_{3pt} to calculate the bending stiffness EI. Brancheriau et al. found that E_{3pt} results in 19% lower values than E_{global} for wooden samples [6]. Which of the two should thus be chosen for the geodesic dome model? In axially loaded dome struts, the only bending deformation occurs during Euler buckling (figure 4.3). The moment distribution in the Euler column is sinusoidal, whereas 4-point bending results in a trapezoidal distribution and 3-point bending results in a triangular distribution. Obviously, 4-point bending results in a closer approximation of the moment distribution (and subsequently also deformation) of Euler buckling. Using E_{global} is thus more accurate and economical, whereas E_{3pt} is more conservative.

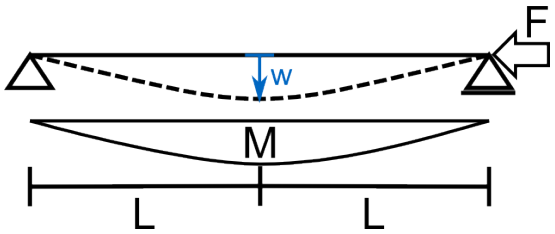

Figure 4.3: Euler buckling

Relationship between E_{static} and E_{dyn} To the present date, Lin et al. were the only research group to derive a relationship between the static MOE (E_{3pt}) and E_{dyn} for Moso laminae (figure 4.2b) [56]. They found $E_{3pt,node}/E_{dyn} = 0.74$ and $E_{3pt,internode}/E_{dyn} = 0.77$ for node material and internode material respectively. It is assumed, that the difference between laminae and full-culm bamboo can be neglected, considering that fibre orientation is identical and influence of nodes was included.

As this is the only available data for bamboo, it is chosen to assume the following relationship in the geodesic dome model:

$$E_{static} = 0.75 E_{dyn}$$

Note that E_{3pt} is very conservative and it is suggested to conduct tests in 4-point bending and measurements of E_{dyn}. This will help to isolate the shear contribution and establish a more economic relationship between the static and dynamic MOE.

4.2.2.2 Related Research

In literature, various values of E_{static} from three point and four point bending can be found for *Guadua angustifolia* and *Phyllostachys pubescens* (table 4.3). Additionally, values of E_{dyn} are given for sound pulse technique and vibration measurements (table 4.4). In the following, values obtained from experimental testing are compared to those found in literature.

Table 4.3: Static Modulus of Elasticity from three point and four point bending, rounded values, t culm wall thickness in mm, D_0 outer culm diameter in mm, ρ density in kg/m^3

Source	Species	Test set-up	E_{static} [GPa]	Notes
Correal et al. [14]	Guadua	4 point	17.2	regardless of age and culm position
Luna et al. [59]	Guadua	not known	13.9	
Gnanaharan et al. [34]	Guadua	4 point	$24.3\rho + 25.6D_0$ $20.7\rho + 221.8t$	
Jiang et al. [24]	Moso	3 point	$11.81\text{MC} - 0.15\%$	
Chung et al. [11]	Moso	3 point	11.4	MC $5 - 30\%$
Lin et al. [56]	Moso	3 point	11.5 10.9	internode node

Table 4.4: Dynamic Modulus of Elasticity from literature, rounded values

Source	Species	Test set-up	E_{dyn} [GPa]	Notes
Cardenas et al. [9]	Guadua	acoustic waves	16 ... 25	sound pulse technique
Lin et al. [56]	Moso	vibrations	14.9 14.8	internode node

4.2.2.3 Test Set-Up

Set-Up A vibration based test is used to determine the dynamic Modulus of Elasticity of bamboo culms (E_{dyn}). The method makes use of vibration measurements of a bamboo culm in which a longitudinal stress wave is initiated (figure 4.4). From vibration measurements, the natural frequency can be determined by means of Fourier Transform. The dynamic Modulus of Elasticity can then be calculated as $E_{dyn} = 4f^2l^2\rho$. This method has been long established for timber[67]. Even though full-culm measurements of E_{dyn} are entirely new to bamboo engineering, similar behaviour as for knot-free timber (e.g. tropical hardwood) can be expected as both materials are orthotropic and possess a similar microstructure.

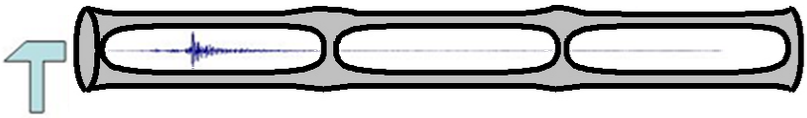

Figure 4.4: test set-up (Dynamic MOE)

Procedure As specimen length and geometry affects accuracy of results, the experiments were conducted on axially straight specimens of at least 1 metre length. The measurements took place in a climate chamber with 65% relative humidity and a temperature of 20°C. The moisture content was obtained as follows:

MC $= \frac{m_w - m_d}{m_d}$; m_w wet mass at test conditions; m_d dry mass after oven drying at 103°C

The Moso specimens had an average moisture content of 11.30% and the Guadua specimens had an average moisture content of 13.58%. Average outside culm diameter and thickness were measured four times at both ends of the culm and averaged over the length to obtain the volume of the culm. Volume of nodes was calculated by assuming the height of nodes in Guadua as 5 mm and Moso as 3 mm. The culms were weighed and the density was calculated. The culms were placed on two supports of timber strips of approximately 2 cm width to minimize the influence of the support[3]. Subsequently, the natural frequency f_{nat} was obtained from signals that contained a single distinct peak. For measurements of natural frequency, the measuring instrument *Timber Grader MTG* and correspondent software were used (figure 4.5).

(a) Measurement of natural frequency f (b) Two thin supports

Figure 4.5: Measurement of E_{dyn} with *Timber Grader MTG*

[3]Note that this is common practice for measurements on timber beams. However, the support area of the bamboo culms is even smaller due to the round geometry.

4.2.2.4 Test Results

Table 4.5 displays the results that were obtained for 14 Moso and 7 Guadua culms[4]. Detailed results can be found in the appendix in table C.1 and C.2.

Table 4.5: Dynamic Modulus of Elasticity for *Phyllostachys pubescens* (Moso) and *Guadua angustifolia*

Species	no. specimens	f_{nat} [Hz]	D_0 [cm]	t [cm]	m [kg]	l_{culm} [cm]	no. nodes	ρ [kg/m^3]	E_{dyn} [MPa]
Moso $\overline{x}$	14	1762	10.29	1.0	2.34	117.3	5.7	660	11431
Moso σ	14	177	0.65	0.14	0.43	12.7	1.2	74	1866
Guadua $\overline{x}$	7	1641	12.91	1.4	5.82	158.2	5.7	740	19681
Guadua σ	7	266	1.73	0.16	0.62	23.3	1.9	151	3536

4.2.2.5 Discussion and Conclusions

Two linear regression formulas could be derived for density ρ and E_{dyn} of Guadua and Moso bamboo (figure 4.6). All test results were significant for both bamboo species. The coefficient of determination R^2 was greater than 0.7 in both cases which is relatively high considering the small sample size and unknown age of the individual culm. R^2 is smaller for Guadua than for Moso; however, for Guadua only half as many specimens as for Moso were available. The following two linear relationships could be established (E_{dyn} in MPa and ρ in kg/m^3):

$$\text{Moso: } E_{dyn} = 21.692\rho - 2894.5; \quad R^2 = 0.7407; \quad p = 0.00004; \quad \alpha = 0.05$$
$$\text{Guadua: } E_{dyn} = 19.687\rho + 5111.7; \quad R^2 = 0.7047; \quad p = 0.00914; \quad \alpha = 0.05$$

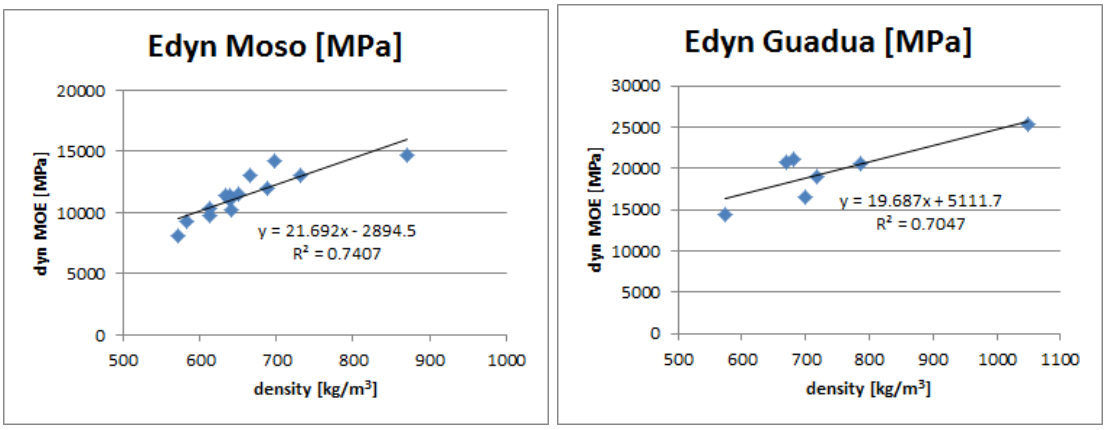

(a) *Phyllostachys pubescens* (Moso) (b) *Guadua angustifolia*

Figure 4.6: Relationship of density and dynamic MOE

The generally lower R^2 value for timber can be explained by the influence of knots. In bamboo, nodes could be seen as a similar imperfection, but they occur more regularly and affect the entire cross-section which leads to more homogeneous results.

[4] f_{nat} natural frequency, D_0 outside culm diameter, t wall thickness, m mass, l_{culm} length of culm, ρ density, E_{dyn} dynamic Modulus of Elasticity

Comparison to Literature The average measured dynamic Modulus of Elasticity for Moso was 11 431 MPa. This value is lower than the values measured by Lin et al. [56]. This can be explained by the fact that Lin et al. used bamboo lamella and not full culms. Bamboo lamella are node-free and all fibres are axially oriented which results in higher values of MOE. Furthermore, the Moso test results are higher than values of E_{static} for dry and wet condition given by Jiang et al. [24]. This should be the case as E_{static} is generally lower than E_{dyn}. The average dynamic Modulus of Elasticity for Guadua was 19 681 MPa. This value is higher than the values for E_{static} given by Correal et al. [14] and Luna et al. [59], which should be the case. Additionally, the value lies in the same range as the value for E_{dyn} obtained by sound pulse technique by Cardenas et al. [9].

Apparently it is possible to use NDT to derive the static MOE from E_{dyn}. The remaining question is, whether is is possible to use a straight forward relationship between culm geometry, density and static MOE. In the following, an attempt is made to use the formulas of Gnanaharan (1994) given in table 4.3, using the average material properties measured for *Guadua angustifolia*: $\rho = 740$ kg/m^3; $D_0 = 129.1$ mm; $t = 13.9$ mm.

$$E_{global} = 24.309\rho + 25.557D_0 = 21\,285\,\text{MPa}$$
$$E_{global} = 20.72\rho - 221.842t = 12\,249\,\text{MPa}$$
$$E_{global} = 25.571\rho + 475.843t - 163.925D_0 = 4390\,\text{MPa}$$

Ideally, all three values should be the same and smaller than the measured dynamic Modulus of Elasticity ($E_{dyn} = 19\,681$ MPa). This is not the case. Apparently, more research is needed to establish generally valid relationships between geometry, density and MOE. Using E_{dyn} to estimate E_{static} provides a good alternative for the time being.

Conclusions Additional measurements of E_{global} and E_{local} in 4-point bending for both Guadua and Moso bamboo are necessary, to establish relationships similar to those found for timber, and in order to quantify the shear contribution. As argued above, a conservative relationship of $E_{static} \approx 0.75E_{dyn}$ can be assumed:

$$\text{Moso: } E_{static} = 11431 \cdot 0.75 \approx 8570\,\text{MPa}$$
$$\text{Guadua: } E_{static} = 19681 \cdot 0.75 \approx 14\,760\,\text{MPa}$$

4.2.3 Compressive Strength Parallel to Fibre (ISO 2004b) (experiments)

First, results from related previous research are presented. Subsequently, the experimental program is described and results are discussed.

4.2.3.1 Related Research

In literature, values for compressive strength of both *Phyllostachys pubescens* and *Guadua angustifolia* can be found. An overview of mean strength values from related research is given in table 4.6. Note that the introduction of the ISO 2004b standard is relatively recent and tests in literature were conducted according to different standards, e.g. the *Chinese national standard for performance testing of bamboo 1995* (GB/T 15780-1995) and Columbian standard (NTC), which is based on the ISO 22157 (2004b) standard.

Table 4.6: Mean compressive strength f_c and design values $f_{c,d}$, t culm wall thickness in mm, D_0 outer culm diameter in mm, n number of specimens, ρ density in kg/m^3, moisture content MC in %

Source	*Species* Norm	n	f_c [MPa]	Notes
Janssen [46] [47]	-	-	$f_{c,d} = 0.013\ \rho = \frac{1}{7} f_c$	species independent
Chung and Yu [11]	*Moso* L=2D	213	$f_c = 50$, 70 $f_c = 134$, 75 , 57	bottom, top; $t \approx 0.1 D_0$ MC<5%, 5-30%, >30%
Lo et al. [57][58]	*Moso* ISO	- -	$f_c = -0.28\ D_0 + 71.5$ $f_c = 2.63\ B + 36$	12.5-13% MC B vascular bundles %
Shao et al. [77]	*Moso* GB/T	-	$f_c = 56.4$, 59.8	strips: internode , node $\rho = 712$, MC 12%
Jiang et al. [24]	*Moso* GB/T	20 20	$f_c = 96.44 - 2.50$ MC[%]	strips
Wang et al. [96]	*Moso* GB/T	640	$\frac{f_c}{\rho} = \left(76.62 + \frac{739.90-76.62}{1+e^{\frac{MC+13.46}{7.6296}}}\right)$ $f_c = 0.15123\ \rho - 33.37$	strips MC=wet...oven dried
Dixon and Gibson [19]	*Moso* -	36	$f_c = 0.1984\ \rho - 49.69$	blocks
Correal et al. [14]	*Guadua* NTC	-	$f_c = 36.8$	independent of height ideal age 3 years
Luna et al. [59]	*Guadua* NTC	-	$f_{c,d} = 34$, 60 , 60	bottom, middle, top
Corto et al. [15]	*Guadua* NTC	120	$f_c = 41.6$	h=35-70cm Drilling of diaphragm has no effect!

4.2.3.2 Test Set-Up

Set-up The compressive test according to the ISO 2004b standard is used to determine the full-culm compressive capacity parallel to the fibres f_c. For commercial purposes, the height of the specimen should be equal to the outer culm diameter ($h = D_0$). The applied compressive force (F_c) is divided by the cross-sectional area of the entire culm (A). Friction between the loading plates and the culm should be minimized by using an intermediate layer, e.g. a combination of Teflon and wax on steel shims that glide freely. One end plate of the testing machine should be equipped with a hemispherical bearing to obtain uniform load distribution (ISO 22157-1/9.3). As literature contains contradicting results regarding the influence of nodes (chapter 2.2.3), tests on specimens with and without nodes are carried out on both *Guadua angustifolia* and *Phyllostachys pubescens.*

$$f_c = \frac{F_c}{A} \quad \text{with } A = \frac{\pi}{4}(D_0^2 - D_i^2) = \frac{\pi}{4}\left(D_0^2 - (D_0 - 2t)^2\right)$$

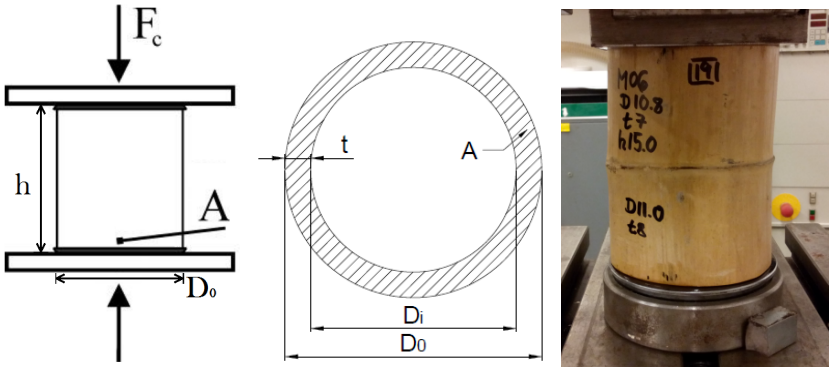

(a) Load application (b) Culm cross-section (c) Test set-up

Figure 4.7: ISO 2004b Compression test

Expected Failure Modes Two failure modes are possible: Crushing failure (similar to timber) given the culm wall is thick enough, and splitting failure as the maximum lateral strain $\epsilon_\perp$ is exceeded.

Procedure The specimens were cut from a batch of culms whose average density was closest to the average density of all culms. ISO 2004b requires specimens to be taken from three different locations in the culm: bottom, middle, top (ISO 22157-1/9.4.1). For Guadua, all culms were cut $1.6m$ above the ground which translates to a middle position. For Moso, the position was unknown. Both edges of the specimens were cut parallel to each other and perpendicular to the culm axis[5]. In specimens with nodes, the node was located in the centre of the specimen. As the ISO 2004b standard does not require a specific D_0/h relationship for scientific research, it was chosen to use specimens with a height of approximately $h = 150$mm for both Guadua and Moso, which is an average height to diameter ratio of $h = 1.5\ D_0$ for Moso and $h = 1.15\ D_0$ for Guadua. The diameter D_0 was measured at two locations at both ends of the specimen, the thickness t was measured at four locations at each end respectively. The average diameter and thickness were used to calculate the surface area A. The specimens were weighed and rounded off to grams. The thickness of the nodes was taken as 3mm for Moso and 5mm for Guadua in order to determine the density.

[5]For specimens that contained nodes, this was not always possible, as the culm changed growth direction at the node.

Two different test machines were used for Guadua and Moso, due to the fact that the Guadua culms had a greater surface area and thus required a higher loading force. For both species, the displacement rate was 0.01mm/s as prescribed in the ISO 2004b standard (ISO 22157-1/9.5.2). For the Guadua specimens, one of the loading plates was hinged so that the load was always applied axially. For the Moso specimens, the bottom plate was made from a hemispherical bearing that could glide freely (figure 4.8a and 4.8b). For both species, friction between the loading plate and the specimens was reduced by greasing the specimen with a cast lubricant (figure 4.8c). The difference of a test without reduced friction and a test with lubricant application can be seen in figure 4.8d and figure 4.8e. The great difference in the observed failure pattern indicates that the lubricant reduced friction sufficiently. For Moso, the displacement was measured between the two loading plates as the machine experienced internal set. For Guadua, the test machine was rigid enough so that actual displacements were identical to the computer-controlled displacement. In both load cases, the loading plate was set with a force of less than 1kN before computer-controlled displacement took over.

(a) Initial position

(b) Rotation of loading plate

(c) Lubricant application

(d) Failure with lubricant

(e) Failure without lubricant

Figure 4.8: Pot bearing loading plate and application and effect of lubricant to reduce friction

4.2.3.3 Test Results

Table 4.7 displays the average test results obtained for *Phyllostachys pubescens* (Moso) and *Guadua angustifolia*[6]. The moisture content was 13.58% for Guadua and 11.30% for Moso. Detailed results can be found in the appendix in table C.3 and C.4.

Table 4.7: Average compression results for *Phyllostachys pubescens* and *Guadua angustifolia*

Species	no. samples	D_0 [mm]	t [mm]	h [mm]	ρ [kg/m^3]	f_c [MPa]	E_c[7] [MPa]
Moso $\overline{x}_{clear}$	6	96.5	7.8	150.7	711	49.93	7745
Moso $\overline{x}_{node}$	7	96.5	9.0	154.0	731	47.49	6817
Moso $\overline{x}$	13	96.5	8.5	152.5	722	48.62	7246
Moso σ	13	7.7	2.0	4.4	80	5.31	1820
Guadua $\overline{x}_{clear}$	9	123.7	12.4	149.1	781	60.73	9845
Guadua $\overline{x}_{node}$	6	123.3	13.0	152.5	818	58.57	8968
Guadua $\overline{x}$	15	123.6	12.6	150.5	796	59.87	9540
Guadua σ	15	7.9	2.1	3.2	95	14.83	2736

Note: The density measurement was based on weight and geometry after 4 months storage in a climate chamber at 20°C and relative humidity of RH = 65%. The thickness of the nodal diaphragm was assumed to be 5mm for Guadua and 3mm for Moso, based on the longitudinal cross-section of 3D nodal specimens. The average specimen density was 9% higher for Moso and 8% higher for Guadua than full-culm density. The difference for clear specimens was larger than for specimens with nodes, which suggests that the height of the diaphragm was assumed rather accurately. A different moisture content of culm and compression specimens is unlikely, as all specimens were stored in the same climate during the entire process except for sawing, which took place several days before testing during a single day. However, it is likely that the full-culm volume was estimated too grossly, as culm wall thickness increases around the node. This could possibly be the reason why culm density was found to be lower than specimen density.

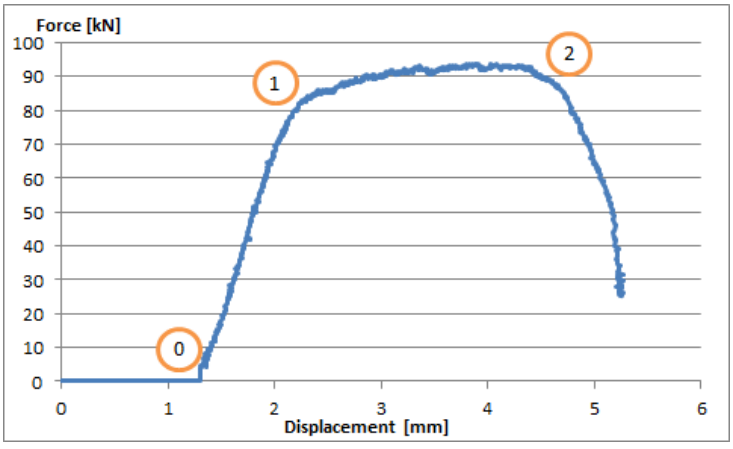

Figure 4.9: Typical load displacement curve for bamboo compression test

Figure 4.9 shows a typical load displacement curve for compression specimens (independent of species): ⓪ The load is applied. Single longitudinal cracks emerge either close to the loading plates or in the centre of the specimen ① and continue growing until a second crack emerges.

[6] culm outer diameter D_0, wall thickness t, height h, density ρ, compressive strength f_c, compressive Modulus of Elasticity E_c

[7] obtained from individual stress strain diagram according to ISO 2004b 9.6.2 as an alternative to strain gauge

Once a crack has propagated to both ends of the specimen ②, the entire culm bulks out as displacement continues and force decreases dramatically. Figure 4.10i and 4.10j show an example of crack propagation between fibre strands in the parenchyma matrix. Figure 4.10k shows the deformation at the end of the experiment.

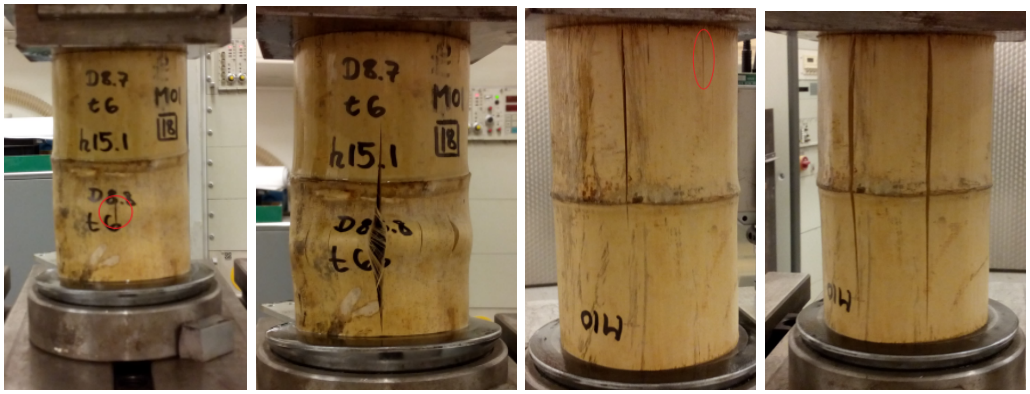

(a) Crack initiation (b) Crack propagation (c) Crack initiation (d) Second crack

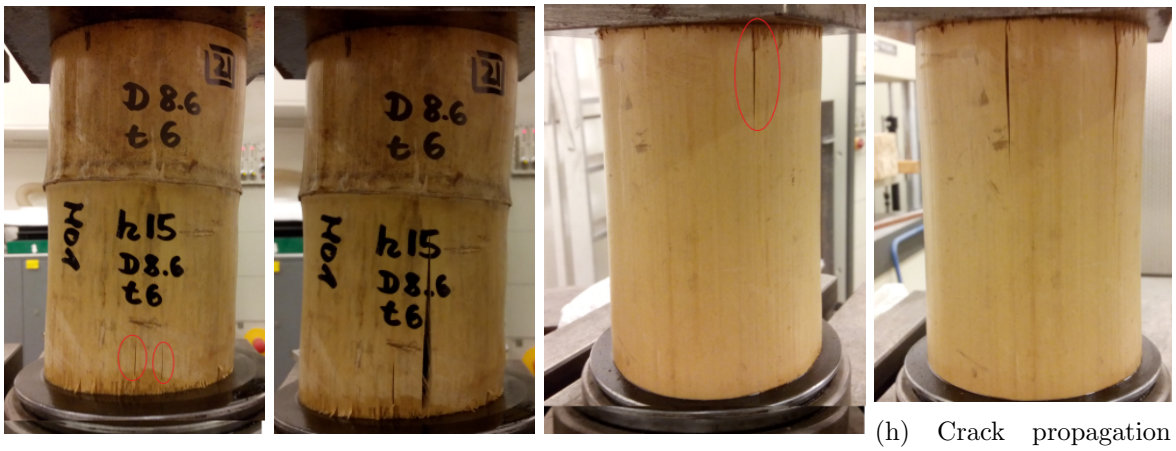

(e) Crack initiation (f) Crack propagation (g) Crack initiation (h) Crack propagation and second crack

(i) Crack initiation (j) Crack propagation (k) End of experiment

Figure 4.10: Crack initiation and propagation in Moso bamboo

All specimens of *Phyllostachys pubescens* failed by longitudinal cracks that were opened as the maximum lateral strain $\epsilon_{\perp}$ was exceeded (figure 4.10). This suggests that the parenchyma matrix is weaker in its transverse direction than in its radial direction. Most *Guadua angustifolia* specimens failed by longitudinal cracks (figure 4.11a to 4.11d). Two specimens showed a compressive

crushing failure prior to cracking (figure 4.11e and 4.11f). For both species, crack initiation was always in the clear part of the culm, never in the node itself (figure 4.10).

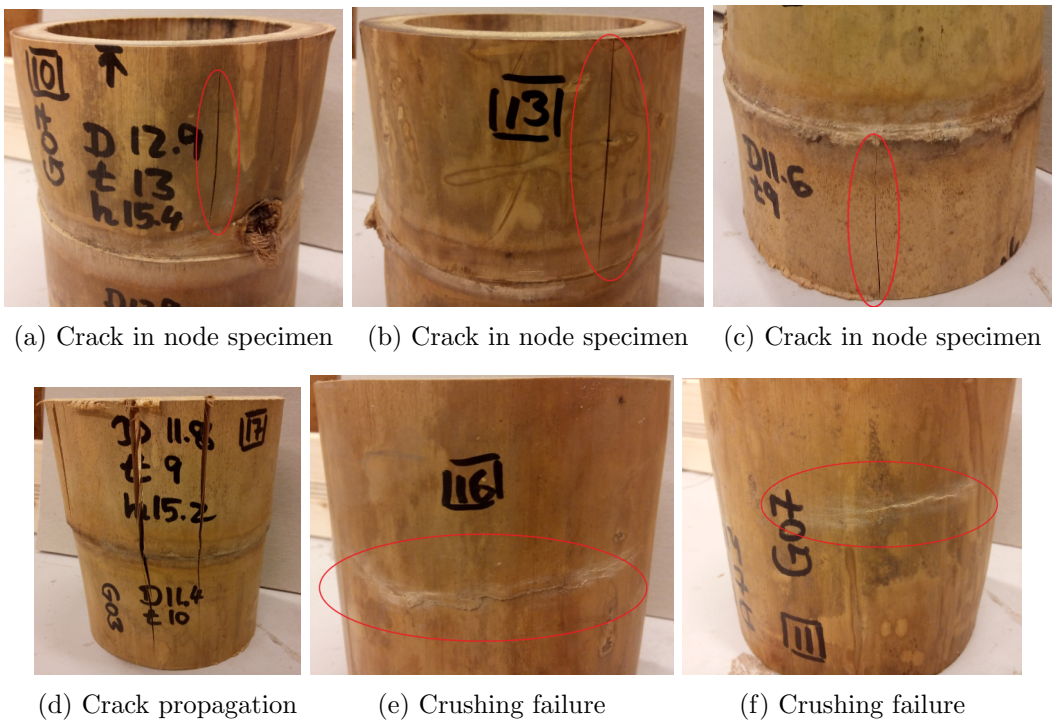

(a) Crack in node specimen (b) Crack in node specimen (c) Crack in node specimen

(d) Crack propagation (e) Crushing failure (f) Crushing failure

Figure 4.11: Different failure modes in Guadua bamboo

4.2.3.4 Discussion and Conclusions

For both species, linear regression formulas could be derived for the density ρ and the compressive strength f_c as well as compressive Modulus of Elasticity E_c. E_c was determined from the individual stress-strain-diagrams of a single specimen between 20% and 80% of the maximum force $F_{c,max}$ as suggested by ISO 2004b 9.6.2[8]. In few cases, the stress-strain-curve was not linear past 70% of the maximum load. In those cases, only the linear part of the curve was considered.

A linear regression and p-value (p) analysis were carried out for both species. All results were significant for a significance level of $\alpha = 0.05$. Coefficients of determination were relatively high, considering the small sample size and seeing that the age of the culm was unknown and moisture content was not taken into account. The following linear relationships were established for samples with and without nodes (clear):

[8]This was done as an alternative to the application of strain gauges.

Moso (clear): $f_{c,clear} = 0.0554\ \rho + 10.6$; $R^2 = 0.9963$; $p = 0.00005$; $\alpha = 0.05$

Moso (node): $f_{c,node} = 0.0721\ \rho - 5.1948$; $R^2 = 0.9408$; $p = 0.0003$; $\alpha = 0.05$

Moso (clear): $E_{c,clear} = 11.236\ \rho - 238.63$; $R^2 = 0.9585$; $p = 0.0007$; $\alpha = 0.05$

Moso (node): $E_{c,node} = 24.546\ \rho - 11121$; $R^2 = 0.6705$; $p = 0.00243$; $\alpha = 0.05$

Guadua (clear): $f_{c,clear} = 0.1772\ \rho - 77.602$; $R^2 = 0.833$; $p = 0.0006$; $\alpha = 0.05$

Guadua (node): $f_{c,node} = 0.1325\ \rho - 49.76$; $R^2 = 0.9916$; $p = 0.00003$; $\alpha = 0.05$

Guadua (clear): $E_{c,clear} = 31.965\ \rho - 15113$; $R^2 = 0.7517$; $p = 0.0025$; $\alpha = 0.05$

Guadua (node): $E_{c,node} = 21.579\ \rho - 8564$; $R^2 = 0.8658$; $p = 0.0071$; $\alpha = 0.05$

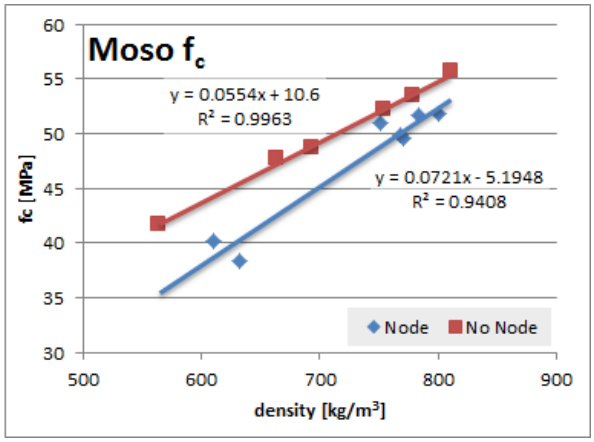

(a) Relationship of ρ and f_c *Phyllostachys pubescens* (Moso)

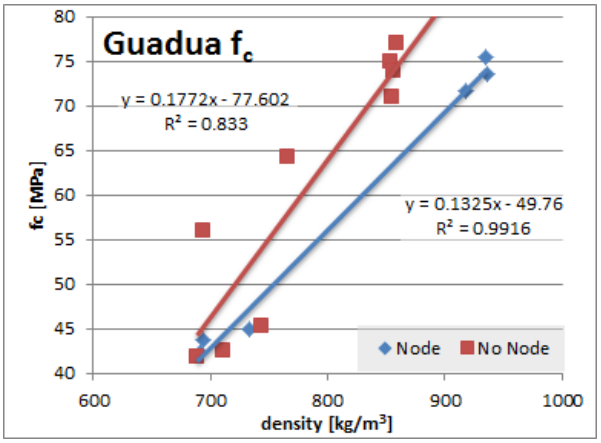

(b) Relationship of ρ and f_c *Guadua angustifolia*

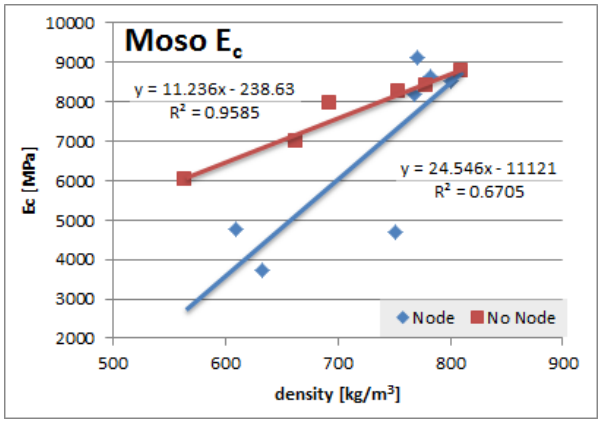

(c) Relationship of ρ and E_c *Phyllostachys pubescens* (Moso)

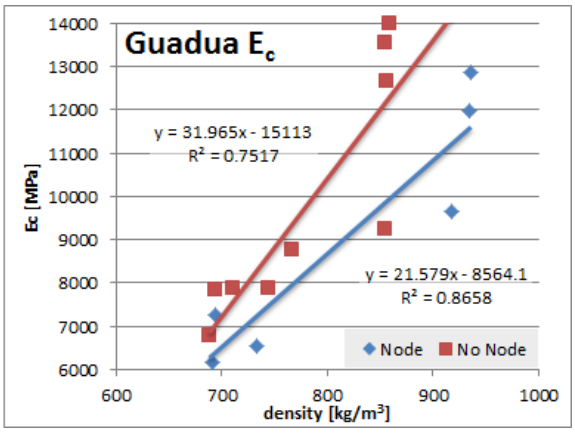

(d) Relationship of ρ and E_c *Guadua angustifolia*

Figure 4.12: Relationship of density and compressive MOE

Table 4.8: Summary of compression results for *Phyllostachys pubescens* and *Guadua angustifolia*

Species	$f_{c,clear}$ [MPa]	$f_{c,node}$ [MPa]	$\frac{f_{node}}{f_{clear}}$ [−]	E_{clear} [MPa]	E_{node} [MPa]	$\frac{E_{node}}{E_{clear}}$ [−]
Moso	49.9	47.5	0.95	7746	6817	0.88
Guadua	60.7	58.6	0.96	9845.0	9081.8	0.92

In average, for both species $f_{c,max}$ and E_c of clear specimens were higher than for those that contained nodes (table 4.8). The difference of was E_c smaller or equal to 12%. For $f_{c,max}$, the difference was only 5% or less and crack initiation occurred always in the clear part, never in the node itself. This failure mechanism is expected, as radial nodal fibres act as reinforcement and are able to transfer tangential stresses, causing the first crack to emerge in the clear part of the specimen. The slightly lower compressive strength of specimens with nodes (4% for Guadua and 5% for Moso) could be due to the fact that the culm diameter and wall thickness change close to the nodes which results in stress concentration.

For E_c, the clear specimens were in average 12% stiffer for Moso and 8% stiffer for Guadua. This can be explained by the microstructure of the node: In the nodes, some vascular bundles deviate from the axial orientation. Vascular bundles consist not only of fibres but also of vessels, which get compressed easily in transverse vascular bundles which causes the full-culm stiffness to decrease. One could argue that nodes make only a small section compared to the rest a culm. However, decrease in compressive stiffness is not negligible and should be taken into account.

Comparison of E_c to E_{dyn} makes little sense at this point, as compressive specimens were taken from too few culms to establish a relationship.

Comparison to Literature Let's compare the test results to values from literature: Though harvested beyond the "optimal" age of 3 years, the Guadua specimens achieved a compressive strength higher than values reported by Correal et al. [14] and Corto et al. [15]. The measured f_c comes closest to the design values obtained by Luna et al. [59] which were 60MPa for specimens at the middle of the culm.

Let's try to apply the rule of thumb by Janssen on both Guadua and Moso: According to Janssen [47], the mean compressive strength is $f_{c,d} = 0.091\rho$. Inserting mean density of the test specimens, we obtain a calculated value of $f_{calculated} = 66\,\text{MPa}$ for Moso and $f_{calculated} = 72\,\text{MPa}$ for Guadua. The measured values (49 MPa for Moso and 60 MPa for Guadua) are only 74% and 83% respectively. **Janssen's rule of thumb thus clearly overestimates the strength in the given case!**

For Moso, Chung and Yu [11] predict a strength of 50 MPa for bottom pieces and 70 MPa for top pieces. If the Moso specimens were cut from the bottom of the culm, the predicted and measured strength match exactly. Using the formula of Lo et al. [57] relating outer culm diameter and compressive strength of Moso, we arrive at a compressive strength of only 44.5 MPa for the examined specimens. This is 91% of the measured value. Using the formula of Wang et al. [96] and inserting the measured average density of the Moso specimens, we arrive at 76 MPa which is 1.6 times the measured compressive strength. This however, does not take moisture content into account. Last but not least, the formula of Dixon and Gibson suggests 93 MPa which is almost 2 times the measured compressive strength of Moso.

It can be concluded that the measured values agree with some suggested by literature, whereas the difference to other values is very large. This emphasizes the need of continued research.

Conclusions It could be shown that a strong correlation of density ρ and compressive strength f_c exists, and also a clear relationship between ρ and E_c. Few culms were chosen for compression specimens to reduce scatter. This made it impossible to derive a relation between E_{dyn} and E_c. It can be said for sure that nodes do impart negative effects on full-culm compression strength and Modulus of Elasticity of both *Phyllostachys pubescens* and *Guadua angustifolia*. Splitting was never initiated in the node which hints to a reinforcing effect in the transverse direction. Further information on the influence of nodes can be found in chapter 2.2.3 and 4.2.5. More research needs to be carried out to establish general relationships between ρ, f_c, E_c and E_{dyn}.

4.2.4 Bolt Shear Test (Janssen 1981; Sharma 2010) (experiments)

First, related research is presented. Subsequently, the experimental program is described, results are reported and discussed.

4.2.4.1 Related Research

Several research groups conducted experiments on bolted connections. Fu et al. [29] investigated the performance of Moso bamboo single bolted connections under tensile load. The culm wall thickness was 10 mm and the edge distance was 60 mm. The tested specimen failed at 4.2 kN in splitting failure: $f_{s_{\parallel}} = \frac{4200}{60 \cdot 10} = 7\,\text{MPa}$ (single crack).

Moreira and Ghavami [63] made a finite element model of a simple bamboo pin joint, based on previous test results of Moso by Moreira et al. They included bearing, shear and splitting failure into their model. They concluded that splitting failure has an *"additional geometrical resistance"* compared to shear failure. They stated that shear stress has a *"free path to propagate through parenchyma cells"*, whereas the risk of splitting is reduced if a node is located under the pin. They also found that compression perpendicular to the fibres restrains crack initiation even under relatively high shear stress and that splitting could be counteracted by steel reinforcement under the pin hole.

Shao et al. [77] investigated the effect of the node on shear strength of Moso. They found that average shearing strength of full-culm samples with nodes was 29% higher. For processed samples (blocks), an increase from 18.3 MPa at the internode to 18.9 MPa at the node was found. This contradicts the findings of Moreira and Ghavami [63].

Wang et al. [95] determined the Mode I interlaminar fracture toughness of Moso bamboo (for failure modes see figure 4.13b). They found an average fracture toughness of 498 J/m^2 and 1431 J/m^2 for internode and node material respectively.

Ramirez et al. [66] determined the dowel-bearing strength of glued-laminated *Guadua angustifolia* under nail and threaded bar fasteners with different diameters in different loading directions, and developed a FEM. They concluded that, similar to timber, bamboo bearing strength depends on both the dowel diameter and the specimen width-to-diameter ratio. They established the following two relations for bearing strength perpendicular to the grain (though correlation coefficients were rather low). It can be assumed, that a similar formula can be derived for *Phyllostachys pubescens*.

$$f_b = -4.1\ d + 55.9 \qquad \text{(nail)}$$
$$f_b = -0.55\ d + 36.9 \qquad \text{(threaded bar)}$$

Corto [15] investigated the effect of drilling of the diaphragm on shear and compression strength of *Guadua angustifolia*. He reported a shear strength of 3.08 MPa; drilling of the diaphragm had no influence on either property. Tests were conducted according to the ISO 2004b standard and the Columbian NTC 2007 standard. It can be assumed that drilling of the diaphragm also has no influence on *Phyllostachys pubescens*.

Placing a bolted connector before a node seems to have a positive influence which will be examined in the following. Influence of nodes on material properties is further discussed in related literature in chapter 2.2.3 and experimental results in chapter 4.2.5.

4.2.4.2 Test Set-Up

Set-up The bolt shear test is not part of the ISO 2004b standard yet. Janssen [46] and Sharma [81] investigated the effect of a single round bolt in full-culm bamboo. They observed, that the failure mode strongly depends on the edge distance of the bolt (l_{edge}) and the load angle (θ). For angles close to parallel to the fibre ($\theta \approx 0°$) and relatively short edge distances, block shear occurs if a gap at the load plate allows this failure mode (Mode II figure 4.13b). If the culm is restrained or $\theta \approx 90°$, bearing failure followed by longitudinal tensile splitting is more likely to occur (Mode I, figure 4.13b) [81]. The name "bolt shear test" is misleading as bearing strength rather than shear strength is measured. However, the test is known in literature by this name and therefore the name was adopted in this research.

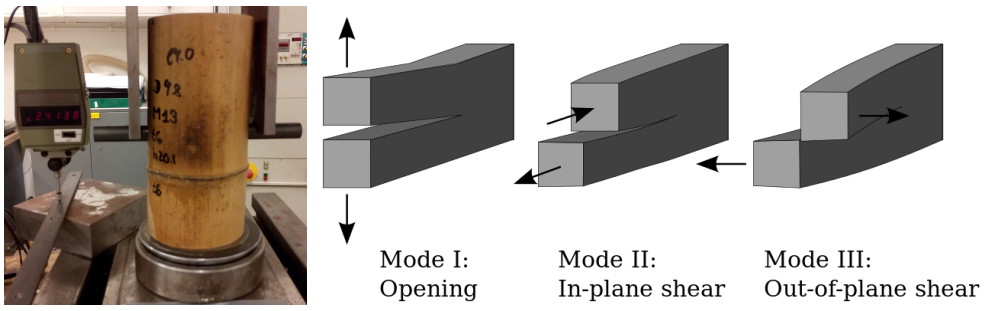

(a) Test set-up (b) Three fracture modes [88]

Figure 4.13: Bolt shear test

In his tensile timber connector design of 2000, de Vries employed square cross dowels [91]. At first sight, introducing a square hole seems unfavourable due to stress concentrations in the corners. This is generally true for an isotropic infinite plate loaded in uni-axial tension. However, in the given case, an orthotropic circular hollow section is loaded by a rigid pin, which is an entirely different situation[9]. As the de Vries connector was already successfully used in practice, it was decided to use square bolts and compare them to round bolts of a similar diameter. Furthermore, literature suggests that nodes can have an impact on the prevailing failure mode and strength of the connection (see chapter 2.2.3). Therefore, it was decided to conduct experiments on both specimens with and without nodes.

Expected Failure Modes A tensile connector that transfers both tensile and compressive stresses prescribes an end plate without gaps. This rules out the possibility of block shear (figure 4.14d).

For **round** bolts (○), bolt embedment (figure 4.14b) followed by tensile splitting (figure 4.14c) can occur. For **square** bolts (□), embedment (figure 4.14f) followed by tensile splitting at a corner (figure 4.14g) or out of plane shear (figure 4.14h) can occur.

Independent of the bolt shape, the strength is calculated as follows:

bearing failure:	$f_b = \frac{F_{bolt}}{2A_b} = \frac{F_{bolt}}{2dt}$	(figure 4.14b and 4.14f)
splitting failure:	$f_{s_\parallel} = \frac{F_{bolt}}{A_{cr}} = \frac{F_{bolt}}{l_{edge}t_{cr}}$	(figure 4.14c and 4.14g)
block shear failure:	$f_{v_{bolt1}} = \frac{F_{bolt}}{A_{shear}} = \frac{F_{bolt}}{4l_{edge}t}$	(prevented by end plate)

[9] it is suggested to model the resulting stress distribution in future research

Out-of-plane shear is expected to only occur for square bolts:

$$\square \text{ out-of-plane shear failure: } f_{v_{bolt2}} = \frac{F_{bolt}}{A_{shear}} = \frac{F_{bolt}}{4 l_{edge} t} \qquad \text{(figure 4.14h)}$$

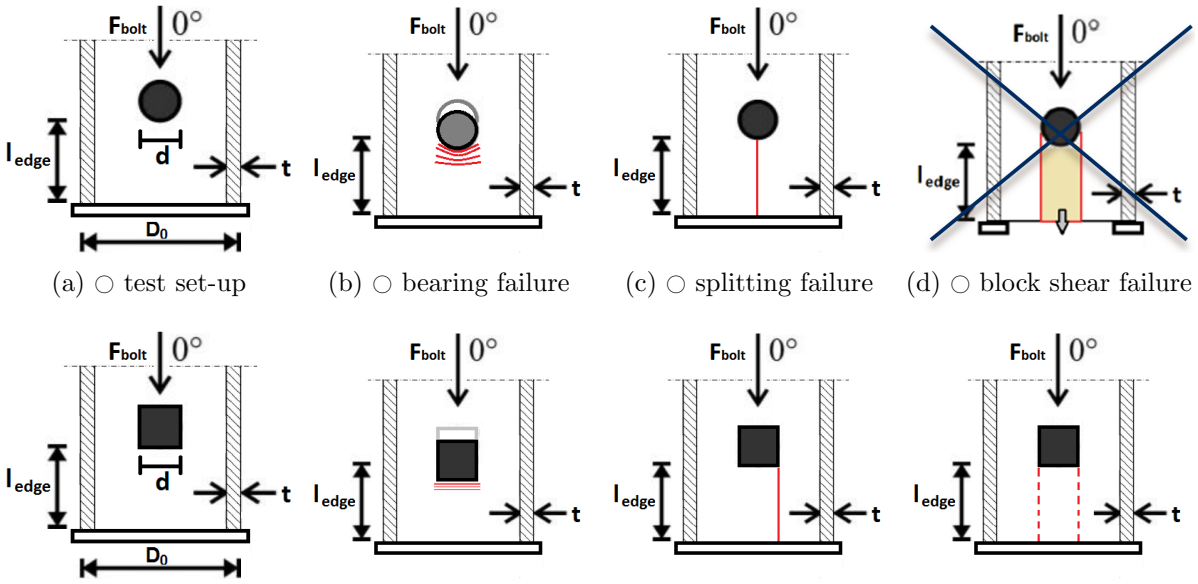

(a) ○ test set-up (b) ○ bearing failure (c) ○ splitting failure (d) ○ block shear failure

(e) □ test set-up (f) □ bearing failure (g) □ splitting failure (h) □ out-of-plane shear

Figure 4.14: Bolt test round and square configuration

Procedure Similar to the compression test set-up in chapter 4.2.3, a pot bearing bottom load plate without gap was employed. The specimens were not greased to simulate the application in the end plate connector. The experiment was displacement-controlled with a prescribed displacement of 0.01mm/s, measured between the two loading plates which is identical to the displacement of the bolt, as slip between steel components is small.

The test was only conducted on Moso specimens and required 10 specimens per bolt type (round and square); each 5 with and 5 without nodes. For clear specimens, the height was chosen to be $h = 2D_0 = 20\,\text{cm}$. The bolt was placed in the centre with a distance of at least 1 d to the node which resulted in an edge distance of $l_{edge} \approx 10\,\text{cm}$. The bolt diameter for both square and round bolts was chosen $d = 16\,\text{mm}$. A detailed drawing of the test set-up can be found in appendix D. The specimens were stored in a climate chamber with relative humidity RH = 65% and temperature of 20°C which resulted in a Moso moisture content of 11.30%; experiments were conducted under the same conditions. For both round and rectangular holes, one node-free specimen showed a longitudinal continuous tensile crack prior to load application. The cracks developed only some time after manufacturing and the specimens were included in the experiments. The crack in the specimen with the round hole did not run close to the hole and did not affect strength in any kind. The crack in the specimen with the rectangular hole ran through the corners of the hole. This specimen reached 87% of the average bearing strength of similar initially intact specimens.

Experiments with round bolts were stopped after a significant force drop due to continuous longitudinal splitting. The square configuration was stopped when a displacement of approximately $\Delta s \approx 10\,\text{mm}$ was reached. Note that this chosen maximum displacement is greater than the maximum displacement prescribed by the European standard on timber testing EN 383 [26].

4.2.4.3 Test Results

Table 4.9 displays the bolt test results for round ○ and square □ bolts[10]. The specimens with initial cracks are included. Note that the tensile splitting capacity ($f_{s_\parallel}$) has the character of a hypothetical material property as the bolt force and crack surface cannot be directly translated into Mode I splitting capacity. This issue is discussed in detail by Mitch [62] and will not be further addressed here. Instead, a fracture mechanics approach will be used in the discussion of the experimental results. Note that bearing stiffness E_b was established and found lower than compression stiffness E_c. However, for deformation capacity of a bolted connector, the elastic bearing deformation is of little interest. Samples size was as follows: 5 clear ○, 5 node ○, 5 clear □, 6 node □. Detailed results can be found in the appendix in table C.5.

Table 4.9: Average bolt test results for *Phyllostachys pubescens* (round ○; square □)

bolt shape	D_0 [mm]	t [mm]	l_{edge} [mm]	ρ [$\frac{kg}{m^3}$]	t_{cr} [mm]	A_b [mm^2]	A_{cr} [mm^2]	F_b [kN]	f_b [MPa]	F_{cr} [kN]	$f_{s_\parallel}$ [MPa]
$\overline{x}_{clear}$○	105	8.7	93	657	8.6	138	797	15.28	55.41	14.48	18.18
$\overline{x}_{node}$○	98	8.9	93	738	8.8	141	825	17.58	62.56	17.05	20.89
σ_{clear}○	5	0.9	2	12	0.5	9	63	1.77	3.56	1.33	1.11
σ_{node}○	9	1.1	4	41	1.1	18	132	2.91	7.83	2.28	2.71
$\overline{x}_{clear}$□	100	8.4	101	686	8.6	138		14.51	52.66		
$\overline{x}_{node}$□	98	9.6	98	692	9.6	153		16.54	54.27		
σ_{clear}□	11	0.8	1	128	0.4	7		3.11	10.69		
σ_{node}□	8	1.4	8	111	1.4	23		1.78	3.26		

Two typical load-displacement curves could be observed for the round and square bolt configuration[11] (figure 4.15). For the square bolt configuration, embedment displacements were at least twice as large as maximum displacements of round bolts.

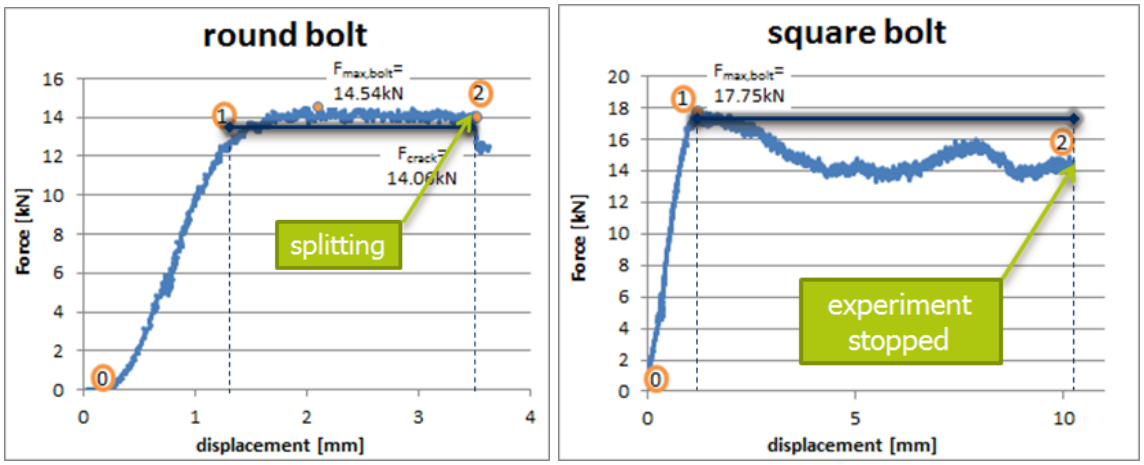

(a) round bolt (b) square bolt

Figure 4.15: Typical load-displacement curves bolt test

[10] outer diameter D_0, thickness t, edge distance l_{edge}, density ρ, culm thickness at the point of the continuous crack t_{cr}, bearing surface $A_b = dt$, splitting surface A_{cr}, maximum bolt force F_b, bearing strength $f_b = F_b/2A_b = 2dt$, crack opening force at onset of final tensile splitting (F_{cr}) and splitting capacity $f_{s_\parallel} = F_{cr}/A_{cr}$

[11] The maximum bolt force $F_{max,bolt}$ represents one data point of table C.5.

(a) round bolt clear (b) round bolt node (c) square bolt clear (d) square bolt node

(e) round bolt clear (f) round bolt node (g) square bolt clear (h) square bolt node

(i) crack ↓ ○ (j) crack ↓, ↑ ○ (k) crack ↓ ○ (l) crack ↓, ↑ ○ (m) crack ↓ □ (n) crack ↓, ↑ □

Figure 4.16: Bolt embedment and splitting failure

For **round** bolts, the individual points in figure 4.15a indicate the following events: ⓪ Contact is made between bolt and adjacent bamboo material. Bearing (embedment) takes place (figure 4.16a and 4.16b) until the first crack begins to form at ①. Crack growth of first crack and new cracks emerge. ② One crack has grown towards the bottom plate (figure 4.16i and 4.16k) or towards both ends of the specimen (figure 4.16j and 4.16l). Force drops rapidly; end of experiment. Splitting strength of round bolts in table 4.9 is established at point ② of figure 4.15a by dividing the bolt force by the area of one crack ($A_{cr} = l_{edge} t_{cr}$).

For **square** bolts the events in figure 4.15b are as follows : ⓪ Contact is made between bolt and adjacent bamboo material. Start of embedment of the bolt. Simultaneously, two cracks form at the corners of the square hole. When cracks are ca. 5 mm long, the fibres under the bolt buckle and a wedge is pushed out ① (figure 4.16c and 4.16d). At 10 mm displacement[12], the

[12]This chosen maximum displacement is more than the displacement prescribed by the European standard on timber testing EN 383 [26].

experiment is stopped ②. Crack growth that resulted in entire tensile splitting occurred only in half of the specimens and the cracks only propagated to the bottom loading plate[13](figure 4.16m and 4.16n). Splitting strength for square bolts was thus not established. Note: The wedge resulted from buckling of the culm wall but it was not clear, whether the cracks resulted from Mode I or Mode III failure.

Due to manufacturing of the specimens, the distance between square bolts and node was so great that only one experiment could be continued until the wedge reached the node without jeopardizing the intactness of the external displacement gauge. An interesting behaviour could be observed in the resulting load-displacement diagram which is displayed in figure 4.17a: After initial embedment ①, a wedge is formed and the force decreases ②. As displacement continues, tensile splitting sets in and the bolt force increases again as soon as the displaced bolt reaches the nodal region ③. Due to comparability, the first force peak of 15.38 kN was used in table 4.9 and C.5. Figure 4.17d depicts failure of the node and subsequent splitting. It was not possible to observe whether the node failed in Mode I (tensile splitting), Mode II (interlaminar shear) or Mode III (out-of-plane shear) failure. In order to answer this question, the nodal fracture toughness Mode I to III of Moso needs to be examined. Below the nodal region, the specimen clearly failed in Mode I (tensile splitting).

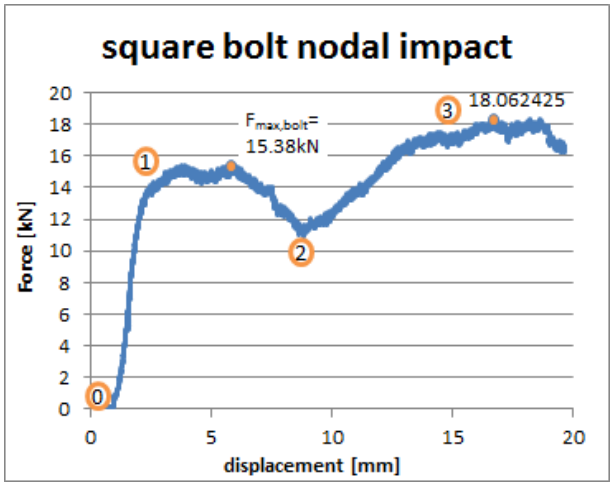

(a) Load displacement curve

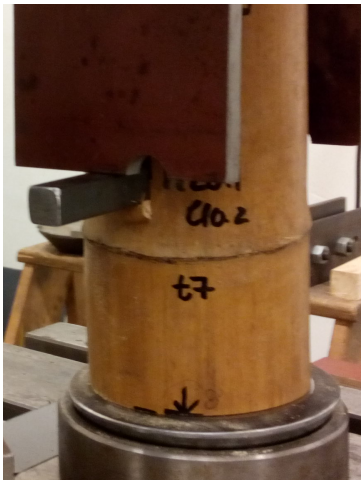

(b) wedge forming

(c) bearing failure

(d) bearing and splitting

Figure 4.17: Nodal impact on square bolt embedment

[13]except in the case of an initial continuous crack which was further opened by the load

4.2.4.4 Discussion and Conclusion

Figure 4.18 shows plots of the bearing (embedment) and splitting strength versus density and bearing strength versus splitting strength.

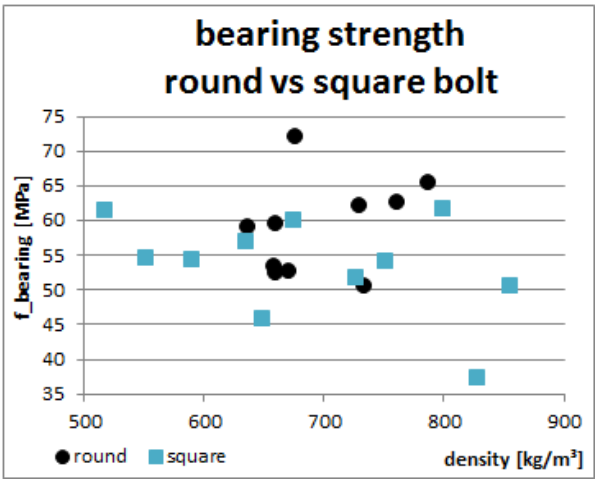

(a) bearing strength (f_b) versus density (ρ) round bolts (○) and square bolts (□)

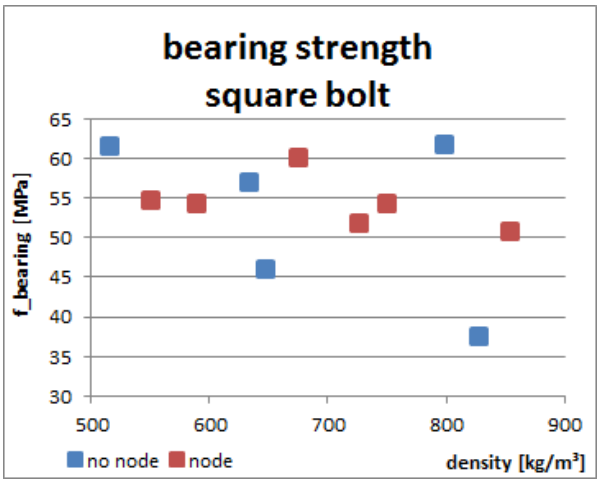

(b) bearing strength (f_b) versus density (ρ) square bolts (□)

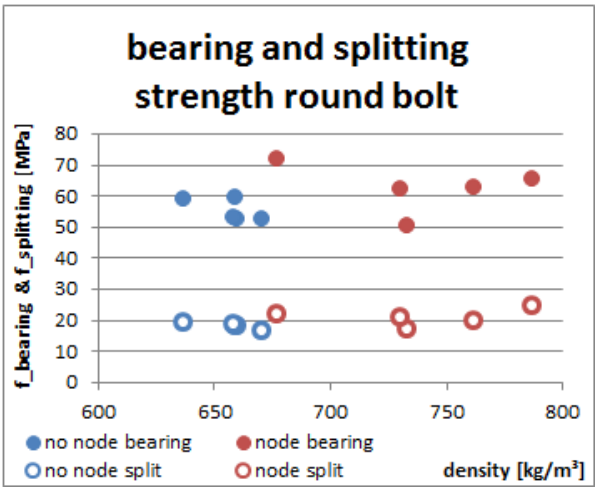

(c) bearing strength (f_b) and splitting strength ($f_{s_\parallel}$) versus density (ρ); round bolts (○)

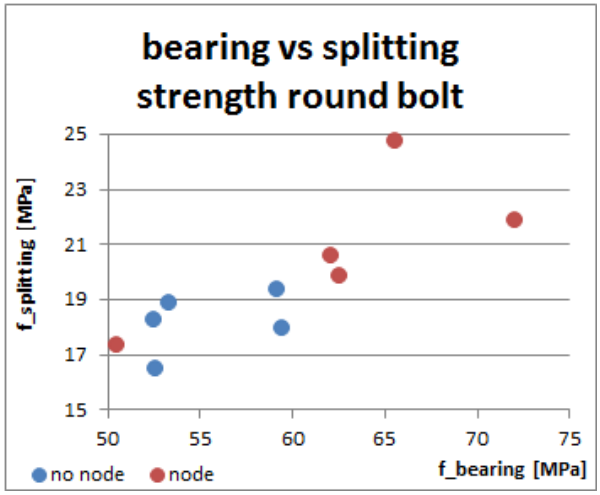

(d) bearing strength (f_b) versus splitting strength ($f_{s_\parallel}$); round bolts (○)

Figure 4.18: Bearing and splitting strength of round and square bolts

It was not possible to establish a correlation between bearing or splitting strength and density. However, there was a weak correlation between bearing and splitting strength of specimens with round bolts (figure 4.18d). For round bolts, average density of specimens with nodes was higher than those without nodes (figure 4.18c).

Table 4.10: Summary of bolt test results for round and square bolts

Bolt Shape	ρ_{clear} [kg/m^3]	ρ_{node} [kg/m^3]	$\frac{\rho_{clear}}{\rho_{node}}$ [−]	$f_{b,clear}$ [MPa]	$f_{b,node}$ [MPa]	$\frac{f_{b,clear}}{f_{b,node}}$ [−]	$f_{s_\parallel,clear}$ [MPa]	$f_{s_\parallel,node}$ [MPa]	$\frac{f_{s,clear}}{f_{s,node}}$ [−]
○	657	738	0.89	55.41	62.56	0.89	18.18	20.89	0.87
□	686	692	0.99	52.66	54.27	0.97			

The average bolt force that led to tensile splitting F_{cr} was 95% of the average bolt bearing force F_b for clear specimens and 97% for specimens with nodes. Both bearing strength $f_{b,node}$ and splitting strength $f_{s_\parallel,node}$ of specimens with nodes was higher than of clear specimens ($f_{b,clear}$ and $f_{s_\parallel,clear}$, see table 4.10) which is in agreement with the theory presented in chapter 4.2.5. As there was no correlation between density and bearing or splitting strength, it can be assumed that the higher density of specimens with nodes is not the cause for the higher strength but that the favourable microstructure of nodes leads to the strength increase.

For square bolts, average density of specimens with and without nodes was almost the same (table 4.10). There was little difference between bearing strength of specimens with and without nodes. However, the displaced bolt did barely enter the nodal region which makes it impossible to evaluate the influence of nodes on a square bolt configuration. The square bolt showed distinct embedment prior to crack propagation and final tensile splitting.

Remarkably, there is little difference in mean bolt bearing strength (f_b) between a round or square configuration. However, the displacement capacity of square bolt specimens was much higher than of round specimens. Furthermore, splitting did only occur in half of the cases for square bolts whereas every specimen with a round bolt showed at least one distinct continuous longitudinal crack.

Comparison to Literature In the given case, it can only be said that splitting strength was much higher than observed by Fu et al. [29]. Nodes had a positive influence on bearing and splitting capacity which was suggested by literature.

Furthermore, the obtained bearing strength can be compared to the compressive strength that was determined earlier. For Moso, compressive strength was $f_{c,node} = 49.9\,\text{MPa}$ and $f_{c,clear} = 47.5\,\text{MPa}$. The average bearing strength for specimens with and without nodes with square and round bolts was up to 25% higher than the compressive strength! This shows that a tensile connector with an end plate is very suitable in terms of bearing, especially if square bolts (cross dowels) are employed. In terms of nodes it seems favourable to place a connector close to a node and use it as natural reinforcement. Still, the great bearing strength of clear specimens ($f_{b,clear}$) suggests that bolts can also be placed at a greater distance from the node. In all cases, the edge distance l_{edge} should be long enough to allow for ductile bearing failure and wedge forming before crack growth can lead to brittle tensile splitting failure. The edge distance of 10 cm that was employed in the experiments satisfied this requirement and can thus be adopted in the connector design.

Fracture Mechanics: Influence of Bolt Shape and Node The remaining task is to attempt to explain the different failure modes that were induced by the different bolt shapes, and quantiy the impact of the node. An attempt is made to provide an explanation using fracture mechanics.

Shao et al. conducted experiments on Mode I interlaminar fracture toughness of Moso bamboo [79]. Wang et al. investigated the toughness contribution of the bamboo node to the Mode I interlaminar fracture toughness of Moso bamboo [95]. Wang et al. conducted experiments on Mode II interlaminar fracture toughness [94] of Moso bamboo. The findings were the following:

$$
\begin{aligned}
G_{IC,clear} &= 358\ \text{J/m}^2 \quad [79] \\
G_{IC,clear} &= 498\ \text{J/m}^2 \quad [95] \\
G_{IC,node} &= 1431\ \text{J/m}^2 \quad [95] \\
G_{IIC,clear} &= 1303\ \text{J/m}^2 \quad [94]
\end{aligned}
$$

Orthotropic composites (such as timber and bamboo) are in general more brittle than isotropic materials and local stress concentrations are higher. For round bolts, there is one distinct stress peak at the bottom centre of the hole [21][18] and for square bolts there are two stress peaks in the corners. Round specimens failed clearly in Mode I splitting failure. For square specimens, it was not clear whether the wedge was formed due to Mode I or Mode III failure. As $G_{IIIC,clear}$ has not been determined yet, fracture mechanics cannot answer this question. However, fracture mechanics suggest, that the wedge was not formed in Mode II, as $G_{IIC,clear}$ is up to three times higher than $G_{IC,clear}$.

The node had a clearly positive impact on splitting capacity of round bolts which is confirmed by fracture mechanics ($G_{IC,clear} << G_{IC,node}$). $G_{IIC,node}$ and $G_{IIIC,node}$ have not been determined yet and no statement can be made about shear capacity.

Conclusions For full-culm bamboo bolted connections, square bolts perform much better in terms of failure mode and displacement capacity. Apparently, the stress concentrations in the corners of the rectangular hole are crack initiators that lead to prescribed ductile wedge forming rather than brittle splitting. The embedment surface is prescribed by the bolt shape and thickness; a square bolt results in the more favourable contact area. Manufacturing of square holes should be improved by using a square-hole drill instead of a saw chain.

For the round configuration, nodes have a positive effect on bearing and splitting capacity. In future research, the impact of nodes on the square configuration could be examined by placing the bolt closer to the node and continuing the experiment until splitting occurs.

It can be assumed that embedment capacity of square bolts can be increased by using a larger bolt diameter. Additional research needs to be conducted to explore whether the relationship of bolt diameter and embedment strength is linear.

The fact that Mode I fracture toughness of clear specimens is substantially lower than Mode II fracture toughness suggests that splitting prevails in most cases. By changing the bottom loading plate to a plate with a gap, increasing the bolt diameter d, and decreasing the edge distance l_{edge}, it can be investigated whether block shear can actually occur and whether the node has a positive or negative effect. With the given square bolt configuration and edge distance, it is safe to assume that connector strength is governed by embedment and splitting as long as the end plate is in place. This conclusion will be used in chapter 7.

4.2.5 Influence of Nodes (experiments)

In chapter 2.2.3, a literature review describes the macroscopic and microscopic structure of nodes, and the influence of nodes on material properties. This chapter focusses on the experimental program which consisted of a 3D nano scan and an electron microscopy of Guadua and Moso nodes. The findings are discussed and related to results from compression and bolt shear experiments.

4.2.5.1 3D Scan

Set-up A 3D nano scan of the nodal region of *Phyllostachys pubescens* and *Guadua angustifolia* specimens was made in order to examine and compare the 3D microstructure of nodes. The engaged scanner was a *Phoenix Nanotom* high resolution CT-scanner with a resolution of 5µm. Figure 4.19 shows the preparation of the specimens, which were later cut into smaller pieces for electron microscopy. The dimensions of the employed cross-sections were also basis for the height assumption of the nodal diaphragm in the other experiments (3 mm for Moso and 5 mm for Guadua).

(a) Moso specimen (b) Guadua specimen

Figure 4.19: Preparation of specimens for 3D nano scanner

Results Figure 4.20 shows the scan of the *Phyllostachys pubescens* (Moso) node and figure 4.21 shows the *Guadua angustifolia* node. On the scans it can be observed that most vascular bundles run longitudinally through the culm wall without changing direction (solid arrow in figure 4.22). Some vascular bundles close to the inside culm wall deviate into the nodal diaphragm. Bundles from the diaphragm also run radially into the culm wall (dashed arrow in figure 4.22). This results in an interwoven structure of longitudinal and transverse vascular bundles in the culm wall. The 3D scan of the Moso nodes also shows vascular bundles that run circular close to the inside culm wall at the top of the diaphragm (dotted arrow in figure 4.22). For Guadua, this is also the case but less clearly developed. In the diaphragm itself, vascular bundles become shorter and randomly oriented which can be especially well observed in the Guadua sample. For both species, bundles close to the the outside culm wall end in the sheath where bamboo leaves emerge. The 3D scans also suggested bifurcation of vascular bundles but it was not possible to observe whether single fibre strands split up into two new strands.

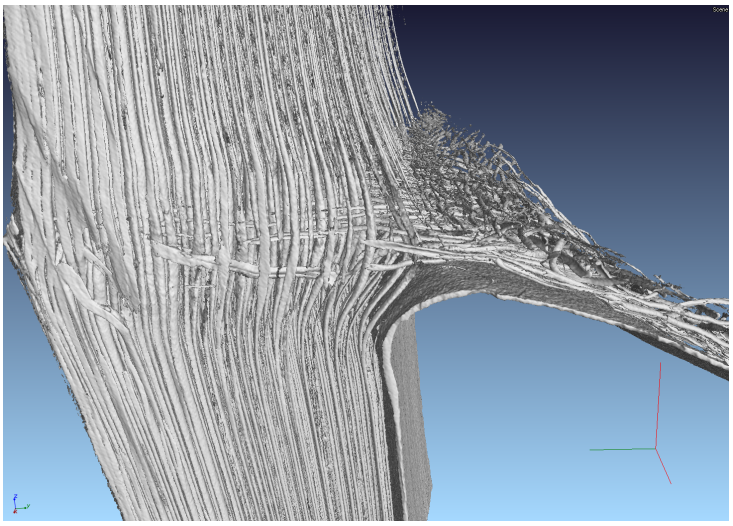

Figure 4.20: 3D scan of Moso node

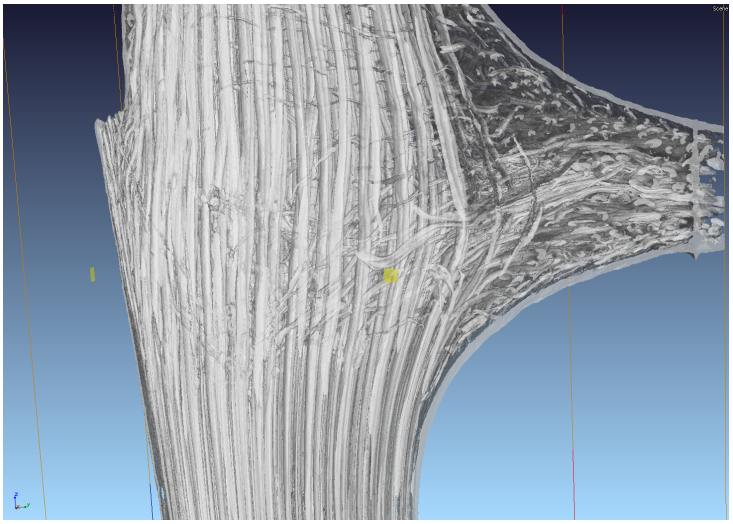

Figure 4.21: 3D scan of Guadua node

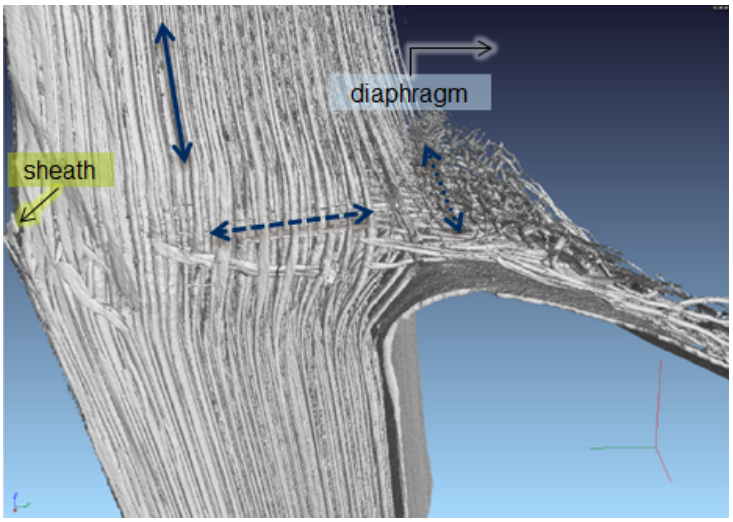

Figure 4.22: Directions of vascular bundles in Moso node

4.2.5.2 Electron Microscopy

Set-up From the 3D scans it was not possible to determine whether bifurcation of fibre strands occurs. Therefore, small pieces of the scanned *Guadua angustifolia* node were examined in an *Environmental Scanning Electron Microscope* (ESEM) with an enlargement up to 2000. The obtained pictures in figure 4.23 have a resolution of 200µm (enlargement 100 respectively 125).

Results Although the fibre strand was slightly damaged by the preparation process, it can be clearly observed that fibre bifurcation does indeed occur in the nodal region (figure 4.23b). Fibre bifurcation could potentially add to the stability and isotropy of the interwoven nodal structure. However, exact location of bifurcation and orientation of the new strands still need to be examined. The remaining length of the strands after bifurcation also needs to be considered to make a statement about additional stability of the weave.

Figure 4.23a shows a cross-section of a vascular bundle embedded in parenchyma tissue. The structure of fibre strand, sclerenchyma sheath, phloem and metaxylem can be clearly observed (figure 2.3 contains the respective labelling).

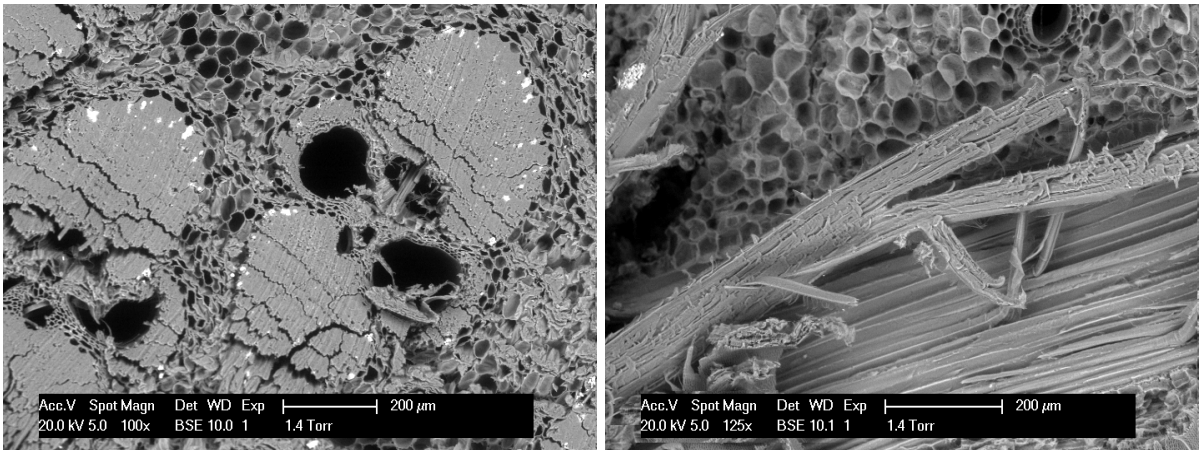

(a) Cross-section vascular bundle (b) Fibre bifurcation nodal region

Figure 4.23: Guadua electron microscope images

4.2.5.3 Discussion and Conclusion

The macroscopic findings of the influence of nodes on mechanical properties can be attributed to the nodal microstructure. In the following, the results are summarized and a link between macroscopic and microscopic properties is made. The findings are compared to relevant literature.

Axial Strength Full-culm compressive strength of both *Guadua angustifolia* and *Phyllostachys pubescens* is negatively impacted by the presence of nodes. Cracking always occurred in the clear part of the specimen, never in the node itself. This agrees with the findings of Shao et al. [77], who found higher compression strength of small samples extracted from the nodal region. The tangential fibre strands increase compression capacity of the node itself. However, change in culm geometry at the edge of the nodal region leads to stress concentration and overall compression capacity of the full-culm specimen is decreased. This agrees with the findings of Ghavami et al. [32].

Tensile strength is negatively impacted by nodes on a small and large scale due to non-uni-axial fibre orientation in the nodes [77][99].

Both tensile and compressive Modulus of Elasticity suffer from the changed orientation of vascular bundles. While tensile Modulus of Elasticity is decreased as there are less axial fibres that contribute to the stiffness, compressive Modulus of Elasticity is decreased as transverse vessels get compressed.

Bolts: Bearing, Splitting and Shear Strength For both bearing and splitting strength of bolted connections, nodes have a positive influence. The tangential fibres in the node act as reinforcement and result in 13% higher average splitting capacity and 11% higher bearing capacity for round bolts. Subsequently, it makes sense to place bolts close to nodes and use them as natural reinforcement. As block shear was prevented by the bottom loading plate configuration, further research is needed in order to determine the impact of nodes on shear capacity. However, as Mode II fracture toughness of clear specimens is about 3 times higher than Mode I fracture toughness, and the shear area is twice the splitting area, Mode I splitting is expected to be governing in round bolted connections, independent of the presence of nodes.

Square bolts introduced embedment and wedge forming due to either two Mode I or Mode III cracks at the edges of the hole. In the wedge, the culm wall buckled to the outside which can be attributed to the functionally graded microstructure of the culm wall: The fibre volume fraction increases along the thickness of the wall, leading to less rigidity and a greater displacement capacity at the inside culm wall. Therefore, the culm wall buckles to the outside.

There was only a single case in which the square dowel reached the nodal region: Culm wall buckling did not occur until the nodal region was passed which resulted in an increase of force by 17% compared to the initial bearing force. The late buckling can be attributed to the microstructure of the node, which contains radial and tangential reinforcing fibres. From the failure pattern it was not clear, whether the nodal region failed in Mode I or Mode III. More research needs to be done to determine the average macroscopic effect of nodes on bearing strength of square bolts. Variation of square bolt width d and edge distance l_{edge} could provide additional insight into the interaction of bearing, splitting and shear failure of square bolted connections. Furthermore, future research should include the species *Guadua angustifolia*, in order to see whether the small differences in the nodal microstructure have an impact of macroscopic mechanical properties. Finally, G_{IC}, G_{IIC} and G_{IIIC} of the node and internode should be determined for both species.

Conclusion Nodes have a clear negative effect on tensile strength. They have a local positive effect on compression strength but a negative effect on full-culm compression strength and Modulus of Elasticity. Nodes have a positive effect on bolt bearing and splitting strength, independent of the bolt shape. More research needs to be done to make a statement about longitudinal and out-of-plane shear strength.

4.3 Summary and Conclusions

A linear relationship between density ρ and dynamic Modulus of Elasticity E_{dyn} was found for both *Guadua angustifolia* and *Phyllostachys pubescens*. Yet, a relationship between static and dynamic Modulus of Elasticity still needs to be established.

Additionally, a very strong linear relationship between density ρ and compressive strength f_c and a relatively strong relationship between density ρ and compressive Modulus of Elasticity E_c was found for both species. Crack initiation always occurred in the clear part of the specimen, never in the node. This hints to a higher compressive capacity of the node itself, possibly as a result of lateral reinforcing fibres. Compressive strength of clear specimens was approximately 5% higher than of specimens that contained nodes; Modulus of Elasticity was in average 10% higher. The lower overall strength of specimens with nodes can be explained by changes of culm geometry close to the node that induce stress concentrations which can lead to premature cracking.

No relationship could be established for bolt bearing strength f_b, bolt splitting strength $f_{s_\parallel}$ and density ρ. The reinforcing nature of nodes had a positive effect on both bearing and splitting strength. The square bolt resulted in a more favourable failure mechanisms (embedment with large displacement) than the round bolt (little embedment and subsequent tensile splitting). More research is needed concerning block shear and out-of-plane shear in bolted connection.

The following linear relationships were established (all of them significant: $\alpha = 0.05$):

Phyllostachys pubescens	E_{dyn}	$= 21.692\ \rho - 2895;$	$R^2 = 0.7407;$	$p = 0.00004$
	$E_{c,clear}$	$= 11.236\ \rho - 238.63;$	$R^2 = 0.9585;$	$p = 0.0007$
	$E_{c,node}$	$= 24.546\ \rho - 11121;$	$R^2 = 0.6705;$	$p = 0.00243$
	$f_{c,clear}$	$= 0.0554\ \rho + 10.6;$	$R^2 = 0.9963;$	$p = 0.00005$
	$f_{c,node}$	$= 0.0721\ \rho - 5.1948;$	$R^2 = 0.9408;$	$p = 0.0003$
Guadua angustifolia	E_{dyn}	$= 19.687\ \rho + 5112;$	$R^2 = 0.7047;$	$p = 0.00914$
	$E_{c,clear}$	$= 31.965\ \rho - 15113;$	$R^2 = 0.7517;$	$p = 0.0025$
	$E_{c,node}$	$= 21.579\ \rho - 8564;$	$R^2 = 0.8658;$	$p = 0.0071$
	$f_{c,clear}$	$= 0.1772\ \rho - 77.602;$	$R^2 = 0.8330;$	$p = 0.0006$
	$f_{c,node}$	$= 0.1325\ \rho - 49.76;$	$R^2 = 0.9916;$	$p = 0.00003$

Table 4.11 provides a summary of the test results of the average dynamic Modulus of Elasticity. Table 4.12 gives an overview of the average values of compression test results. Table 4.13 summarizes the findings of the bolt shear test with a round (○) and square (□) bolt.

Table 4.11: Summary of average dynamic Modulus of Elasticity for *Phyllostachys pubescens* and *Guadua angustifolia*

Species	f_{nat} [Hz]	D_0 [cm]	t [cm]	m [kg]	l_{culm} [cm]	ρ [kg/m^3]	E_{dyn} [MPa]	$E_{stat} \approx 0.75 E_{dyn}$ [MPa]
Moso $\overline{x}$	1762	10.29	1.0	2.34	117.3	660	11431	8573
Guadua $\overline{x}$	1641	12.91	1.4	5.82	158.2	740	19681	14760
Moso σ	178	0.65	0.1	0.43	12.7	74	1866	
Guadua σ	266	1.73	0.2	0.62	23.3	151	3536	

Table 4.12: Summary of average compression test results for *Phyllostachys pubescens* and *Guadua angustifolia*

Species	D_0 [mm]	t [mm]	h [mm]	ρ [$\frac{kg}{m^3}$]	$f_{c,clear}$ [MPa]	$f_{c,node}$ [MPa]	$\frac{f_{node}}{f_{clear}}$ [−]	$E_{c,clear}$ [MPa]	$E_{c,node}$ [MPa]	$\frac{E_{node}}{E_{clear}}$ [−]
Moso $\overline{x}$	96.5	8.5	152.5	722	49.9	47.5	0.95	7746	6817	0.88
Guadua $\overline{x}$	123.6	12.6	150.5	796	60.7	58.6	0.96	9845	9082	0.92
Moso σ	7.7	2.0	4.4	80	5.0	5.7		1030	2296	
Guadua σ	7.9	2.1	3.2	95	14.6	16.4		2775	2867	

Table 4.13: Summary of average bolt test results for round and square bolts for *Phyllostachys pubescens*

Bolt Shape	ρ_{clear} [kg/m^3]	ρ_{node} [kg/m^3]	$\frac{\rho_{clear}}{\rho_{node}}$ [−]	$f_{b,clear}$ [MPa]	$f_{b,node}$ [MPa]	$\frac{f_{b,clear}}{f_{b,node}}$ [−]	$f_{s_\parallel,clear}$ [MPa]	$f_{s_\parallel,node}$ [MPa]	$\frac{f_{s,clear}}{f_{s,node}}$ [−]
○$\overline{x}$	657	738	0.89	55.41	62.56	0.89	18.18	20.89	0.87
□$\overline{x}$	686	692	0.99	52.66	54.27	0.97			
○σ	12	41		3.56	7.83		1.11	2.71	
□σ	128	111		10.69	3.26				

Non-destructive testing e.g. by measurements of E_{dyn} provides a feasible way of measuring material properties without destructive testing. However, more destructive experiments need to be conducted in order to establish relationships between non-destructively and destructively obtained properties. The bolt shear test confirmed the positive influence of nodes on splitting and bearing strength of round bolts. In only one specimen with a square bolt the nodal region was entered and the positive effect of the node was confirmed. The remaining tasks for future research are to (a) quantify the influence of the bolt diameter (b) adapted the bottom loading plate to see whether block shear occurs and what influence the node has (c) determine $K_{IC...IIIC}$ by fracture mechanics (d) make a FEM which simulates the stress distribution around the bolt and accounts for the functionally graded structure. This way, the observed failure mechanisms for different bolt shapes can be explained and predicted, and formulas for bolt embedment and splitting strength depending on the bolt shape, l_{edge}, θ and d can be derived.

The obtained results are sufficient to serve as input for the *Grasshopper* dome model. Furthermore, a tensile connector can be proposed and a component based strength prediction can be conducted.

Chapter 5

Geodesic Dome Model

The aim of this research is to work towards a parametric design tool for bamboo geodesic dome structures. For this purpose, two example load cases are analysed in detail: self-weight and point load on top of the dome. They serve to illustrate the underlying methods of the parametric structural analysis and cover the analytical challenges of global buckling and geometrical non-linearity.

Superimposed dead load by dome cladding, wind load, and snow load are implemented in the model but are not included into the theoretical analysis. Dynamic load cases are not part of the model.

The model input is based on mean strength values from experiments and literature. **The principle of superposition does generally not hold for global buckling and geometrically non-linear analysis!** In the following, it will be shown that for medium sized domes[1], global buckling does not occur. On the other hand, effects of geometrical non-linearity cannot be neglected; linear superposition of load case is thus only possible for linear load cases. Strength of tensile connectors is not considered in this chapter as it is not a material property but dependent on connector design. The case study in chapter 8 takes connector strength into account and makes use of a structural safety concept in the style of the Eurocodes[2].

In chapter 5.1, general information about *Grasshopper* is given and the model and input parameters are explained. Subsequently, the research questions of chapter 1.3 are investigated:

- The effect of opening size and position on the maximum strut stresses is explored in a parametric study in chapter 5.2.
- In chapter 5.3, the effect of the dome frequency $\mathfrak{f}$ on strut stresses of half-spherical domes is illustrated. The concept of stress normalization is explained and general relationships between strut length L, dome frequency $\mathfrak{f}$ and dome diameter D are derived.
- The phenomena of global and local buckling is explored in a parametric study in chapter 5.4 for self-weight and a point load on top of the dome. Boundary conditions are derived for which global buckling does not occur and linear superposition of load cases is possible. Additionally, rules of thumb are derived which indicate the limit diameter for geodesic domes made of *Guadua angustifolia* and *Phyllostachys pubescens*.
- As an extension of the subject, the performance of shells and domes with respect to stability is compared in chapter 5.5.
- Chapter 5.6 summarizes the findings and draws conclusions.

[1] e.g. $D = 50\,\mathrm{m}, \mathfrak{f} = 8$

[2] more information on probabilistic design is given in chapter 6

5.1 Dome Model and Input

A parametric geodesic dome model is designed using the *Rhinoceros* plug-in *Grasshopper*. The model data can be exchanged between *Grasshopper* and the finite element analysis software *Oasys GSA* using the plug-in *Geometry Gym*. The *Grasshopper* script was partly inspired by the MSc thesis of Arend van Waart [93], and is further discussed in appendix A. The general characteristics of geodesic domes are explained in chapter 3.2.

5.1.1 General Information about *Grasshopper*

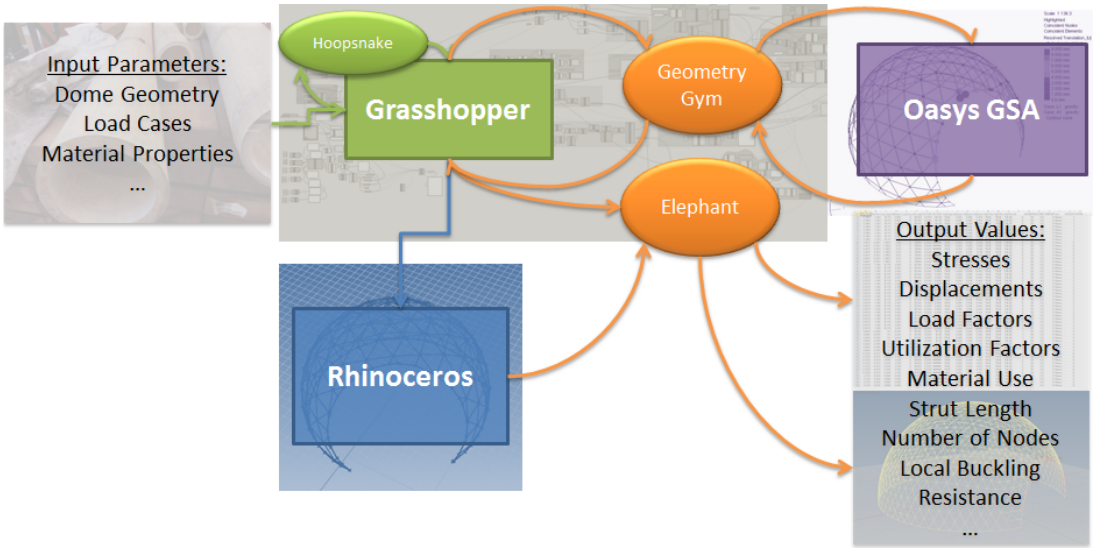

Figure 5.1: Flow Chart

Grasshopper is a graphical algorithm editor that allows to generate and interlink prepared pieces of programming code by plugging *wires* (links) into *components* (pieces of code). This defines the order in which the pieces of code are executed. A *component* performs an action based on an input (incoming wires) and gives an output (outgoing wires). As the underlying programming script is by default not seen by the user, a *component* works like a black box and results can only be verified by checking the output data. All input data can be defined parametrically and stored in variables (e.g. a number, an integer or a Boolean). Using the plug-in *Geometry Gym*, the geometry generated by *Grasshopper* can be transformed into finite elements and exported to various FE software, including *Sofistik* and *Oasys GSA* (GSA). In the given case, the structural analysis was performed in GSA[3], including linear static, geometrically non-linear (GNL) and global buckling (GB) analysis. Results including load factors, stresses and displacements are extracted by *Geometry Gym* and can be displayed in *Grasshopper* and *Rhinoceros* (figure 5.2). Arend van Waart programmed a set of *Grasshopper* components called *Elephant* that export results into an *Excel* file and automatically take screen shots of the *Rhinoceros* model. The *Hoopsnake* component programmed by Yiannis Chatzikonstantinou allows to automatically loop through sets of parameters, e.g. different dome sizes or load cases. Combining these tools, an automated parametric structural analysis can easily be performed (figure 5.1)[4].

[3] *Geometry Gym* is developed furthest for the exchange between *Grasshopper* and GSA; also simple beam and bar elements of a geodesic domes don't require a 'sophisticated' analysis.

[4] Links for modelling with *Grasshopper* (accessed January 30, 2015): *Grasshopper* download and info `http://www.grasshopper3d.com`; *Geometry Gym* download and info `http://geometrygym.blogspot.nl/`; *Hoopsnake* download `http://www.food4rhino.com/project/hoopsnake?etx`; *Elephant* download `https://github.com/arendvw/ExportTools/commits/master`.

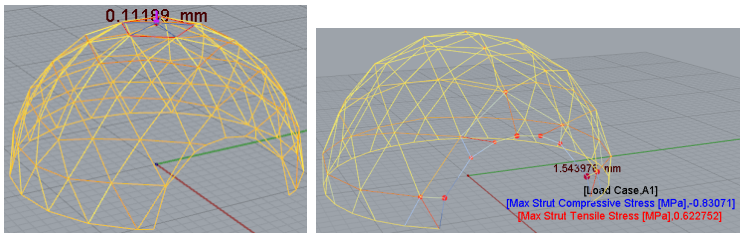

(a) Point load (b) Self-weight

Figure 5.2: Strut stresses and displacements

5.1.2 Input Physical and Mechanical Properties

The model input data in table 5.1 is based on experimental results ($D_0; t; f_c; \rho : E$) and values from literature (all other values). Nature only provides a limited range of bamboo culm geometry: While the strut length L can be increased by axial connection of culms, the strut outer diameter D_0 and wall thickness t cannot be varied freely; a relationship of $D_0 = 0.1\ t$ with $D_0 \in [90; 130]$mm is assumed unless stated differently. Limit values of dome diameter and frequency are based on this input; rules of thumb cannot be applied beyond the given range of input data.

Table 5.1: Input parameters strut and beam materials

property	unit	bamboo struts *Guadua angustifolia*	bamboo struts *Phyllostachys pubescens*	steel beams S235
tensile strength	f_t [MPa]	37	100	235
compr. strength	f_c [MPa]	60	50	235
Modulus of Elasticity	E [MPa]	14760	8570	210000
strut diameter	D_0 [mm]	130	100	free
wall thickness	t [mm]	13	10	$0.1D$
density	ρ [kg/m^3]	740	660	7850
Poisson's ratio	ν	0.38	0.38	0.3

5.1.3 Geodesic Dome Model

All geodesic domes presented in the following are based on icosahedra (figure 5.3a). Other Platonic solids such as octahedron and tetrahedron can serve as an initial polyhedron, but result in an unfavourable stress distribution due to greater variation in strut length [17]. Table 5.2 displays the denotation of model parameters.

Table 5.2: Model parameters and denotations

Parameter	Denotation	Unit	Description
Dome diameter	D	[m]	Results in linear scaling of entire dome
Frequency	ƒ	[−]	Number of subdivisions of initial triangle
Trimming plane	$T \in [-0.5; 0.5]D$	[m]	Trims spherical polyhedron to dome: $T = -0.5$ Geodesic Sphere
Opening size	$\in [0; 1]D$	[m]	$0.5D$: Opening diameter is half the dome diameter
Z-position	$z \in [0; 1]D$	[m]	Position of opening with respect to z $z = 0$: no intersection (figure 5.4)
Opening rotation	$\in [0; 360]$	[°]	Counter clockwise rotation of opening around dome‘s z-axis
Strut diameter	D_0	[mm]	External strut diameter
Wall thickness	t	[mm]	If not defined differently: $t = 0.1\ D_0$
Strut length	L	[m]	Maximum strut length
Load case	LC	[−]	LC1: self-weight; LC2: point load (linear or GNL)
Point load	F	$[kN]$	If not defined differently: $F = 1\,\text{kN}$

The number of triangles that result from subdivision of the initial polyhedron's faces is defined by the frequency ƒ (figure 5.3b and 5.3c). A higher frequency provides a better approximation of a sphere. The model x-y-z-coordinate system is located in the centre of the approximated sphere (figure 5.3c; red:x, green:y, up:z). The sphere can be trimmed to a dome at any perimeter parallel to the equator. The z-coordinate of the trimming plane is denoted as T. The initial polyhedron stays untrimmed for $T = -0.5D$ and the dome vanishes entirely for $T = 0.5D$ (figure 5.3d to 5.3f). The dome diameter is denoted as D and equal to the initial sphere's diameter which is not the 'true' diameter D_{true}[5] of the trimmed dome. D can be varied freely and results in mere scaling of the entire model.

An approximated ellipse opening is introduced by intersecting a cylinder with the dome and linearly connecting the intersecting points (figure 5.4). The opening's size as well as vertical position with respect to the dome's base plane can be changed freely (size: figure 5.3g to 5.3i; z-position: figure 5.3j to 5.3l). The opening can also be rotated counter clockwise about the dome's z-axis (figure 5.3j to 5.3l). The edge of the opening is modelled as a rigid steel beam that possesses enough stiffness to prevent buckling. The base points, which result from trimming at T, are connected by a rigid steel beam and pinned supported by springs with stiffness $\xi = 0.5$ in x- and y-direction.

The dome can be subjected to self-weight (LC1) or a point load at the highest point of the dome (LC2). Three different strut materials are implemented: S235, Guadua and Moso bamboo. All struts are modelled as pinned-ended bars[6] made from circular hollow sections. The nodal structure of bamboo culms and stiffness of dome hubs are neglected.

[5] D_{true} is obtained by measuring the greatest distance of the dome's base points. $D_{true} < D$ always holds and the inequality is greater for small frequencies and for trimming planes $T \neq 0$

[6] In real life application, torque and lateral displacements of bamboo struts are partially restrained by the dome hub. However, it can be assumed that bending moments and shear forces cannot be transferred by the proposed tensile connector without large deformations. Therefore, it is safe to assume that the bamboo struts are indeed pinned-ended bars. Note that the actual strength of the tensile connector is only included in chapter 8.

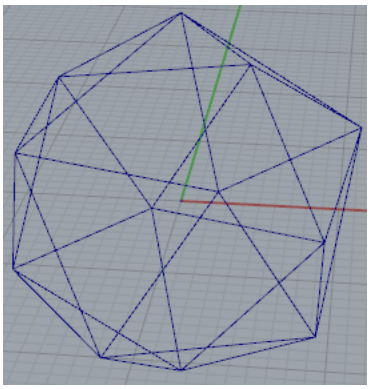

(a) Icosahedron $\mathfrak{f} = 1$

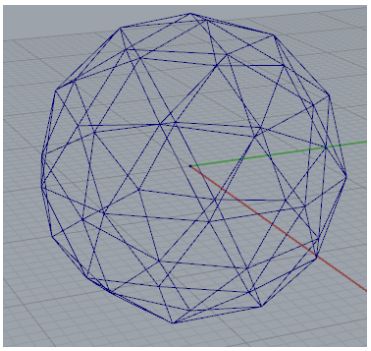

(b) Icosahedron-based polyhedron $\mathfrak{f} = 2$

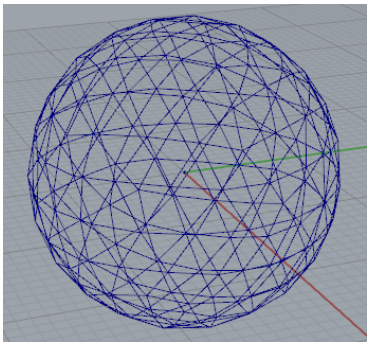

(c) Icosahedron-based polyhedron $\mathfrak{f} = 4$

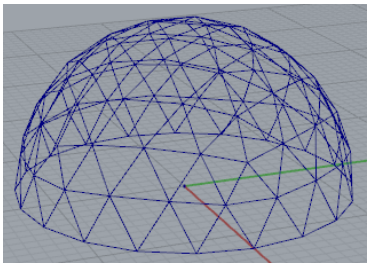

(d) Half-spherical geodesic dome, $T = 0$

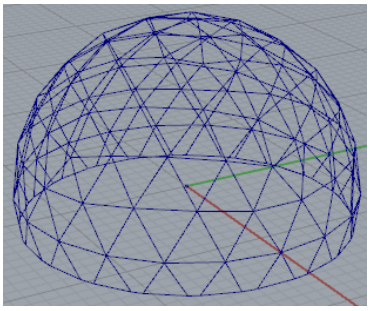

(e) Geodesic dome $T = -0.2$

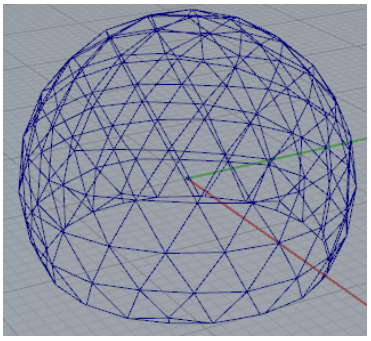

(f) Geodesic dome $T = -0.7$

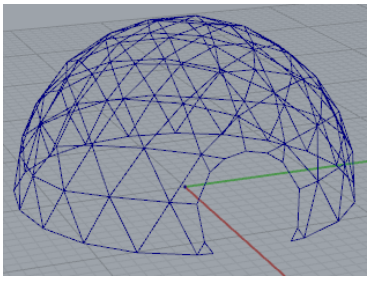

(g) Opening size $0.2D$

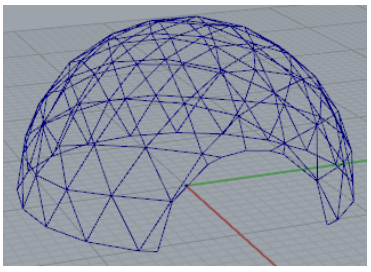

(h) Opening size $0.5D$

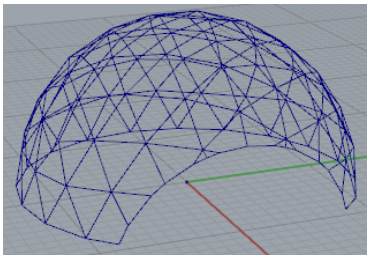

(i) Opening size $0.9D$

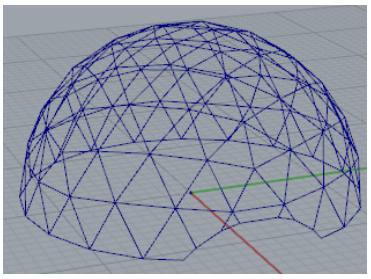

(j) z=0.2, size $0.5D$

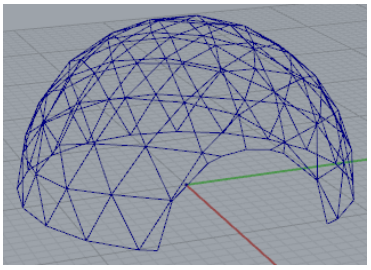

(k) z=0.5, size $0.5D$

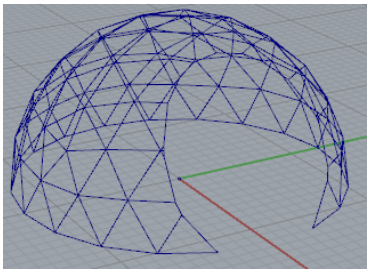

(l) z=0.9, size $0.5D$

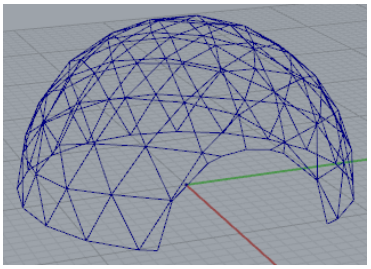

(m) Rotation 0°, z=0.5, size $0.5D$

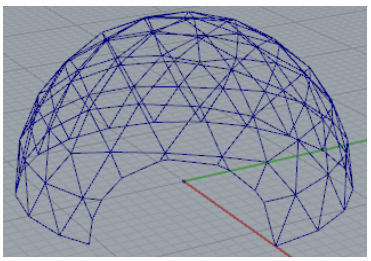

(n) Rotation -30°, z=0.5, size $0.5D$

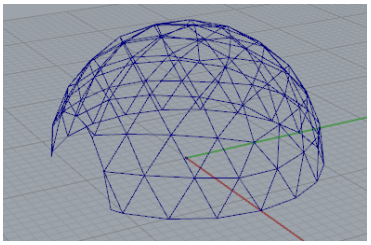

(o) Rotation -90°, z=0.5, size $0.5D$

Figure 5.3: Model parameters

5.2 Parametric Study - Position and Size of Opening

5.2.1 Input Parameters

An opening is introduced and rotated around the z-axis of the dome for LC1 (self-weight). The results are displayed in maximum strut stresses [MPa] which are material and geometry dependent. Obviously, a change of strut surface area ($D_0; t$) results in different strut stresses. But also a change of material or geometry of the opening edge beam has an impact on strut stresses. In chapter 5.3.1, the principle of normalizing stresses is presented. However, for the given application, real stresses are considered more illustrative and the results will be discussed qualitatively. For all results in this entire chapter (5.2), the following parameters were used[7]:

Table 5.3: Parameters used for parametric study of opening position

Geodesic dome	Icosahedron-based
Dome diameter	$D = 50\,\text{m}$
Trimming plane	$T = 0$
Opening size	0.5 D (except figure 5.6)
Z-position	$z \in [0; 1]$
Struts	Moso bamboo
Outer diameter	$D_0 = 69\,\text{mm}$
Wall thickness	$t = 7\,\text{mm}$
Opening edge beam	steel S235
Outer diameter	$D_0 = 150\,\text{mm}$
Wall thickness	$t = 20\,\text{mm}$

5.2.2 Creation of Opening and Explanation of Z-Position

An opening is introduced by intersecting a cylinder with the initial geodesic dome (figure 5.4). The opening size is 0.5 D which corresponds to 50% of the initial dome diameter. The z-position indicates where the highest point of the cylinder is located with respect to the base plane of the geodesic dome. Note that the base plane of the dome is generally not equivalent to the x-y-plane of the initial sphere's coordinate system unless $T = 0$.

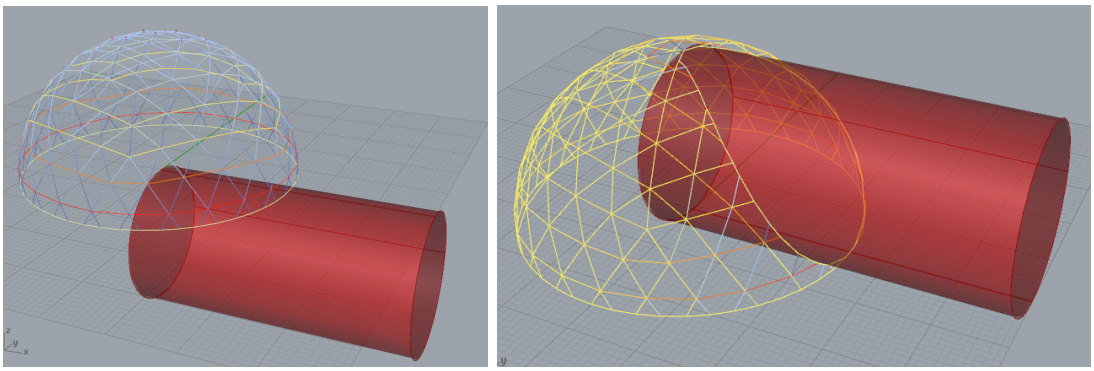

(a) z=0 (b) z=1

Figure 5.4: Creation of opening by intersecting cylinder with geodesic dome in Rhinoceros

[7]The input of Moso was based on a literature study as this part of the model analysis was conducted prior to experiments

The z-position can be varied between 0 and 1 (figure 5.5). $z = 0$ results in no intersection of dome and cylinder, thus no opening (figure 5.4a). $z = 1$ indicates that the top vertex of the geodesic dome and the top of the cylinder coincide (figure 5.4b). The intersecting points of cylinder and dome are detected by *Grasshopper* and connected by linear beam segments. The resulting polyline is defined as a rigid steel beam and is referred to as "opening edge beam" in this entire thesis.

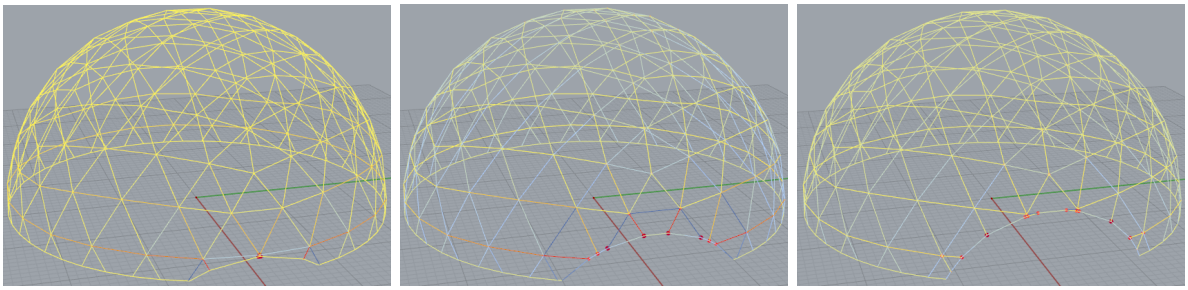

(a) z=0.1 (b) z=0.2 (c) z=0.3

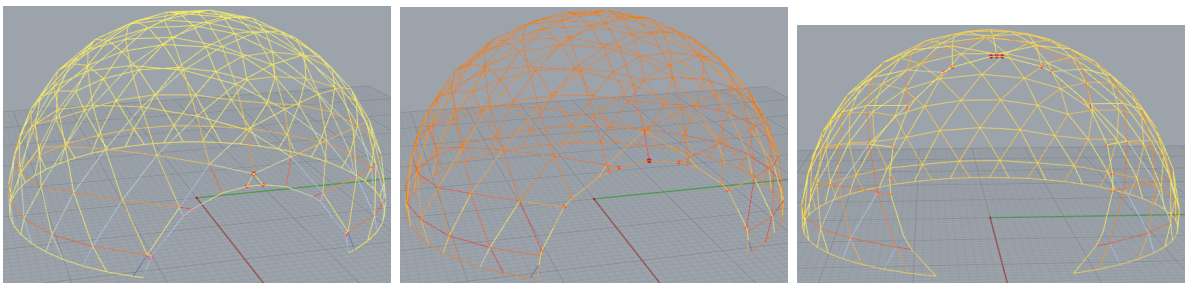

(d) z=0.4 (e) z=0.5 (f) z=0.9

Figure 5.5: Icosahedron-based geodesic dome. $\mathfrak{f} = 5$, $T = 0$, opening size 50%.

Next to the z-position, the opening size can also be adapted from 0 to 1 D. Different opening sizes result in different stress distributions. Independent of the size, the highest stresses are always located close to the bottom of the dome or close to the opening edge beams. Examples of different combinations of frequencies $\mathfrak{f}$, opening sizes and z-positions z are displayed in figure 5.6. The dimensions were kept constant according to table 5.3 except for the opening size. For the following analysis, only openings of 0.5 D are considered. As an infinite number of size, position and material combinations are possible, designers are encouraged to conduct their own parametric analysis to find the optimal opening dimensions that fits the boundary conditions of their given project.

Possible boundary conditions for a parametric study could be:

- Minimum opening height
- Minimum opening width
- Prescribed opening edge beam material
- Prescribed opening rotation due to connection of a secondary structure (e.g. intersections with another geodesic dome or another building)
- Desired opening shape (aesthetics or connection of a secondary structure)
- Trimming plane different from $T = 0$ (often the case in larger structures!)
- ...

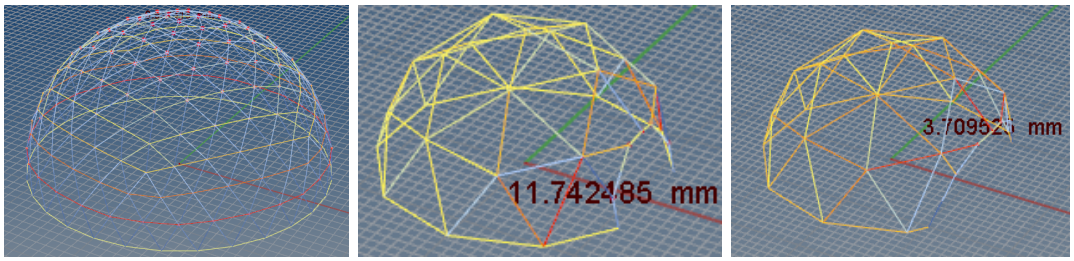

(a) $\mathfrak{f} = 6$, size=$0.0D$ (b) $\mathfrak{f} = 2$, size=$0.4D$ (c) $\mathfrak{f} = 2$, size=$0.7D$

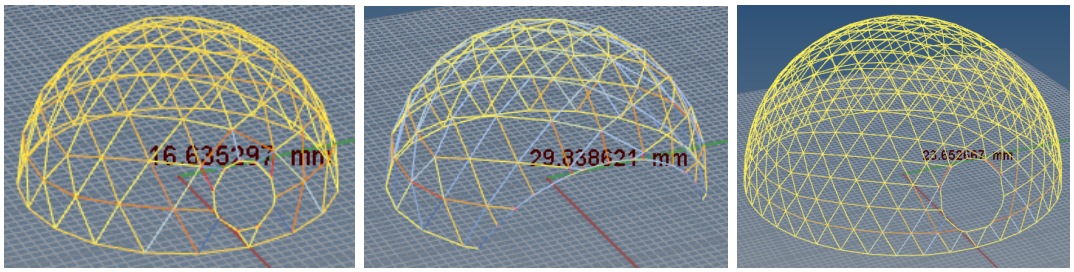

(d) $\mathfrak{f} = 4$, size=$0.2D$ (e) $\mathfrak{f} = 4$, size=$0.8D$ (f) $\mathfrak{f} = 8$, size=$0.2D$

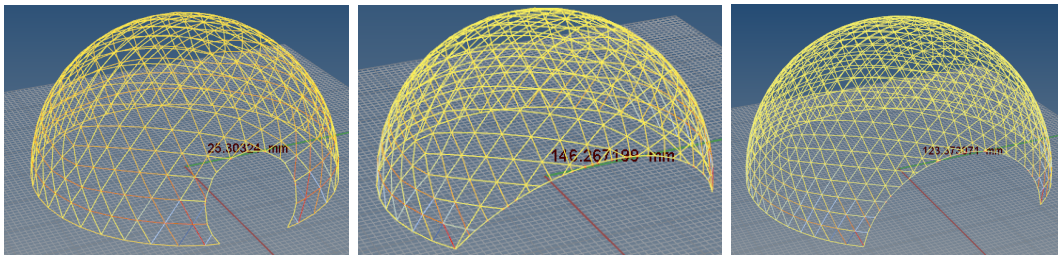

(g) $\mathfrak{f} = 8$, size=$0.3D$ (h) $\mathfrak{f} = 8$, size=$0.9D$ (i) $\mathfrak{f} = 12$, size=$0.6D$

Figure 5.6: Icosahedron-based geodesic dome. z=0.5, $T = 0$, various opening sizes

5.2.3 Stress Patterns

Frequency 1 Five equilateral triangles connect in one point at the top of a perfect icosahedron. If this icosahedron is trimmed at its equator ($T = 0$), a base plane in the shape of a decagon is obtained, which is the base plane of a geodesic dome with frequency $\mathfrak{f} = 1$. However, the perimeter above the equator is still a pentagon which causes half of the trimmed triangles to lean inward and the other half to lean outward (figure 5.7).

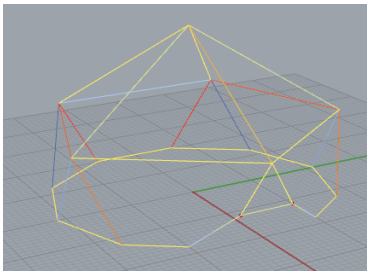

Figure 5.7: $\mathfrak{f} = 1$, size=$0.5D$

Rotating an opening around the z-axis, symmetric openings will be created 5 times. This indicates that peak stresses should be repeated 5 times in every 360° thus once in 72°. Indeed we see one distinct stress peak for tensile and compressive strut stresses in a 72° period for $z = 0.1$,

namely at 36°(figure 5.8a). For $z = 0.5$, the stress pattern has changed its shape and magnitude as the opening intersects the pentagonal top perimeter (figure 5.8b). It is remarkable, that stress peaks again occur around 36°. This is not generally the case, as can be seen in figure 5.10 and the appendix figure A.22 to A.25!

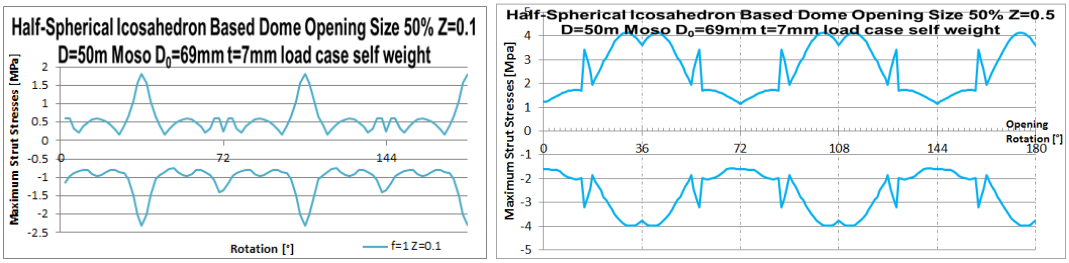

(a) Maximum strut stresses, ƒ = 1, z=0.1 (b) Maximum strut stresses, ƒ = 1, z=0.5

Figure 5.8: Frequency 1, opening size 50%

Frequency 2 For geodesic domes without openings that are subjected to self-weight, we can observe that high stresses occur close to the bottom perimeter. For geodesic domes with openings, we expect the highest stress to occur in struts that are close to the opening and/or close to the bottom perimeter [8] (figure 5.6). The z-position and opening size determine the symmetry pattern for the peak stresses that occur due to rotation. For a geodesic dome with frequency ƒ = 2, opening size $0.5D$ and $z = 0.1$, the peak stresses occur in the struts between the base plane and first perimeter. The first perimeter is not flat which is the case for all even frequencies. It consists of 5-way and 6-way knots which occur 5 times each (figure 5.9a). The initial edges of icosahedron's triangles were divided by two. The base plane of the dome is a regular decagon. We therefore expect 10 stress peaks in 360° thus once in a 36° period. This is the case as can be seen in figure 5.9d. We can also observe that a symmetric location of the opening results in a favourable stress distribution (12°, 36°, etc.) but a small deviation from these angles can cause high peak stresses (e.g. 74°).

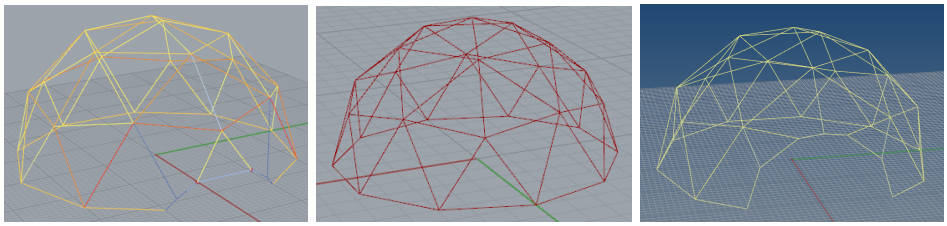

(a) ƒ = 2, z=0.1 (b) ƒ = 2, no opening (c) ƒ = 2, z=0.5

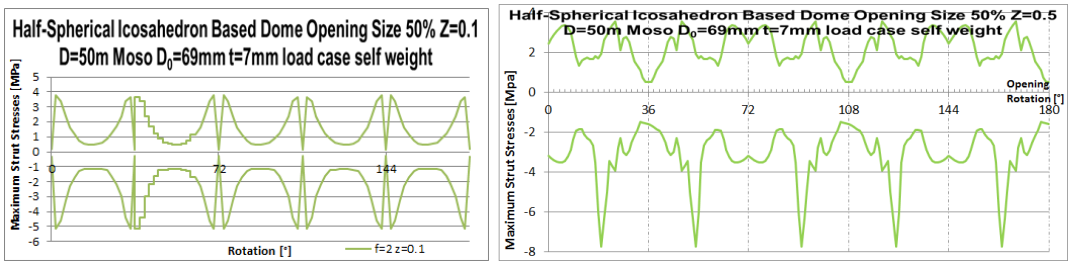

(d) Maximum strut stresses, ƒ = 2, z=0.1 (e) Maximum strut stresses, ƒ = 2, z=0.5

Figure 5.9: Frequency 2, dome with opening size 50% and without opening

[8] We are not interested in opening beam stresses as the steel profile can be adapted to those.

In general, a non-symmetrical location of the opening is unfavourable for two main reasons: 1) Possible cause for high stresses as observed in figure 5.9d. 2) Introduction of very short additional struts and thus requirement of extra joints which increase labour costs. For $z = 0.5$ we observe a different stress pattern, as the opening intersects the first perimeter above the equator (figure 5.9c and figure 5.9e). Note that there are still 10 distinct compressive stress peaks in a 360° rotation.

Higher frequencies The same analytical approach can be applied for higher frequencies: In figure 5.10 maximum strut stresses are shown for $z = 0.1$ for frequency 1 to 5 and an opening size of $0.5D$. The dependence of number of stress peaks on frequency is clearly shown. In a 72° period we obtain one stress peak for $\mathfrak{f} = 1$, two peaks for $\mathfrak{f} = 2$, three peaks for $\mathfrak{f} = 3$, and so on. However, one has to be careful as soon as the opening size is increased or if the opening intersects one or more perimeters above the equator. Different effects will then take over. For higher frequencies ($\mathfrak{f} > 10$), the peaks level out which is a result of generally shorter struts: When an opening is introduced, struts must be cut to insert the steel opening edge beam. The higher the frequency, the smaller the length difference of the new small struts in comparison to the long struts. However, a higher frequency does not necessarily result in smaller stresses which will be shown in chapter 5.3. While small tensile stresses are desirable for bamboo connector design, small compressive stresses are desirable for local buckling. Compressive and tensile stress peaks often occur together, but their magnitude might vary significantly. Therefore, a parametric study is advised, i.e. if an opening is to be introduced non-symmetrically, and different frequencies, z-positions and opening sizes need to be explored. More figures for different z-positions and higher frequencies can be found in the appendix A.4.

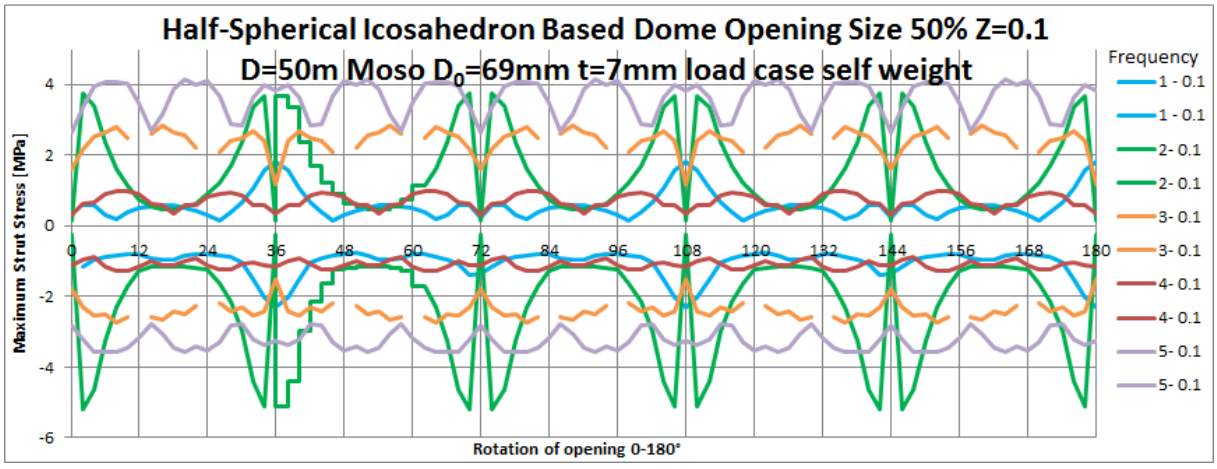

Figure 5.10: Strut stresses for different frequencies z=0.1

5.2.3.1 Conclusions

The necessity for introduction of openings depends on several boundary conditions prescribed by the application. Finding an optimal opening shape remains challenging. In this research, only elliptical openings were explored. Nevertheless it could be demonstrated, that small variations in opening size and position can lead to great changes in strut stresses. Special care must be taken when openings are introduced non-symmetrically and a parametric study is advised in all cases.

5.3 Parametric Study - Half-Spherical Geodesic Domes Without Openings - Influence of Dome Frequency

A parametric study for different frequencies $\mathfrak{f}$ and dome diameters D was conducted for half-spherical icosahedron-based geodesic domes made out of steel struts. The following parameters were kept constant: $\rho = 7850\text{kg/m}^3$, strut diameter $D_0 = 69\text{mm}$, strut thickness $t = 7\text{mm}$, trimming plane $T = 0$, load case LC1 (self-weight). With increasing dome diameter, axial maximum strut stresses increase linearly which is expected. Surprisingly at first, a higher dome frequency does not lead to smaller strut stresses even though the individual strut length L is decreased. A simplified explanation is that the total amount of struts is increased which results in greater self-weight. On the upside, short struts are favourable for Euler buckling resistance ($f_{LB} = \frac{\pi^2 EI}{AL^2}$); the effect of local and global buckling is further explored in chapter 5.4.

Another phenomena is the difference of stresses between even and odd frequencies. Tensile maximum stresses have the same magnitude for frequency $\mathfrak{f} = 1$ and $\mathfrak{f} = 2$ and the lines are overlaid in figure 5.11. Tensile stresses for frequency 1, 2 and 4 are smaller than tensile stresses for frequency 3, and for frequency 6 and 8 they are still smaller than for frequency 5. Only domes with even frequencies have a 'natural equator' which is a perimeter of horizontally running struts at $T = 0$. For odd frequencies, a perimeter below or above the equator has to be chosen, or a new perimeter is inserted at the equator, which results in the maximum stresses of figure 5.11. The last perimeter above the equator is subjected to high stresses (figure 5.14c). For odd frequencies, this perimeter lies closer to the equator which results in an unfavourable stress distribution.

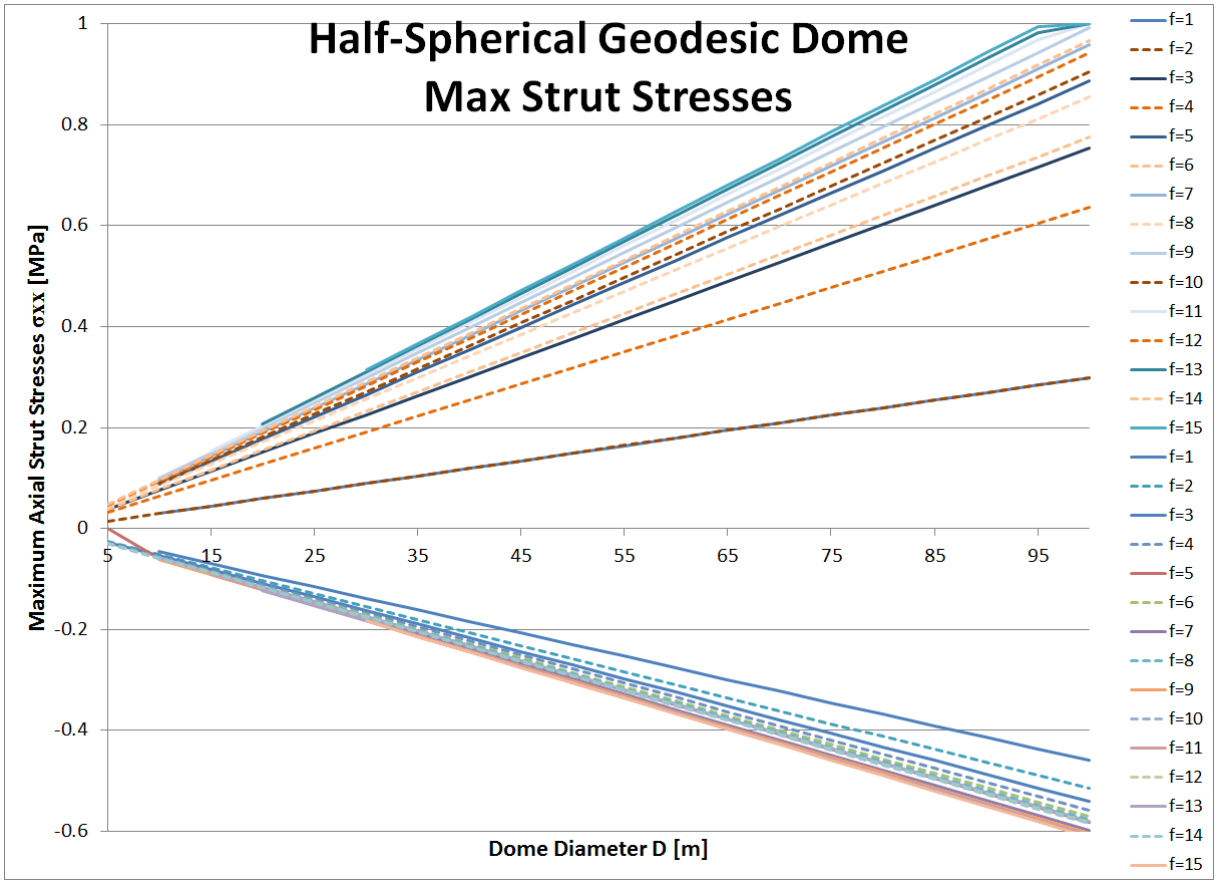

Figure 5.11: Maximum strut stress in icosahedron-based geodesic domes. $T = 0$

5.3.1 Normalized Stresses (Shell Approach)

The stresses in geodesic dome struts can be normalized. Dimensionless quantities are useful when the influence of different input parameters is compared. First, an approach derived from monolithic shells is used. Later, other decisive parameters will be isolated to obtain dimensionless quantities.

For shells, the normal force flow due to distributed self-weight p_z is known:

$$n_{xx} = \frac{1}{2} p_z a = p_z \frac{D}{4} = \rho g t_s \frac{D}{4} \quad \text{for a half-spherical dome with } a = \frac{D}{2}$$

A shell segment of length L, width b and thickness t_s can be transformed into a dome strut of length L and area A with equivalent self-weight (figure 5.12). Every strut represents $\frac{1}{3}$ of the weight of two neighbouring shell triangles. A regular triangle has the area $\frac{\sqrt{3}}{4} L^2$. The width b of an equivalent rectangular shell segment is thus

$$b = 2 \frac{1}{3} \frac{\sqrt{3}}{4} L^2 / L = \frac{\sqrt{3}}{6} L$$

By setting the weight of a shell segment and strut equal, the equivalent shell thickness t_s is obtained

$$\rho g t_s \frac{\sqrt{3}}{6} L^2 = \rho g A L \quad \Rightarrow t_s = \frac{6}{\sqrt{3}} \frac{A}{L}$$

The stresses in the struts can be obtained with

$$\sigma_{xx} = n_{xx} L / A \quad \Rightarrow \sigma_{xx} = \rho g \frac{6}{\sqrt{3}} \frac{D}{4}$$

The normalized strut stress is: $\sigma_{xx,norm} \sim \frac{\sigma_{xx}}{\rho g D} [-]$

The normalized stresses are independent of the surface area of the strut A, the dome diameter D and the density of the struts ρ. Figure 5.13 displays normalized strut stresses for self-weight of half-spherical icosahedron-based domes.

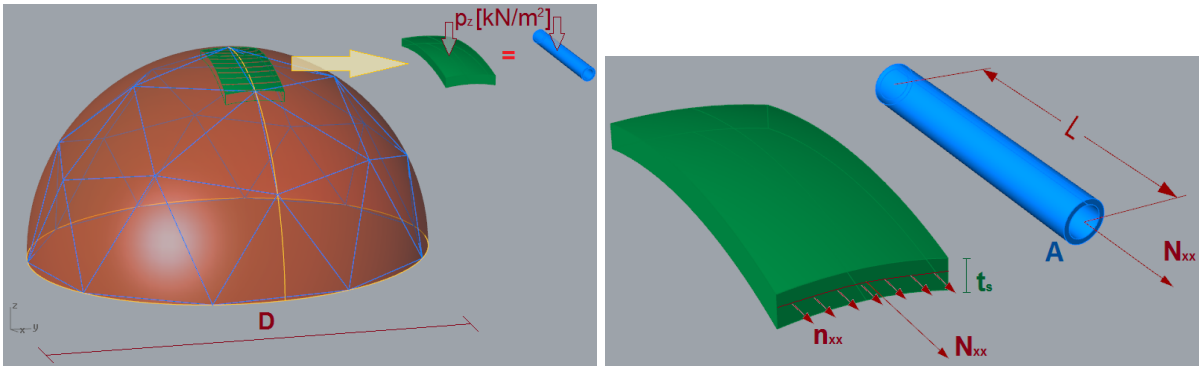

(a) Shell segments approximated by struts (b) Normal forces N_{xx}

Figure 5.12: Transformation of shell membrane into geodesic dome struts

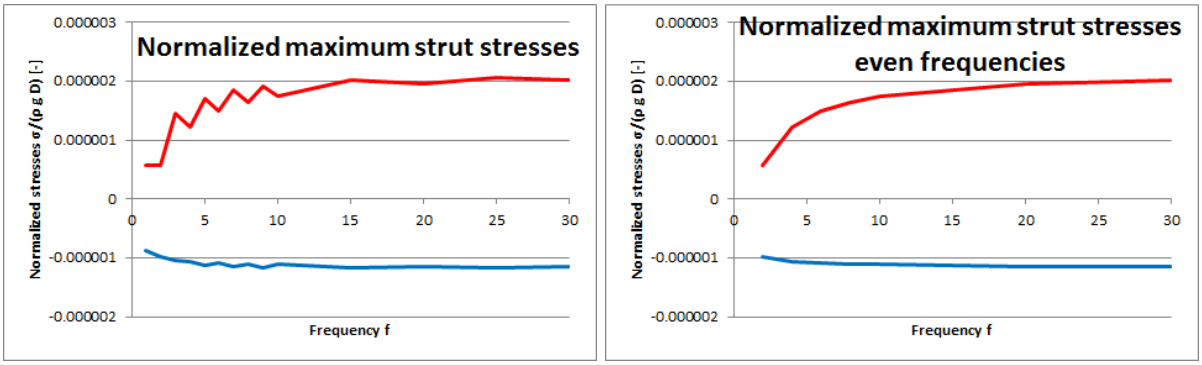

(a) Normalized maximum strut stresses

(b) Normalized stress for even frequencies

Figure 5.13: Normalized maximum strut stresses icosahedron-based half-spherical geodesic domes

Two phenomena can be observed in figure 5.13a:
(1) Maximum stresses alternate for odd and even frequencies.
(2) Normalized stresses increase with and increasing frequency.

The first observation is expected due to the unfavourable strut distribution of odd frequencies. The second observation is puzzling at first, as $\mathfrak{f}$ was not part of the derivation of $\sigma_{xx,norm}$ and one would assume that the magnitude of normalized stresses should thus be independent of the frequency. Still, maximum compressive strut stresses increase, e.g. by a factor $\alpha_{2\to4} = 1.0824$ for a change from $\mathfrak{f} = 2$ to $\mathfrak{f} = 4$ (figure 5.13b). The explanation is found by the following considerations:

If the frequency is doubled, the edge length of a single triangle increases approximately from $3L$ to $9\frac{L}{2} = 4.5L$ (figure 5.14d and 5.14e) and the entire edge length increases by a factor of 1.5. A doubled frequency leads thus to an increase of self-weight by a factor 1.5 (and a small factor that compensates the vertex projection[9]).

The highest tensile stresses occur in the lowest perimeter above the equator and the highest compressive stresses occur just above the equator (figure 5.14c). For frequency $\mathfrak{f} = 4$, 40 bottom struts are available to carry the dome's weight instead of the 20 for $\mathfrak{f} = 2$. The dome's weight is thus distributed on twice as many bottom struts if the frequency is doubled.

The last important aspect is the strut distribution within the dome: For $\mathfrak{f} = 2$, a total of 20 compressive struts in the bottom ring have to carry the weight of another 35 struts that are located higher. This is equal to $35/55 = 63.6\%$ of the dome's weight. For $\mathfrak{f} = 4$, a total of 40 bottom compressive struts have to carry the weight of 190 struts which equals $19/23 = 82.6\%$ of the dome's weight.

Combining these insights, the increase of strut stress is $\alpha_{2\to4} = 1.5 \cdot 1.107/2 \cdot 0.826/0.636 = 1.079$. This is close enough to the stress increase obtained by the *Grasshopper* model (1.0824).

The stress increase α is independent of the dome material. For $\mathfrak{f} = 4$ to $\mathfrak{f} = 6$ it is only $\alpha_{4\to6} = 1.0223$ and for $\mathfrak{f} = 12$ to $\mathfrak{f} = 14$ it is only $\alpha_{12\to14} = 1.0036$. For higher frequencies, the maximum strut stresses thus converge to a constant magnitude independent of the frequency. This agrees with figure 5.13b and makes sense, as for $\mathfrak{f} \to \infty$, the geodesic dome becomes a shell.

[9]The real increase is slightly larger, as the new vertices are projected onto the initial sphere which means that the new struts are slightly longer (1.107 [17] times for $\mathfrak{f} = 1$ to $\mathfrak{f} = 2$).

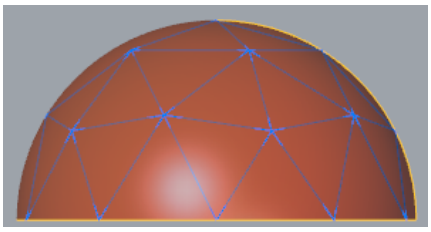

(a) Dome ƒ = 2

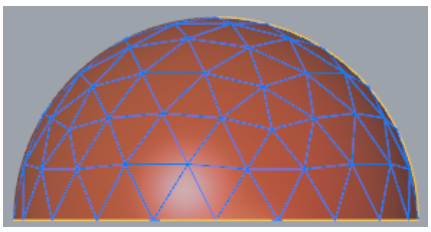

(b) Dome ƒ = 4

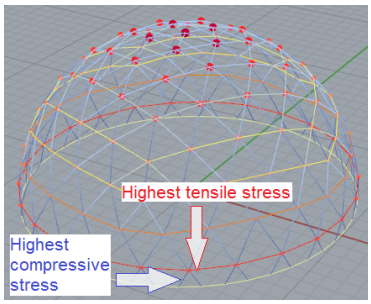

(c) Location of highest strut stresses

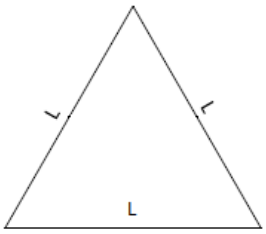

(d) Struts ƒ = 1

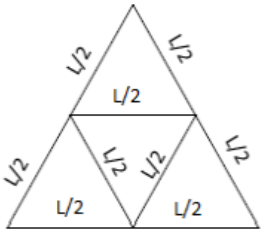

(e) Struts ƒ = 2

Figure 5.14: Distribution of struts for ƒ = 2 and ƒ = 4

5.3.2 Relationships of Strut Length, Dome Diameter and Frequency

For a constant dome diameter D, the strut length L of an icosahedron-based dome is inversely linearly-dependent on the dome frequency ƒ. This is a logical property, as for ƒ = 2, the initial triangle is divided into four triangles (figure 5.15b), dividing the initial strut length by two[10]. For frequency 3, we arrive at three edges, for frequency 4 at four edges, etc. The new vertices are projected onto a sphere and the length of the flat edge changes, resulting in a factor 1.515 in figure 5.15c. If the dome diameter is increased, the strut length is increased by the same factor as the entire dome is scaled. The same approach can be used for the sum of all struts $\sum L$. We can derive the following relationships for the maximum strut length L and entire strut length $\sum L$ of a half-spherical icosahedron-based geodesic dome with diameter D and frequency ƒ:

$$\frac{L}{D} = 0.66\frac{1}{\mathfrak{f}} \Leftrightarrow \frac{D}{L} = 1.515\mathfrak{f} \qquad \frac{\sum L}{D} = 8.674\mathfrak{f} \tag{5.1}$$

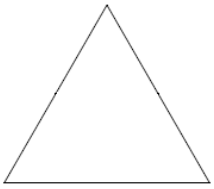

(a) ƒ = 1

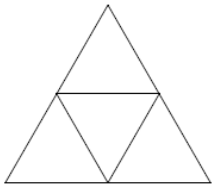

(b) ƒ = 2

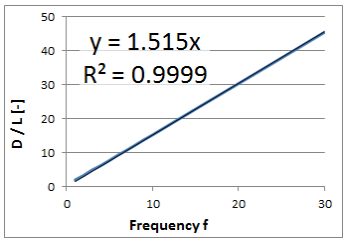

(c) Relationship of D/L, ƒ

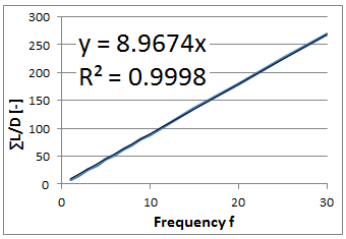

(d) Relationship of $\sum L/D$, ƒ

Figure 5.15: Relationships of D, L, $\sum L$, ƒ

[10]Note that for frequencies higher than 1, there will be different strut sizes as the surface triangles will not be equilateral any more. We can use the maximum or average strut length in order to compare results.

5.4 Parametric Study - Instability of Half-Spherical Geodesic Domes and Limit Dome Diameter

For geodesic domes, two instability limit states exist: Local buckling (LB) of a single strut and global buckling (GB), where several struts simultaneously 'snap through' into a deformed state. If the frequency ƒ of a geodesic dome is increased, the strut length L becomes shorter and local buckling is less likely to occur. At the same time, the dome approaches the shape of a monolithic shell which is prone to global buckling. There is thus a transition point for a certain frequency ƒ, where local buckling changes into global buckling. It is interesting to determine this transition point as designers generally want to avoid the risk of global buckling for several reasons: Global buckling is a sudden and dangerous failure that is hard to grasp and almost impossible to calculate by hand. Furthermore, the derived global buckling load factors can not be combined by superposition as every load combination results in a different global buckling shape. Therefore, it is useful for the designer to establish boundary conditions under which global buckling is not decisive, so it can be excluded from an automated structural analysis. Subsequently, rules of thumb can be derived which indicate the limit dome diameter for geodesic domes made of *Guadua angustifolia* and *Phyllostachys pubescens*. In the following, the dome struts are modelled as pinned-pinned bars which results in local buckling Euler case 2. The Modulus of Elasticity is derived from tests and literature (chapter 4.2.2). All domes are half-spherical with $T = 0$.

5.4.1 Load Case 1: Self-Weight

Prior to investigating the transition point from global to local buckling, it makes sense to look at the two instability cases separately.

5.4.1.1 LC1: Local Buckling

For local buckling of half-spherical icosahedron-based geodesic domes subjected to self-weight, it is possible to derive an analytical expression for the maximum possible dome diameter $D_{max,LB}$. For even frequencies and bamboo domes with $t = 0.1D_0$ this expression reads:

$$D_{max,LB,t=0.1D_0} = 1.373\Big(\frac{D_0^2 \mathfrak{f}^2 E}{\rho g}\Big)^{1/3} \qquad \text{(5.2a derivation below)}$$

A local buckling analysis can also be conducted in *Grasshopper* by comparing the maximum strut stress to the Euler buckling resistance of the longest strut. A safe zone can be derived for different materials (figure 5.16). Note that in real life application adequate safety factors need to applied and the safe zone might become a lot smaller!

Naturally, one would expect that a greater outer diameter D_0 increases the local buckling resistance if the t/D_0 ratio stays the same. In figure 5.16 however, the curve of *Guadua130* runs slightly lower than the curve of *Guadua100*. The answer is found in the dimensionless quantity D/D_0 of the ordinate:

$$D_{max,LB,t=0.1D_0} = 1.373\Big(\frac{D_0^2 \mathfrak{f}^2 E}{\rho g}\Big)^{1/3} \quad \Rightarrow D_{max,LB} \sim D_0^{\frac{2}{3}} \quad \Leftrightarrow \quad \frac{D_{max,LB}}{D_0} \sim \Big(\frac{1}{D_0}\Big)^{1/3}$$

An increased outer strut diameter D_0 results in higher maximum dome diameter $D_{max,LB}$ but a smaller $D_{max,LB}/D_0$ ratio. For the above example of *Guadua100* ($D_0 = 100\,\text{mm},\ t = 10\,\text{mm}$) and *Guadua130* ($D_0 = 130\,\text{mm},\ t = 13\,\text{mm}$) we find:

$$D_{max,LB} \sim D_0^{\frac{2}{3}} \qquad D_{max,LB,1.3D_0} \sim (1.3D_0)^{\frac{2}{3}} = 1.1911 D_0^{\frac{2}{3}}$$

$$\frac{D_{max,LB}}{D_0} \sim \Big(\frac{1}{D_0}\Big)^{1/3} \qquad \frac{D_{max,LB,1.3D_0}}{1.3D_0} \sim \frac{1.1911}{1.3}\Big(\frac{1}{D_0}\Big)^{1/3} = 0.9163\frac{D_{max,LB}}{D_0}$$

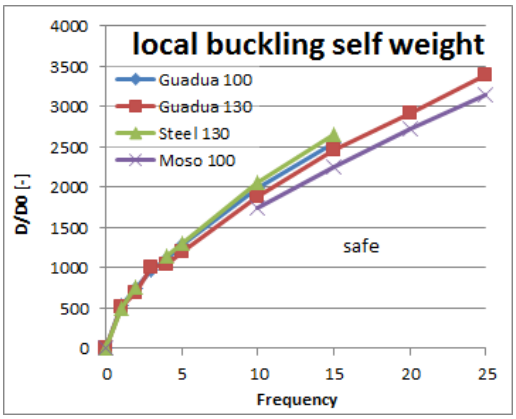

Figure 5.16: LB for different materials, self-weight

Apparently, a 1.3 times larger strut diameter D_0 allows for 1.19 larger dome diameter $D_{max,LB}$ but decreases the D/D_0 ratio to 0.916. If figure 5.16 was normalized by $(D_0^2 \mathfrak{f}^2 E/\rho g)^{1/3}$, we would get the same curves for all materials! However, this is impractical once we compare local and global buckling.

Derivation An expression for $D_{max,LB}$ can be derived that depends on material properties and strut geometry. A conservative failure criterion for local buckling is met, when the local buckling resistance of the longest strut f_{LB} equals the highest compressive strut stress due to self-weight $\sigma_{max,LC1}$. We can derive an expression for the maximum strut length L by replacing the surface area A and inertia I by expressions containing D_0 and t. Note that the wall thickness t is assumed to be $0.1D_0$ for the given application. For sake of simplicity we will only consider even frequencies $\mathfrak{f} = 2n$ to derive an exact formula[11].

$$f_{LB} = \frac{\pi^2 EI}{AL^2} = \frac{\pi^2 E\big(4(\frac{t}{D_0})^2 - 4\frac{t}{D_0} + 2\big)D_0^2}{L^2} \overset{t=0.1D_0}{\approx} 1.0116\frac{ED_0^2}{L^2}$$

$$\text{with} \quad \frac{D}{L} = 1.515\mathfrak{f} \quad \text{(figure 5.15c)} \quad \Rightarrow f_{LB} \approx 2.3219\frac{ED_0^2\mathfrak{f}^2}{D^2}$$

The maximum strut stress in the bottom struts is equal to the self-weight of the dome F_G divided by the strut area and the number of bottom struts. For even frequencies, the number of bottom struts is equal to $10\mathfrak{f}$:

$$\sigma_{max,LC1} = \frac{F_G}{\#\text{bottom struts}} \overset{\mathfrak{f}=2n}{=} \frac{\sum LA\rho g}{10A\mathfrak{f}} = \frac{\sum L\rho g}{10\mathfrak{f}}$$

$$\text{with} \quad \sum L = 8.967\mathfrak{f}D \quad \text{(figure 5.15d)} \quad \Rightarrow \quad \sigma_{max,LC1} = 0.8967D\rho g$$

The local buckling criterion is met for $\mu_{LB} = \sigma_{max,LC1}/f_{LB} = 1.0$

$$f_{LB} = \sigma_{max,LC1} \quad \Leftrightarrow \quad 2.32\frac{ED_0^2\mathfrak{f}^2}{D^2} = 0.8967D\rho g$$

We arrive at the maximum possible dome diameter $D_{max,LB}$ for LC1:

$$\text{even frequencies}: \quad D_{max,LB,t=0.1D_0} \approx 1.373\Big(\frac{D_0^2\mathfrak{f}^2 E}{\rho g}\Big)^{1/3} \quad \left[\left(\frac{\text{m}^2\frac{\text{N}}{\text{m}^2}}{\frac{\text{kg}}{\text{m}^3}\frac{\text{N}}{\text{kg}}}\right)^{1/3}\right] = [\text{m}] \qquad (5.2a)$$

[11] This approach is conservative: For odd frequencies, maximum compressive stresses are slightly higher than for even frequencies (figure 5.13) but Euler buckling strength is 4 times higher as bottom struts are $1/2L$ long.

The same analysis can be conducted for different t/D_0 ratios:

$$\begin{aligned} &\text{even frequencies :} \quad D_{max,LB} = C_1\Big(\frac{D_0^2 \mathfrak{f}^2 E}{\rho g}\Big)^{1/3} \\ &C_1 = 1.1313\Big(\frac{t}{D_0}\Big)^2 - 1.2067\Big(\frac{t}{D_0}\Big) + 1.4837 \quad R^2 = 0.9995; t \in [0.08; 0.5]D_0 \end{aligned} \tag{5.2b}$$

5.4.1.2 LC1: Global Buckling

Let's take a closer look at global buckling of geodesic domes subjected to self-weight: The dots in figure 5.17a indicate the location and magnitude of global displacements of nodes due to linear static self-weight. The colour code of the struts is: red = tensile stress, blue = compressive stress. The global buckling pattern for mode 1 is non-symmetrical (figure 5.17b). The higher the frequency, the more it will approximate the buckling shape of a shell: Close to the bottom edge beam of the dome, several struts start to bulge out. The struts themselves do not buckle but the nodal displacement leads to a global buckling deformation. The global buckling load factor can be extracted from GSA which is the reciprocal of the global buckling utilization μ_{GB}.

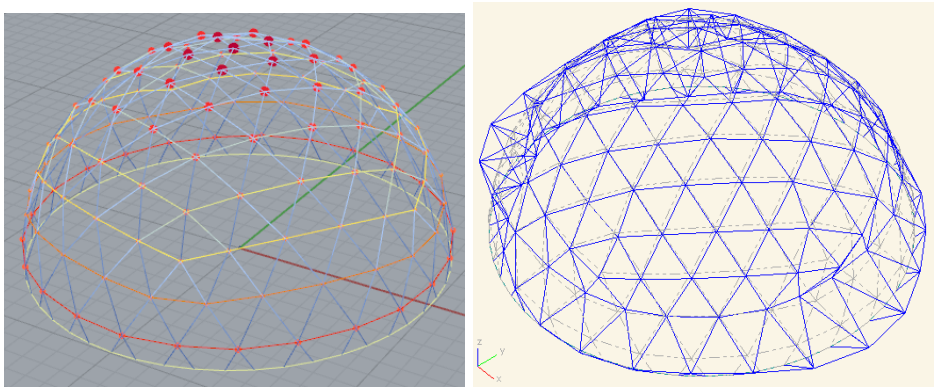

(a) Linear displacements for LC1 (b) Displacements for GB mode 1 LC1

Figure 5.17: LC1: self-weight

5.4.1.3 LC1: Transition Local to Global Buckling

It is possible to derive the frequency $\mathfrak{f}$ and D/D_0 ratio at which the utilization of global and local buckling are identical ($\mu_{GB} = \mu_{LB}$). This is the point at which the governing stability limit state changes from local buckling to global buckling if the frequency $\mathfrak{f}$ is further increased. The transition graph in figure 5.18 is derived for $t = 0.1D_0$.

The transition point is independent of Young's Modulus, density and strength of the material!

A formula for the transition of global to local buckling for circular hollow sections with $t = 0.1\ D_0$ can be established[12]:

$$\text{LC1}, t = 0.1D_0 : \quad \frac{D}{D_0}_{(\mu_{GB}=\mu_{LB})} = 5.0515\ \mathfrak{f}^2 - 4.398\ \mathfrak{f} \tag{5.3}$$

[12]This D_0/t ratio is derived from measurements on Moso bamboo (D_0 = 100mm, t = 10mm) and Guadua bamboo (D_0 = 130mm, t = 13mm).

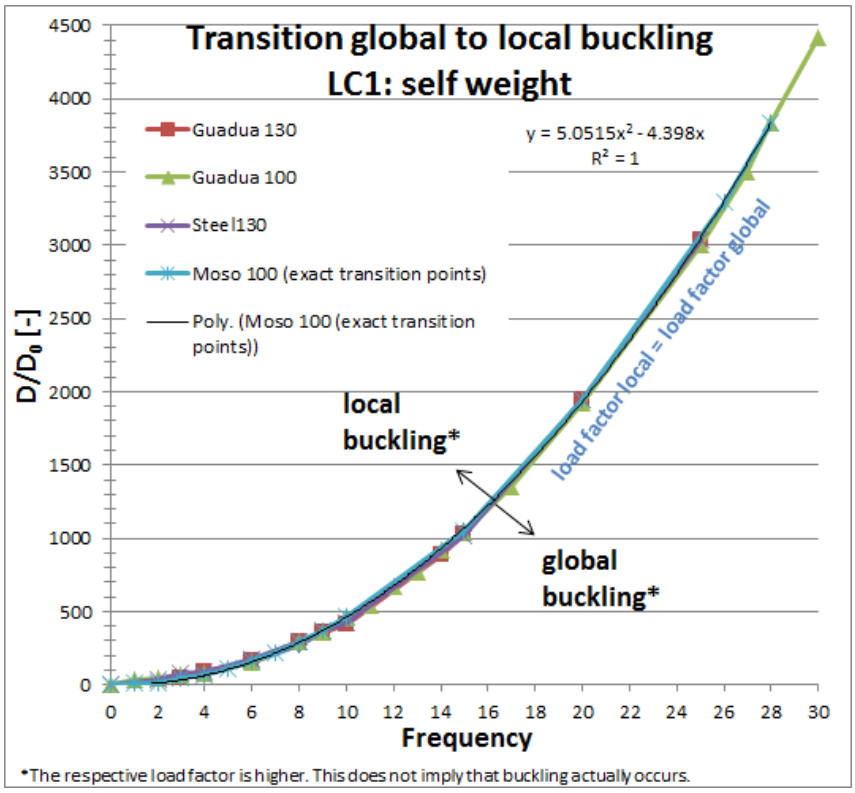

Figure 5.18: Transition GB to LB for different materials, $t = 0.1D_0$, LC1: self-weight

5.4.1.4 LC1: Limit Dome Diameter

A maximum frequency $\mathfrak{f}_{max}$ can be determined, where both local and global buckling resistance are utilized to their maximum ($\mu_{LB} = \mu_{GB} = 1.0$). The dome fails simultaneously in local and global buckling. A higher frequency $f > \mathfrak{f}_{max}$ will automatically result in global buckling failure, unless the D/D_0 ratio is decreased. For LC1, there are three methods to derive at $\mathfrak{f}_{max}$:

Method 1 $\mathfrak{f}_{max}$ can be derived by plotting the utilization of the transition curve ($\mu_{LB} = \mu_{GB}$) against the frequency. For $\mu = 1.0$, the maximum frequency $\mathfrak{f}_{max}$ is reached and can be read from the graphs in figure 5.19. Substituting $\mathfrak{f}_{max}$ into equation 5.3, we find the limiting D/D_0 ratio. Figure 5.19a displays a plot for Guadua bamboo with $t = 0.1D_0$ and $D_0 = 100\,\text{mm}$. We find $\mathfrak{f}_{max,Guadua} = 28$ with $D/D_0 = 3836.5$ and utilization $\mu = 90.52\%$ for both local and global buckling[13]. The same is done for Moso bamboo with the same dimensions in figure 5.19b. The respective values are $\mathfrak{f}_{max,Moso} = 25$ with $D/D_0 = 3300$ and $\mu = 91.06\%$.

Method 2 Alternatively, we can overlap the local buckling graphs of figure 5.16 and the transition graph of figure 5.18 which results in figure 5.20. The intersection of the transition graph ($\mu_{LB} = \mu_{GB}$) and the local buckling graph ($\mu = 1.0$) results in the maximum frequency $\mathfrak{f}_{max}$. For *Guadua100* and *Moso100*, we arrive at the same frequency $\mathfrak{f}_{max,Guadua} = 28$ and $\mathfrak{f}_{max,Moso} = 25$, that we derived before.

[13] $D/D_0 = 3836.5$ is found for $\mathfrak{f} = 28$. The actual limiting D/D_0 ratio for failure ($\mu_{LB} = \mu_{GB} = 1.0$) is approximately 4000 which translates to a frequency $\mathfrak{f} = 28.6$ which of course doesn't make any sense.

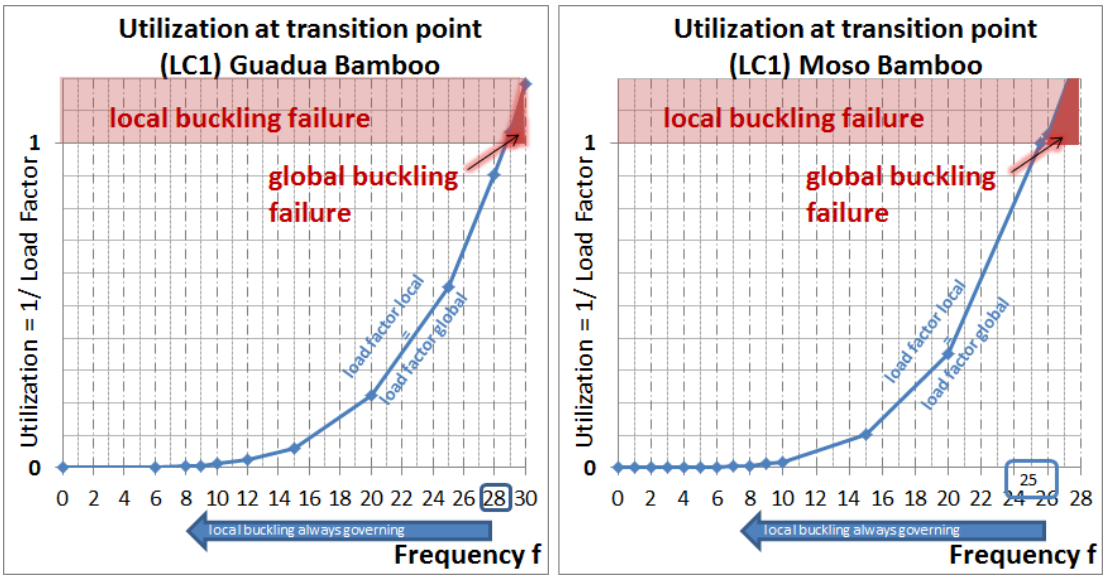

(a) Utilization at transition point GB to LB Guadua bamboo $D_0 = 100\text{mm}, t = 10\text{mm}$

(b) Utilization at transition point GB to LB Moso bamboo $D_0 = 100\text{mm}, t = 10\text{mm}$

Figure 5.19: Method 1: Utilization at transition point GB to LB

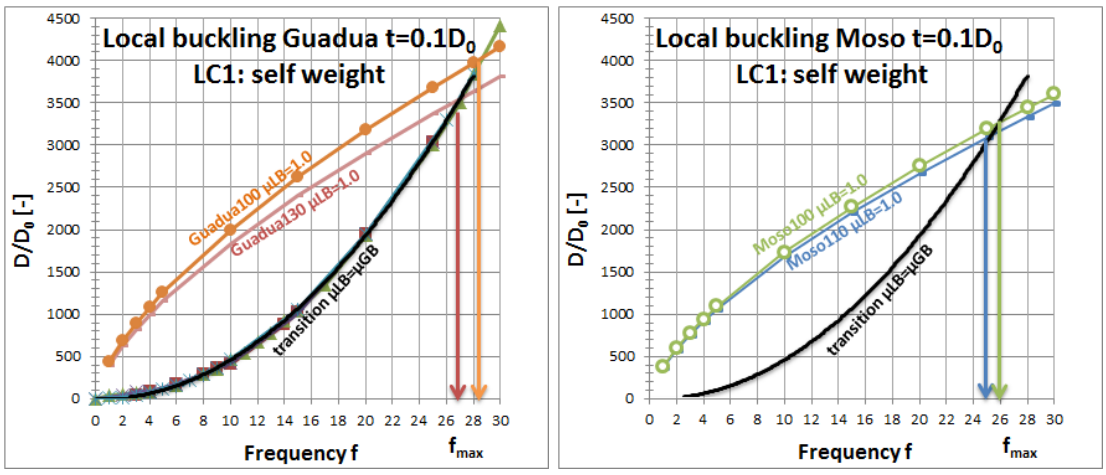

(a) LB intersection *Guadua angustifolia*

(b) LB intersection *Phyllostachys pubescens*

Figure 5.20: Method 2: Intersection of LB and transition curve

Method 3 The third method is purely numerical: We divide equation 5.2a by D_0, set it equal to equation 5.3 and solve for ƒ. This is the maximum frequency $ƒ_{max}$:

$$1.373\Big(\frac{ƒ^2 E}{D_0 \rho g}\Big)^{1/3} = 5.0515\ ƒ^2 - 4.398\ ƒ \quad \Rightarrow ƒ_{max}$$

ƒ can be re-substituted into equation 5.3 to derive the maximum D/D_0 ratio. Using the property $D_{max,LB,1.3D_0}/1.3D_0 \sim 0.9163 D_{max,LB}/D_0$ we find for *Guadua100* and *Guadua130*:

$$\text{Guadua100:} \quad ƒ = 28.5 \to 28 \quad \Rightarrow \frac{D_{max}}{D_0} = 5.0515\ ƒ^2 - 4.398\ ƒ = 3836.5$$

$$\text{Guadua130:} \quad ƒ = 27.3 \to 27 \quad \Rightarrow \frac{D_{max}}{D_0} = 0.916 \cdot 3836.5 = 3514$$

Rule Of Thumb Method 3 can be used to derive a linearised expression for the maximum possible dome diameter $D_{max,LBGB,LC1}$ where global and local buckling occur simultaneously (derivations are provided in the appendix A.5.1.2[14]). For Moso and Guadua, the only t/D_0 ratios that occur in nature lie between 0.8 and 1.2. Figure 5.21 shows that both the transition curves for $t \in [0.08; 0.12]D_0$ and local buckling curves can be approximated by $t = 0.1D_0$. We will thus only derive one equation assuming $t = 0.1D_0$ for different values of D_0. An analysis for significantly different t/D_0 ratios of steel circular hollow sections can be found in the appendix A.5.1.1.

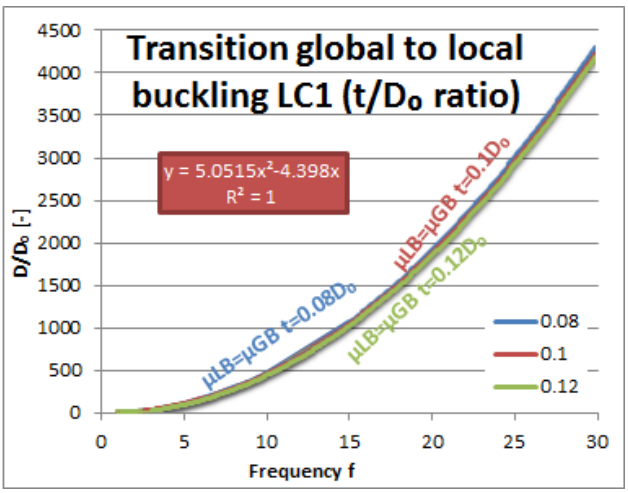

(a) Transition global to local buckling for $t \in [0.08; 0.12]D_0$

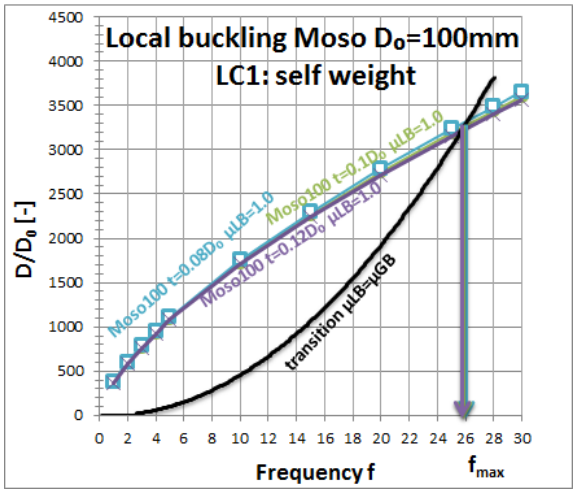

(b) Local buckling of Moso $D_0 = 100\,\text{mm}$ for $t \in [0.08; 0.12]D_0$

Figure 5.21: Influence of t/D_0 ratio for bamboo

$$\left.\begin{aligned} D_{max,LBGB,LC1} &= (5760.5 - 16.81D_0)D_0; \quad \text{Guadua} \\ D_{max,LBGB,LC1} &= (4853.6 - 15.43D_0)D_0; \quad \text{Moso} \end{aligned}\right\} \quad \begin{aligned} t &\in [0.08; 0.12]D_0 \\ D_0 &\in [90; 130]\text{mm} \end{aligned} \tag{5.4a}$$

$$\left.\begin{aligned} \mathfrak{f}_{max,GB} &= 35.28 - 0.0613D_0; \quad \text{Guadua} \\ \mathfrak{f}_{max,GB} &= 32.41 - 0.0613D_0; \quad \text{Moso} \end{aligned}\right\} \quad \begin{aligned} &\text{safe lower bound for global buckling} \\ &t \in [0.08; 0.12]D_0;\ D_0 \in [90; 130]\text{mm} \end{aligned} \tag{5.4b}$$

Note that D_{max} and D_0 need to have the same dimensions. These limit values are derived from theory and adequate safety factors need to be applied prior to real life application.

[14]Note that there is a difference of 15% between model data and formula 5.2b due to the assumption of F_g which is overestimating the amount of material leading to the highest strut stress σ_{max}.

5.4.1.5 LC1: Conclusions

Figure 5.22 shows a general scheme of the global buckling curve ($\mu_{GB} = 1.0$), local buckling curve ($\mu_{LB} = 1.0$), transition curve ($\mu_{LB} = \mu_{GB}$) and the intersection point ($\mu_{LB} = \mu_{GB} = 1.0$) which defines the maximum frequency $\mathfrak{f}_{max}$ and maximum possible dome diameter ($D_{max,LBGB}$) which still needs to me multiplied by D_0.

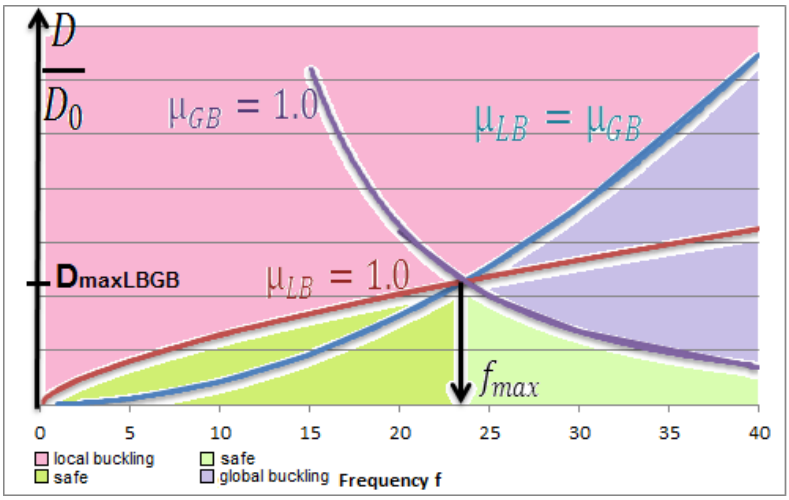

Figure 5.22: Scheme of transition LB to GB and $\mathfrak{f}_{max}$ LC1

We can conclude the following:

1. For frequencies below $\mathfrak{f} \leq \mathfrak{f}_{max}$, local buckling is the decisive stability limit state[15] and global buckling does not occur. This corresponds to a maximum frequency of 27 for Guadua and 25 for Moso respectively.

2. The outer strut diameter D_0 has a positive correlation with the maximum possible dome diameter $D_{max,LB}$. However, an increased outer strut diameter D_0 results in a smaller maximum frequency $\mathfrak{f}_{max}$. This effect is negligible for bamboo (limited range of D_0) but needs to be considered for steel.

3. The maximum possible dome diameters can be found by substituting D_0 into equation 5.4a. We find 475.4 m for *Guadua angustifolia* and 331.1 m for *Phyllostachys pubescens*.

[15]This can be said for sure as at the point of local buckling ($\mu_{LB} = 1.0$), tensile and compressive stresses are less than 10% of the tensile and compressive capacity for all investigated materials, frequencies and dome diameters. Whether local buckling actually occurs, depends on the strut diameter D_0, the density ρ, Young's Modulus E, frequency $\mathfrak{f}$ and dome diameter D.

5.4.2 Load Case 2: Point Load

A point load $F = 1\,\text{kN}$ is applied at the top of the dome (figure 5.23a); self-weight is not applied[16]. Global buckling (GB) and local buckling (LB) analysis are computed for a static linear and static geometrically non-linear (GNL) analysis. The straight-forward theoretical derivation of the local buckling limit diameter $D_{max,LB}$ is only possible for a linear analysis. Geometrically non-linear analysis requires the load F to be applied incrementally, i.e. the resulting deformation δ_n must be added as initial imperfection in the next load step $n+1$ (figure 5.23b). Alternatively, an equivalent load $(F_{n+1}; M_{n+1})$ can be applied that results in the same deformation.

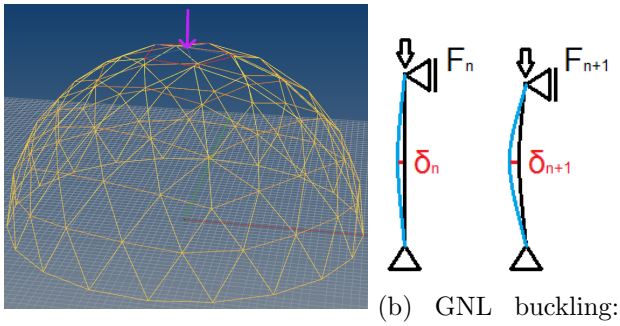

(a) *Grasshopper* point load (b) GNL buckling: Initial imperfections

Figure 5.23: LC2: Point load

It is possible to derive a correction factor for equation 5.5 of chapter 5.4.2.1 (this is often done in practice for non-linear column buckling). However, this is tedious work, as the geometry of the entire dome changes with every load step, which changes the boundary conditions of the Euler bar. Instead, there is a much smarter solution to avoid this, as will be shown in chapter 5.4.2.4.

5.4.2.1 LC2: Local Buckling Geometrically Linear

The local buckling limit diameter $D_{max,LB}$ can be described by a power law similar to equation 5.2a for linear load application. Note that the struts directly under the point load will buckle first. These are always five struts independent of the frequency f!

$$D_{max,LB,t=0.1D_0} = 1.472\left(\frac{\mathfrak{f} D_0^4 E}{F}\right)^{1/2} \qquad \text{(5.5 derivation below)}$$

Derivation First we need to derive the compression force F_s in one of the five struts under the point load. We will use the definitions in figure 5.24. The complete derivation can be found in the appendix A.5.2.

$$\cos(\phi) = 1 - \frac{L^2}{2\left(\frac{D}{2}\right)^2} = 1 - \frac{1}{2\left(\frac{1.515\mathfrak{f}}{2}\right)^2} = 1 - \frac{2}{(1.515\mathfrak{f})^2}$$

$$F_s = \frac{F}{5}\sqrt{\left(\frac{\sin(\phi)}{1-\cos(\phi)}\right)^2 + 1} = \frac{1.515}{5} F\mathfrak{f}$$

[16] As mentioned before, the load cases are treated separately and can be combined by superposition.

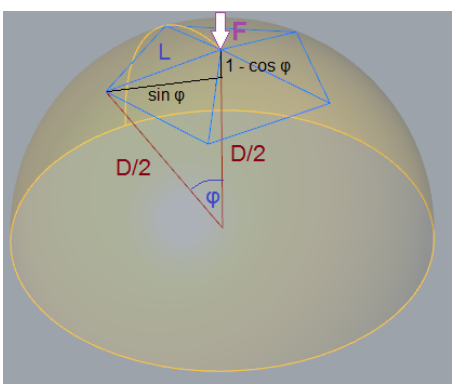

(a) Equilateral triangle in dome

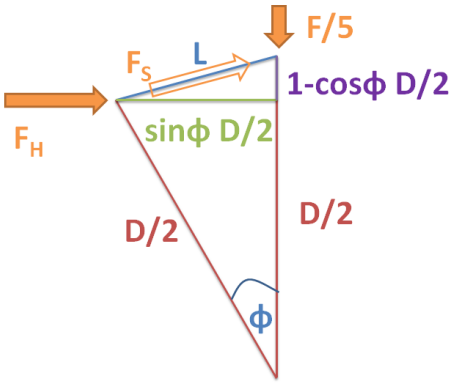

(b) Strut force F_s

Figure 5.24: Relationship of ϕ and L

Buckling occurs for $f_{LB} = \sigma_{max,LC2}$

$$f_{LB} = \frac{\pi^2 EI}{AL^2} \overset{t=0.1D_0}{=} 0.009225\pi^3 \frac{ED_0^4}{AL^2} = \sigma_{max,LC2} = \frac{F_s}{A} = \frac{1.515F\mathfrak{f}}{5A}$$
$$\Rightarrow L = \left(0.009225\pi^3 \frac{5}{1.515} \frac{ED_0^4}{F\mathfrak{f}}\right)^{1/2} = 0.972\left(\frac{ED_0^4}{F\mathfrak{f}}\right)^{1/2} \quad \text{with } D = 1.515\mathfrak{f}L$$

$$\Rightarrow D_{max,LB,t=0.1D_0} = 1.472\left(\frac{\mathfrak{f}D_0^4 E}{F}\right)^{1/2} \quad \text{units: } \left[\left(\frac{\mathrm{m}^4 \frac{\mathrm{N}}{\mathrm{m}^2}}{N}\right)^{1/2}\right] = [\mathrm{m}] \tag{5.5}$$

$$\text{For different } t/D_0 \text{ ratios: } \quad D_{max,LB} = C_2 \left(\frac{\mathfrak{f}D_0^4 E}{F}\right)^{1/2}$$
$$C_2 = -5.6638\left(\frac{t}{D_0}\right)^2 + 4.4528\left(\frac{t}{D_0}\right) + 1.0806 \quad R^2 = 0.9779; t \in [0.08; 0.5]D_0 \tag{5.6}$$

5.4.2.2 LC2: Global Buckling

For a given material with strut diameter D_0, wall thickness t, E-Modulus E and dome frequency $\mathfrak{f}$, the global buckling load factor is constant but depends on the analysis type (geometrically linear or non-linear). Figure 5.25 displays the global buckling utilization μ_{GB} for different materials and strut diameters with $t = 0.1\ D_0$. For each material with strut diameter D_0 and thickness t, a maximum frequency $\mathfrak{f}_{max}$ can be derived that leads to global buckling in the linear or non-linear load case. For Guadua with $D_0 = 130\,\mathrm{mm}, t = 13\,\mathrm{mm}, F = 1\,\mathrm{kN}$, the maximum frequency for non-linear global buckling is $\mathfrak{f}_{max,GB,GNL} = 20$ and independent of the dome diameter (figure 5.27). For Moso with $D_0 = 100\,\mathrm{mm}, t = 10\,\mathrm{mm}, F = 1\,\mathrm{kN}$, the maximum frequency for global buckling is $\mathfrak{f}_{max,GB,GNL} = 14$. For the linear load case, the maximum frequencies are 26 and 18 respectively.

For frequencies $\mathfrak{f} < 9$, the difference between linear and non-linear global buckling utilization is negligible. Or vice versa: The higher the point load, the smaller the difference in maximum frequency for the linear and GNL case.

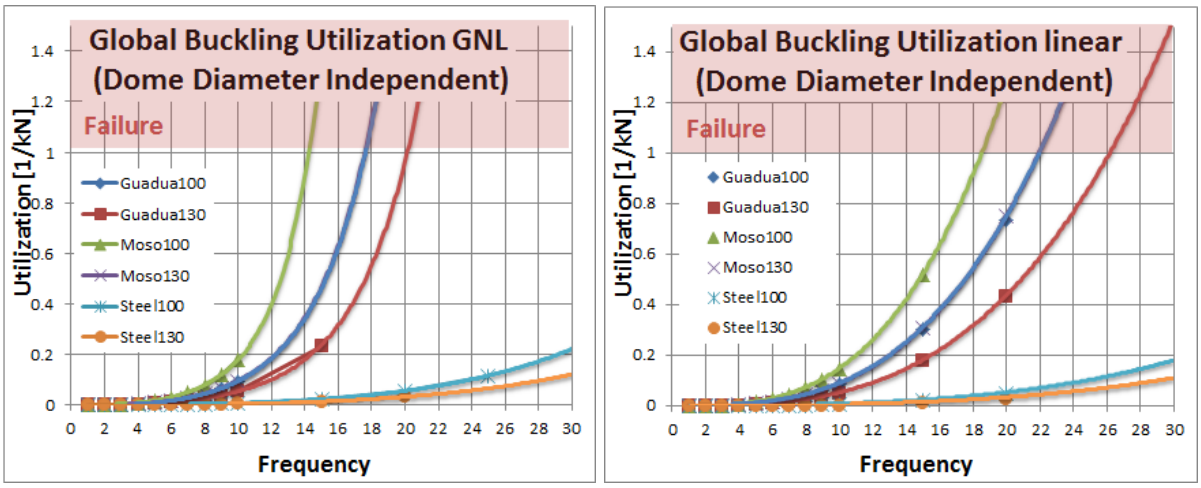

(a) GB utilization, LC2 non-linear

(b) GB utilization, LC2 linear

Figure 5.25: GB utilization, material dependent, independent of dome diameter, $t = 0.1D_0$

5.4.2.3 LC2: Transition Local to Global Buckling

The transition curve from global to local buckling is almost the same for both linear and non-linear analysis[17] (figure 5.26). A transition curve similar to equation 5.3 can be derived:

$$\text{LC2}, t = 0.1D_0 : \quad \frac{D}{D_0}_{(\mu_{GB}=\mu_{LB})} = 6.667\ \text{ʃ}^2 - 3.7311\ \text{ʃ} \tag{5.7}$$

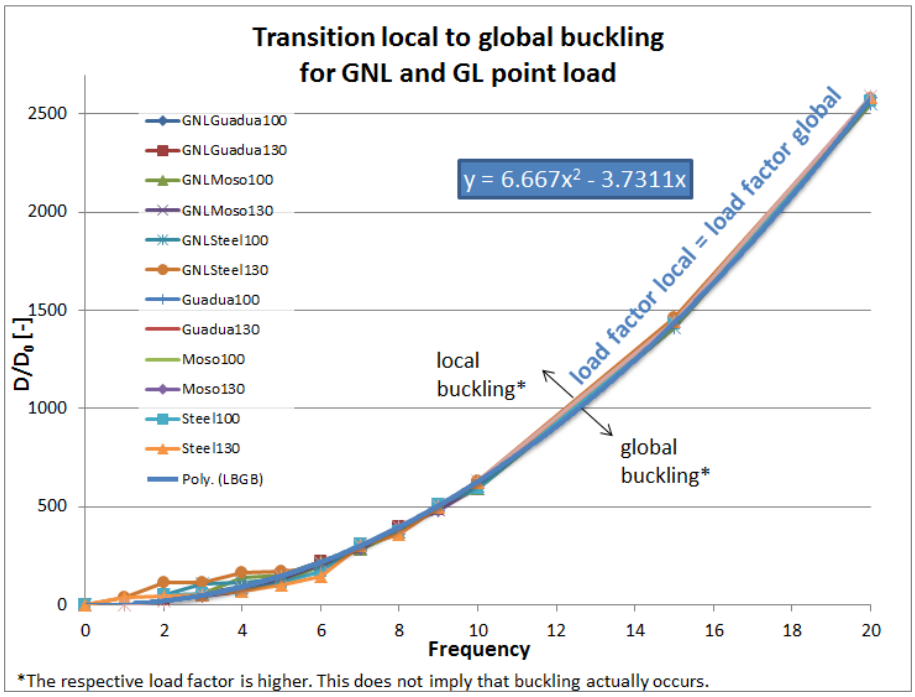

Figure 5.26: Transition from global to local buckling, point load

[17] Mode 1 global buckling only affects one ring of struts under the point load (figure 5.31e). This is also the area where local buckling occurs. Changed boundary conditions due to incremental increase of the load affect both local and global buckling. The effects of geometrical non-linearity are therefore negligible for the **transition** from local to global buckling.

5.4.2.4 LC2: Limit Dome Diameter $t = 0.1D_0$

There are three different methods to derive the limit dome diameter $D_{max,LBGB,LC2}$.

Method 1 This method is available for any magnitude of F and holds for both geometrically linear and GNL load application. Graphs similar to figure 5.25 can be produced with the results from *Grasshopper*. Depending on the type of material (D_0, t and E) and the magnitude of the applied load F, the maximum frequency $\mathfrak{f}_{max}$ can be determined graphically and then inserted into equation 5.7. For example, for an incremental force application of $F = 2\,\text{kN}$, we find a maximum frequency of $\mathfrak{f}_{max} = 12$ and $D_{max,LBGB,LC2} = 91.5\text{m}$ for Moso bamboo with $D_0 = 100\,\text{mm}$ and $t = 0.1D_0$.

Method 2 Alternatively, we can plot a graph for local buckling (equation 5.5) and add it to figure 5.26. We can derive a "safe" zone for every material, where neither local or global buckling occurs if only a point load of $F = 1\,\text{kN}$ is applied (figure 5.27). The same graph can be produced for geometrical non-linearity if a correction factor is applied to equation 5.6. This method has the disadvantage, that a new local buckling curve must be produced if the magnitude of the point load is changed.

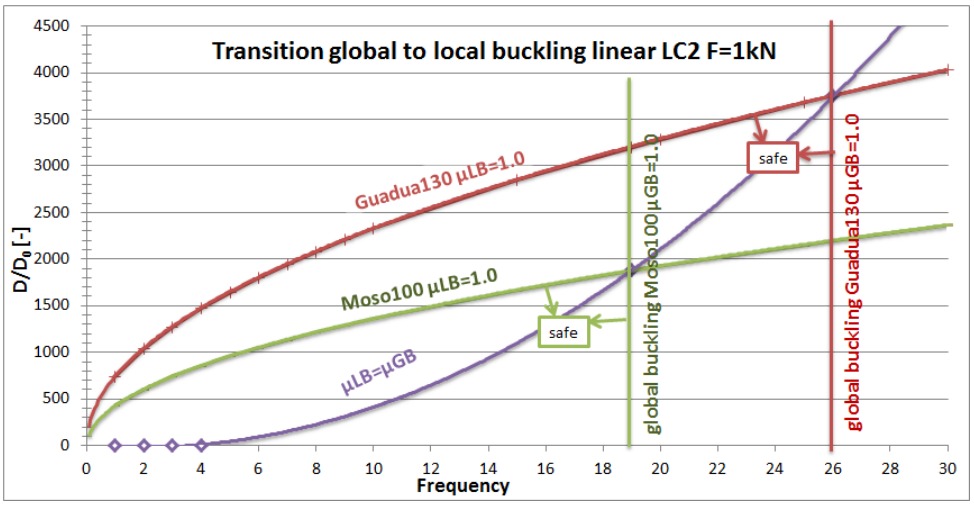

Figure 5.27: Transition from global to local buckling, linear point load

Method 3 The maximum possible dome diameter $D_{max,LBGB,LC2}$ can also be obtained by setting equation 5.6 equal to equation 5.7. This results in a cubic formula for $\mathfrak{f}_{max}$ and ultimately in the same maximum frequency as obtained in chapter 5.4.2.2. As we already implicitly used this information to derive equation 5.7, it is of course easier to insert $\mathfrak{f}_{max}$ directly into equation 5.6. Method 3 has the drawback, that the formula only holds for geometrically linear load application unless a correction factor is applied.

$$D_{max,LBGB,LC2} = C_2 \left(\frac{\mathfrak{f}_{max} D_0^4 E}{F} \right)^{\frac{1}{2}} \tag{5.8}$$

Note that $\mathfrak{f}_{max}$ does not only depend on the type of material, D_0, t and E but also on the magnitude of the applied load F. Figure 5.25 can be used to derive a maximum frequency for different forces.

5.4.2.5 LC2: Influence of t/D_0 Ratio

The impact of different t/D_0 ratios on global buckling utilization of Moso bamboo and the material independent transition point from global to local buckling is displayed in figure 5.28. Note that for LC1, different t/D_0 ratios (within 0.08 and 0.12) had a negligible impact on the transition curve. This is not the case for LC2!

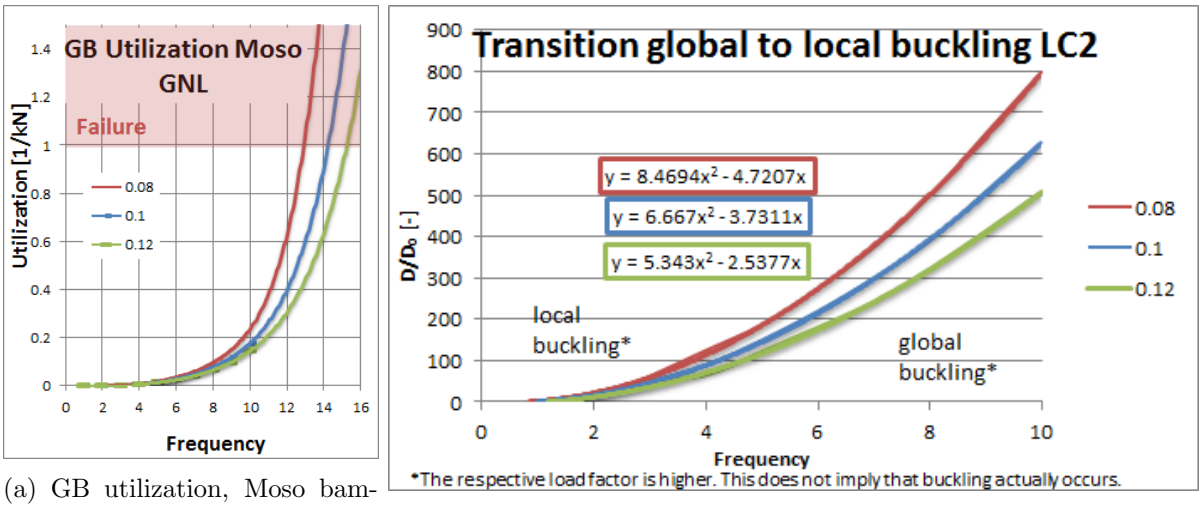

(a) GB utilization, Moso bamboo, different t/D_0 ratios, GNL

(b) Transition from global to local buckling, different t/D_0 ratios

Figure 5.28: Impact of different t/D_0 ratios

A higher t/D_0 ratio apparently leads to a higher maximum frequency f_{max} but also to a smaller maximum dome diameter D_{max}. This effect is illustrated for Moso in figure 5.29.

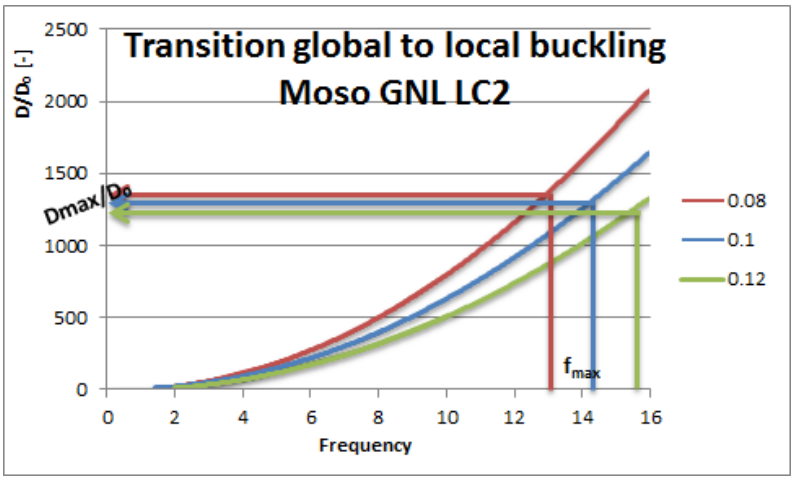

Figure 5.29: Maximum frequency and dome diameter, different t/D_0 ratios, Moso, GNL

5.4.2.6 LC2: Conclusions

Figure 5.30 shows a scheme of the local buckling curve ($\mu_{LB} = 1.0$), the global buckling curve ($\mu_{GB} = 1.0$), the transition curve ($\mu_{GB} = \mu_{LB}$), the maximum frequency $\mathfrak{f}_{max}$ and the maximum diameter $D_{max,LBGB}$ which still needs to be multiplied by D_0. The nature of the scheme is independent of the material, type of load application (geometrically linear or non-linear) and t/D_0 ratio. Note that global buckling will definitely occur, once $\mathfrak{f}_{max}$ is exceeded. This was not the case for load case self-weight. However, also for self-weight it is highly recommended not to exceed $\mathfrak{f}_{max}$., as it does not lead to higher dome diameters and the sudden global buckling failure will occur before a single strut buckles which is dangerous and should be avoided in all cases!

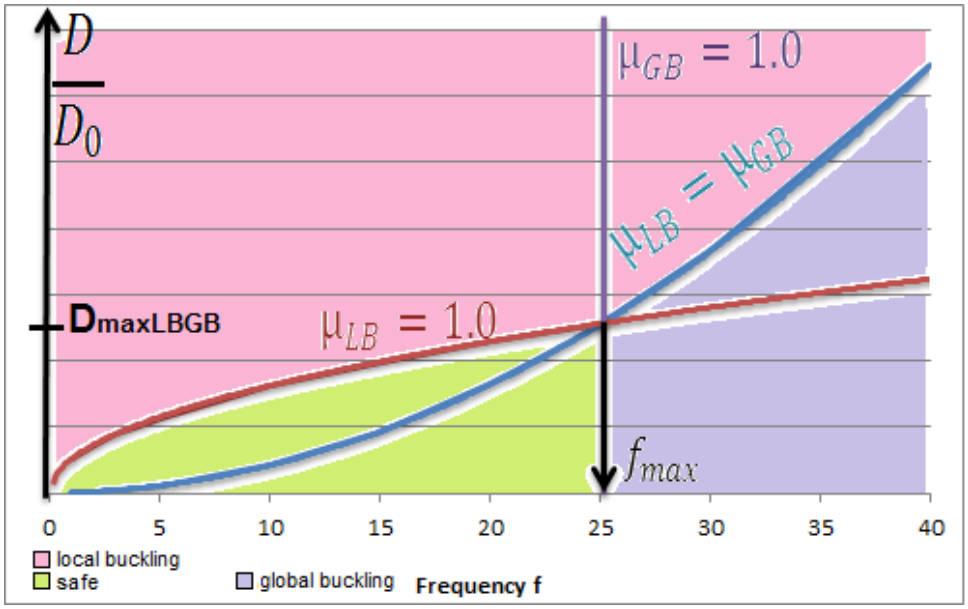

Figure 5.30: Scheme of transition local to global buckling and maximum frequency LC2

We can conclude the following:

1. The global buckling load factor and maximum frequency $\mathfrak{f}_{max}$ are independent of the dome diameter D.

2. The maximum possible dome diameter $D_{max,LBGB,LC2}$ depends on the type of material, in particular the t/D_0 ratio, and the magnitude of the applied load.

3. The impact of geometrical non-linearity is negligible for the transition from local to global buckling but needs to be taken into account for the derivation of $\mathfrak{f}_{max}$ and $D_{max,LBGB,LC2}$.

4. Linear superposition of load cases is only possible for geometrically linear point load application. For small frequencies however ($\mathfrak{f} < 9$), the difference between linear and non-linear global buckling is small. For local buckling, non-linearity can have a strong impact even for small displacements and GNL analysis is strongly advised.

5.4.2.7 Displacements in GSA

Note that mode 1 global buckling is displayed with an upward displacement in GSA for geometrically linear load application (figure 5.31e). This is of course not the case in reality. For a geometrically linear analysis, GSA increases the load until bifurcation (global buckling) occurs. This is done without 'knowing' in which direction the dome will actually buckle – for geometrically linear load application, buckling occurs suddenly. This effect can be compared to local buckling of a pinned-pinned bar in figure 5.31a: For a perfectly straight bar it is impossible to predict whether it will buckle to the left or right side. For the geometrically non-linear analysis on the contrary, small load increments are applied. The first increments determines the direction of the displacement and we arrive at the "real" buckling pattern (figure 5.31f). In order to determine the transition point of GB to LB, only the load factor needs to be known and it does not matter that the displacement is displayed in the wrong direction.

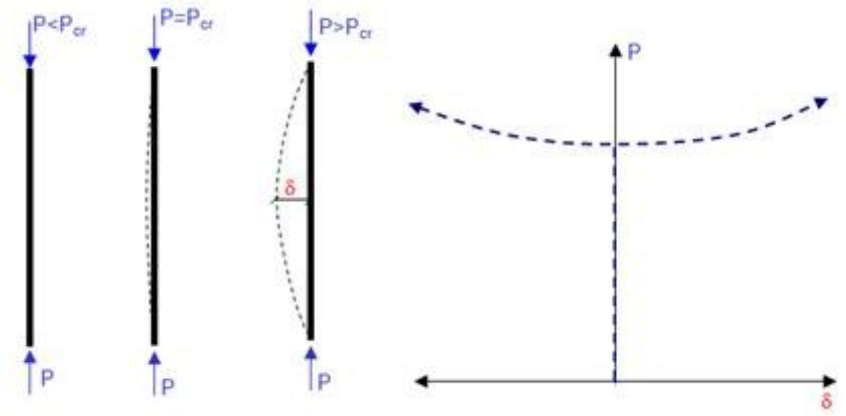

(a) Instability and bifurcation of pinned-pinned bar, Euler case 2 [61]

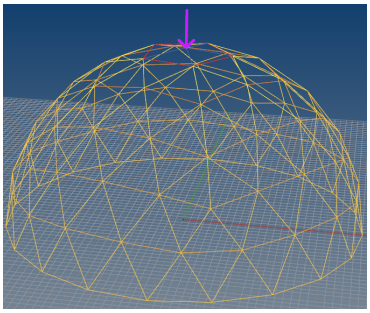

(b) *Grasshopper* point load

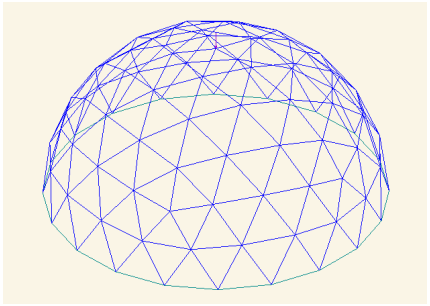

(c) GSA point load

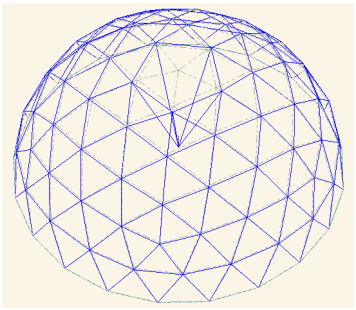

(d) linear displacement

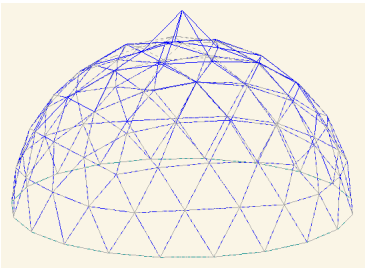

(e) GB mode 1, linear static

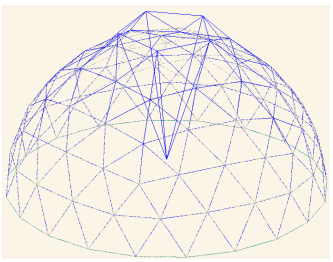

(f) GB mode 1, GNL

Figure 5.31: Load application and displacements for LC2: point load, $\mathfrak{f} = 4$

5.5 Comparison of Shells and Geodesic Domes

5.5.1 Influence Length of Edge Disturbances

In chapter 5.3.1 it was found that the thickness of a half-spherical shell can be expressed in geometrical properties of a geodesic dome:

$$\rho ALg = \rho t_s \frac{\sqrt{3}}{6} g L^2 \Rightarrow t_s = \frac{6}{\sqrt{3}} \frac{A}{L}$$

With equation 5.1

$$\frac{D}{L} = 1.515\mathfrak{f} \Rightarrow t_s = \frac{6}{\sqrt{3}} \frac{A}{\frac{D}{1.515\mathfrak{f}}} \approx 5.248 \frac{A}{D}\mathfrak{f}$$

We know from shell analysis [41], that the influence length of edge disturbances for spherical caps is approximately:

$$l_i = 2.4\sqrt{a t_s} \quad \text{with} \quad a = \frac{1}{2}D \quad \text{for half-spherical shells (Hoogenboom, 2014)}$$

$$\Rightarrow l_i = 2.4\sqrt{\frac{1}{2} D t_s} = 2.4\sqrt{\frac{1}{2} D \; 5.248 \frac{A}{D}\mathfrak{f}} \approx 3.888\sqrt{A\mathfrak{f}}$$

$$\text{for } t = 0.1 D_0 : \quad l_{i;t=0.1D_0} \approx 2.067 D_0 \sqrt{\mathfrak{f}}$$

This suggests that the edge disturbance length is independent of the dome diameter D and only depends on the frequency $\mathfrak{f}$ and strut diameter D_0. Previously, we observed in chapter 5.3.1 that the highest compressive stresses are located in the bottom ring of struts and the highest tensile stresses are located in the first perimeter above the equator. The length of these struts is of course dependent on the dome diameter D. So the derived influence length l_i is not really useful for geodesic domes.

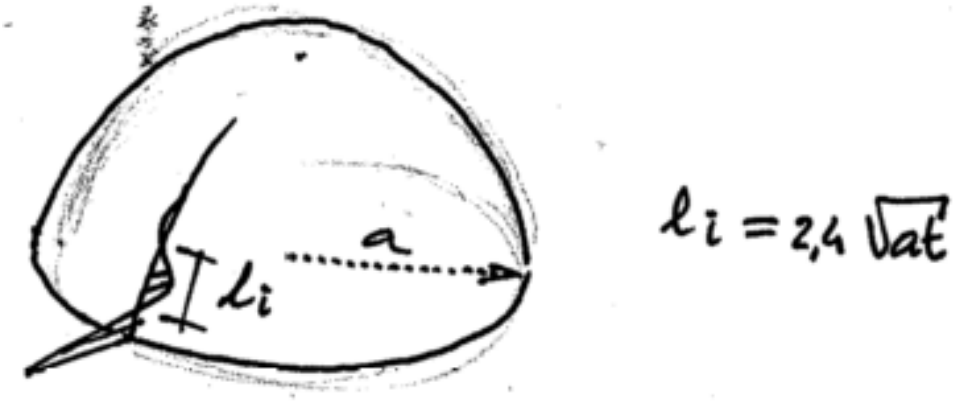

Figure 5.32: Influence length l_i (Hoogenboom, 2014) [41]

5.5.2 Shell Buckling Self-Weight

We observed previously that geodesic domes will fail in local buckling prior to global buckling, given the frequency is not too high and there is no superposition of load cases. This means that up to a specific frequency, global buckling does not need to be taken into account in a structural analysis. This maximum frequency is material dependent and for Moso and Guadua bamboo it lies well above $\mathfrak{f} = 20$. Let's imagine we construct a shell made out of isotropic OSB bamboo with randomly oriented fibre strands. This material has the same density, strength and Young's Modulus as full bamboo culms and can be supplied in any thickness t_s. We want to know, whether there is a criteria to choose a geodesic dome over a shell when both have the same self-weight. We will ignore imperfections (knock-down factors) for now and assume bamboo struts with $t = 0.1D_0$. We will see, that it makes sense to choose a geodesic dome of a frequency $\mathfrak{f} \geq 4$ over a shell from a stability point of view. Let's first have a look at the derivation and then discuss the results.

Derivation We know that a half-spherical shell buckles for a critical loading [42] of:

$$p_{cr} = \frac{2}{\sqrt{3(1-\nu^2)}} \frac{Et_s^2}{a^2} \overset{a=1/2D;\ \nu=0.38(\text{bamboo})}{\approx} 4.993 \frac{Et_s^2}{D^2} \qquad \text{(Hoogenboom, 2014)}$$

The thickness of a shell segment t_s can be approximated by a dome strut of length L and surface area A with similar weight (see chapter 5.3.1):

$$t_s \hat{=} \frac{6}{\sqrt{3}} \frac{A}{L} \overset{D/L=1.515\mathfrak{f}}{=} 5.248 \frac{A\mathfrak{f}}{D} \overset{t=0.1D_0}{=} 1.484 \frac{D_0^2\mathfrak{f}}{D}$$

Buckling of the shell occurs for $p_{cr} = p_z = \rho g t_s$

$$\Rightarrow 4.993 \frac{Et_s^2}{D^2} = \rho g t_s \Leftrightarrow 1 = 4.993 \frac{Et_s}{D^2 \rho g} = 4.993 \cdot 1.484 \frac{ED_0^2\mathfrak{f}}{D^3 \rho g} = 7.4095 \frac{ED_0^2\mathfrak{f}}{D^3 \rho g}$$

$$\Rightarrow D_{max,Shell} = 1.9495 \Big(\frac{ED_0^2\mathfrak{f}}{\rho g} \Big)^{1/3} \tag{5.9}$$

We can compare this value to the previously obtained value for local buckling of geodesic domes:

$$D_{max,GeoDome,LB} = 1.3732 \Big(\frac{ED_0^2\mathfrak{f}^2}{\rho g} \Big)^{1/3} \qquad \text{(5.2a see above)}$$

Results Figure 5.33 shows a plot of equation 5.2a and 5.9. A shell and a geodesic dome with a similar diameter D and same self-weight buckle simultaneously at the intersection point $\mathfrak{f} = 2.86 \ \rightarrow \ 3$; the shell fails in global buckling, the geodesic dome fails in local buckling of one of the bottom struts. As we only considered even frequencies in equation 5.2a, it is safe to say that it makes sense to choose a geodesic dome with $\mathfrak{f} \geq 4$ over a shell in terms of stability! Or in other words: **When constructing a geodesic dome, it makes sense to choose at least a frequency $\mathfrak{f} = 4$!** This result does not take imperfection sensibility into account. The real capacity of a shell is much lower (approximately 6 times!) due to this effect [42], and also Euler buckling capacity of dome struts is decreased by initial imperfections. Note that the chosen $t = 0.1D_0$ ratio and $\nu = 0.38$ are the only limitations of this conclusion!

Note: If a comparison to geodesic domes is not necessary, $D_{max,Shell}$ can be also be calculated straight forward for $p_{cr} = p_z$:

$$4.993 \frac{Et_s^2}{D_{max,Shell}^2} = \rho g t_s \Rightarrow D_{max,Shell} = 2.2345 \Big(\frac{Et_s}{\rho g} \Big)^{1/2} \tag{5.10}$$

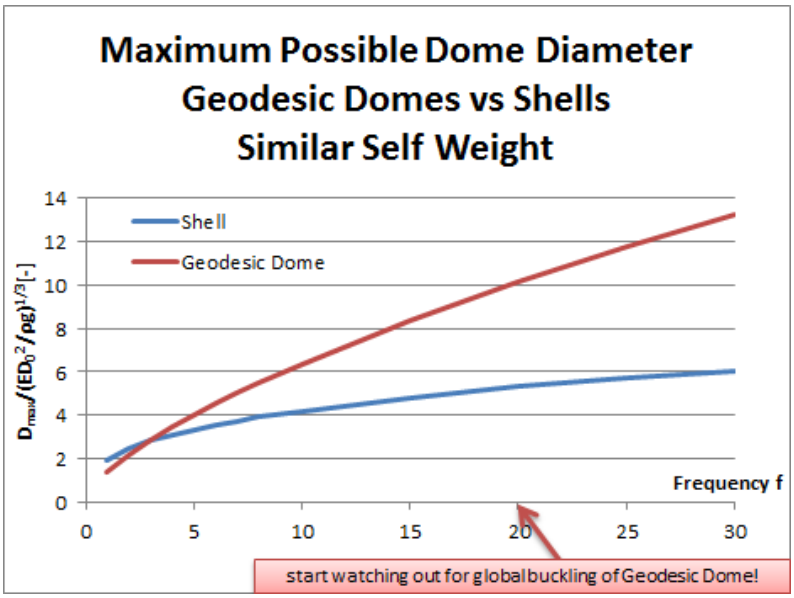

Figure 5.33: Shell buckling and local buckling of geodesic domes

Remark In chapter 5.5.1 it was shown that it is not possible to find a straight forward relationship between "local buckling" of shells (edge effects) and local buckling of geodesic dome struts. However, the global buckling curve[18] of geodesic domes can be added to figure 5.33 which results in figure 5.34. The global buckling curve (red) converges with the shell buckling curve (blue) as a geodesic dome with $\mathfrak{f} \to \infty$ becomes a shell. Note that these curves do not converge with a finite value; still, there is a definite limit diameter $D_{max,Shell}$ as material strength (f_c or f_t) is exceeded for $t_s \to \infty$ ($D_0 \to \infty$). For geodesic domes, the limit diameter $D_{max,GeoDome}$ is determined by the maximum frequency $\mathfrak{f}_{max}$ which depends on the dome material.

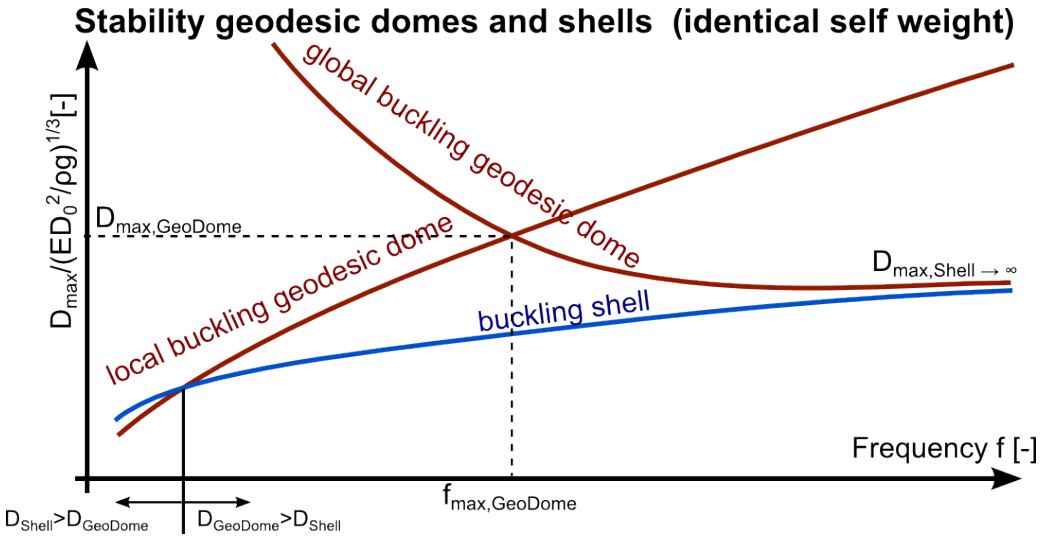

Figure 5.34: Scheme of stability shells and geodesic domes

[18]Note that this curve is a trend. More research needs to be done to determine the nature of the global buckling curve and derive an exact global buckling expression $D_{max,GeoDome,GB}$

5.5.3 Shell Buckling Point Load

Let's imagine another case. We want to construct a bamboo half-spherical shell of thin isotropic bamboo panels with a point load applied on top. From the shell equations we know that this is theoretically impossible as the membrane forces would be infinitely large. The point load thus needs to be spread out. However, we could also replace the top part of the shell by five dome struts and an edge ring, that equally distributes the loads and transfers them to the shell membrane. The resulting opening should be as small as possible and at the same time, the shell should not buckle. Another requirement is that the self-weight stays the same. We are thus looking for an opening angle ϕ and related frequency $\mathfrak{f}$, where both geodesic dome struts and the shell membrane buckle simultaneously. This hypothetical consideration has a real life application, e.g. when a window is supposed to be inserted into a shell and at night it is to be illuminated by a light installation that is fixed at the top of the shell (point load).

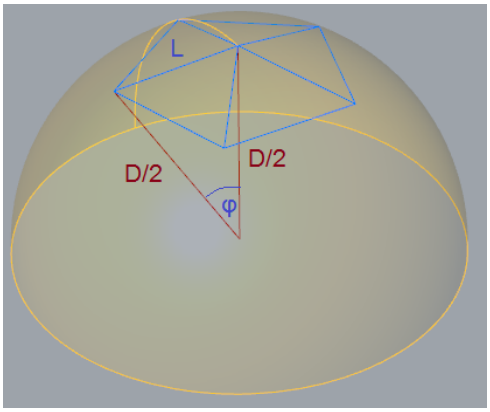

Figure 5.35: Replacement of part of shell by geodesic dome struts

Derivation Previously, we found a formulation for the maximum dome diameter D_{max} for local buckling of geodesic domes that are subjected to a point load:

$$D_{max,GeoDome} = 1.472 \left(\frac{\mathfrak{f} D_0^4 E}{F}\right)^{1/2} \qquad \text{(5.5 see above)}$$

We also found that there are dome diameter independent maximum frequencies $\mathfrak{f}_{max}$, where global buckling will occur depending on the applied material (figure 5.26). Global buckling due to point load is a localized phenomenon in the first ring of struts under the point load. With this information, we can try to find the smallest possible ring of struts (or the diameter of the "skylight" $D_{skylight}$) that is needed to safely introduce a point load to a shell.

The membrane force in a shell at any angle ϕ due to an applied point load R is [28]:

$$n_\phi = \frac{-R}{2\pi r_0 \sin(\phi)} \qquad \text{(Farnsworth, 1999)}$$

for a half-spherical dome with $r_0 = a = D/2$; $-R = F$: $\quad \Rightarrow n_\phi = \dfrac{F}{\pi D \sin(\phi)}$

the critical membrane force that leads to shell buckling is

$$n_{cr} = \frac{1}{\sqrt{3(1-\nu^2)}} \frac{E t_s^2}{a} \overset{a=1/2D;\ \nu=0.38(\text{bamboo})}{\approx} 1.2483 \frac{E t_s^2}{D} \qquad \text{(Hoogenboom, 2014)}$$

buckling occurs for $n_{cr} = n_\phi \quad \Rightarrow \dfrac{F}{\pi D \sin(\phi)} = 1.2483 \dfrac{E t_s^2}{D}$

with the previous derivation of $t_s = 5.248\frac{A\mathfrak{f}}{D} \overset{t=0.1D_0}{\approx} 1.4839\frac{D_0^2\mathfrak{f}}{D}$ we arrive at

$$\frac{F}{\pi D\sin(\phi)} = 1.2483\frac{E}{D}\Big(1.4839\frac{D_0^2\mathfrak{f}}{D}\Big)^2$$
$$\Rightarrow D_{max,shell} = \Big(8.6353\sin(\phi)\frac{D_0^4E\mathfrak{f}^2}{F}\Big)^{\frac{1}{2}} = 2.9386\ \mathfrak{f}\ \sin(\phi)^{\frac{1}{2}}\Big(\frac{D_0^4E}{F}\Big)^{\frac{1}{2}}$$

we can set the maximum diameters equal $D_{max,shell} = D_{max,GeoDome}$ and arrive at

$$1.472\ \mathfrak{f}^{\frac{1}{2}}\Big(\frac{D_0^4E}{F}\Big)^{\frac{1}{2}} = 2.9386\ \mathfrak{f}\ \sin(\phi)^{\frac{1}{2}}\Big(\frac{D_0^4E}{F}\Big)^{\frac{1}{2}} \quad\Leftrightarrow\quad \frac{1.472}{2.9386}\mathfrak{f}^{-\frac{1}{2}} = \sin(\phi)^{\frac{1}{2}}$$
$$\Rightarrow \sin(\phi) = \frac{0.251}{\mathfrak{f}}$$

from the equilateral triangle we know (figure 5.35):

$$\cos(\phi) = 1 - \frac{L^2}{2\big(\frac{D}{2}\big)^2} = 1 - \frac{1}{2\big(\frac{1.515\mathfrak{f}}{2}\big)^2} = 1 - \frac{2}{(1.515\mathfrak{f})^2}$$
$$\sin(\phi)^2 = 1 - \cos(\phi)^2 \quad\Leftrightarrow\quad \frac{0.251^2}{\mathfrak{f}^2} = 1 - \Big(1 - \frac{2}{(1.515\mathfrak{f})^2}\Big)^2$$
$$\Rightarrow 1 - 1 + 2\frac{2}{(1.515\mathfrak{f})^2} - \frac{2^2}{(1.515\mathfrak{f})^4} - \frac{0.251^2}{\mathfrak{f}^2} = 0 \quad \frac{4}{1.515^2}\mathfrak{f}^2 - 0.251^2\mathfrak{f}^2 - \frac{4}{1.515^4} = 0$$
$$\Rightarrow \mathfrak{f} = \sqrt{0.452} = 0.6723 \quad \Rightarrow \phi = 9.71°$$

the length L of the struts at this angle is

$$L = \sqrt{2\Big(\frac{D}{2}\Big)^2\big(1 - \cos(\phi)\big)} = D\sqrt{\frac{1}{2}\big(1 - \cos(9.71°)\big)} = 0.0847D$$
$$\Rightarrow \quad D_{skylight} = 2\sin(\phi)\frac{D}{2} = 0.167D$$

a possible solution for this problem is to choose one ring of struts of a frequency $\mathfrak{f} = 7$

$$\Rightarrow \mathfrak{f} = \frac{D}{1.515L} = \frac{D}{1.151\cdot 0.0847D} = 7.8 \to 7$$
$$\cos(\phi_2) = 1 - \frac{2}{(1.515\mathfrak{f})^2} = 1 - \frac{2}{(1.515\cdot 7)^2} \quad \Rightarrow \phi_2 = 10.82°$$

Results This result shows that at an angle $\phi = 9.71°$, the critical membrane stress of a shell is reached. We can thus replace the top part of a shell with a geodesic dome skylight with $D_{skylight} = 0.167D$ in order to safely distribute the point load to the shell membrane. The derived frequency $\mathfrak{f} = 7$ with adapted opening angle $\phi_2 = 10.82°$ is one possibility to do this efficiently without cutting struts in half. We could of course also use two rings of struts of a frequency $\mathfrak{f} = 14$ or any other approximation. However, we need to make sure that global buckling does not occur! If the angle ϕ is changed (it can only be increased in order to prevent shell buckling), a new optimal frequency has to be found. It makes sense to adapt ϕ to a frequency and not the other way around to prevent cutting struts. Note that the chosen $t = 0.1D_0$ ratio and $\nu = 0.38$ are the only limitation of this conclusion!

5.6 Conclusions

5.6.1 Transition Local to Global Buckling

Two instability limit states exist for geodesic domes: Local buckling (LB) of a single strut and global buckling (GB), where several struts snap simultaneously into a deformed state. If the frequency ƒ of a geodesic dome is increased, the strut length L becomes shorter and local buckling is less likely to occur. At the same time, the dome approaches the shape of a monolithic shell which is prone to global buckling. There is a transition point where local buckling changes into global buckling and utilization of both limit states is equal ($\mu_{LB} = \mu_{GB}$). A transition curves can be plotted for different frequencies ƒ and D/D_0 ratios (figure 5.36). The transition curve depends on the t/D_0 ratio of the struts[19] but is independent of the material!

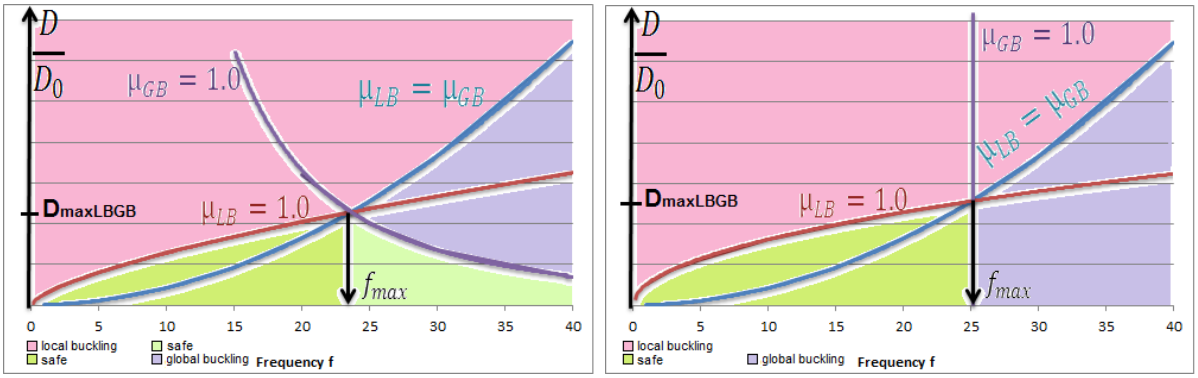

(a) Scheme of transition LB to GB and f_{max} LC1 (b) Scheme of transition LB to GB and f_{max} LC2

Figure 5.36: Transition scheme

Explanation of figure 5.36:

- In the green zones, neither local nor global buckling occurs ($\mu_{GB} < 1.0$ and $\mu_{LB} < 1.0$), this zone is ”safe” in terms of stability.
- In the pink zone, local buckling occurs ($\mu_{LB} > 1.0$).
- In the purple zone, global buckling occurs ($\mu_{GB} > 1.0$).
- The point where both local and global buckling utilization are identical and equal to 1.0 ($\mu_{GB} = \mu_{LB} = 1.0$) determines the maximum frequency f_{max}.
- For LC2, global buckling **does** occur if $f > f_{max}$.
- For LC1, global buckling **can** occur if $f > f_{max}$.
- **Note:** As global buckling is a brittle failure without warning, f_{max} should also not be exceeded in LC1 for safety reasons.
- At the point of $f = f_{max}$, the maximum dome diameter $D_{max,LBGB}$ is obtained by multiplying the D/D_0 ratio by D_0 or inserting f_{max} into the equation of the transition curve ($\mu_{GB} = \mu_{LB}$).

[19] except for $t/D_0 \in [0.08; 0.12]$ for LC1; the difference is of transition curves is negligible

- The transition curve (blue; $\mu_{GB} = \mu_{LB}$) has the nature $D/D_0 = A\mathfrak{f}^2 + B\mathfrak{f}$ (equation 5.3 and 5.7):

$$\text{LC1}, t = 0.1D_0: \quad \frac{D}{D_0}_{(\mu_{GB}=\mu_{LB})} = 5.0515\ \mathfrak{f}^2 - 4.398\ \mathfrak{f}$$
$$\text{LC2}, t = 0.1D_0: \quad \frac{D}{D_0}_{(\mu_{GB}=\mu_{LB})} = 6.667\ \mathfrak{f}^2 - 3.7311\ \mathfrak{f}$$

- The geometrically linear local buckling curve (red; $\mu_{LB} = 1.0$) can be derived analytically:

Local Buckling Load Case 1 (even frequencies)

$$D_{max,LB,LC1} = C_1\Big(\frac{D_0^2\mathfrak{f}^2E}{\rho g}\Big)^{1/3}$$
$$C_1 = 1.1313\Big(\frac{t}{D_0}\Big)^2 - 1.2067\Big(\frac{t}{D_0}\Big) + 1.4837 \quad t \in [0.08; 0.5]D_0$$

Local Buckling Load Case 2 (linear point load)

$$D_{max,LB,LC2} = C_2\ \Big(\frac{\mathfrak{f}D_0^4E}{F}\Big)^{1/2}$$
$$C_2 = -5.6638\Big(\frac{t}{D_0}\Big)^2 + 4.4528\Big(\frac{t}{D_0}\Big) + 1.0806 \quad t \in [0.08; 0.5]D_0$$

- An expression for the global buckling curve (purple; $\mu_{GB} = 1.0$) still needs to be found. This is in theory possible with the present geodesic dome model but very time consuming and a task for future research.

Similar graphs can be derived for load cases such as superimposed distributed dead load[20], snow and wind. However, detailed analysis of these load cases was beyond the scope of this research project.

5.6.2 Limit Dome Diameter

Formulas for the maximum possible dome diameter can be derived with equation 5.3 and equation 5.7. They are independent of the dome material.

Load Case 1 (requires knowledge of $\mathfrak{f}_{max}$ which depends on the material)

$$t = 0.1D_0: \quad D_{max,LBGB,LC1} = \big(5.0515\ \mathfrak{f}_{max}^2 - 4.398\ \mathfrak{f}_{max}\big)D_0 \quad \text{applicable for any material}$$

Load Case 2 (requires knowledge of $\mathfrak{f}_{max}$ which depends on the material and magnitude of applied load F)

$$t = 0.1D_0: \quad D_{max,LBGB,LC2} = \big(6.667\ \mathfrak{f}_{max}^2 - 3.7311\ \mathfrak{f}_{max}\big)D_0 \quad \text{applicable for any material}$$

For load case 1, equation 5.4a provides a straight forward formula for *Guadua angustifolia* and *Phyllostachys pubescens*. Nodes and imperfections are neglected and the values are based on mean strength. The rules of thumb do not take maximum available length of bamboo culms into account.

$$\left.\begin{array}{ll} D_{max,LBGB,LC1} = (5760.5 - 16.81D_0)D_0; & \text{Guadua} \\ D_{max,LBGB,LC1} = (4853.6 - 15.43D_0)D_0; & \text{Moso} \end{array}\right\} \quad \begin{array}{l} t \in [0.08; 0.12]D_0 \\ D_0 \in [90; 130]\text{mm} \end{array}$$

[20]Note: As the LC1 transition curve is independent of the magnitude of the load, superimposed dead load results in the same transition curve as LC1.

Substituting D_0 and $\mathfrak{f}_{max}$ of the culms used in experiments, we find:

Load case 1 (self-weight):

$$D_{max} = (5760.5 - 16.81 \cdot 130)130 = 475.4\text{m}; \quad \text{Guadua}$$
$$D_{max} = (4853.6 - 15.43 \cdot 100)100 = 331.1\text{m}; \quad \text{Moso}$$

Load case 2 (GNL, point load of 1kN)

$$D_{max} = (6.667 \cdot 20^2 - 3.7311 \cdot 20)130 = 337.0\text{m}; \quad \text{Guadua}$$
$$D_{max} = (6.667 \cdot 14^2 - 3.7311 \cdot 14)100 = 125.4\text{m}; \quad \text{Moso}$$

Load case 2 (GNL, point load of 2kN)

$$D_{max} = (6.667 \cdot 15^2 - 3.7311 \cdot 15)130 = 187.7.0\text{m}; \quad \text{Guadua}$$
$$D_{max} = (6.667 \cdot 12^2 - 3.7311 \cdot 12)100 = 91.5\text{m}; \quad \text{Moso}$$

Load case 2 (GNL, point load of 5kN)

$$D_{max} = (6.667 \cdot 14^2 - 3.7311 \cdot 14)130 = 163.1\text{m}; \quad \text{Guadua}$$
$$D_{max} = (6.667 \cdot 10^2 - 3.7311 \cdot 10)100 = 62.9\text{m}; \quad \text{Moso}$$

Load case 2 (linear, load of 1kN)

$$D_{max} = (6.667 \cdot 26^2 - 3.7311 \cdot 26)130 = 573.3\text{m}; \quad \text{Guadua}$$
$$D_{max} = (6.667 \cdot 16^2 - 3.7311 \cdot 16)100 = 164.7\text{m}; \quad \text{Moso}$$

5.6.3 Superposition

Superposition of load factors resulting from geometrical non-linearity or global buckling is generally not possible. However, it was found that global buckling does not occur for self-weight or point load unless a maximum frequency $\mathfrak{f}_{max}$ is exceeded. Additionally, for frequencies $\mathfrak{f} < 9$, the difference of global buckling load factors resulting from linear and non-linear analysis of a single point load is negligible. However, non-linearity has a huge impact for larger frequencies and cannot be neglected, in particular for deflections and local instabilities. Superposition is thus only possible for linear load cases with $\mathfrak{f} < \mathfrak{f}_{max}$.

5.6.4 Stability of Shells and Geodesic Domes

In terms of stability of shells loaded by self-weight, it makes sense to replace the shell by a geodesic dome with a frequency 3 (4) or higher. For application of point loads, the top part of the shell can be replaced by geodesic dome struts; formulas can be derived for the opening angle that leads to most efficient material use while preventing buckling of the shell and dome struts. **In general, it makes sense to choose a geodesic dome with $\mathfrak{f} \geq 4$ over a shell, for both self-weight and point load or a combination of both**.
Sometimes, for aesthetic or acoustic reasons, architects choose shell structures. These can then be reinforced by a geodesic dome of a frequency 4 up to $\mathfrak{f}_{max}$.

Chapter 6

Safety Concepts and Probabilistic Design

A common approach to guarantee a certain degree of structural safety, is the employment of probabilistic design. This can for example be realized with partial safety factors. Statistical distributions of loads and material properties are used to derive these factors based on a certain percentile (usually 5%) in which the load may be exceeded or the assumed strength is not met. For different materials, the probability curves are differently wide spread, depending on the spread of experimental results. Man-made materials such as steel have well controlled material properties and the spread is small. Natural materials such as timber and bamboo have a wider spread as can be seen in figure 6.1.

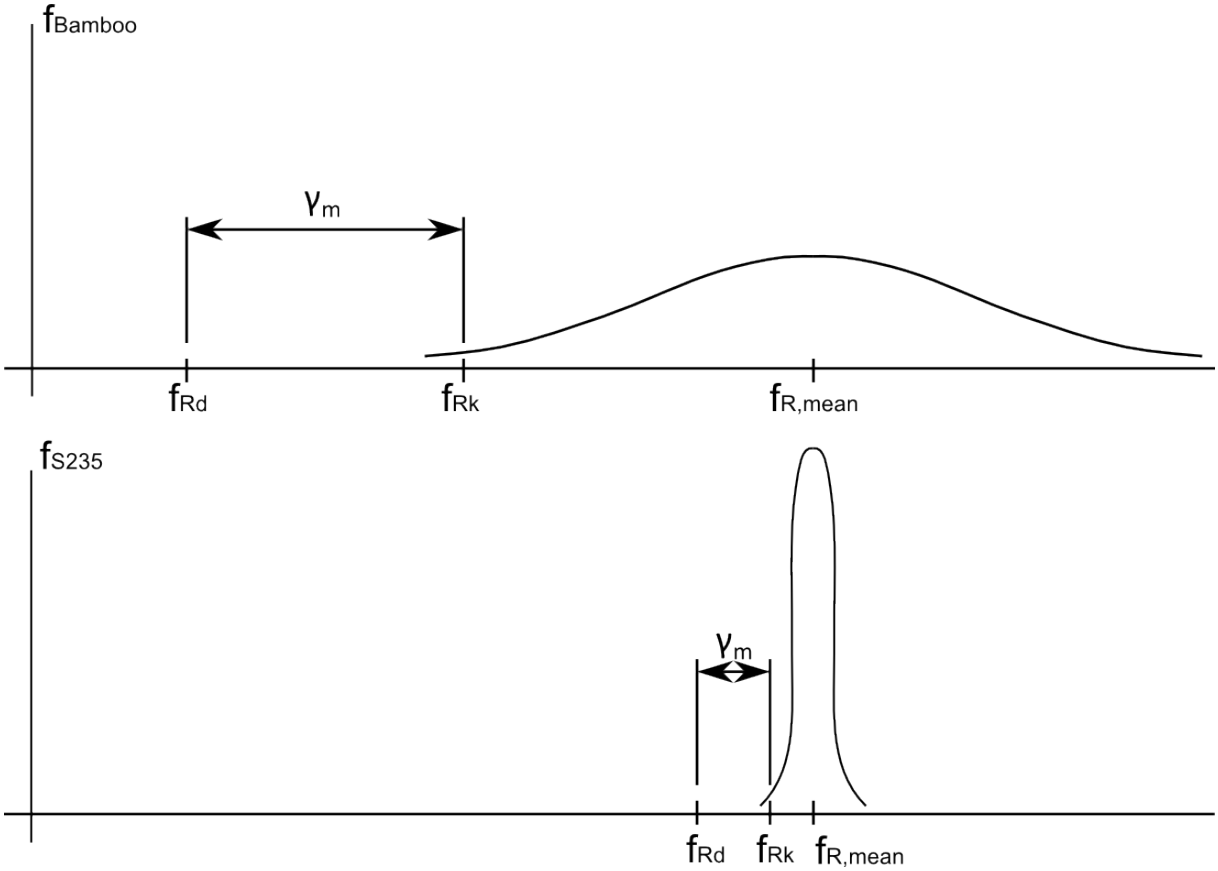

Figure 6.1: Gaussian distribution of strength

In chapter 5, all assumed strength values are experimental mean strength values (denoted as $f_{R,mean}$, $\overline{x}$ or μ) if not stated differently. However, $f_{R,mean}$ is not a safe assumption for the strength of the material, as 50% of the times this strength is not met. Of course, an architect or engineer wants to construct a safe structure with little risk of failure. Unfortunately, high safety also implies high costs. Therefore, the designer needs to choose a threshold below which the material strength is not met. Common consensus for buildings is a "characteristic" strength f_{Rk}, which is not met in 5% of the cases (5%-percentile). The 5%-percentile is calculated using the mean value μ and standard deviation σ of a population, for example experimental results similar to those of chapter 4. A wide-spread strength distribution results in lower 5%-values and less structural efficiency. Therefore, it is important to reduce scatter of test results.

The design value of the action is denoted as f_{Ed} and is derived from the probabilistic distribution of the load that acts on the structure. Examples of the implementation can be found in chapter 7 and 8. A structure is very efficient if the design value of the action f_{Ed} and the design value of the provided strength f_{Rd} lie close together or are identical. In general, f_{Rd} is obtained by reducing f_{Rk} by a partial material safety factor γ_m. Additional reduction depends on exposure and purpose of the structure. One way to derive safety factors is the application of a *target reliability index* β, which defines the probability of failure ($f_{Rd} < f_{Ed}$) in a certain time span. This is an ethical and economical decision and often statements can be made like: "the dyke's strength may be exceeded once in 500 years".

For natural materials, material strength often depends on external factors. Therefore, modification factors are applied that represent the load duration, nature of the load (static or dynamic), exposure (e.g. moisture content) and creep of the material. On the load side, safety factors are applied according to type of load and the use of the structure – if it is a public building for example, the structure needs to withstand fire and other extreme events for a certain time. Naturally, different countries employ different safety concepts that meet the needs of their people. The Eurocodes try to enable this concept through National Annexes. While in the Netherlands, there is little need for consideration of snow loading in combination with strong winds, in the Alps in Germany it would be a horrendous mistake not to combine the two. Accordingly, earthquake design is not necessary in most parts of Europe but for countries with seismic activity, it is a crucial part of structural safety. Still, different countries have different safety philosophies. In Germany, the partial safety factor for dead load is defined as 1.35, whereas in the Netherlands, it is only taken as 1.2. While in practice, this has little impact on the user, the designer has to be aware of these standards. Especially if the utilization of a building is changed or structural safety has to be assessed after damage due to natural disasters, it is useful to know what safety concept was employed.

In chapter 5, theoretical limits for dome dimensions were derived which makes them universally applicable beyond national borders and safety concepts. However, these values only hold within the boundary conditions of experiments and model calculations conducted. The found results and derived rules of thumbs should be seen as "raw data" rather then a ready-made design guide. Providing entire sets of test results, including the boundary conditions of the experiments, enables scientists to compare their own research to values obtained by other researchers. Structural designers and architects are encouraged to use the model results and test results provided in this thesis to aid their own design. However, verification of all provided values is strongly advised! The need for employment of safety factors (or any other method of probabilistic design that provides sufficient safety) prior to real life application is emphasized accordingly.

Chapter 7

Tensile Connector

7.1 Proposal: Cross Dowel Joint 2014 TU Delft

A bolted connector is proposed inspired by the connector of Peter de Vries [91]. Two perpendicular bolts (cross dowels) are connected by a threaded rod that runs through an end plate and can be fastened to a dome hub by a nut (figure 7.1). If the threaded rod is loaded in tension, the cross dowels transfer the tensile force to the bamboo culm by bolt bearing, shear and / or tensile splitting. A node can be used as natural reinforcement. Compressive forces are transferred by contact of the end plate to the culm cross-section. All calculations are based on Moso bamboo. However, the connector could be applied for any bamboo species, given the mechanical properties are known.

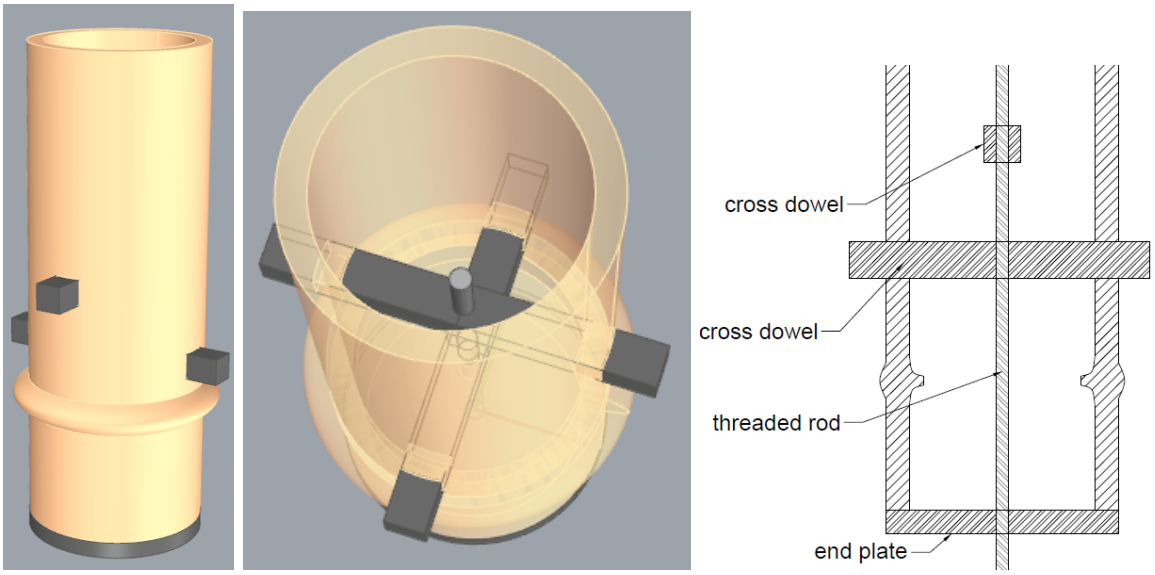

(a) View from side (b) Transparent view from top (c) Schematic sketch

Figure 7.1: Cross dowel connector

In chapter 4.2.4 it was found that a square cross dowel provides a much safer failure mode (wedge forming and large displacements during embedment, figure 7.2b) than a round cross dowel (brittle tensile splitting, figure 7.2a). The dowel geometry and edge distance are adopted from experiments with a square dowel diameter $d = 16\,\text{mm}$ and edge distance $l_{edge1} = 100\,\text{mm}$ and $l_{edge2} = 150\,\text{mm}$.

(a) Splitting round dowel (b) Embedment square dowel (c) Square cross dowel

Figure 7.2: Failure modes and dowel geometry

7.2 Predicted Strength

In order to compare the strength of steel and bamboo components in this chapter, safety factors in the style of the Eurocodes are employed. Any other safety concept could be used to dimension the steel components. For the proposed connector, the threaded rod is designed to fail in ductile yielding. This results in better predictability and reduced scatter of test results once the connector is assembled and tested. Chapter 6 provides a more detailed explanation of the philosophy of safety concepts.

All calculations in chapter 7 and 8 are based on the following assumptions:

- Material properties are distributed in a normal distribution.
- The the sample mean $\overline{x}$ and population mean μ are almost identical.
- In the given application (case study of chapter 8), the design life is less than a year and consequence in case of failure is small. The target reliability index for a one year reference period is $\beta = 4.25$ which corresponds to a probability of failure of $P = 1.05\ 10^{-5}$ per year[1]. For comparison: for buildings with a design life of 50 years and low to medium consequence in case of failure, a common reliability index is $\beta = 3.6$ ($\beta = 4.5$ for one year) (Eurocode 0 table B1 and B2 [25]).
- According to Eurocode 0 it is safe to assume $\alpha_R = -1.0$ and $\alpha_E = 0.4$ for the calculation of partial safety factors[2] γ (Eurocode 0, C7(4) [25]).
- A modification factor $k_{mod} = 0.6$ for permanent use (self-weight) is adopted in the style of Eurocode 5 table 3.1 [27] to account for the load duration and exposure of the structure. This is a very conservative value as it assumes a load duration of more than 10 years. Greater values of k_{mod} are possible, depending on the application.
- A creep factor k_{def} is not included in the strength calculation of the connector. Janssen [47] states that creep is negligible in bamboo. However, recent research suggests that creep has a strengthening effect on compressive strength and a weakening effect on tensile

[1]This probability is less than the odds of being struck by lightning in a person's lifetime: $P_{\text{lightning}} = 0.84\ 10^{-5}$ [7].

[2]The larger absolute α value is used for the property with more scatter. In general, the scatter of the load is larger than the scatter of the material properties, which results in larger material safety factors. While this might not be the case for bamboo, it is certainly the case for steel. As the connector is designed in such a way, that steel fails prior to bamboo, it makes sense to assume larger scatter in the load.

strength [36][87]. Further research is necessary to establish values for k_{def}. In chapter 8, k_{def} is adopted from Eurocode 5 in order to derive the design value of the Modulus of Elasticity E_d which is needed for stability considerations.

- In accordance with the Eurocodes, values of resistance are denoted with the subscript X_R and values of actions are indicated with a subscript X_E. Characteristic values (5%-percentile values) are indicated by the subscript X_k, design values are denoted as X_d.
- Design strength values f_{Rd} of bamboo are calculated individually for each material property as ductile failure (e.g. bearing) results in little scatter of test results and higher design values f_{Rd} than brittle failure (e.g. splitting, tensile failure). Using only one γ_m for bamboo would punish ductile failure modes [92][16]:

$$\gamma_m = \frac{f_{Rk}}{f_{Rd}}; \quad f_{Rk} : 5\% - \text{percentile}; \quad f_{Rd} = \mu(f) + \alpha_R \beta \sigma(f)$$

Table 7.1: Material properties Moso, $\beta = 4.25$, nodes taken into account if negative effect

property	unit	$\overline{x} \approx \mu$	f_{Rk}	σ	f_{Rd}	γ
tensile strength	f_t [MPa]	102.7	76.7[3]	15.81	35.5	2.2
compression strength	f_c [MPa]	47.5	38.1	5.7	23.3	1.6
bearing strength	f_b [MPa]	52.7	49.9	1.7	45.5	1.1
splitting strength[4]	f_s [MPa]	18.18	16.4	1.1	13.5	1.2
shear strength	f_v [MPa]	18.33	13.2[3]	3.12	5.1	2.6
Modulus of Elasticity	E [MPa]	8570				
Strut diameter	D_0 [mm]	100				
wall thickness	t [mm]	10				
density	ρ [kg/m^3]	660				

For steel components, S235 is used with $f_y = 235\,\text{MPa}$, $f_u = 360\,\text{MPa}$, $E = 210\,000\,\text{MPa}$. The cross dowels are square with $d = 16\,\text{mm}$, $d_1 = 16 + 1 = 17\,\text{mm}$ (figure 7.2c).

The material safety factors are adopted from Eurocode 3[5]:

Table 7.2: Safety factors steel components

tension	bending	shear
γ_{M0}	γ_{M1}	γ_{M2}
1.0	1.1	1.25

The following calculations should be seen as an example of connector design and not as the actual strength of the connector, which requires experimental testing!

[3]Shao et al. [77] assuming a Gaussian distribution: $x_{5\%} = \overline{x} - 1.645\sigma$

[4]Note that this is a hypothetical property obtained from a round bolt shear test and not e.g. a split pin test.

[5]As the design life is one year, these factors could be reduced. However, the connector is designed to fail in tensile yielding which prescribes $\gamma_{M0} = 1.0$ and a safety factor smaller than 1.0 makes little sense.

7.2.1 Bamboo Components

7.2.1.1 Bamboo Axial Tensile Strength of Net Cross-Section

In order to calculate the axial tensile strength of the culm, the net cross-section at the height of one cross dowel has to be considered. The net cross-section can be approximated by:
$A_{net} = A - \left(2\ d_1\ t\right)$ (figure 7.3b)

$$F_{t,Rd} = f_{t,Rd}\ A_{net} = f_{t,Rd}\left[A - \left(2\ d_1\ t\right)\right]$$
$$= f_{t,Rd}\left[\left(\frac{\pi}{4}(D_0^2 - D_i^2)\right) - \left(2\ d_1\ t\right)\right] = f_{t,Rd}\left[\left(\frac{\pi}{4}\left(D_0^2 - (D_0 - 2t)^2\right)\right) - \left(2\ d_1\ t\right)\right]$$
$$= 35.5 \cdot 2487 = 88.32\,\text{kN}$$

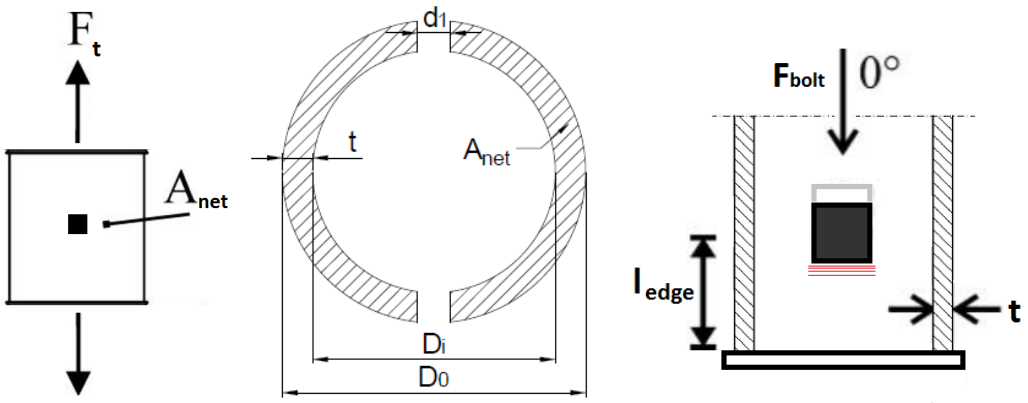

(a) Tensile load (b) Net cross-section (c) bearing failure

Figure 7.3: Tensile, compressive and bearing strength

7.2.1.2 Bamboo Axial Compressive Strength of Net Cross-Section

Compression is transferred by contact between hub and end-plate. Again the net cross-section is used to derive the maximum allowable compression force.

$$F_{c,Rd} = f_{c,Rd}\ A_{net} = 23.3 \cdot 2487 = 57.90\,\text{kN}$$

7.2.1.3 Bamboo Bearing Strength under Cross Dowel

The bearing strength f_b is obtained by bolt testing (figure 7.3). Experiments showed that mean bearing strength f_b is close to equal to the mean compression strength f_c which is in agreement with the assumption of Widyowijatnoko [99]. However, scatter for bearing is significantly smaller, which results in a much higher design value $f_{b,Rd}$!

$$F_{b,Rd} = 4\ f_{b,Rd}\ d\ t = 4 \cdot 45.5 \cdot 16 \cdot 10 = 29.10\,\text{kN}$$

7.2.1.4 Bamboo Shear Strength under Cross Dowel

When the dowels start to displace in embedment, the tight fit of the end plate is not given any more and block shear can theoretically occur[6]. The orientation of the cross dowels results in eight shear planes that don't intersect each other. Dowel interaction does not need to be considered. The shear plane is assumed to run over the thickness of the culm until the edge $A_v = l_{edge}\ t$. Every dowel introduces two shear planes at each end, resulting in a total of eight shear planes for two orthogonal cross dowels. Note that the influence of the node is neglected.

$$\begin{aligned} F_{v,Rd} &= 4\ f_{v,Rd}\ t\ l_{edge1} + 4\ f_{v,Rd} t\ l_{edge2} = 4\ f_{v,Rd}\ t\ \left(l_{edge1} + l_{edge2}\right) \\ &= 4 \cdot 5.1 \cdot 10\ (100 + 150) = 50.70\,\text{kN} \end{aligned}$$

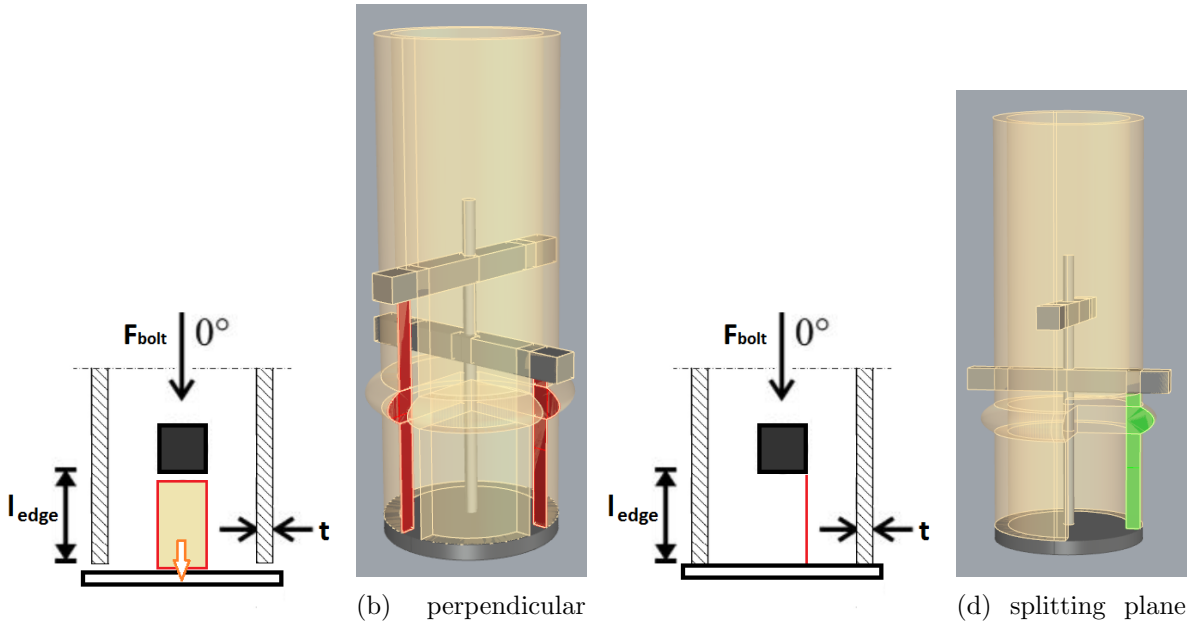

(a) shear planes single dowel (b) perpendicular shear planes (c) splitting plane single dowel (d) splitting plane perspective view

Figure 7.4: shear failure and tensile splitting failure

7.2.1.5 Bamboo Tensile Splitting Strength under Cross Dowel

For splitting failure, nodes have a positive effect which can be neglected in a conservative approach. It is assumed that interaction of the splitting planes does not occur and one distinct crack per bolt end (4 cracks in total) is required for final failure of the connection.

$$\begin{aligned} F_{s,Rd} &= 2\ f_{s,Rd}\ t\ \left(l_{edge1} + l_{edge2}\right) \\ &= 2 \cdot 13.5 \cdot 10\ (100 + 150) = 67.53\,\text{kN} \end{aligned}$$

[6]In chapter 4.2.4 it was argued that splitting will occur rather than block shear. Nevertheless, the calculation for block shear is included here for sake of completeness.

7.2.2 Steel Components

For the bamboo components, ductile bolt bearing $F_{b,Rd} = 29.10\text{kN}$ is decisive. A modification factor for permanent action $k_{mod} = 0.6$ is adopted from Eurocode 5 [7]. The final design force is:

$$F_{b,Rd,mod} = k_{mod} F_{b,Rd} = 0.6 \cdot 29.10 = 17.46\,\text{kN}$$

The diameter of the threaded rod is chosen to yield with $\gamma_{M0} = 1.0$

$$F_{rod,y,Rd} = \frac{f_y}{\gamma_{M0}} \frac{\pi}{4} D_{rod}^2 \leq F_{b,Rd} \quad \Rightarrow \quad D_{rod} \leq \sqrt{\frac{1746}{235\frac{\pi}{4}}} = 9.7\,\text{mm}$$

$$\rightarrow D_{rod} = 8\,\text{mm}$$

The maximum resistance of the threaded rod is

$$F_{rod,y,Rd} = 11.81\,\text{kN}$$

Each cross dowel can be verified elastically as follows:

shear force: $V_{Ed} = F_{rod}/4 = 11.81/4 = 2.95\,\text{kN}$

shear resistance: $V_{dowel,Rd} = \frac{f_y}{\gamma_{M2}\sqrt{3}} A_v = \frac{235}{1.25\sqrt{3}} 16^2 = 27.79\,\text{kN} > 2.95\,\text{kN}$ okay

bending moment: $M_{Ed} = \frac{F_{rod}}{4} \frac{D_0 - 2t}{2} = \frac{11.81}{4} \frac{100 - 2 \cdot 10}{2} = 118.12\text{kNmm}$

bending resistance: $M_{dowel,Rd} = \frac{f_y W}{\gamma_{M1}} = \frac{235 \cdot d^3/6}{1.1} = 145.84\text{kNmm} > 118.12\text{kNmm}$ okay

It is assumed that stripping of the thread does not occur. Material of sufficient quality needs to be used.

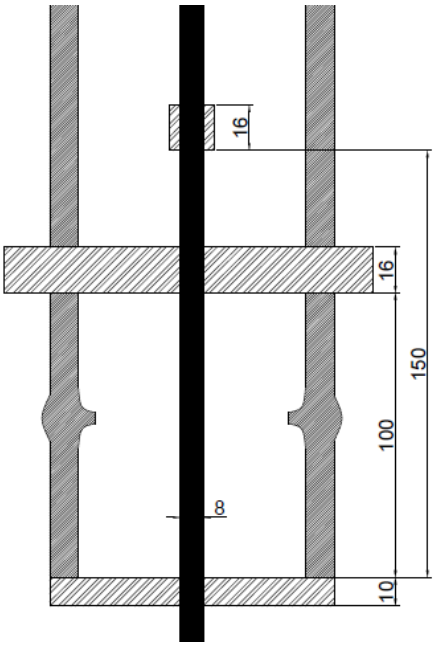

Figure 7.5: Bamboo square cross dowel connector steel components

[7] k_{def} does not need to be applied as creep as a positive influence on compressive strength [36] and it can be assumed that creep also has a positive influence on bearing strength.

7.2.3 Predicted Connector Strength

The connector strength is determined by yielding of the threaded rod. The strength of the entire connector with a 8 mm rod is thus $F_{rod,y,Rd} = 11.81\,\text{kN}$[8].

7.2.3.1 Comparison to Literature

In chapter 2.3, several tensile connectors were presented. The *Phyllostachys pubescens* single bolted joint tested by Fu et al. [29] only reached a tensile strength of 4.2 kN and failed in splitting. The predicted strength of the single lashing joint by Widyowijatnoko [99] made from *Guadua angustifolia* was 19 kN by bearing failure. In experiments, the joint failed in radial crushing and reached a maximum strength of 31 kN to 38 kN.

The predicted bearing strength of the *Phyllostachys pubescens* cross dowel connector proposed as part of this research is $F_{b,Rd} = 29.10\text{kN}$, which is close to the capacity measured by Widyowijatnoko. As the connectors are made of different species, a direct strength comparison makes little sense. In order to find out whether tensile capacity lies in a similar range, the two connectors could be assembled and tested in future research, i.e. by mounting the different connector types at the opposite ends of the same culm. In this context, ease of assembly and work intensity should also be assessed.

7.3 Connection to Dome Hub

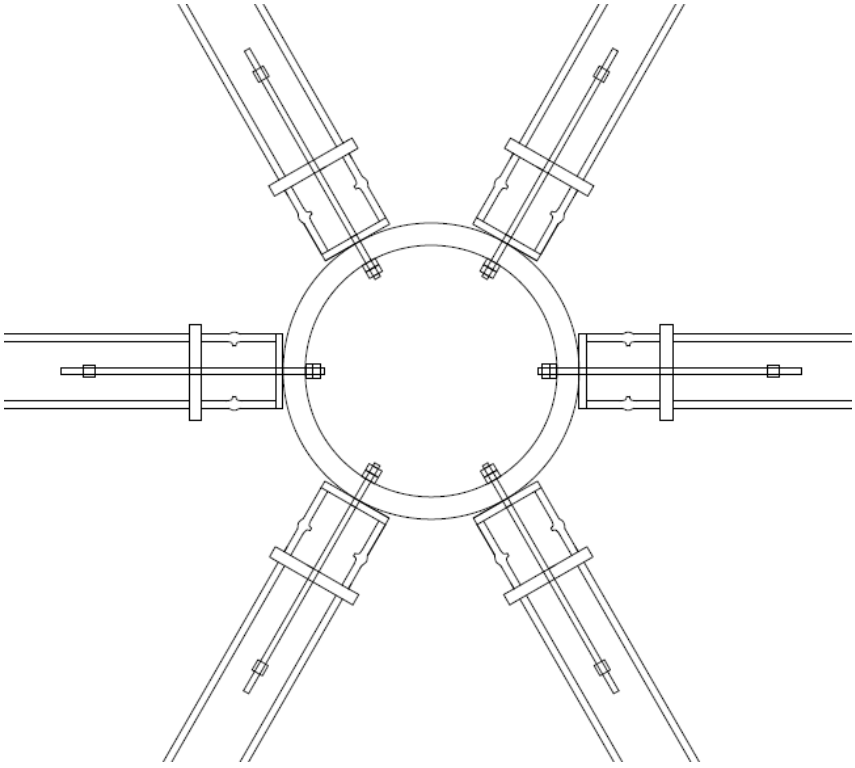

Figure 7.6: Bamboo square cross dowel joints connected to dome hub

The dome hub could be made out of a conical steel ring. Both thickness and strength class of the hub should be chosen so that large deformations of the hub occur prior to yielding of the

[8]This corresponds to a design tensile strut stress of $f_{t,Rd} = \frac{F}{A} = \frac{1181}{2827} = 4.18\,\text{MPa}$ which is used in chapter 8

threaded rod and thus prior to failure of any bamboo component in any manner. Yielding and plastic deformation in the hub is easily recognized and clearly shows if overloading occurs. In case of overloading or damage, the hub can be easily replaced. Alternatively, it can be chosen that yielding of the threaded rod is decisive. This is also recognized rather easily and in case of overloading, only the rod needs to replaced and not the entire connector. Assembly becomes easy if a hexagonal socket is cut into the end of the rod. Prior to assembly, the rod is located entirely within the culm. After all struts are fit around a hub, the rods can be extracted with a hex-wrench (Allen key®).

7.4 Discussion and Conclusions

A tensile connector is proposed which makes use of two perpendicular square cross dowels. The decisive failure mechanism in the bamboo culm is bolt bearing which is a ductile failure mode that provides great deformation capacity. The diameter of a threaded steel rod is chosen such that ductile yielding occurs prior to bolt bearing failure. This increases predictability of connector strength and facilitates replacement after overloading, as only the rod needs to be replaced. If connected to a dome hub, the hub can be designed to be the weakest link and show large displacements prior to yielding of the rod. This way, overloading can be easily observed by the user. The strength of the connector can be increased by using a larger dowel diameter d which results in higher embedment strength. Experiments need to be conducted first, as the relationship of bearing strength and dowel diameter is not necessarily linear.

Chapter 8

Case Study

Let's study the following case:

A geodesic dome made out of Moso bamboo is constructed inside an exhibition hall as part of a scientific conference that promotes the advancements in bamboo research. The conference host formulates the following requirements:

- The dome can have a maximum diameter of 20 m, and a height of 5 m. It needs to have an opening with a height of at least 2 m and a bottom width of at least 4 m so that people can enter and exit the dome.
- At the top of the dome, 5 spot lights are installed to illuminate the dome, which weigh 75 kg in total.
- The minimum frequency is $\mathfrak{f} = 4$ to demonstrate the geodesic design, but should not be higher than $\mathfrak{f} = 6$ as making connections is expensive and time consuming.

We can assume the following boundary conditions for the preliminary design:

- As the frequency is well below $\mathfrak{f} = 9$, linear analysis is justifiable in terms of global stability. For tensile strength, positive effects of non-linear material behaviour (yielding of steel rod in connector) can be used as a simplistic counterweight to the negative effects of geometrical non-linearity; if tensile strength is governing, both material and geometry are thus assumed linear-elastic. If local buckling is decisive, GNL analysis is strongly advised for final verification of stresses and strains.
- It is assumed that connections undergo only small, elastic deformation. Therefore, dome nodes (hub connections) are modelled as hinged.
- As neither snow nor wind act on the structure, all loads are permanent and Eurocode 0 theoretically allows for smaller FORM sensitivity factors α (Eurocode 0, C7(4)) [25]. However, care must be taken, as bamboo and steel are employed. Scatter of steel strength is still smaller than scatter of bamboo dead load. Therefore, $\alpha_R = -1.0$ and $\alpha_E = 0.4$ must be employed. This results in a self-weight safety factor of $\gamma_{G,1} = 1.46$, which is close to $\gamma_{G,2} = 1.35$ (spot lights) prescribed by Eurocode 0 (table A1.2(A)) [25].
- $k_{mod} = 0.6$ and $k_{def} = 0.6$ are adopted from Eurocode 5 (table 3.1 and table 3.2) [27] for static permanent load. If variable action was applied (wind, snow), the value of k_{mod} would be more favourable but k_{def} would also be much larger (unfavourable)!

- The strength of the proposed connector with $d = 16$mm square cross dowels and a 8 mm rod is $F_{t,Rd} = 11.81$ kN. This corresponds to a design tensile strut strength of $f_{t,Rd} = F_{t,Rd}/A = 11812/2827 = 4.18$ MPa which is 12% of the culm's tensile design strength.
- Creep has a negative effect on stiffness (Modulus of Elasticity) and tensile strength of bamboo [36]. As tensile strength is governed by yielding of the threaded rod in the tensile connector, k_{def} only needs to be included into E_d .

8.0.1 Input Materials

Table 8.1 displays the model input of material properties. Note that these are design strength values. Density ρ is applied as a mean value as the stresses resulting from self-weight are later multiplied by $\gamma_{G,1}$.

Table 8.1: Material properties case study

property	**unit**	**design value**	γ	k_{mod}	k_{def}
tensile strength [1]	$f_{t,Rd}$ [MPa]	4.18	2.2	0.6	-
compression strength	$f_{c,Rd}$ [MPa]	13.97	1.6	0.6	-
Modulus of Elasticity	E_d [MPa]	2328.5	1.74	-	0.6
property	**unit**	**mean value**			
strut diameter	D_0 [mm]	100.0			
wall thickness	t [mm]	10.0			
beam diameter	D_{CHS} [mm]	130.0			
beam thickness	t_{CHS} [mm]	26.0			
density bamboo	ρ [kg/m^3]	660			

$$f_{t,Rd} = \frac{F_{rod,y,Rd}}{A}; \qquad A = \frac{\pi}{4}\left(D_0^2 - (D_0 - 2t)^2\right);$$

$$f_{c,Rd} = k_{mod}\frac{f_{c,Rk}}{\gamma_{m,c}}; \qquad \gamma_{m,c} = \frac{f_{c,Rk}}{\mu(f_c) + \alpha_R\beta\sigma(f_c)} = 1.6 \quad (\alpha_R = -1.0;\ \text{chapter 7.2})$$

$$E_d = \frac{E_k}{\gamma_{m,E}(1 + k_{def})}; \quad \gamma_{m,E} = 1.74\ (\text{average of } \gamma_{m,i} \text{ from experiments});$$

$$k_{def} = 0.6\ (\text{adopted from EC 5})$$

The buckling resistance of a pinned-pinned bar is calculated according to the British Steel Code BS5950 [103] which is almost similar to Eurocode 3. This is done for convenience as the Robertson Constant a of Moso culms was determined by Yu et al. [103]. Note that it would also be possible to use Eurocode 5, which only leads to a change of denotation. Initial out-of-straightness and second order effects are not considered in this geometrically-linear analysis.

$$f_{cr,Rd} = \pi^2\frac{E_d I}{AL^2}; \quad f_{cc,Rd} = \frac{f_{cr,Rd}f_{c,Rd}}{\Phi + (\Phi^2 - f_{cr,Rd}f_{c,Rd})^{1/2}}$$

$$\Phi = \frac{f_{c,Rd} + f_{cr,Rd}(1+\eta)}{2}; \quad \eta = 0.001\ a(\lambda_1 - \lambda_0); \quad a = 15 \text{ for Moso}$$

$$\lambda_0 = 0.2\pi\sqrt{E_d/f_{c,Rd}}; \quad \lambda_1 = \frac{L}{\sqrt{I/A}}$$

[1] limited by connector capacity

Note that Yu et al. used E_{mean} which is not modified by material safety factors or creep factors. This results in much higher Euler buckling strength $f_{cr,Rd}$ [103]. This case study makes use of $E_d = \frac{E_k}{\gamma_{m,E}(1+k_{def})}$ for two reasons:

1. Using E_d instead of E_{mean} is one possibility to apply a safety factor to global buckling and include the effects of creep.

2. Using E_d in the local buckling analysis preserves the comparability of local and global buckling.

Note further that the interaction formula for the compressive local buckling capacity $f_{cc,Rd}$ is based on design strength values ($f_{cr,Rd}$ and $f_{c,Rd}$). This is punishing in comparison to the calculation of other design strength values. However, as several different material safety factors $\gamma_{m,i}$ are employed in this case study, an interaction of strength values needs to be based on design values in order to be consistent[2]. On the upside, resulting utilisation for local buckling μ_{LB} can be directly compared to the utilisation factor μ_{GB} obtained by the global buckling analysis in *Oasys GSA*.

The load safety factor $\gamma_{G,1}$ for self-weight of bamboo struts is based on the density:

$$\gamma_{G,1} = \frac{\rho_d}{\rho_k} = 1.46; \quad \rho_k : 5\% - \text{percentile}; \quad \rho_d = \mu + \alpha_E \beta \sigma; \quad \alpha_E = 0.4$$

For the point load that is introduced by the spot lights, a load safety factor $\gamma_{G,2} = 1.35$ according to Eurocode 0 (table A1.2(A)) is adopted [25]. The actions are then combined in the following manner:

$$X_{Ed} = \gamma_{G,1} G_k + \gamma_{G,2} F_k; \quad \left.\begin{array}{l} G_k \text{ characteristic static dead load (self-weight)} \\ F_k \text{ characteristic static geometrically linear point load} \end{array}\right\}$$

The utilisation factors μ_i are obtained as follows:

$$\mu_t = \frac{f_{t,Ed}}{f_{t,Rd}}; \qquad f_{t,Rd} \text{ is the design strength of the tensile connector}$$

$$\mu_c = \frac{f_{c,Ed}}{f_{c,Rd}};$$

$$\mu_{LB} = \frac{f_{c,Ed}}{f_{cc,Rd}}; \qquad f_{cc,Rd} \text{ as an interaction of } f_{cr,Rd} \text{ and } f_{c,Rd}$$

$$\mu_{GB} = \frac{1}{LF}; \qquad \text{load factor } LF \text{ depends on } E_d \text{ (from GSA analysis)}$$

[2] If one single material safety factor γ_m is used (e.g. for steel or timber constructions where such material safety factors are well established), the author of this thesis suggests that $f_{cc,Rk}$ should be obtained with characteristic values and then reduced by γ_m and k_{mod}.

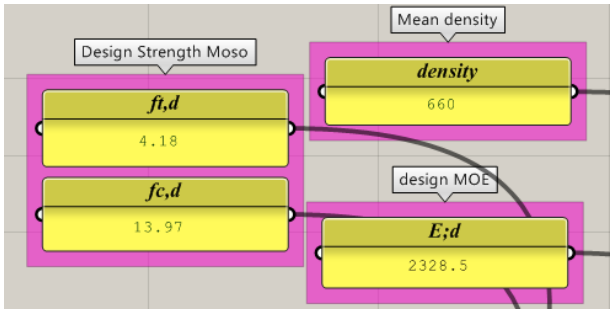

(a) Material properties

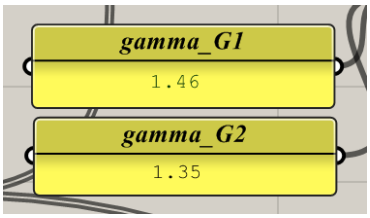

(b) γ_G

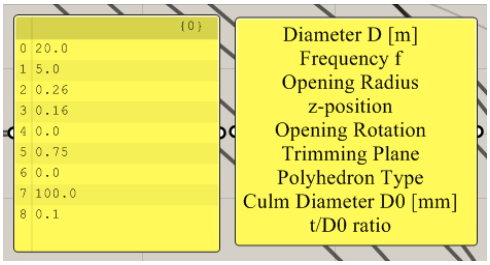

(c) Dome input values

Figure 8.1: Input data

8.0.2 Input Dome Geometry

The dome parameters in the *Grasshopper* model can be determined as follows:

- The dome diameter is $D = 20\,\text{m}$ and the trimming plane is $T = 0.75D$ which results in a height of $20(1 - 0.75) = 5\,\text{m}$.
- The opening radius is chosen $0.26D$ which results in an maximum opening width of $4.1\,\text{m}$ for $z = 0.1$.
- The z-position should be greater than or equal to $z = 0.1D = 2\,\text{m}$ to provide sufficient opening height.

8.0.3 Parametric Study

First, the influence of the frequency is examined. The z-position is adapted later in a parametric study to obtain optimal stress utilisation and displacements.

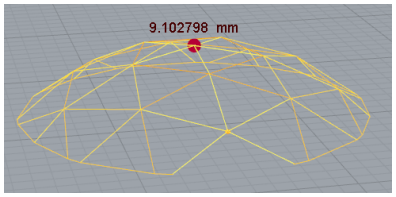

(a) $\mathfrak{f} = 4$

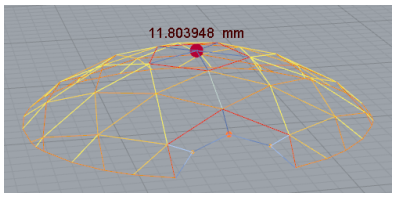

(b) $\mathfrak{f} = 5$

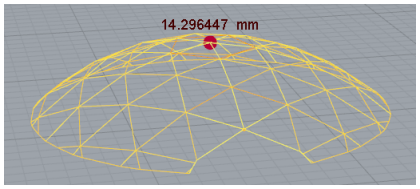

(c) $\mathfrak{f} = 6$

Figure 8.2: Displacement and stresses for $z = 0.1D = 2\,\text{m}$ and opening width $4.1\,\text{m}$

The results are shown in table 8.2.

Table 8.2: Results frequency

frequency	μ_t	μ_c	μ_{LB}	μ_{GB}	δ [mm]
$\mathfrak{f} = 4$	0.538	0.253	**0.733**	0.133	9.1
$\mathfrak{f} = 5$	0.102	0.070	0.141	**0.178**	11.8
$\mathfrak{f} = 6$	**0.609**	0.279	0.388	0.399	14.3

Obviously, frequency $\mathfrak{f} = 5$ results in the smallest utilization factors. We will thus proceed with this frequency. In a next step, the z-position is varied to find a compromise between displacement and tensile stresses. The results are shown in table 8.3.

Table 8.3: Results z-position $\mathfrak{f} = 5$

z	μ_t	μ_c	μ_{LB}	μ_{GB}	δ [mm]
0.10	0.102	0.070	0.142	0.178	11.8
0.11	0.135	0.084	0.170	0.179	11.7
0.12	0.165	0.096	0.196	0.179	11.6
0.13	0.199	0.111	0.225	0.229	11.5
0.14	0.239	0.128	0.259	0.418	11.8
0.15	0.789	0.352	0.714	0.355	11.1
0.16	0.149	0.103	0.210	0.179	10.8
0.17	0.213	0.129	0.261	0.181	10.4
0.18	0.282	0.153	0.311	0.184	11.9
0.19	0.405	0.172	0.349	0.762	**120.3**
0.20	0.414	0.209	0.423	0.333	18.5

Apparently, $z = 0.19$ results in very large displacements which hints to a loose node in the model. In practice, often displacements in SLS become critical and not the utilisation of strength in ULS. In our case, $z = 0.16$ and $z = 0.17$ result in the smallest displacements. In terms of tensile strength utilisation, $z = 0.16$ performs much better than $z = 0.17$ and the other utilisation factors are also smaller. If for example, an additional membrane should be attached to the dome or the point load becomes heavier, we are on the safe side if we choose $z = 0.16$!

8.0.4 Verification ULS

The final design and strength utilisation factors in ULS are indicated in table 8.4.

Table 8.4: Results $\mathfrak{f} = 5; z = 0.16$

$\mathfrak{f}$	z	μ_t	μ_c	μ_{LB}	μ_{GB}	δ [mm]
5	0.16	0.149	0.103	0.210	0.179	10.8

All unity checks in ULS are met. However, as local buckling is governing, an addition GNL analysis should be conducted!

8.0.5 Verification SLS

Another important aspect is the verification of displacements in SLS and the practicality of the design as shown in figure 8.3.

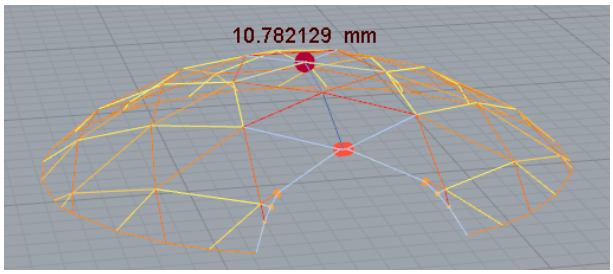

Figure 8.3: Displacement and stresses for $z = 0.16D$

We can state the following:

- The maximum length of struts is $L = 2.62\,\text{m}$ which does not exceed the length of a normal sized bamboo culm.
- The maximum ULS displacement at the top of the dome is 10.78mm. The true dome diameter is $D_{true} = 12.936\,\text{m}$. The displacement is thus $\frac{10.78}{12936} = 0.83\%$ of the true dome diameter, which is a very acceptable displacement.
- For SLS verification, it is allowed to use the mean value of E_{global} which results in $E_{global} = 1.19E_{3pt} = 1.19 \cdot 8570 = 10198.3\text{MPa}$. Additionally, the load safety factors can be reduced to $\gamma_G = 1.0$ (we can simply divide by 1.35 to be conservative). The SLS deflection is then only $E_d/E_{global} \cdot \delta/1.35 = 2328.5/10198.3 \cdot 10.78/1.35 = 1.82\text{mm}$ which corresponds to $\frac{2.46}{2620} = 0.07\%$ of a strut length. Obviously, there is large safety margin in case the dead load is increased, e.g. by a membrane or heavier point load.
- Note that in practice, displacements become larger if connector stiffness and geometrical non-linearity are considered.

8.0.6 Next Steps and Conclusions

In a next step, the model can be exported to *Oasys GSA* to perform a detailed analysis. The stresses in the steel edge beams can be extracted and the beams can be dimensioned accordingly. For the given circular hollow section, the axial stresses in the steel beams are smaller than the maximum strut stresses. As the yield strength of S235 is much higher than the strength of Moso bamboo, a detailed structural analysis of the steel beams does not need to be performed at this point.

At this preliminary design stage, all unity checks are met and the construction is safe. Prior to construction, a detailed structural analysis including the steel elements and connections (e.g. dome hub and welds in steel beams) needs to be performed. Limited stiffness of connectors must be modelled accordingly. Initial out-of-straightness of culms should be considered and a GNL analysis should be conducted.

With respect to the research questions of chapter 1.3, it could be shown that it is possible to design a bolted tensile connector that avoids splitting and provides sufficient strength and ductility for geodesic dome application. The main limiting parameters in real life application are tensile connector strength (e.g. $z = 0.15$, table 8.3) and stability (e.g. local $z = 0.17$ and global $z = 0.10$). Care should be taken, that global buckling does not occur. If local buckling is governing, a GNL analysis needs to be conducted; alternatively, a higher frequency can be chosen to reduce strut length. If tensile connector strength is governing, the cross dowel diameter d can be increased or different dome parameters can be chosen that reduce tensile stresses.

Figure 8.4a shows the final design as retrieved from *Grasshopper*. Note that the shape of the opening can be improved (figure 8.4c) which results in more efficiency, less joints and a better stress distribution.

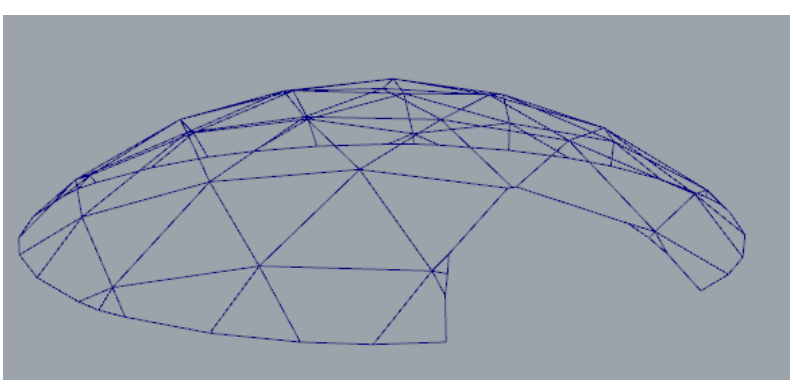

(a) perspective view

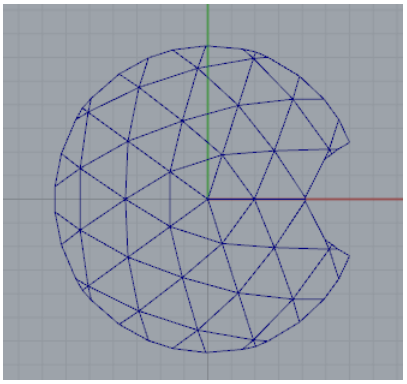

(b) top view

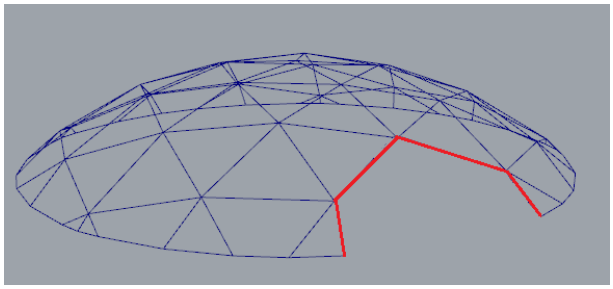

(c) improved design

Figure 8.4: Design of bamboo geodesic dome

This case study has shown, that a parametric model is very useful to obtain an optimized preliminary design. General rules of thumb concerning stability and geometrical non-linearity are handy when making a first guess of the required frequency. If the geodesic dome model is equipped with a user-friendly interface, it can become a useful tool for dome designers. After sufficient testing, the bamboo tensile connector is also suited for practice application – in geodesic domes or other structures.

Chapter 9

Conclusions and Future Work

9.1 Contributions

In the present Master of Science final project, a parametric geodesic dome model was designed using the graphical algorithm editor *Grasshopper* which is a plug-in of the 3D CAD software *Rhinoceros*. The model offers variation of the polyhedron type (e.g. icosahedron, octahedron or tetrahedron), dome frequency $\mathfrak{f}$ (number of subdivisions of the polyhedron's initial surfaces), dome diameter D, and the introduction of elliptical openings. The structural analysis includes the load cases self-weight, a point load on top of the dome, superimposed dead load by dome cladding, and snow and wind load. Additionally, geometrical non-linearity and local and global stability can be analysed. Material input data can be based on mean strength values or design strength values, including partial safety factors and design strength of individual components, i.e. tensile connectors. The model allows for combination of load cases, including non-linear and stability cases, and performs unity checks for dome strut stresses and deflections. All results can be exported graphically as *JPEG* and numerically in an *Excel* file.
As a result of the model analysis, rules of thumb were derived for the maximum possible dome diameter of half-spherical icosahedron-based geodesic domes made of *Guadua angustifolia* and *Phyllostachys pubescens* loaded by self-weight and point load, the latter including non-linearity. For this purpose, relationships between the strut length, dome diameter and frequency were established. For both load cases, a manual linear local buckling analysis was performed and confirmed by model calculation, and exact formulas for the maximum dome diameter governed by local buckling were derived. Additionally, a material independent formula for the transition point of local to global buckling was derived for circular hollow sections with different t/D_0 ratios (t wall thickness, D_0 outer diameter). For both load cases, formulas for the maximum dome frequency $\mathfrak{f}_{max}$ were established below which global buckling does not occur. Furthermore, stability of geodesic domes and shells was compared, and it was found that geodesic domes of a frequency $\mathfrak{f} \geq 4$ are superior to shells in terms of self-weight induced buckling. Last but not least, a formula was derived that indicates how the top part of a shell can be replaced by geodesic dome struts in order to safely introduce point loads to the shell membrane.

Experiments were conducted to determine the dynamic Modulus of Elasticity, and full-culm compression strength and stiffness of *Guadua angustifolia* and *Phyllostachys pubescens*. Linear relationships were established between density and dynamic Modulus of Elasticity, compression Modulus of Elasticity, and compression strength. Additionally, the behaviour of bolted connections in full-culm *Phyllostachys pubescens* was examined by determination of the bolt bearing and splitting strength in a single bolt test with square and round bolts. It was found that square bolts are superior to round bolts of the same diameter in terms of failure mode and deformation capacity. A tensile connector with square cross dowels was proposed which avoids splitting and whose governing failure mode is ductile bolt embedment. Special focus was paid to the influence

of nodes on compression strength and stiffness, and bolt bearing and splitting capacity. For this purpose, a 3D scan (ESEM) and electron microscopy of the nodes of *Guadua angustifolia* and *Phyllostachys pubescens* were conducted, showing that some nodal fibre strands deviate from the orthotropic orientation, and that fibre strands and single fibres bifurcate; this confirms previous findings of other research groups. In experiments it was found that nodes increase bolt bearing, splitting, and local compression strength owing to radial and tangential fibres in the node. On a larger scale, full-culm compression strength is decreased due to stress concentrations induced by the change of culm geometry in the nodal region. Full-culm compression stiffness is also negatively impacted by nodes as vascular bundles in non-axial nodal fibres are compressed easily.

9.2 Conclusions

A parametric structural analysis of bamboo geodesic domes was performed, assessing the influence of openings and local and global stability of domes constructed with *Guadua angustifolia* and *Phyllostachys pubescens*. It can be concluded that non-symmetrical openings result in high strut stress-concentrations that are reduced with increasing frequency ϧ; a preliminary parametric study and subsequent manual design adaptation are advisable in all cases. In terms of stability, global buckling does not occur for half-spherical icosahedron-based domes loaded in self-weight, unless a frequency 27 for *Guadua angustifolia* and a frequency 25 for *Phyllostachys pubescens* is exceeded. For point load, this frequency depends on magnitude and application of the load. The respective maximum possible dome diameters were 475.4m in self-weight and 337.0m for a 1 kN point load on top of the dome for *Guadua angustifolia* (geometrically non-linear analysis). For *Phyllostachys pubescens* they were 331.1m in self-weight and 125.4m for a 1 kN point load. These conclusions are based on mean strength values, a linear-elastic material and don't take connector strength into account.

Nodes have a negative influence on full-culm compression strength and compressive Modulus of Elasticity, although the compressive strength of the node itself is higher than the strength of clear specimens. For *Phyllostachys pubescens* a mean compression strength of 49.9 MPa and mean compression Modulus of Elasticity of 7746 MPa were found for clear specimens, respectively 47.5 MPa and 6817 MPa for specimens with nodes. For *Guadua angustifolia* the values were 60.7 MPa and 9845 MPa for clear specimens, respectively 58.6 MPa and 9082 MPa for specimens with nodes. These findings can be attributed to change of culm geometry around nodes and nodal microstructure. The dynamic Modulus of Elasticity was established by vibrational measurements and a mean value of 11 431 MPa was found for *Phyllostachys pubescens* and 19 681 MPa for *Guadua angustifolia*. Linear relationships between density and dynamic Modulus of Elasticity, and density and compressive strength and Modulus of Elasticity were found for both species, which suggests that fibre content and density are correlated. Yet, a relationship between static and dynamic Modulus of Elasticity still needs to be established.

Nodes have a positive influence on bolt embedment and splitting strength of *Phyllostachys pubescens*. Square bolts result in a more favourable failure mechanism than round bolts: Square bolts fail in large displacements and embedment, whereas round bolts fail in tensile splitting after small embedment. The strength values for round bolts were a mean embedment strength of 55.4 MPa for clear specimens and 62.6 MPa for specimens with nodes. For square bolts the values were 52.7 MPa for clear specimens and 54.3 MPa for specimens with nodes; whereas in the latter, the bolt was located too far from the node to reflect the nodal influence. Bolt splitting strength was only established for round bolts, resulting in a mean strength of 18.2 MPa for clear specimens and 20.9 MPa for specimens with nodes. No relationship could be established for density and bolt embedment or splitting strength. All findings agreed with results from microscopic analysis of the node.

9.2.1 Answers to Research Questions

The research questions are answered briefly; more information is provided in the referenced chapters.

Q1: What are the limiting parameters in the design of bamboo geodesic domes and can a maximum diameter be derived?
Answer: The limiting factor is often the strength of tensile connectors. If a sufficiently strong tensile connector is used, e.g. the one proposed in this research, local buckling of dome struts becomes limiting, unless very high dome frequencies are reached, in which case global buckling becomes decisive for self-weight and a single point load on top of the dome (chapter 5).

Q2: Does a limiting diameter exist for bamboo geodesic domes made of *Guadua angustifolia* and *Phyllostachys pubescens* (if connector strength is not taken into account) and what parameters are decisive?
Answer: There is a definite limit ratio of dome diameter to culm outer diameter for both examined load cases (D_{max}/D_0). The maximum dome diameter D_{max} is reached for a certain maximum frequency $\mathfrak{f}_{max}$, where the dome fails in simultaneous local and global buckling. D_{max} and $\mathfrak{f}_{max}$ depend on the load case, magnitude of the load, material, and the ratio of culm wall thickness and culm outer diameter(t/D_0). For the given material the limiting diameters are (chapter 5):
Guadua angustifolia: 475.4 m in self-weight and 337.0 m for a 1 kN point load on top of the dome, geometrically non-linear (applied in discrete load steps with large deformation enabled; e.g. a heavy construction worker standing on top of the dome).
Phyllostachys pubescens: 331.1 m in self-weight and 125.4 m for a 1 kN point load on top of the dome, geometrically non-linear.

Q3: Is it possible to determine boundary conditions under which global buckling does not occur and is linear superposition then possible?
Answer: Yes. For both examined load cases, maximum frequencies $\mathfrak{f}_{max}$ can be derived below global buckling does not occurs (as local buckling is decisive). Linear superposition is then possible for **linear** load cases (chapter 5).

Q4: What is the effect of opening size and position on the maximum strut stresses in bamboo geodesic dome struts?
Answer: Under certain conditions, very high strut stresses will occur which can lead to tensile connector failure or strut buckling. Especially if openings are inserted non-symmetrically, a preliminary parametric study of different opening shapes is advisable as no general rules of thumb can be derived (chapter 5).

Q5: What is the effect of nodes on compression capacity?
Answer: Compression strength and Modulus of Elasticity are decreased by nodes (about 5% and 10% respectively). This finding agrees with the findings from microstructural investigations (chapter 4.2.3).

Q6: What is the effect of nodes on bearing and splitting capacity of bolted connections?
Answer: The splitting and bearing capacity are increased by nodes as they work as natural reinforcement. This finding agrees with the findings from microstructural investigations (chapter 4.2.4).

Q7: What influence does the shape of the bolt (round or square) have?
Answer: A square configuration allows for large ductile displacements in embedment. This is more favourable than round bolts, which induce tensile splitting after comparatively little displacement (chapter 4.2.4).

Q8: Is it possible to suggest a bolted tensile connector that avoids splitting and provides sufficient strength and ductility for geodesic dome application?

Answer: Yes, it is possible to suggest such a bolted tensile connector, namely a connector with square bolts (chapter 7).

Q9: What are the main limiting parameters in real life application (including limited tensile connector strength) and how can bamboo geodesic dome performance be generally improved?
Answer: The main limiting parameters are stability and tensile strength of connectors. The latter can be improved by using square bolted connections that make use of wide bolts close to nodes. The former requires a dome frequency smaller $\mathfrak{f}_{max}$ in order to avoid global buckling (chapter 8).

9.3 Future Work

Suggestions for future research were made in the respective chapters. This is a summary of all suggestions:

- In the present experiments, the bottom load plate configuration prevented block shear. If a gap is introduced in the load plate, it can be investigated whether block shear actually occurs, and what influence nodes have.
- The nodal region was not reached by the displaced square bolts. If the bolts are placed closer to the node, the effect of nodes on square bolt bearing capacity can be examined.
- Different square and round bolt diameters d could be applied to derive a relationship between bolt diameter and embedment strength.
- A FEM based on fracture mechanics could be created to simulate bolt bearing and splitting, and related stress concentrations. For this purpose, $K_{II,C}$ and $K_{III,c}$ of clear and nodal bamboo should be derived from experiments.
- In the present research, only *Phyllostachys pubescens* was included in the bolt experiments. In a next step, *Guadua angustifolia* could be examined.
- In terms of connector strength, the next step is the assembly and testing of the full connector. For this purpose, the steel rod should still be under-matched as this permits most accurate strength prediction.
- With the present model, a systematic global buckling analysis due to point load and self-weight should be conducted for variation of $\mathfrak{f}$, D_0, t, ρ, E, and F. Subsequently, the nature of the global buckling curve can be determined and an expression can be derived for the maximum possible diameter due to global buckling of geodesic domes $D_{max,GB} = f(\mathfrak{f}, D_0, t, \rho, E)$. For self-weight and $\mathfrak{f} \to \infty$, the expression of $D_{max,GB}$ should converge with the expression for shells $D_{max,Shells}$.
- In a next step, the load cases superimposed dead load, wind and snow could be analysed in detail and formulas for transition of local to global buckling and limit diameters could be derived. Additionally, seismic load could be added to the model.

Bibliography

[1] Bamboos Current Research 2/3. In I.V. Ramanuja Rao, R. Gnanaharan, and Cherla B. Sastry, editors, *Proceedings of the International Bamboo Workshop held in Cochin, India*, pages 127–261, 1988.

[2] Bamboos Current Research 3/3. In I.V. Ramanuja Rao, R. Gnanaharan, and Cherla B. Sastry, editors, *Proceedings of the International Bamboo Workshop held in Cochin, India*, pages 262–395, 1988.

[3] Shigeyasu Amada, Yoshinobu Ichikawa, Tamotsu Munekata, and Hiroyuki Shimizu. Fiber texture and mechanical graded structure of bamboo. *Composites Part B*, 8368(96):13–20, 1997.

[4] Oscar Antonio Arce-Villalobos. *Fundamentals of the Design of Bamboo Structures*. PhD thesis, Eindhoven University of Technology, 1993.

[5] Hector F. Archila-Santos, Martin P. Ansell, and Pete Walker. Low Carbon Construction Using Guadua Bamboo in Colombia. *Key Engineering Materials*, 517:127–134, June 2012. ISSN 1662-9795. doi: 10.4028/www.scientific.net/KEM.517.127. URL `http://www.scientific.net/KEM.517.127`.

[6] L. Brancheriau, H. Bailleres, and D. Guitard. Comparison between modulus of elasticity values calculated using 3 and 4 point bending tests on wooden samples. *Wood Science and Technology*, 36(5):367–383, November 2002. ISSN 0043-7719. doi: 10.1007/s00226-002-0147-3. URL `http://link.springer.com/10.1007/s00226-002-0147-3`.

[7] Robert Roy Britt. The Odds of Dying. pages 1–8, 2005. URL `http://www.livescience.com/3780-odds-dying.html`.

[8] Buckminster Fuller Institute. About Fuller. URL `http://challenge.bfi.org/about-fuller/big-ideas/geodesic-domes`.

[9] J I Cardenas. Elastic Module Study of the Radial Section of Guadua angustifolia Kunth Variety Bicolor. *Advances in Materials Science and Engineering*, 2014:1–6, 2014.

[10] Kai Chen and Lian Chun Long. Analysis of the Effects of Fiber Gradient Distribution on the Mechanical Properties of Moso Bamboo. *Applied Mechanics and Materials*, 590: 13–18, June 2014. ISSN 1662-7482. doi: 10.4028/www.scientific.net/AMM.590.13. URL `http://www.scientific.net/AMM.590.13`.

[11] K. F. Chung and W. K. Yu. Mechanical properties of structural bamboo for bamboo scaffoldings. *Engineering Structures*, 24(4):429–442, 2001.

[12] Dr. Lynn Clark and Iowa State University. distribution of woody bamboos worldwide [online image], 2005. URL http://www.eeob.iastate.edu/research/bamboo/maps/world-total-woody.gif.

[13] Wikipedia contributors. Favela, 2014. URL http://en.wikipedia.org/w/index.php?title=Favela&oldid=613080462.

[14] Juan Francisco Correal D. and Juliana Arbeláez C. Influence of Age and Height Position on Colombian Guadua Angustifolia Bamboo Mechanical Properties. *Maderas. Ciencia y tecnología*, 12(2):105–113, 2010. ISSN 0718-221X. doi: 10.4067/S0718-221X2010000200005. URL http://www.scielo.cl/scielo.php?script=sci_arttext&pid=S0718-221X2010000200005&lng=en&nrm=iso&tlng=en.

[15] Titulo Corto. Compression resistance and shear strength of Guadua angustifolia culms after drilling of the node diaphragm. *Colombia Forestal*, 17(1):117–124, 2014.

[16] CUR. Probability in Civil Engineering. Technical Report September, 1997.

[17] Tom Davis. Geodesic Domes, 2011. URL http://www.geometer.org/mathcircles.

[18] T. De Jong. Stresses Around Pin-Loaded Holes in Elastically Orthotropic or Isotropic Plates. *Journal of Composite Materials*, 11(3):313–331, July 1977. ISSN 0021-9983. doi: 10.1177/002199837701100306. URL http://jcm.sagepub.com/cgi/doi/10.1177/002199837701100306.

[19] P G Dixon and L J Gibson. The structure and mechanics of Moso bamboo material The structure and mechanics of Moso bamboo material. *Journal of the Royal Society, Interface / the Royal Society*, 11(July), 2014.

[20] R. Drake, R. Morton, and C. Torres-Sanchez. Lessons from India : Bamboo as a solution for low-cost housing in India. 2010.

[21] César Echavarría, Peer Haller, and Alexander Salenikovich. Analytical study of a pin-loaded hole in elastic orthotropic plates. *Composite Structures*, 79(1):107–112, June 2007. ISSN 02638223. doi: 10.1016/j.compstruct.2005.11.038. URL http://linkinghub.elsevier.com/retrieve/pii/S0263822305003752.

[22] S. Elizabeth and a. K. Datta. On the seismic performance of bamboo structure. *Bulletin of Earthquake Engineering*, December 2013. ISSN 1570-761X. doi: 10.1007/s10518-013-9561-1. URL http://link.springer.com/10.1007/s10518-013-9561-1.

[23] Martin Estrada, Dorian L. Linero, and Fernando Ramírez. Constitutive relationship of the fiber cluster of bamboo Guadua angustifolia, determined by means of a Weibull probability function and a model of progressive failure. *Mechanics of Materials*, 63:12–20, August 2013. ISSN 01676636. doi: 10.1016/j.mechmat.2013.04.007. URL http://linkinghub.elsevier.com/retrieve/pii/S016766361300063X.

[24] Jiang et al. Sensitivity of Several Selected Mechanical Properties of Moso Bamboo to Moisture Content Change under the Fibre Saturation Point. *BioResources*, 7(4):5048–5058, 2012.

[25] European Committee for Standardization. NEN-EN 1990. Technical Report december 2002, 2002.

[26] European Committee for Standardization. NEN-EN 383. Technical report, 2012.

[27] European Committee for Standardization. Nen-en 1995-1-1. Technical report, 2014.

[28] David B. Jr Farnsworth. Behaviour of Shell Structures, 1999.

[29] Yu Guang Fu, Ming Yuan Wang, Hai Bo Ge, and Lu Li. Experimental Study of Mechanical Properties of Bamboo's Joints under Tension and Compression Load. *Advanced Materials Research*, 450-451:749–755, January 2012. ISSN 1662-8985. doi: 10.4028/www.scientific.net/AMR.450-451.749. URL http://www.scientific.net/AMR.450-451.749.

[30] María Fernanda García-Aladín, Humberto García, Juan Manuel Mosquera, and José Jaime García. The Importance of Shear in the Deflection of Bamboo Beams. *Key Engineering Materials*, 600:87–96, March 2014. ISSN 1662-9795. doi: 10.4028/www.scientific.net/KEM.600.87. URL http://www.scientific.net/KEM.600.87.

[31] Wang Ge, Chen Hong, Yu Zi-xuan, and Sheldon Q Shi. Tensile Properties Of Bamboo Units In Different Sizes. In *Proceedings of the 55th International Convention of Society of Wood Science and Technology August 27-31, 2012 - Beijing, CHINA*, pages 1–12, 2012.

[32] K Ghavami. Bamboo : Low cost and energy saving construction materials. In *Modern Bamboo Structures*, pages 5–21. Taylor & Francis Group, London, UK, 2008.

[33] K Ghavami, S M Allameh, and W O Soboyejo. multiscale study of bamboo phyllostachys edulis. 2003.

[34] R Gnanaharan, Jules J.A. Janssen, and Oscar Arce. Bending strength of bamboo: Comparison of different testing procedures with a view to standardization. 1994.

[35] Mateo Gutierrez Gonzalez, Caori Patricia Takeuchi, and Michel Córdoba Perozo. Variation of Tensile Strength Parallel to the Fiber of Bamboo Guadua Angustifolia Kunth in Function of Moisture Content. *Key Engineering Materials*, 517:71–75, June 2012. ISSN 1662-9795. doi: 10.4028/www.scientific.net/KEM.517.71. URL http://www.scientific.net/KEM.517.71.

[36] Jennifer Gottron, Kent a. Harries, and Qingfeng Xu. Creep behaviour of bamboo. *Construction and Building Materials*, 66:79–88, September 2014. ISSN 09500618. doi: 10.1016/j.conbuildmat.2014.05.024. URL http://linkinghub.elsevier.com/retrieve/pii/S0950061814004966.

[37] Grosser and Walter Liese. On the Anatomy of Asian Bamboos , with Special Reference to their Vascular Bundles. *Wood Science and Technology*, 5:290–312, 1971.

[38] Kent A. Harries, Bhavna Sharma, and Michael Richard. Structural Use of Full Culm Bamboo: The Path to Standardization. *International Journal of Architecture, Engineering and Construction*, 1(2):66–75, 2012. ISSN 1911110X. doi: 10.7492/IJAEC.2012.008. URL http://www.iasdm.org/journals/index.php/ijaec/article/view/79.

[39] Minjuan He, Zheng Li, Yongliang Sun, and Renle Ma. Experimental investigations on mechanical properties and column buckling behavior of structural bamboo. *The structural design of tall and special buildings*, 2014, 2014. doi: 10.1002/tal.

[40] Cecilie Hestbæ k. Favela Homes , One Layer at a Time, September 2010. URL http://riotimesonline.com/brazil-news/rio-real-estate/favela-homes-one-layer-at-a-time/.

[41] Pierre Hoogenboom. Lecture Notes CIE4143 Shell Analysis, Theoery and Application, 2014. URL http://homepage.tudelft.nl/p3r3s/CT4143_handout_7a.pdf.

[42] Pierre Hoogenboom. Lecture Notes CIE4143 Shell Analysis, Theoery and Application, 2014. URL http://homepage.tudelft.nl/p3r3s/CT4143_handout_12.pdf.

[43] Dong Sheng Huang, Ai Ping Zhou, Hai Tao Li, Yi Su, and Guo Chen. Experimental Study on the Tensile Properties of Bamboo Related to its Distribution of Vascular Bundles. *Key Engineering Materials*, 517:112–117, June 2012. ISSN 1662-9795. doi: 10.4028/www.scientific.net/KEM.517.112. URL http://www.scientific.net/KEM.517.112.

[44] Yan-hui Huang, Ben-hua Fei, Yan Yu, and Rong-jun Zhao. Plant Age Effect on Mechanical Properties of Moso Bamboo (Phyllostachys Heterocycla var. Pubescens) Single Fibers. *Wood and Fiber Science*, 44(2):196–201, 2012.

[45] Pieter Huybers. Construction Drawings of an improved wire lacing tool, 1997.

[46] JJA Janssen. *Bamboo in Building Structures*. Phd thesis, Eindhoven University of Technology, 1981.

[47] Jules J A Janssen. Designing and Building with Bamboo. Technical report, INBAR, Eindhoven, 2000.

[48] Jules J A Janssen. International Standards for Bamboo as a Structural Material. *Structural Engineering International*, 1 / 2005:49, 2005.

[49] D.L. Janyanetti and P.R. Follet. Bamboo in Construction: An Introduction. Technical report, INBAR, 1998.

[50] D L Jayanetti and P R Follett. Bamboo in construction. In *Modern Bamboo Structures*, pages 23–32. Taylor & Francis Group, London, UK, 2008.

[51] Simon Kraft. Statische Berechnung einer Bambuskuppel, 2013.

[52] Marek Kubik. Structural Analysis of Geodesic Domes, 2009.

[53] Aakash Kushwaha. Fabrication and Elemental Characterization of Multipurpose Dismountable Bamboo Geodesic Dome, 2012.

[54] Hongbo Li and Shengping Shen. The mechanical properties of bamboo and vascular bundles. *Journal of Materials Research*, 26(21):2749–2756, October 2011. ISSN 0884-2914. doi: 10.1557/jmr.2011.314. URL http://www.journals.cambridge.org/abstract_S0884291411003141.

[55] Walter Liese. The Anatomy of Bamboo Culms. Technical report, INBAR, 1998.

[56] Cheng-Jung Lin, Ming-Jer Tsai, and Song-Yung Wang. Nondestructive evaluation techniques for assessing dynamic modulus of elasticity of moso bamboo (Phyllosachys edulis) lamina. *Journal of Wood Science*, 52(4):342–347, March 2006. ISSN 1435-0211. doi: 10.1007/s10086-005-0772-1. URL http://link.springer.com/10.1007/s10086-005-0772-1.

[57] Tommy Y Lo, H.Z Cui, and H.C Leung. The effect of fiber density on strength capacity of bamboo. *Materials Letters*, 58(21):2595–2598, August 2004. ISSN 0167577X. doi: 10.1016/j.matlet.2004.03.029. URL http://linkinghub.elsevier.com/retrieve/pii/S0167577X04002149.

[58] Tommy Y. Lo, H. Z. Cui, P. W C Tang, and H. C. Leung. Strength analysis of bamboo by microscopic investigation of bamboo fibre. *Construction and Building Materials*, 22 (7):1532–1535, July 2007. ISSN 09500618. doi: 10.1016/j.conbuildmat.2007.03.031. URL http://linkinghub.elsevier.com/retrieve/pii/S0950061807000943.

[59] Patricia Luna, Jorge Lozano, Caori Patricia Takeuchi, and Mateo Gutierrez. Experimental Determination of Allowable Stresses for Bamboo Guadua Angustifolia Kunth Structures. *Key Engineering Materials*, 517:76–80, June 2012. ISSN 1662-9795. doi: 10.4028/www.scientific.net/KEM.517.76. URL http://www.scientific.net/KEM.517.76.

[60] Fitri Mardjono. *A Bamboo Building Design Decision Support Tool*. PhD thesis, Eindhoven University of Technology, 2002.

[61] Gopal Mishra. types of instability. URL http://theconstructor.org/wp-content/uploads/2010/03/clip_image0047.jpg.

[62] Derek R Mitch. Splitting Capacity Characterization of Bamboo Culms, 2009.

[63] Luis Eustáquio Moreira and Khosrow Ghavami. Limits States Analysis for Bamboo Pin Connections. *Key Engineering Materials*, 517:3–12, June 2012. ISSN 1662-9795. doi: 10.4028/www.scientific.net/KEM.517.3. URL http://www.scientific.net/KEM.517.3.

[64] Fumio Nogata and Hideaki Takahashi. Intelligent functionally graded material. *Composttes Engineering*, 5(7):743–751, 1995.

[65] S K Paudel. Engineered bamboo as a building material. In *Modern Bamboo Structures*, pages 33–40. Taylor & Francis Group, London, UK, 2008.

[66] Fernando Ramirez, Juan F Correal, Luis E Yamin, Juan C Atoche, and Carlos M Piscal. Dowel-Bearing Strength Behavior of Glued Laminated Guadua Bamboo. *Journal of Materials in Civil Engineering*, (November):1378–1387, 2012. doi: 10.1061/(ASCE)MT.1943-5533.0000515.

[67] G.J.P. Ravenshorst and J.W.G van de Kuilen. Relationships between local, global and dynamic modulus of elasticity for soft- and hardwoods, 2009.

[68] a. K. Ray, S. K. Das, S. Mondal, and P. Ramachandrarao. Microstructural characterization of bamboo. *Journal of Materials Science*, 39(3):1055–1060, February 2004. ISSN 0022-2461. doi: 10.1023/B:JMSC.0000012943.27090.8f. URL http://link.springer.com/10.1023/B:JMSC.0000012943.27090.8f.

[69] Michael J Richard. *Assessing the Performance of Bamboo Structural Components*. Phd thesis, University of Pittsburgh, 2013.

[70] Dan Ridley-ellis, John Moore, and Aamir Khokhar. Random acts of elasticity : MoE , G and EN408. (April):2–6, 2009.

[71] Gustavo Rivera Jr. Favelas, Public Housing and the Reconfiguration of Urban Space in Brazilian Slums. *The Urban Reinventors Paper Series*, 2009(3):1–13, 2009.

[72] RWTH Aachen. Bamboo as a building material, 2002.

[73] RWTH Aachen. ZERI Pavillon auf der EXPO 2000, 2002. URL http://bambus.rwth-aachen.de/de/PDF-Files/ZERIPavillonEXPO2000-Version2.pdf.

[74] Jay Salsburg. Geodesic Math.

[75] Mauro Sassu, Marco Andreini, Anna De Falco, and Linda Giresini. Bamboo Trusses with Low Cost and High Ductility Joints. *Open Journal of Civil Engineering*, 2012(December):229–234, 2012.

[76] Stéphane Schröder. Bamboo Species of Brazil, 2009. URL http://www.guaduabamboo.com/blog/bamboo-species-of-brazil.

[77] Z P Shao, L Zhou, Y M Liu, Z M Wu, and C Arnaud. Differences in Structure and Strength between Internode and Node Sections of Moso Bamboo. *Journal of Tropical Forest Science 22(2):*, 22(2):133–138, 2010.

[78] Zhuo-Ping Shao, Chang-Hua Fang, Sheng-Xia Huang, and Gen-Lin Tian. Tensile properties of Moso bamboo (Phyllostachys pubescens) and its components with respect to its fiber-reinforced composite structure. *Wood Science and Technology*, 44(4):655–666, November 2009. ISSN 0043-7719. doi: 10.1007/s00226-009-0290-1. URL `http://link.springer.com/10.1007/s00226-009-0290-1`.

[79] Zhuo-Ping Shao, Chang-Hua Fang, and Gen-Lin Tian. Mode I interlaminar fracture property of moso bamboo (Phyllostachys pubescens). *Wood Science and Technology*, 43(5-6):527–536, June 2009. ISSN 0043-7719. doi: 10.1007/s00226-009-0265-2. URL `http://link.springer.com/10.1007/s00226-009-0265-2`.

[80] B Sharma, D Mitch, K a Harries, K Ghavami, and G Kharel. Pushover behaviour of bamboo portal frame structure. *International Wood Products Journal*, 2(1):20–28, May 2011. ISSN 2042-6445. doi: 10.1179/2042645311Y.0000000003. URL `http://www.maneyonline.com/doi/abs/10.1179/2042645311Y.0000000003`.

[81] Bhavna Sharma. *Seismic Performance of Bamboo Structures*. Phd thesis, University of Pittsburgh, 2010.

[82] Emilio Carlos Nelli Silva, Matthew C. Walters, Glaucio H. Paulino, Marek-Jerzy Pindera, Robert H. Dodds, Fernando a. Rochinha, Eshan Dave, and Linfeng Chen. Modelling Bamboo as a Functionally Graded Material. *AIP Conference Proceedings*, 973:754–759, 2008. ISSN 0094243X. doi: 10.1063/1.2896876. URL `http://scitation.aip.org/content/aip/proceeding/aipcp/10.1063/1.2896876`.

[83] Kjell Helge Solli. Modulus of elasticity - local or global values. *CIB W18 paper 33-10-3*, 408:1–6, 1999.

[84] Suwat Sutanun. Macroscopic and Microscopic Gradient Structures of Bamboo Culms. *Walailak Journal Science & Technology*, 2(1):81–97, 2005.

[85] David Trujillo. Bamboo structures in Colombia. *The Structural Engineer*, (March), 2007.

[86] David Trujillo. Prospects for a method to infer non-destructively the strength of bamboo : a research proposal. In *Third International Conference on Sustainable Construction Materials and Technologies*, 2013.

[87] Takashi Tsubaki and Takato Nakano. Creep behavior of bamboo under various desorption conditions. *Holzforschung,*, 64:489–493, 2010. doi: 10.1515/HF.2010.085.

[88] Twisp. Three fracture modes, 2008. URL `http://commons.wikimedia.org/wiki/File:Fracture_modes_v2.svg#mediaviewer/File:Fracture_modes_v2.svg`.

[89] UN-HABITAT. Share of urban population living in slums [online image], 2003. URL `http://www.unmillenniumproject.org/documents/map_3.gif`.

[90] UN-HABITAT. Land and Housing, 2014. URL `http://mirror.unhabitat.org/categories.asp?catid=277`.

[91] Peter De Vries. Zicht op Dunningshout, 2000.

[92] A.C.W.M. Vrouwenvelder and J.K. Vrijling. Probabilistisch ontwerpen. pages 3–5. TU Delft.

[93] Arend Van Waart. Exploring structural design, 2012.

[94] Fuli Wang, Zhuoping Shao, and Yijun Wu. Mode II interlaminar fracture properties of Moso bamboo. *Composites Part B: Engineering*, 44(1):242–247, January 2013. ISSN 13598368. doi: 10.1016/j.compositesb.2012.05.035. URL http://linkinghub.elsevier.com/retrieve/pii/S1359836812003617.

[95] Fuli Wang, Zhuoping Shao, Yijun Wu, and Dong Wu. The toughness contribution of bamboo node to the Mode I interlaminar fracture toughness of bamboo. *Wood Science and Technology*, October 2013. ISSN 0043-7719. doi: 10.1007/s00226-013-0591-2. URL http://link.springer.com/10.1007/s00226-013-0591-2.

[96] Hankun Wang, Wanju Li, Dan Ren, Zixuan Yu, and Yan Yu. A two-variable model for predicting the effects of moisture content and density on compressive strength parallel to the grain for moso bamboo. *Journal of Wood Science*, July 2014. ISSN 1435-0211. doi: 10.1007/s10086-014-1419-x. URL http://link.springer.com/10.1007/s10086-014-1419-x.

[97] Hao Wang, Hankun Wang, Wanju Li, Dan Ren, and Yan Yu. Effects of Moisture Content on the Mechanical Properties of Moso Bamboo at the Macroscopic and Cellular Levels. *BioResources*, 8(4):5475–5484, 2013.

[98] Dongsheng Wei, Olaf Schmidt, and Walter Liese. Durability test of bamboo against fungi according to EN standards. *European Journal of Wood and Wood Products*, 71(5):551–556, June 2013. ISSN 0018-3768. doi: 10.1007/s00107-013-0707-2. URL http://link.springer.com/10.1007/s00107-013-0707-2.

[99] Andry Widyowijatnoko. *Traditional and Innovative Joints in Bamboo Construction*. Phd thesis, RWTH Aachen, 2012.

[100] Dongwei Yu, Hongwei Tan, and Yingjun Ruan. A future bamboo-structure residential building prototype in China: Life cycle assessment of energy use and carbon emission. *Energy and Buildings*, 43(10):2638–2646, October 2011. ISSN 03787788. doi: 10.1016/j.enbuild.2011.06.013. URL http://linkinghub.elsevier.com/retrieve/pii/S0378778811002623.

[101] H Q Yu, Z H Jiang, C Y Hse, and T F Shupe. Selected Physical and Mechanical Properties of Moso Bamboo (Phyllostachys pubescens). *258 Journal of Tropical Forest Science*, 20 (4):258–263, 2008.

[102] Huaqiang Yu, Benhua Fei, Haiqing Ren, Zehui Jiang, and Xing'e Liu. Variation in tensile properties and relationship between tensile properties and air-dried density for moso bamboo. *Frontiers of Forestry in China*, 3(1):127–130, March 2008. ISSN 1673-3517. doi: 10.1007/s11461-008-0008-9. URL http://link.springer.com/10.1007/s11461-008-0008-9.

[103] W. K. Yu, K. F. Chung, and S. L. Chan. Column buckling of structural bamboo. *Engineering Structures*, 25(6):755–768, May 2003. ISSN 01410296. doi: 10.1016/S0141-0296(02)00219-5. URL http://linkinghub.elsevier.com/retrieve/pii/S0141029602002195.

Appendix A

Geodesic Dome Model

A.1 Interaction of Components

Basic information on *Grasshopper* can be found on http://www.grasshopper3d.com/:

"For designers who are exploring new shapes using generative algorithms, Grasshopper® is a graphical algorithm editor tightly integrated with Rhino's 3-D modelling tools. Unlike RhinoScript, Grasshopper requires no knowledge of programming or scripting, but still allows designers to build form generators from the simple to the awe-inspiring."

The interaction of different plug-ins and components is described in chapter 5. The flow chart below illustrates this interaction.

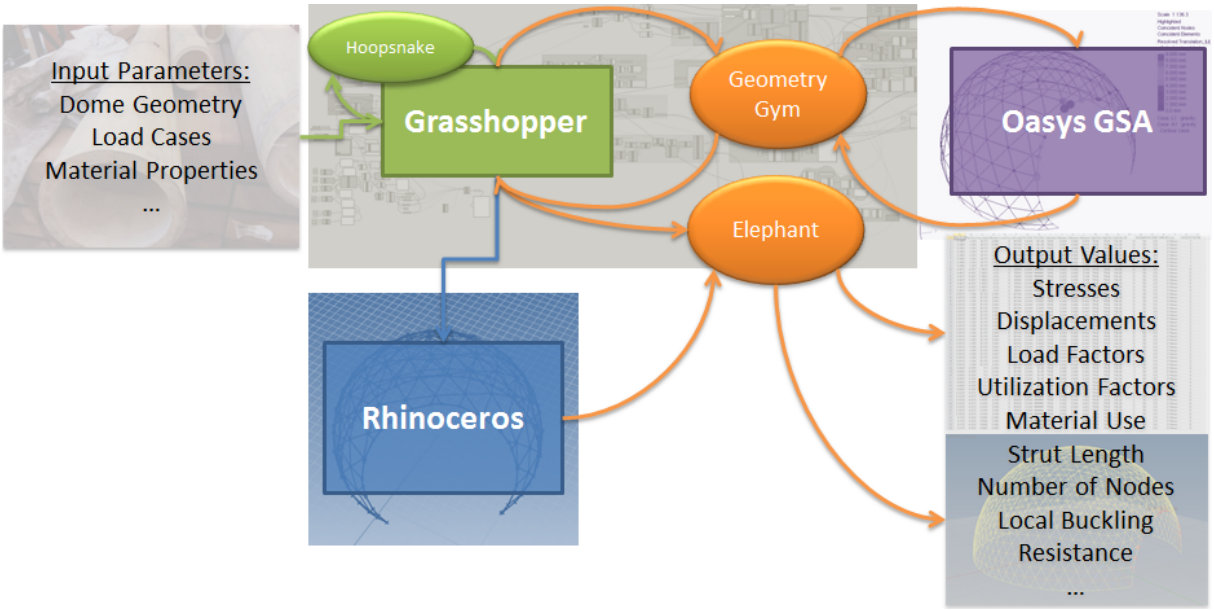

Figure A.1: Flow Chart

A.2 Explanation of *Grasshopper* Script

Large parts of the *Grasshopper* script were inspired by the MSc thesis of Arend van Waart [93]. For a more detailed explanation of the automated generation of geodesic domes in *Grasshopper*, it is advised to read the appendix of his thesis.

A.2.1 Input Parameters

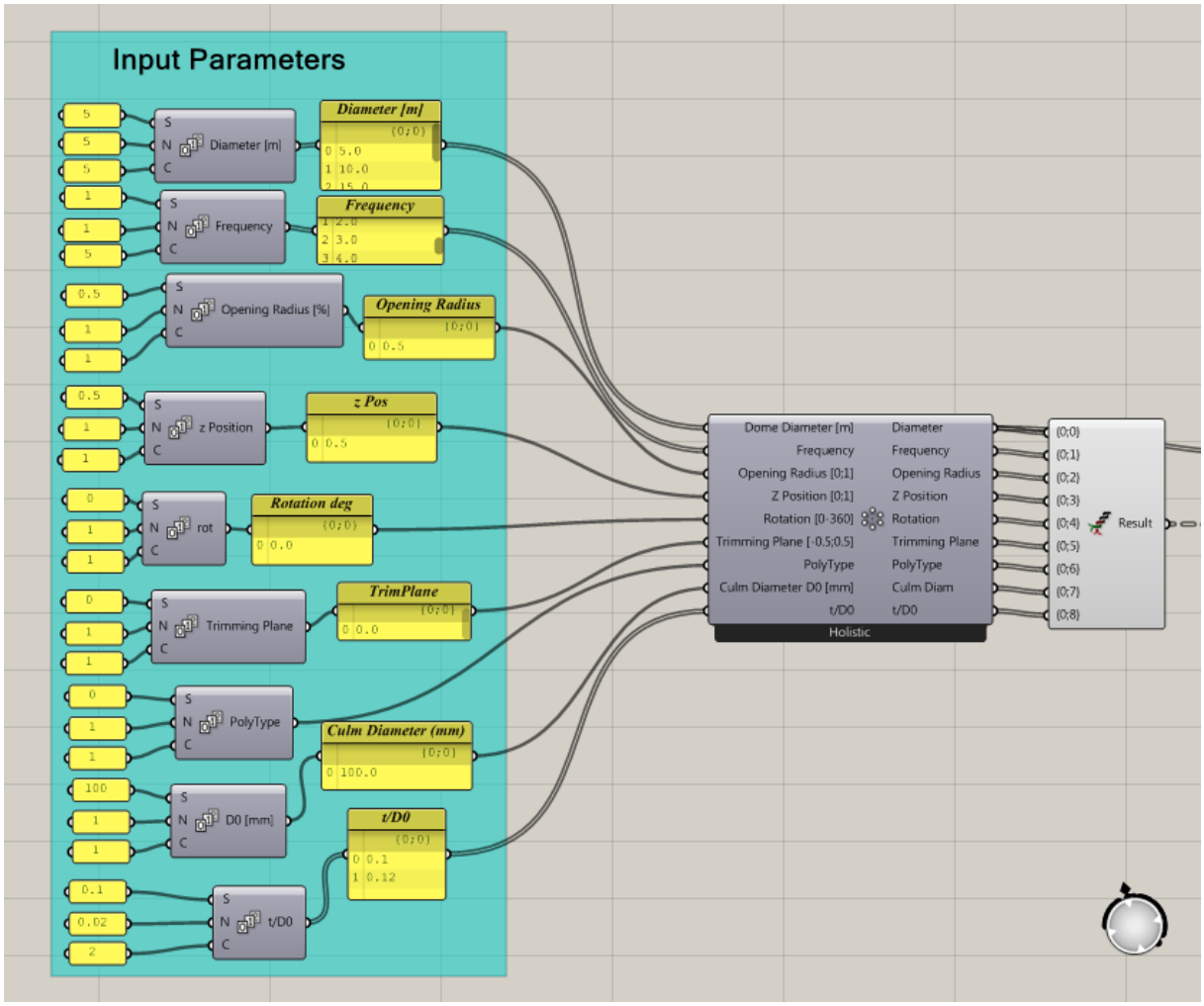

Figure A.2: Input Parameters

In order to run a parametric analysis using *Hoopsnake*, the input parameters are defined as a series of numbers that are combined in all possible combinations (figure A.2). The *Hoopsnake* component allows to automatically loop through all combinations (figure A.3).

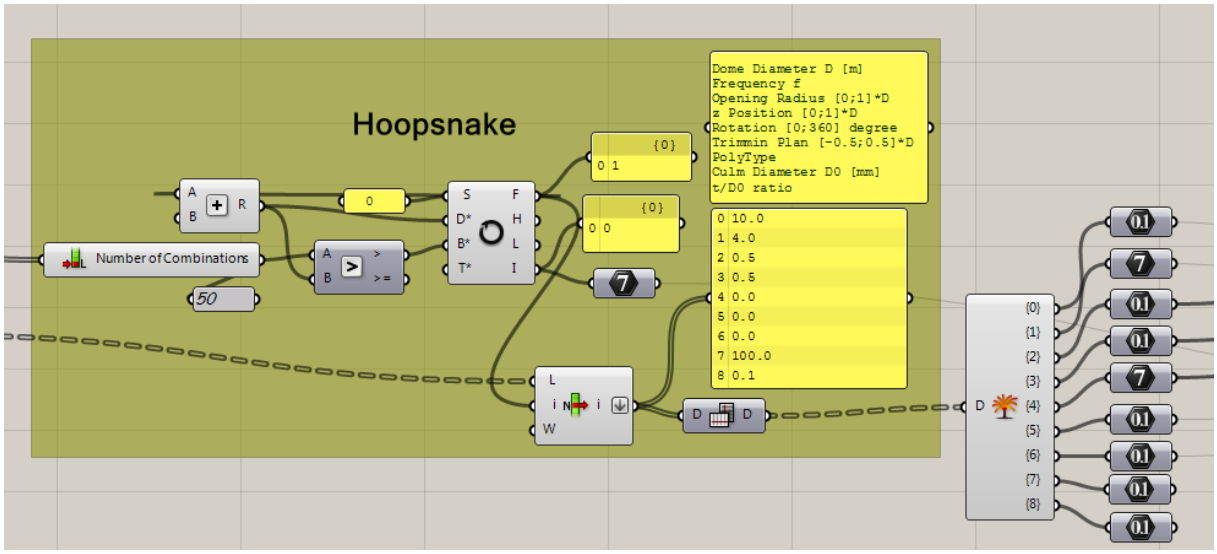

Figure A.3: *Hoopsnake*

The material properties are stored separately and an individual strut material can be selected. Note that the thickness t and outer diameter D_0 of the circular hollow section can either be selected as shown in figure A.4 or defined freely and iterated in *Hoopsnake*. The material of the beams is always steel S235.

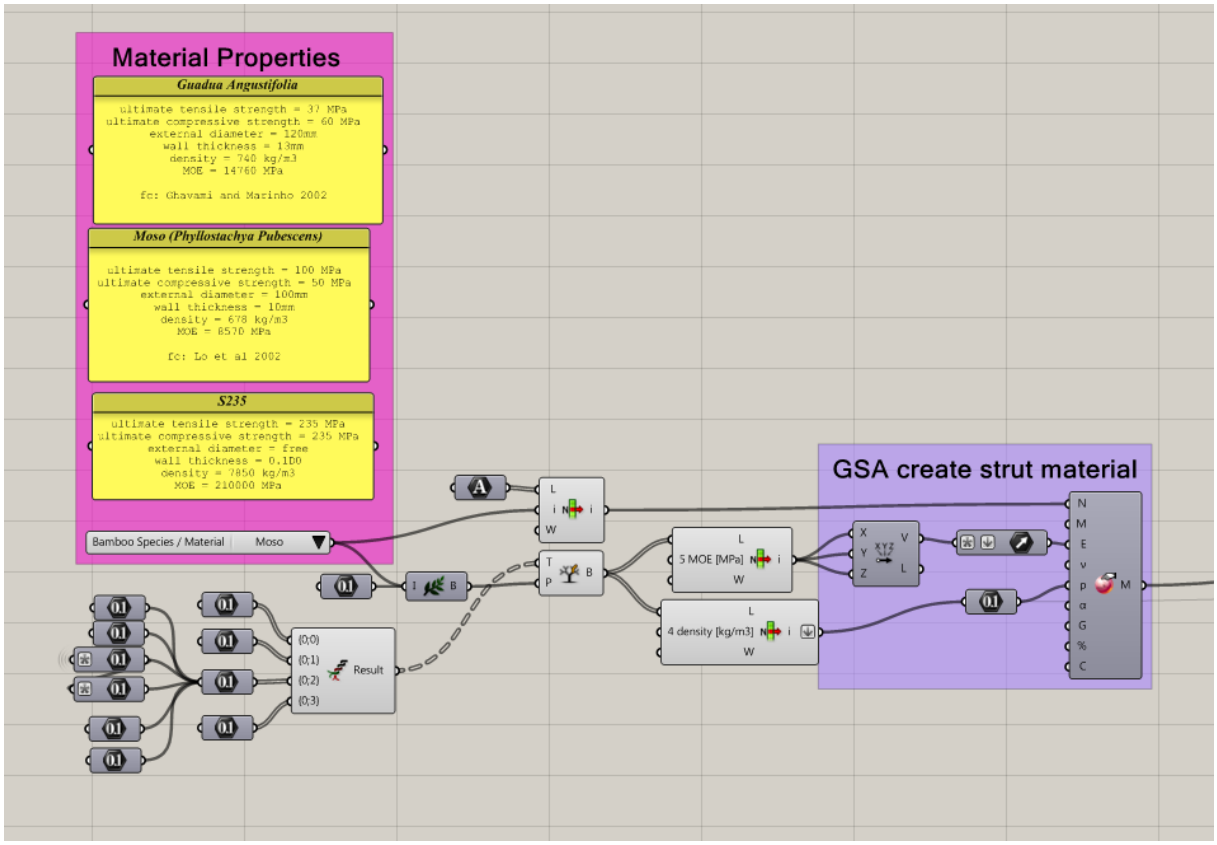

Figure A.4: Material Properties

A.2.2 Generation of a Geodesic Dome in *Grasshopper*

A geodesic sphere can be created by using the *Geometry Gym*[1] component shown in figure A.5a. It generates a geodesic sphere with a given radius ($D/2$), frequency ϱ (the number of struts used to approximate the sphere) and polyhedron type (icosahedron, tetrahedron or octahedron). The input parameters *diameter* D, *frequency* ϱ and polyhedron type (icosahedron) result from the current parameter combination displayed in figure A.2.

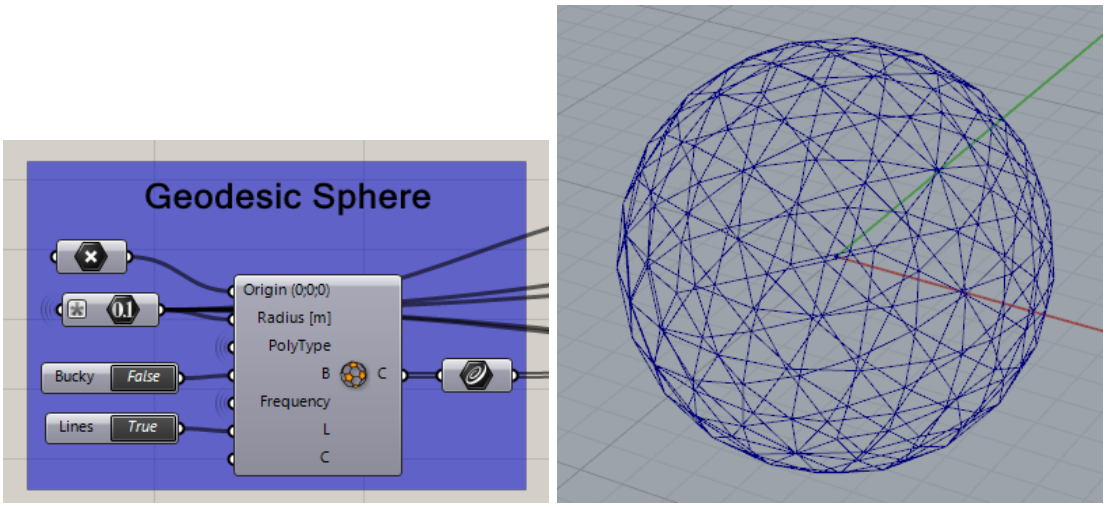

(a) *Grasshopper* (b) *Rhinoceros*

Figure A.5: Generation of geodesic sphere

The geodesic sphere can be trimmed at any plane to a geodesic dome. The distance from the centre of the sphere is defined as $[-0.5; 0.5]D$ which results in an untrimmed geodesic sphere, no dome at all and all shapes in between. In this example, the trimming plane lies at $T = 0$ which is equivalent to cutting the sphere in half at its equator (figure A.6).

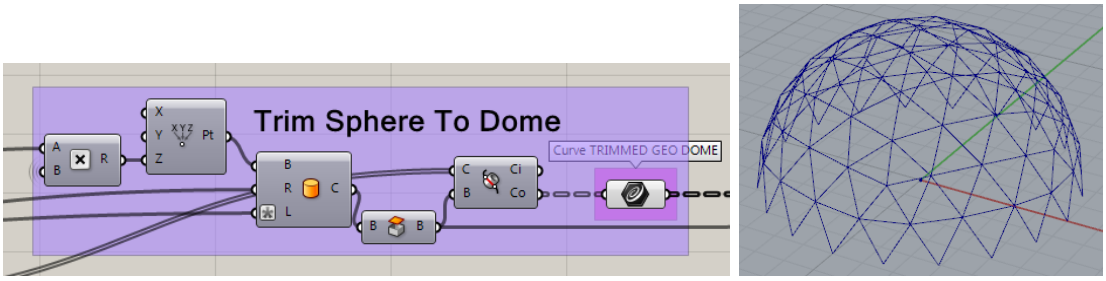

(a) *Grasshopper* (b) *Rhinoceros*

Figure A.6: Trim sphere to dome

Next, an opening can be created in the dome. This is easiest done by intersecting a cylinder with the dome and cutting the struts at the intersecting points (figure A.7). The *z-position* defines the vertical position with respect to the trimming plane. The opening size can be varied between $[0; 1]D$. Additionally, the cylinder can be rotated about the dome's z-axis. All three parameters are defined in the input parameters.

[1] plug-in for *Grasshopper* developed by Jon Mirtschin

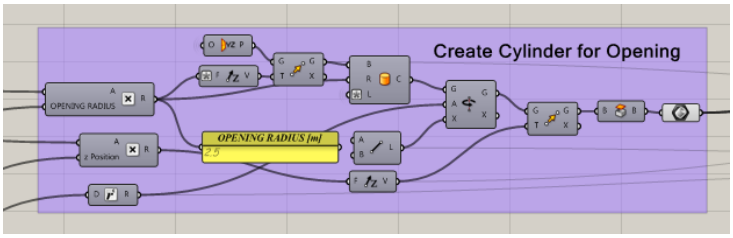

(a) *Grasshopper*

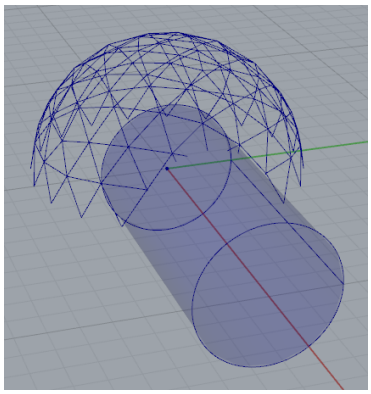

(b) *Rhinoceros*

Figure A.7: Cut out cylinder

All lose nodes are connected by poly-lines that are later defined as steel edge beams. This results in a bottom edge beam, connecting the nodes at the bottom of the dome and an opening edge beam, connecting the nodes around the opening (figure A.8). The longest and shortest strut length can be computed and the actual trimmed dome diameter (depending on the trimming it can be smaller than the defined diameter D). The length of the longest strut (figure A.8b) is important for the local buckling analysis.

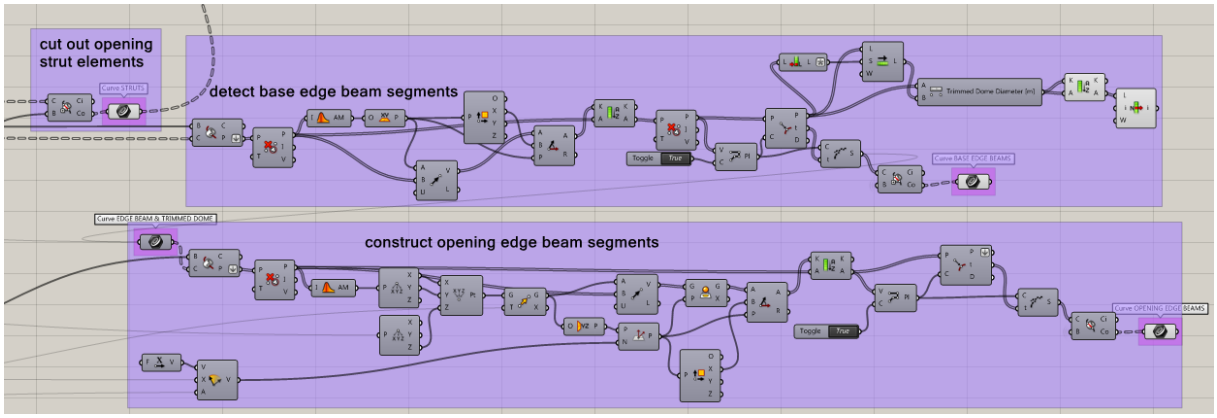

(a) *Grasshopper* creates edge beam poly-lines

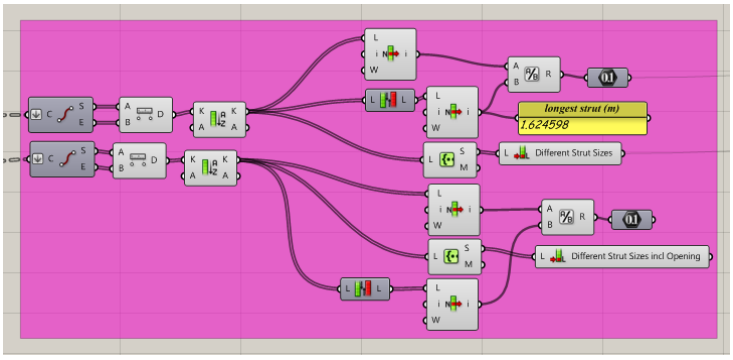

(b) *Grasshopper* computes longest strut length

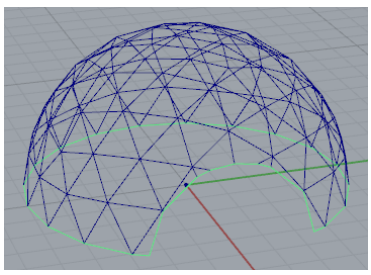

(c) *Rhinoceros*

Figure A.8: Create edge beams

A.2.3 Exporting the *Grasshopper* Model to *Oasys GSA*

So far only points and curves were generated by *Grasshopper*. *Geometry Gym* components are able to assign material properties to these elements and export them as structural elements to *Oasys GSA* (GSA) (figure A.9).

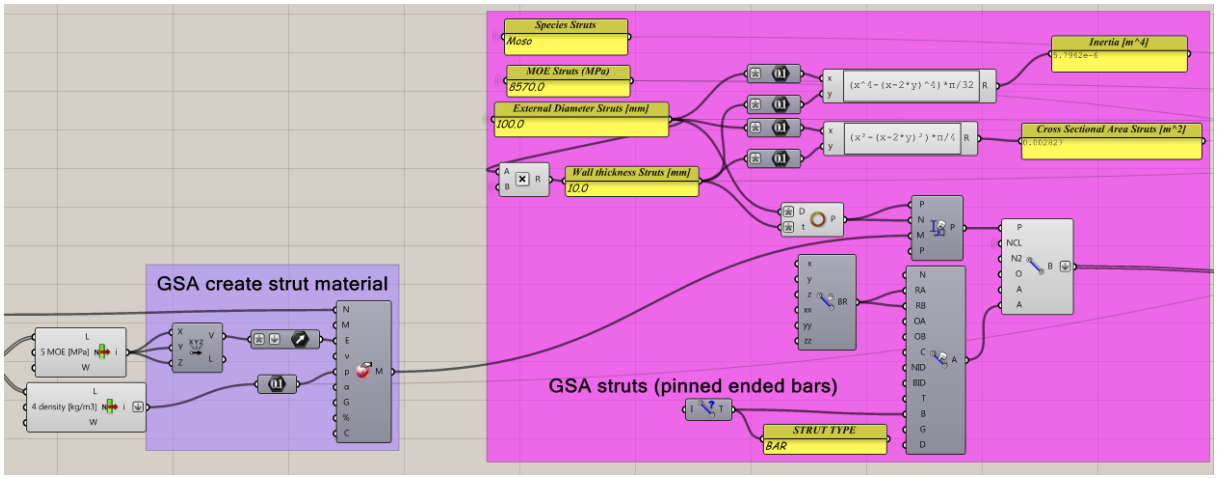

(a) *Grasshopper* defines GSA struts (bars)

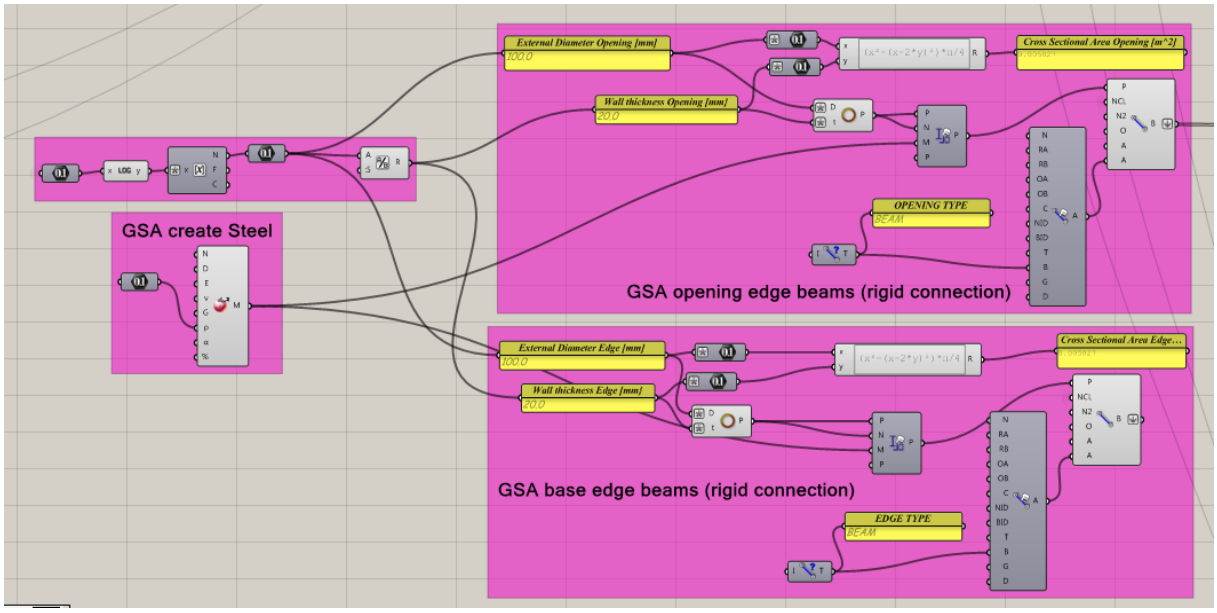

(b) *Grasshopper* defines GSA edge beams (steel)

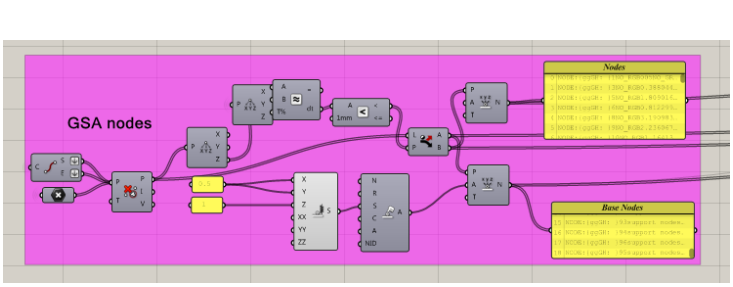

(c) *Grasshopper* detects nodes

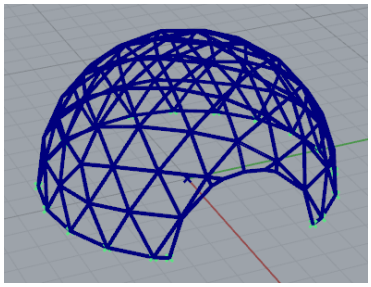

(d) *Rhinoceros*

Figure A.9: Cut out cylinder

The material that is assigned to the bars is an orthotropic material e.g. bamboo. All material parameters can be edited to match the properties of a certain bamboo species. The edge beams are made of steel S235 but the cross-section of the edge beam around the opening and bottom edge beam can be defined independently. The bars are rigidly connected and able to transfer bending moments.

Note that bamboo is modelled by a circular hollow section and material properties such as E-Modulus (E), Shear Modulus (G), density (ρ) and Poisson's Ratio (ν). The influence of nodes is accounted for in the strength properties. All input parameters can be adjusted to match test results of previous and future research.

The nodes are subdivided into base nodes (bottom perimeter) and other nodes. The base nodes are restrained in x, y, z-direction by springs of $\xi = 0.5$ but different boundary conditions are also possible (figure A.9c).

The length of the beams and bars is computed to manually calculate the self-weight of the structure and perform a "sanity check" later on.

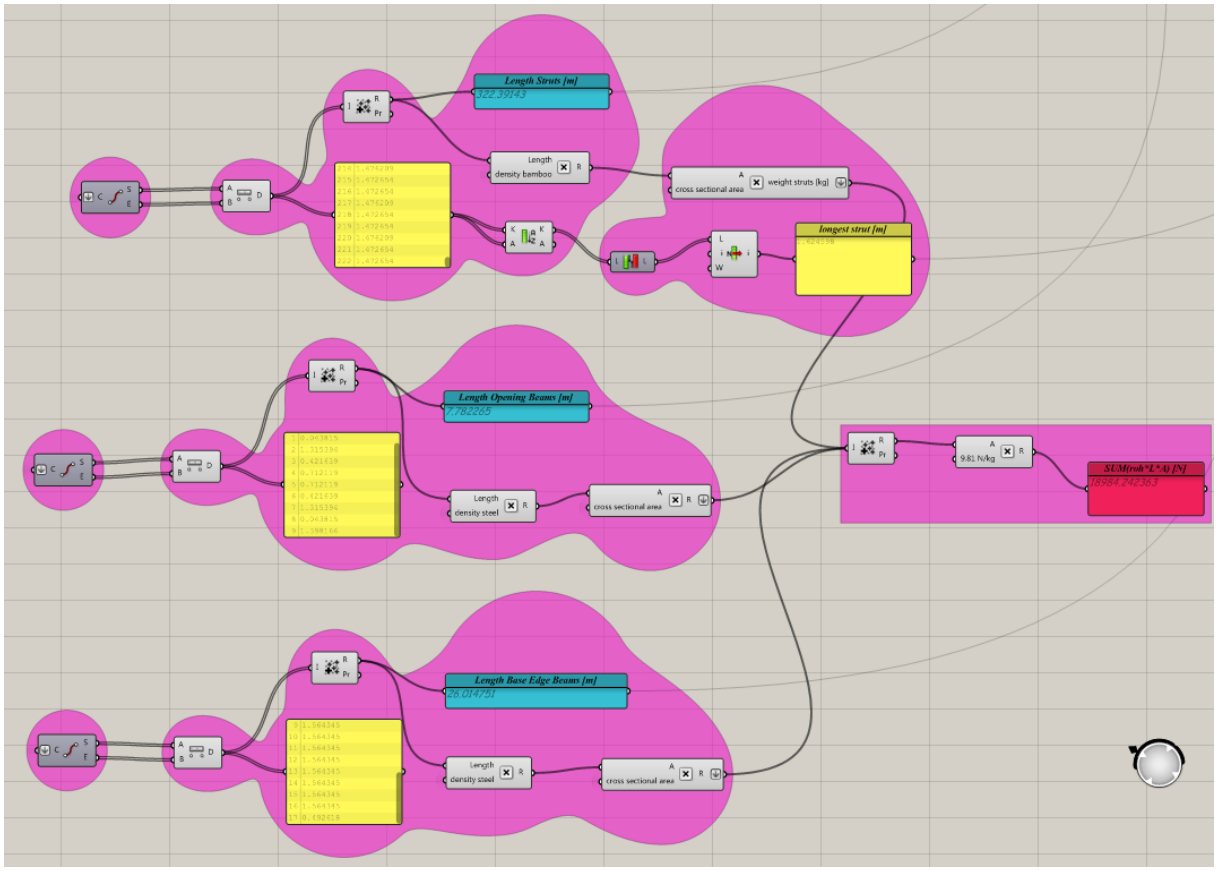

Figure A.10: *Grasshopper* computes length of struts and beams

A.2.4 Structural Analysis

By linking certain parameters to the *Hoopsnake* component, the model is able to automatically iterate through different sets of parameters. The actual structural analysis is performed individually per combination of parameters. *Grasshopper* sends information to GSA, GSA computes a structural analysis in the background and *Grasshopper* requests this data back. The retrieved values (e.g. axial stresses) can be compared to a limit value and the result is exported by the *Elephant* component.

A.2.4.1 Load Case

The most basic load case is self-weight. Additionally, a point load can be applied on top of the dome (figure A.11). Note that superimposed dead load, snow, and wind are not shown here as they are not part of the theoretical analysis. The defined load case and dome geometry are sent to GSA. The GSA analysis can be run in the background and subsequently visualized in *Grasshopper*.

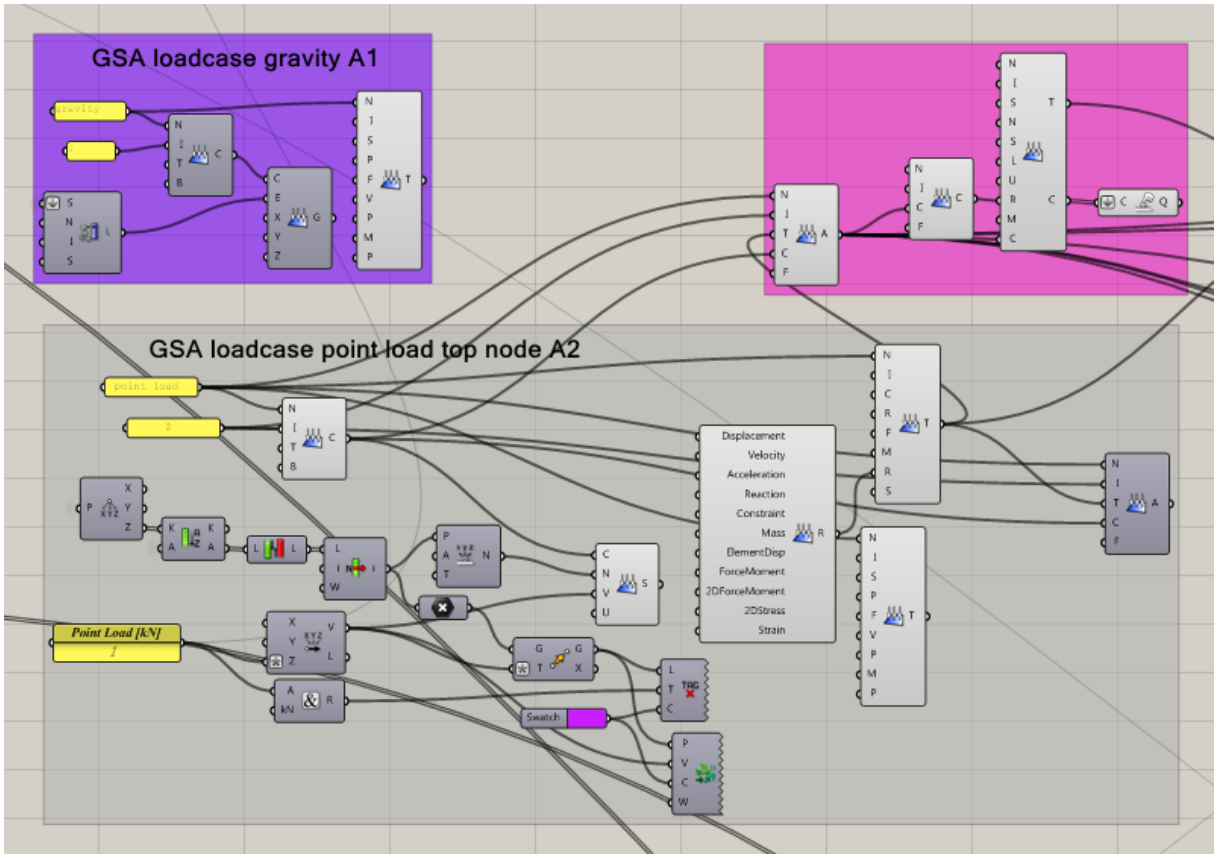

Figure A.11: Load Cases

Another method is to "bake" the model to GSA and analyse it within GSA. This is more time consuming (computation wise [93] as well as for the user) but especially attractive when a dome variant needs to be analysed in detail. Of course the results in GSA and *Grasshopper* should match, which will be shown in the following. Note that matching results don't mean that the analysis results are true from an engineering point of few. It only means that we didn't make a mistake in *Grasshopper* after reimporting the data from GSA.

"Sanity check" A sanity check is conducted in order to see whether reaction forces in z-direction match the self-weight of the model calculated by hand and by GSA (figure A.12).

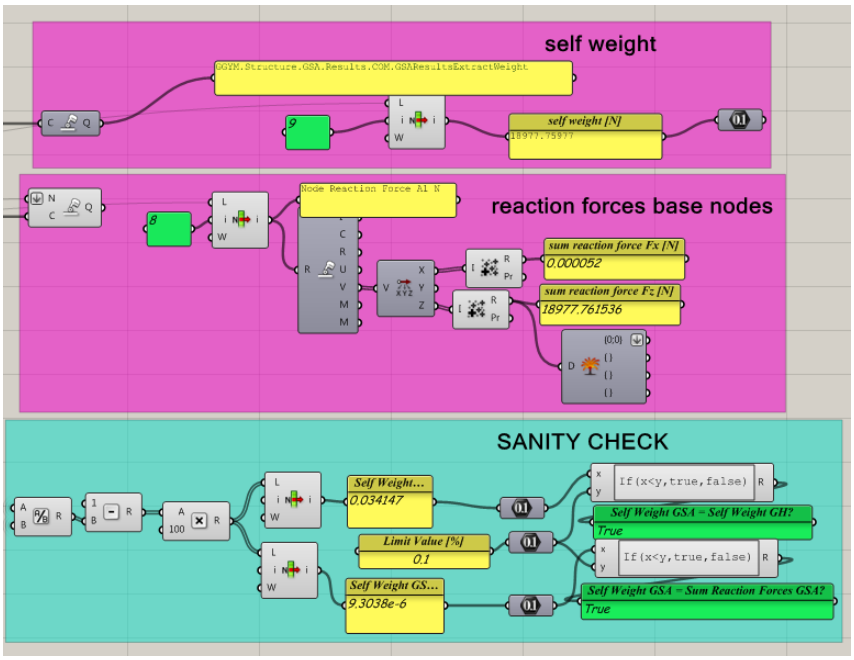

Figure A.12: *Grasshopper*: self-weight = reaction forces?

If these results match, other results can be retrieved, e.g. maximum axial stresses in the struts, maximum bending stresses in the edge beams and nodal displacements. Note that only one solver[2] component is used for the analysis but as there are several input queries also several outputs are generated (figure A.13).

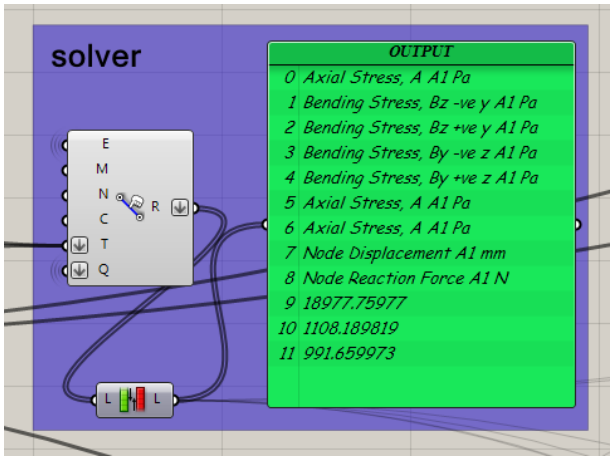

Figure A.13: *Geometry Gym* Solver

[2] A 'solver' is the *Geometry Gym* component that requests results from GSA and reimports them into *Grasshopper*

A.2.4.2 Nodal Displacements and Strut Stresses

We will proceed with the load case point load. Nodal displacements can be visualized in *Rhinoceros* by translating the initial *Grasshopper* nodes along a displacement vector that is imported from GSA. In order to make the displacements visible, an amplification factor is introduced in *Grasshopper*. The axial stresses that are retrieved from GSA can also be visualized (figure A.14b). The results can be compared to results obtained in GSA.

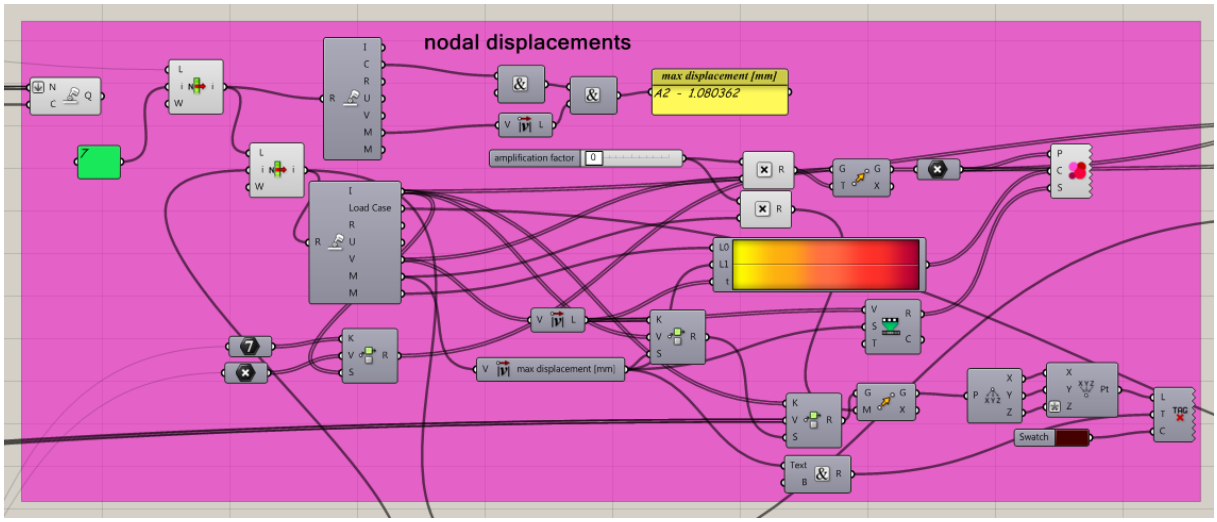

(a) *Grasshopper* displacements

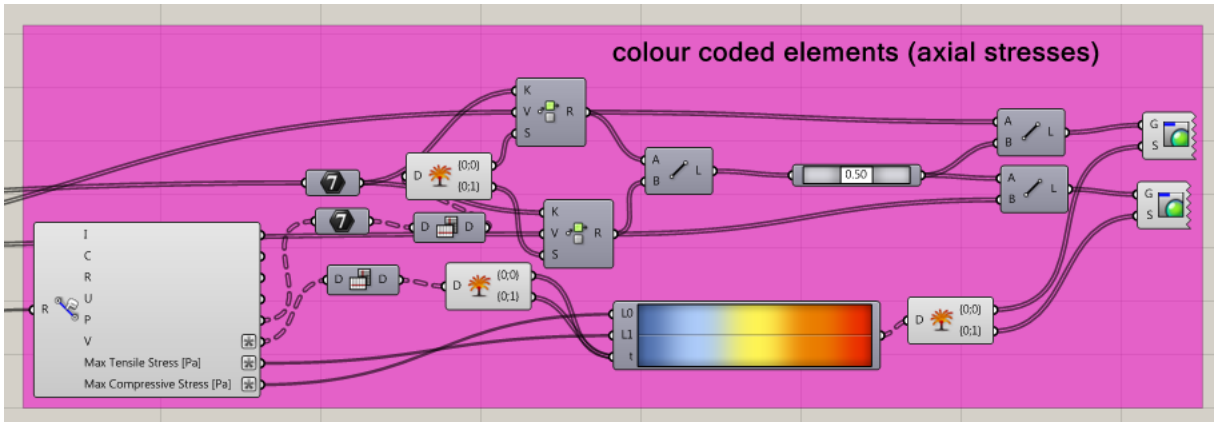

(b) *Grasshopper* stresses

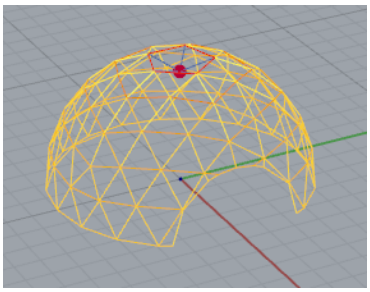

(c) *Rhinoceros*

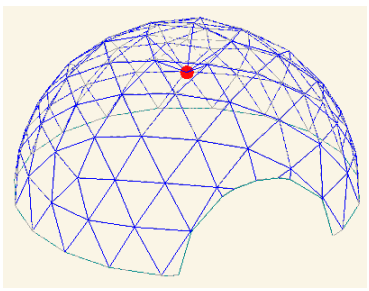

(d) GSA displacements

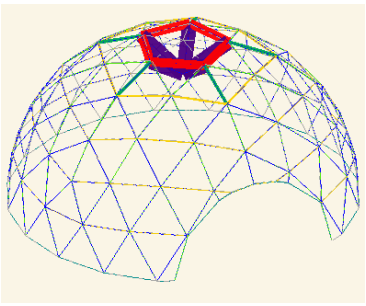

(e) GSA strains

Figure A.14: Strut stresses and displacements

A.2.5 Exporting Results to Excel File

The last step is to perform unity checks and export results to Excel with the *Elephant* components. Additionally, a "screenshot" can be taken of the visualized model in *Rhinoceros*.

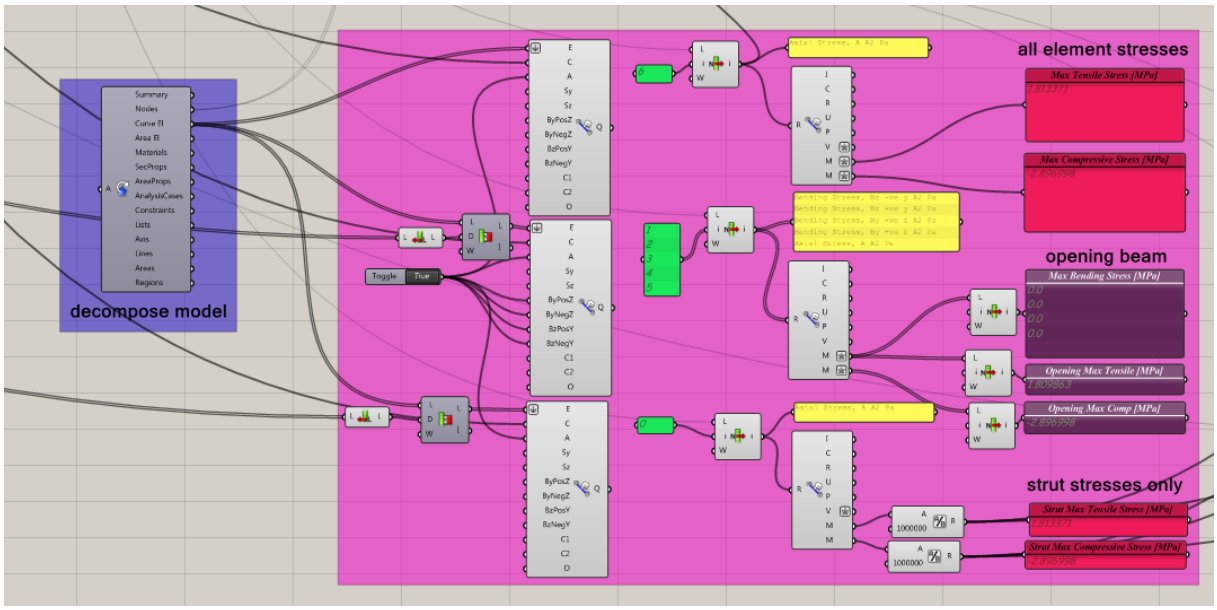

(a) *Grasshopper* stresses

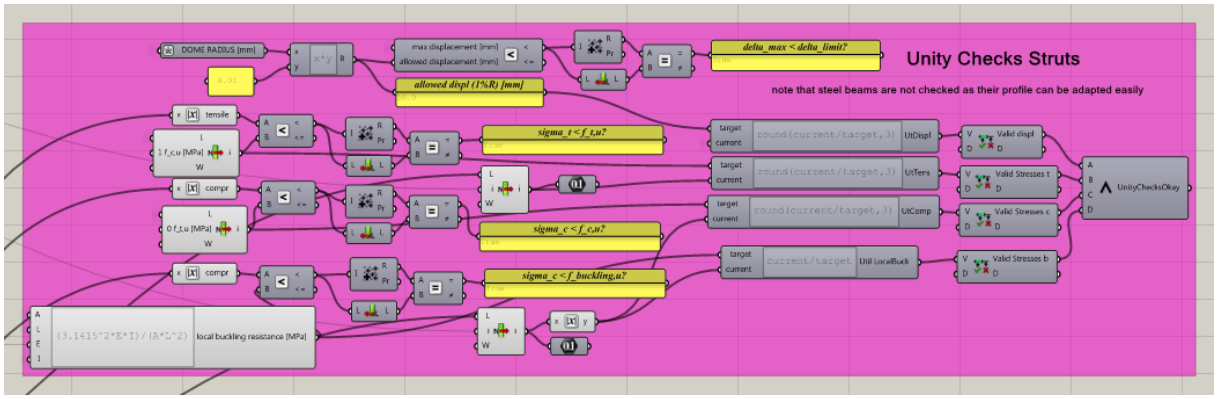

(b) *Grasshopper* unity check

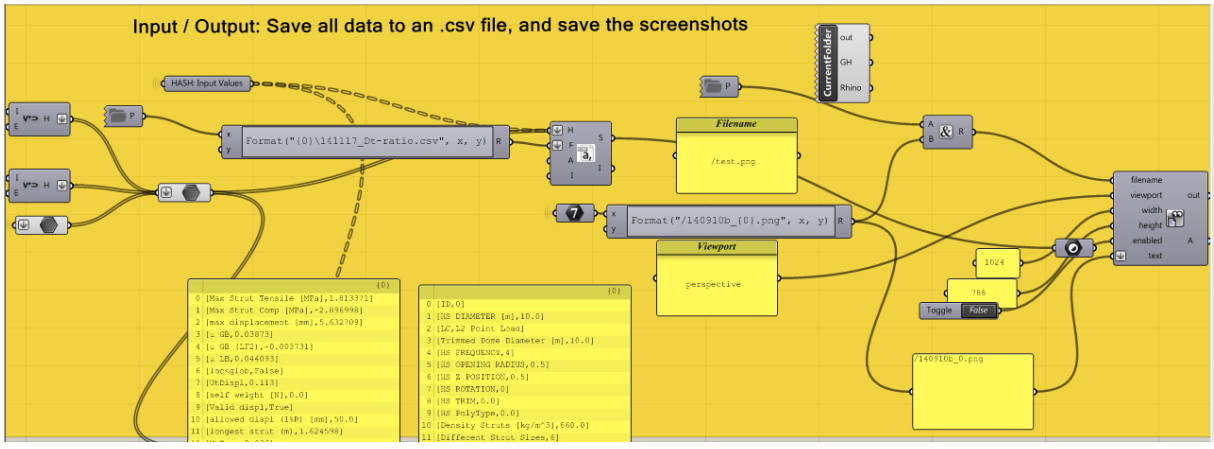

(c) *Grasshopper* export data

Figure A.15: Export results

A.3 Explanation of Dome Parameters

A.3.1 Polyhedron Type

Different polyhedron types can be implemented. Icosahedra result in a smooth, regular appearance with little variance in strut length. This results in a more even stress distribution.

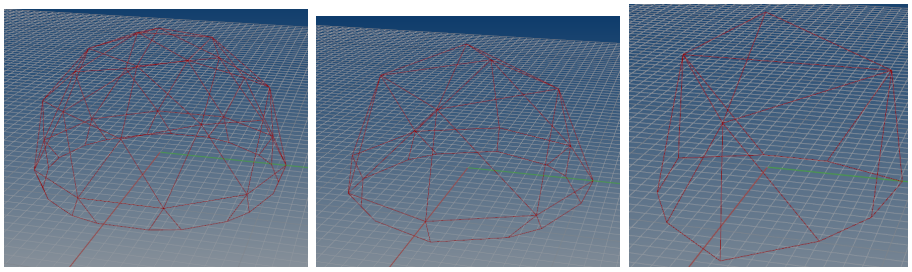

(a) Icosahedron (b) Octahedron (c) Tetrahedron

Figure A.16: Polyhedron Types for Frequency 2

A.3.2 Dome Frequency

The dome frequency ƒ reflects the order of triangulation that is used to approximate the sphere or dome. With higher frequency the struts become short and the dome becomes smoother and appears more elegant. Even frequencies can be cut at the equator of the geodesic sphere without cutting struts in half. Odd frequencies require a bottom edge beam or need to be cut slightly above or below the equator.

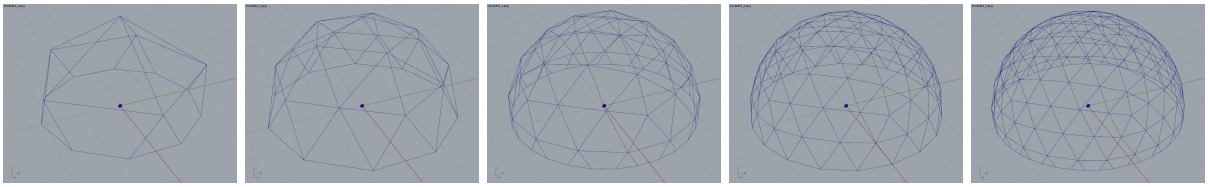

(a) $ƒ = 1$ (b) $ƒ = 2$ (c) $ƒ = 3$ (d) $ƒ = 4$ (e) $ƒ = 5$

Figure A.17: Frequencies

A.3.3 Trimming Plane

The sphere can be trimmed to a dome at any height (in % of initial dome radius). Obviously trimming directly below an existing ring of horizontal struts makes little sense.

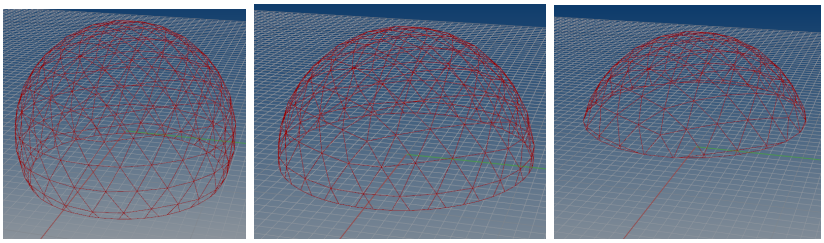

Figure A.18: Trimming Plane: -30% ; 0% ; +40%

A.3.4 Z-Position Opening

The openingis moved up and down with respect to the global z-axis (in % of the initial dome radius) Note that the created opening appraoches an ellipse – not a circle – as a sphere is intersected by a cylinder.

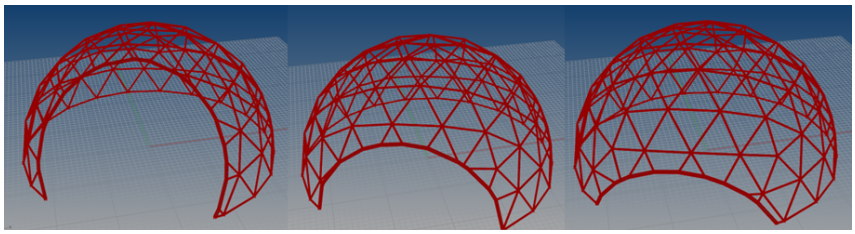

Figure A.19: z-position

A.3.5 Opening Size

A minimum clear height can be defined and the opening size can be increased (in % of the initial dome radius) until only half a dome is left.

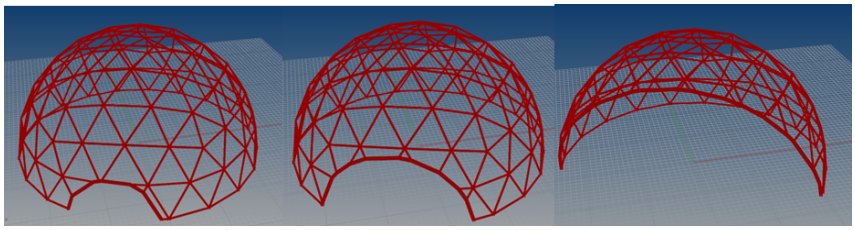

Figure A.20: Opening size

A.3.6 Rotation of Opening around Z-Axis

All angles are possible and for certain angles the opening becomes asymmetric! This results in unfavourable stress distributions which is shown in the parametric study.

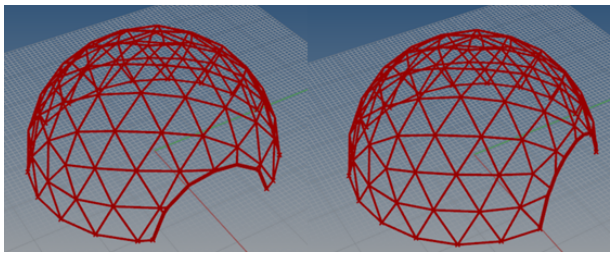

Figure A.21: Opening rotation

A.4 Strut Stresses Opening Rotation

Additional figures for maximum strut stresses resulting from opening rotation are shown below.

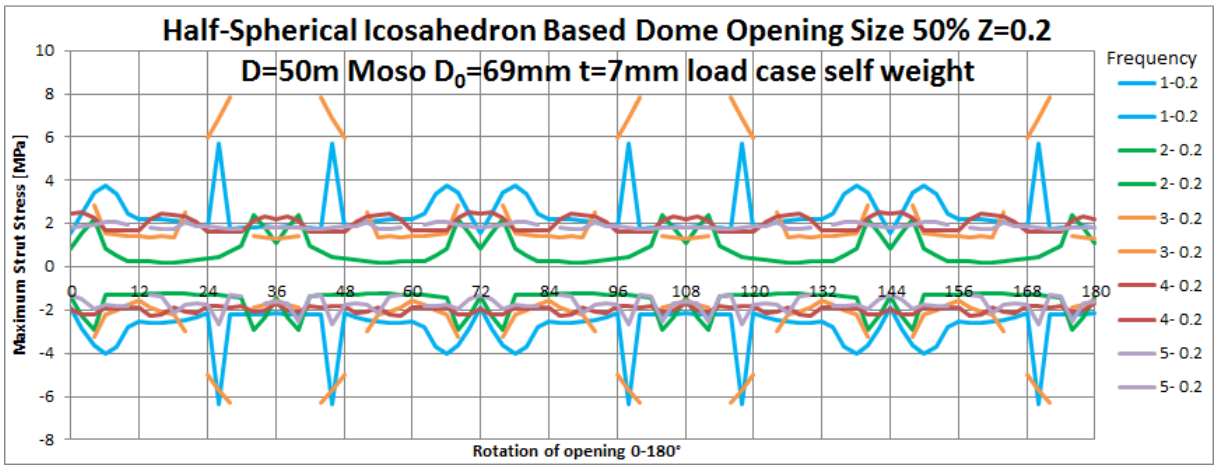

Figure A.22: Strut stresses for different frequencies z=0.2

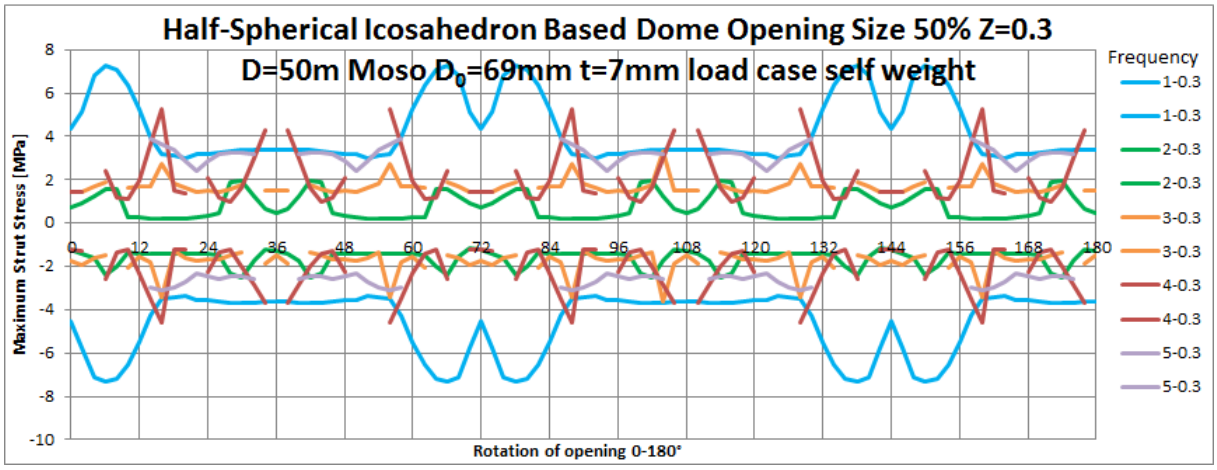

Figure A.23: Strut stresses for different frequencies z=0.3

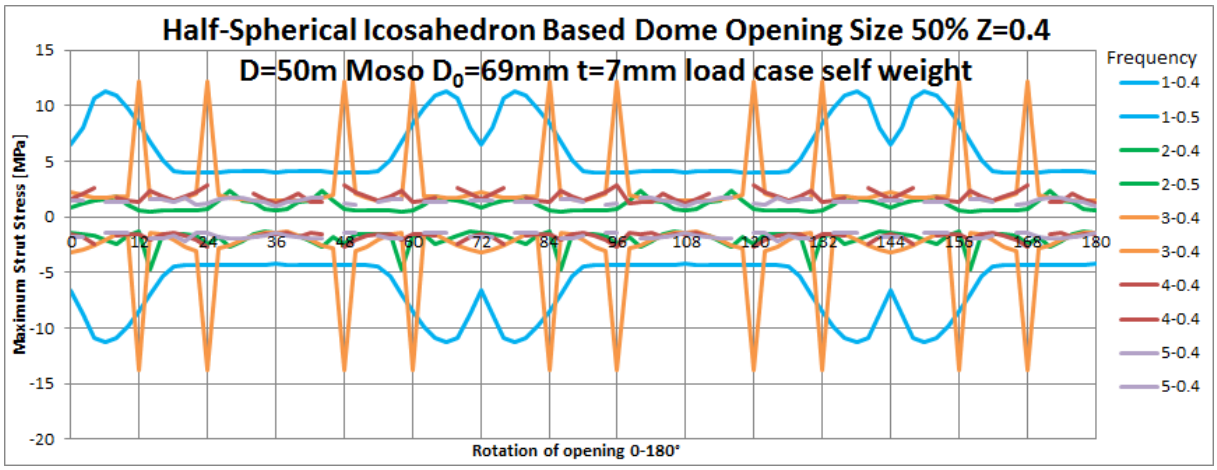

Figure A.24: Strut stresses for different frequencies z=0.4

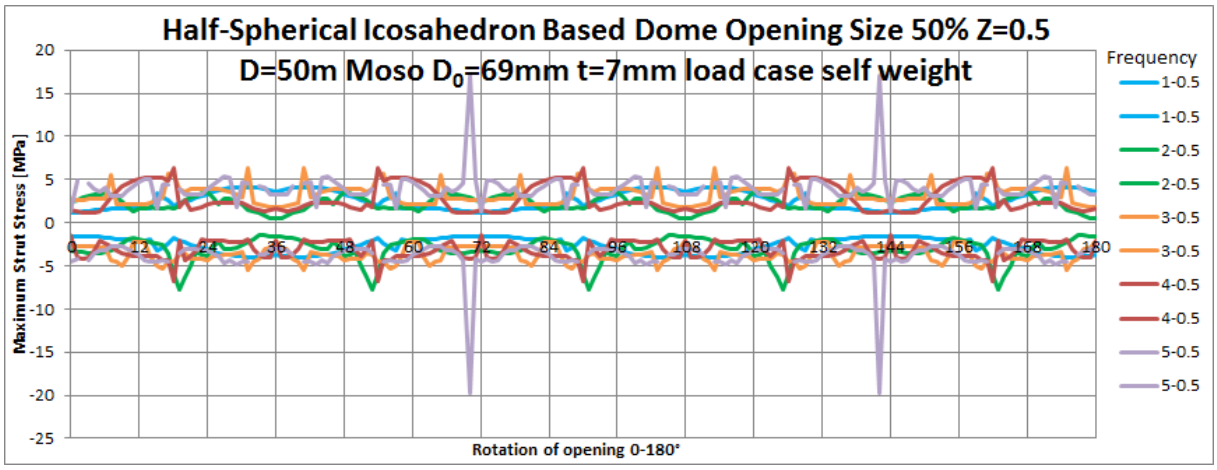

Figure A.25: Strut stresses for different frequencies z=0.5

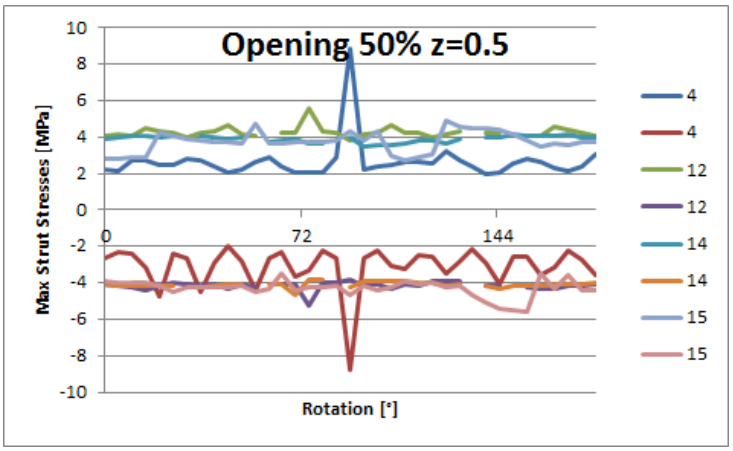

Figure A.26: Strut stresses for higher frequencies z=0.5

A.5 Derivations

A.5.1 Derivations for Transition from Local to Global Buckling

A.5.1.1 Influence of t/D_0 ratio (steel S235)

For bamboo, it was possible to assume $t = 0.1D_0$ for the transition of global to local buckling and the local buckling curve. The only variable in equation 5.4a and 5.4b was D_0 as the t/D_0 ratio remained unchanged. Now we will change the wall thickness t while keeping the outer diameter D_0 constant. As nature only provides $t = 0.1D_0$ for bamboo, we will proceed with steel S235. An analysis for transition from global to local buckling for different t/D_0 ratios is displayed in figure A.27a. The transition point is again independent of the strut material. Note that the regression formula for $t = 0.1\ D_0$ is slightly different from figure 5.18 as only frequencies up to $\mathfrak{f} = 25$ are considered in figure A.27a.

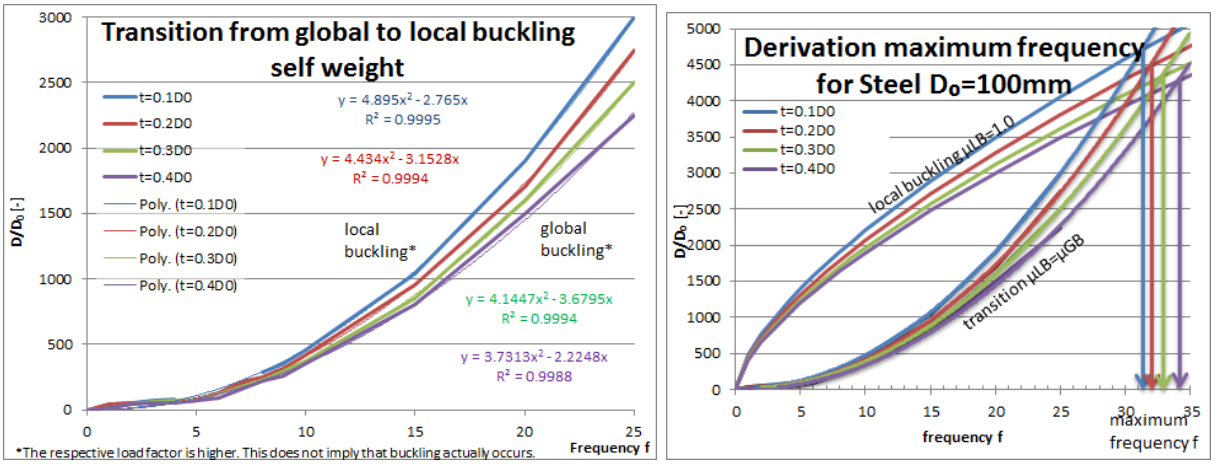

(a) Transition GB to LB for different t/D_0 ratios, independent of material

(b) Derivation of maximum frequency $\mathfrak{f}_{max}$ for Steel S235 $D_0 = 100\,\text{mm}$

Figure A.27: Global and local buckling for different t/D_0 ratios

Figure A.27b shows how the maximum frequencies and D_{max}/D_0 ratios can be derived on the example of Steel S235 $D_0 = 100\,\text{mm}$ with multiple t/D_0 ratios. The same principle can be used for any material. The transition lines from global to local buckling stay unchanged as they are material independent. Only the lines indicating the safe zone ($\mu_{LB} = 1.0$) will change according to figure 5.16.

Again we can set the expressions for transition from global to local buckling equal to the local buckling expression derived in equation 5.2b and linearised to derive the maximum possible dome diameter $D_{max,LBGB}$ for $\mu_{LB} = \mu_{GB} = 1.0$[3]. Examples of how this is done can be found in the appendix A.5.1.2.

We can derive the following equation:

$$D_{max,LBGB,LC1} = \left[s_1\left(\frac{t}{D_0}\right)^2 + s_2\left(\frac{t}{D_0}\right) + s_3\right] D_0; \quad \text{Steel S235} \Bigg\} \quad \frac{t}{D_0} \in [0.1; 0.4] \tag{A.1a}$$

[3]Note that there is a difference of 15% between model data and formula 5.2b due to the assumption of F_g which is overestimating the amount of material leading to the highest strut stress σ_{max}.

$$\left.\begin{aligned} s_1 &= 0.0349D_0^2 - 21.22D_0 + 6341.4 \\ s_2 &= -0.0269D_0^2 + 16.406D_0 - 4812.1 \\ s_3 &= 0.0344D_0^2 - 21.036D_0 + 6099 \end{aligned}\right\} D_0 \text{ in mm} \tag{A.1b}$$

If we linearise equation A.1a, we will find an expression $D_{max,LBGB,LC1} = -s_1' \; t + s_2' \; D_0$. This indicates that low t/D_0 ratios are favourable. Let's try to explain this mathematically:

If we keep the outer strut diameter D_0 constant and only increase the wall thickness t, the area A and inertia I are increased accordingly: $A = \frac{\pi}{4}(D_0^2 - (D_0 - 2t)^2) \quad I = \frac{\pi}{64}\left(D_0^4 - (D_0 - 2t)^4\right)$ This results in the following values for A and I:

Table A.1: Values for A and I for different t and constant D_0

t/D_0	A/D_0^2	I/D_0^4	I/AD_0^2
0.1	0.09π	0.009225π	0.1025
0.2	0.16π	0.013600π	0.0850
0.3	0.21π	0.015225π	0.0725
0.4	0.24π	0.015600π	0.0650
0.5	0.25π	0.015625π	0.0625

The local buckling resistance is similar to $f_{LB} = \frac{\pi^2 EI}{AL^2}$. If E, L and D_0 are kept constant, we arrive at: $f_{LB} \sim \frac{I}{A} = D_0^2\left(\frac{1}{4}(\frac{t}{D_0})^2 - \frac{1}{4}\frac{t}{D_0} + \frac{1}{8}\right)$. The advantage of a larger inertia decreases thus with an increasing wall thickness t. This decrease can also be approximated with a linear fit with $f_{LB} \sim D_0^2(-\frac{1}{8}\frac{t}{D_0} + 0.1125)$ for $t = 0.1D_0$ to $t = 0.4D_0$. A similar linear fit was employed in equation 5.4a in order to simplify the rules of thumb for bamboo.

For bamboo, an analysis for different t/D_0 ratios is mere hypothetical as nature only provides t/D_0 ratios of about 0.8 to 1.2. For steel struts however, this investigation is certainly interesting. If material costs increase linearly, an increase of wall thickness should be considered with care. Let"s consider the following case: We want to reinforce the bottom struts of a $\mathfrak{f} = 2$ geodesic dome to prevent local buckling due to dead load. Doubling the wall thickness from $t = 0.1D_0$ to $t = 0.2D_0$ results in an area increase of $0.16/0.09 = 1.78$. This results in 1.78 times the material costs and a stress reduction to $1/1.78 = 56.1\%$ of the initial stresses. However, the buckling resistance is also decreased to $0.085/0.1025 = 82.9\%$. This means that a geodesic dome with thicker bottom struts has a new utilization factor of $\mu_{LB} = \frac{\sigma_{max}}{f_{LB}} = \frac{56.1}{82.9} = 67.8\%$. This is only a gain of 33.2% of structural safety for $t = 0.2D_0$ compared to the previous version $t = 0.1D_0$. But it comes at 1.78 times the initial material costs for the bottom struts. In the given example we need to reinforce 20 struts for frequency $\mathfrak{f} = 2$ out of 55 struts in total. This results in $(1.78 \cdot 20 + 35)/55 = 1.28$ times the initial costs. As frequencies increase, this relation becomes more favourable and reinforcing bottom struts might be an option to counteract local buckling (similar to edge effects in monolithic shells). Note that the gained safety decreases with increased wall thickness: If utilization is 1.0 for $t = 0.1D_0$, then there is an additional safety of 33.2% from 0.1 to 0.2 – from 0.4 to 0.5 the increase is only 1.1%! Thin circular hollow sections are thus desirable from a structural and economical point of view. If the wall thickness becomes too small however, localized buckling of the hollow section's wall might occur.

A.5.1.2 Derivation of equation A.1a

In the case of self-weight, we found the maximum possible dome diameter due to local buckling for even frequencies:

$$\begin{aligned} \text{even frequencies}: \quad & D_{max,LB} = C_1 \left(\frac{D_0^2 \mathfrak{f}^2 E}{\rho g} \right)^{1/3} \\ \text{with} \quad & C_1 = 1.1313 \left(\frac{t}{D_0} \right)^2 - 1.2067 \left(\frac{t}{D_0} \right) + 1.4837 \quad R^2 = 0.9995 \end{aligned} \tag{A.2}$$

This equation can be set equal with the transition curves for global to local buckling to find the intersecting point (see figure below):

$$\begin{aligned} t = 0.1 D_0: \quad & \frac{D_{\mu GB=\mu LB}}{D_0} = 4.8950 \mathfrak{f}^2 - 2.7650 \mathfrak{f} \\ t = 0.2 D_0: \quad & \frac{D_{\mu GB=\mu LB}}{D_0} = 4.5443 \mathfrak{f}^2 - 4.4138 \mathfrak{f} \\ t = 0.3 D_0: \quad & \frac{D_{\mu GB=\mu LB}}{D_0} = 4.1447 \mathfrak{f}^2 - 3.6795 \mathfrak{f} \\ t = 0.4 D_0: \quad & \frac{D_{\mu GB=\mu LB}}{D_0} = 3.7313 \mathfrak{f}^2 - 2.2248 \mathfrak{f} \end{aligned} \tag{A.3}$$

$$C_1 \left(\frac{\mathfrak{f}^2 E}{\rho g D_0} \right)^{1/3} = C_2 \mathfrak{f}^2 - C_3 \mathfrak{f} \tag{A.4}$$

Table A.2: Coefficients C1, C2, C3

t/D_0	C1	C2	C3
0.1	1.57915691	4.895	2.765
0.2	1.483623277	4.5443	4.4138
0.3	1.40700832	4.1447	3.6795
0.4	1.356714444	3.7313	2.2248

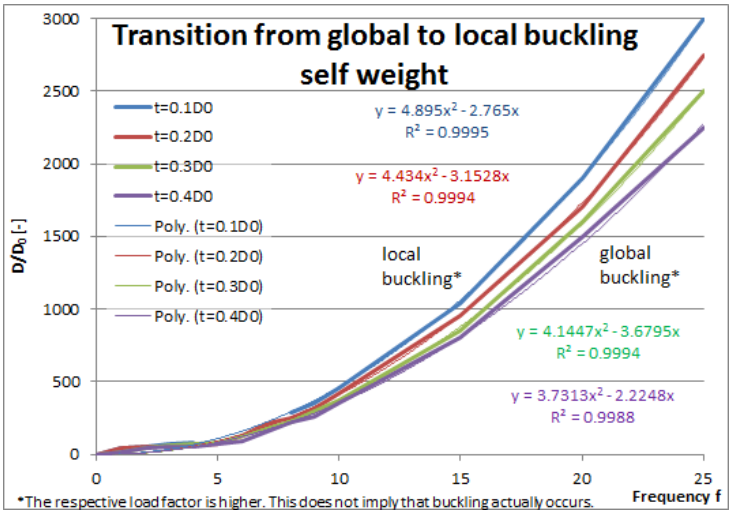

Figure A.28: Transition GB to LB for different t/D_0 ratios

We can solve for $\frac{D_{max,LB}}{D_0} = \frac{D_{\mu GB=\mu LB}}{D_0}$ graphically:

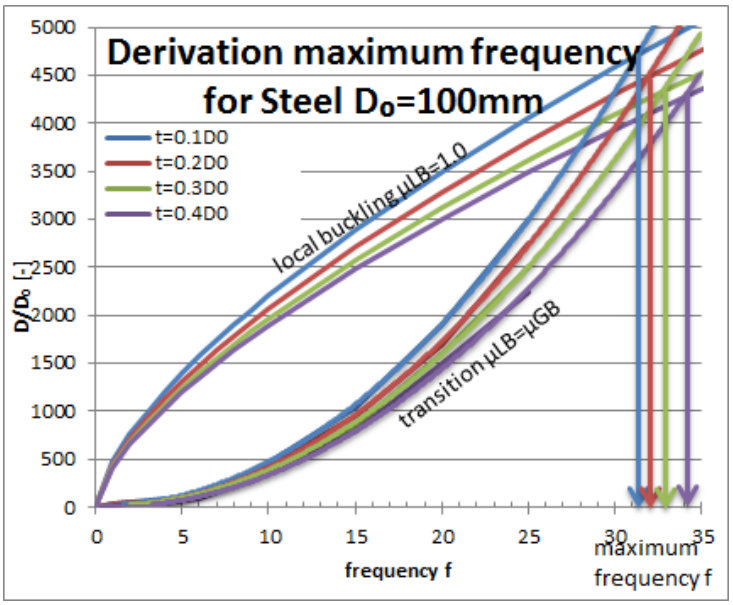

Figure A.29: Simultaneous GB and LB for different t/D_0 ratios

We can also solve equation A.4 numerically and find the following graphs:

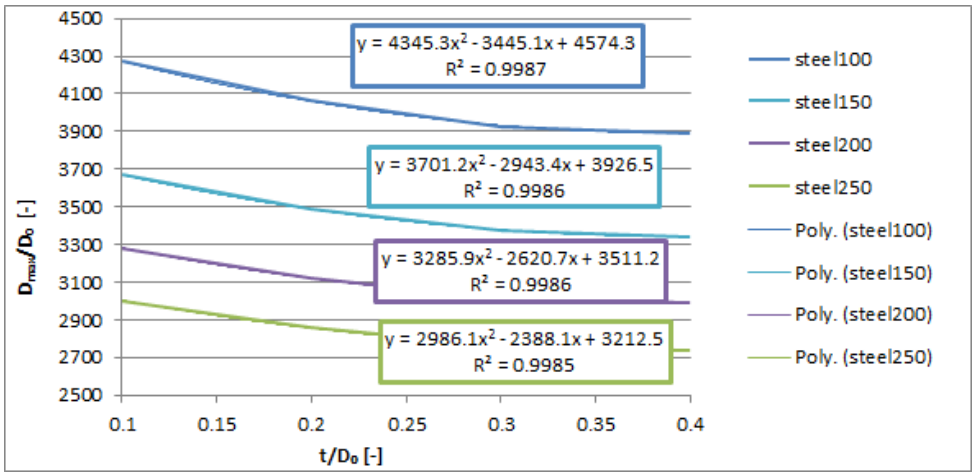

Figure A.30: Relationship of D_{max}, D_0 and t

In general $\frac{D_{max,LBGB}}{D_0} = s_1\left(\frac{t}{D_0}\right)^2 + s_2\left(\frac{t}{D_0}\right) + s_3$.

The coefficients s_1 to s_2 for different diameters D_0 can be displayed in a table:

Table A.3: Coefficients s1, s2, s3

D_0[mm]	s1	s2	s3
100	4345.3	-3445.1	4574.3
150	3701.2	-2943.4	3926.5
200	3285.9	-2620.7	3511.2
250	2986.1	-2388.1	3212.5

And a regression formula can be found:

$$s_1 = 0.0349D_0^2 - 21.22D_0 + 6341.4$$
$$s_2 = -0.0269D_0^2 + 16.406D_0 - 4812.1$$
$$s_3 = 0.0344D_0^2 - 21.036D_0 + 6099$$

We can derive a safe zone for all materials dependent on the t/D_0 ratio and the frequency. For bamboo, ratios other than 0.08 to 0.12 don't occur in nature but are displayed here for sake of completeness. The number after the material indicates D_0 in mm.

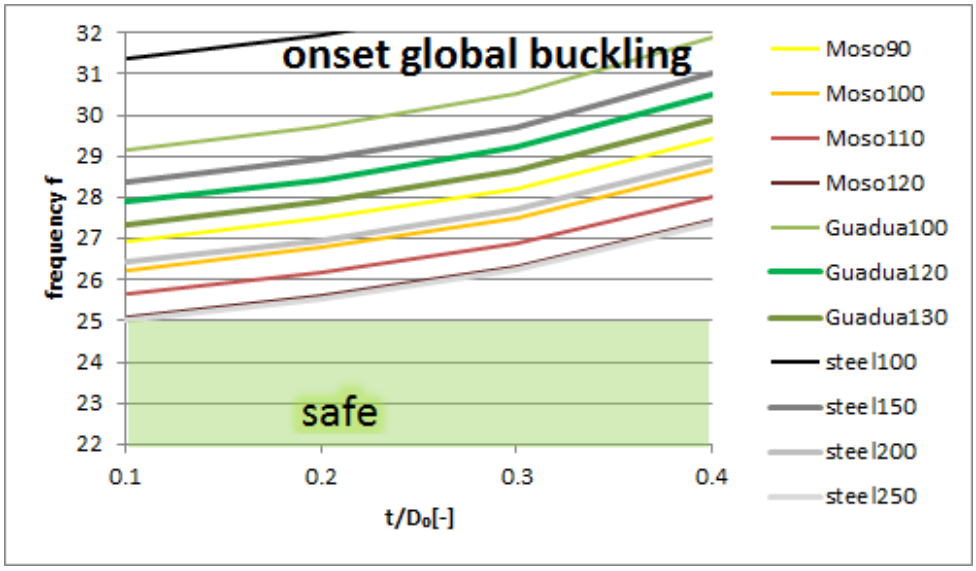

Figure A.31: Onset of global buckling

A.5.2 Derivation of maximum strut force F_s due to point load

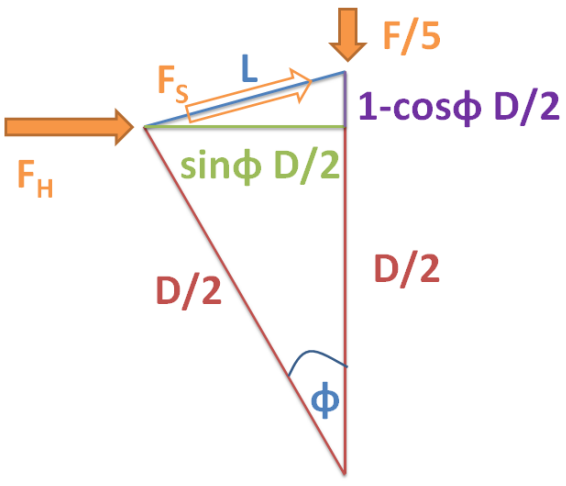

Figure A.32: Strut force F_s

$$
\begin{aligned}
D &= 1.515\mathfrak{f}L \\
\cos(\phi) &= 1 - \frac{L^2}{2\left(\frac{D}{2}\right)^2} = 1 - \frac{1}{2\left(\frac{1.515\mathfrak{f}}{2}\right)^2} = 1 - \frac{2}{(1.515\mathfrak{f})^2} \\
F_s &= \frac{F}{5}\sqrt{\left(\frac{\sin(\phi)}{1-\cos(\phi)}\right)^2 + 1} = \frac{F}{5}\sqrt{\frac{1-\cos(\phi)^2}{\left(1-\cos(\phi)\right)^2} + 1} \\
&= \frac{F}{5}\sqrt{\frac{1-\cos(\phi)^2 + \left(1-\cos(\phi)\right)^2}{\left(1-\cos(\phi)\right)^2}} = \frac{F}{5}\sqrt{\frac{1-\cos(\phi)^2 + 1 - 2\cos(\phi) + \cos(\phi)^2}{\left(1-\cos(\phi)\right)^2}} \\
&= \frac{F}{5}\sqrt{\frac{2\left(1-\cos(\phi)\right)}{\left(1-\cos(\phi)\right)^2}} = \frac{F}{5}\sqrt{\frac{2}{\left(1-\cos(\phi)\right)}} = \frac{F}{5}\sqrt{\frac{2}{\left(1-1+\frac{2}{(1.515\mathfrak{f})^2}\right)}} = \frac{F}{5}1.515\mathfrak{f} \\
\Rightarrow F_s &= \frac{1.515}{5}F\mathfrak{f}
\end{aligned}
$$

Appendix B

Additional Literature Review

B.1 Tensile strength

The tensile strength of bamboo fibres can be very high [47]. However, strength decreases with increasing size of specimens. The ISO 2004b standard prescribes tests on dog-bone shaped specimens, assuming that these reflect full-culm tensile strength sufficiently. Whether this is the case, should be further discussed in future research. At the present time, the dog-bone test is the only available method to obtain bamboo tensile strength and results from previous research on small specimens will be adopted for the present research.

B.1.1 Guadua angustifolia

Ghavami and Marinho 2002 (data retrieved from [81]) conducted a series of tests on six specimens of *Guadua angustifolia*. Amongst other properties they determined the longitudinal tensile strength of 20 x 1 mm coupons and compressive strength for D=h.

Property	n	$\tilde{x}$	s	COV [%]
External Diameter D_o [mm]	6	76.68	43.29	56
Wall thickness t [mm]	6	13.19	7.51	57
Internodal Length [mm]	6	271.65	103.39	38
Tensile strength [MPa]	6	102.7	21.9	21
Compressive strength [MPa]	6	32.9	5.3	16

Table B.1: Mechanical and geometric properties of *Guadua angustifolia* (Ghavami and Marinho, 2002)

In 2008, Ghavami conducted tensile and compressive tests[1] according to the ISO 2004b standard on *Guadua angustifolia* specimens with and without nodes [32] (table B.2). The findings suggest that nodes decrease tensile as well as compressive strength[2]

[1] Dimensions $h = D$, average taken from top and bottom of culm

[2] This contradicts the findings of Shao et al. [77] for *Phyllostachys pubescens*, who found slightly increased compressive strength. In order to find out whether nodes increase or decrease compressive strength, compressive tests on both *Guadua angustifolia* and *Phyllostachys pubescens* should be conducted for specimens with and without nodes (chapter 4.2.3).

Property	node	node free	node/node free
Tensile strength f_t [MPa]	112.3	146.8	0.76
MOE E_t [GPa]	8.87	11.15	0.80
Compression strength f_c [MPa]	35.70	47.80	0.75
MOE E_c [GPa]	2.64	3.33	0.79

Table B.2: Average mechanical properties for *Guadua angustifolia* (Ghavami, 2008)

Tests on compression, tension, shear parallel to the fibre, compression perpendicular to the fibre and bending were carried out by Luna et al. in 2012 [59]. The samples of *Guadua angustifolia* came from different areas of Colombia and were tested in "wet" condition (MC far above fibre saturation point). They found the following characteristic strength values[3]:

Tensile strength $f_{t\|\|}$ [MPa]	40.7
Compression strength $f_{c\|\|}$ [MPa]	20.3
Compression strength perp. $f_{c\perp}$ [MPa]	1.7
Shear parallel $f_{v\|\|}$ [GPa]	3.5

Table B.3: Average mechanical properties for *Guadua angustifolia* (Luna et al., 2012)

In 2012, Gonzalez et al. conducted tensile tests on dog-bone shaped specimens of Colombian *Guadua angustifolia* for different moisture contents (figure B.1). All measured values of tensile strength for a range of 5 to 35% MC were well above 50 N/mm^2 [35]. The moisture content is defined as $MC\% = \frac{m-m_0}{m_0} \times 100$; m...mass before drying; m_0...dry mass

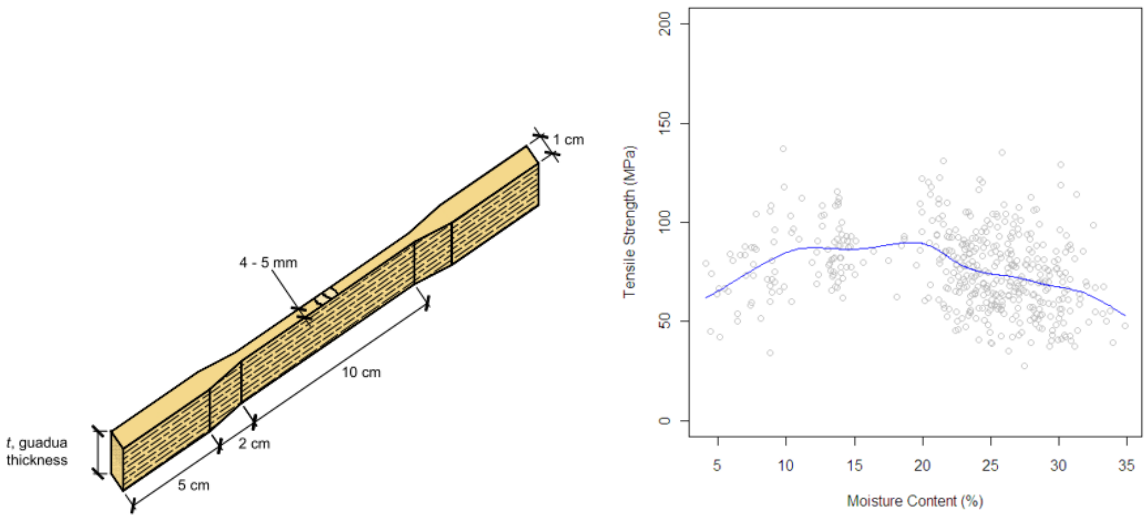

(a) dog-bone shaped specimens

(b) Tensile strength as a function of MC

Figure B.1: Tensile tests on *Guadua angustifolia* (Gonzalez et al., 2012)

In 2013, Estrada et al. modelled the characteristic tensile strength for *Guadua angustifolia* by means of digital image processing. They found a tensile strength of 250 N/mm^2 for a cluster with 5000 fibre bundles and 40% fibre content [23]. If an average fibre content of 40% is assumed and tensile strength of the parenchyma matrix is safely set to 0, the rule of mixture provides:

[3]average taken from top, middle and bottom of culm

rule of mixture: $f_t = f_{t,f} \cdot V_f + f_{t,m} \cdot (1 - V_f) = 250 \cdot 0.4 + 0 = 100\ N/mm^2$
V_f...fibre volume fraction; $f_{t,f}$...tensile strength fibre; $f_{t,m}$...tensile strength matrix

This result agrees with the findings of Ghavami. However, the results of Gonzalez et al. and Luna et al. are significantly lower and cannot be neglected. Combining the findings of Ghavami on the influence of nodes and the values from Gonzalez at al, it can be concluded that a mean tensile strength of $0.76 \cdot 50 = 38 N/mm^2$ is a conservative assumption for full-culm cross-sections with nodes and a moisture content of $MC < 30\%$. This assumption is in close agreement with Trujillo's publication of 2007 in *The Structural Engineer* where he reports a tensile strength of *Guadua angustifolia* of $> 35 N/mm^2$ [85]. For all model calculations and strength predictions, a mean tensile strength of $38 N/mm^2$ is assumed for *Guadua angustifolia* with and without nodes.

B.1.2 Phyllostachys pubescens (Moso)

In 2008, Yu and al sliced Moso bamboo cross-sections into 6 radial layers and determined their tensile strength and MOE [101]. They reported a range of MOE from 8.99 to 27.40 GPa and a longitudinal tensile strength of 115.35 to 309.32 MPa. The highest strength and MOE were found in the most outer layer of the cross-section. In the same year, Yu et al. also developed a linear equation relating tensile strength and MOE to air-dried density $[g/cm^3]$ [102]. The sample geometry is shown in figure B.2. Air-dried density for node as well as internode material typically varies around 0.6 to $0.8[g/cm^3]$ for full cross-sections of Moso bamboo [56] [101] [102]. For an air-dried density of $0.7[g/cm^3]$ we arrive at

compression: $MOE = 41.956 \cdot \rho - 18.431$
tensile strength $f_t = 334.941 \cdot \rho - 93.866$
For an air-dried density of $0.7[g/cm^3]$ we arrive at $f_t = 334.941 \cdot 0.7 - 93.866 = 140.6 N/mm^2$

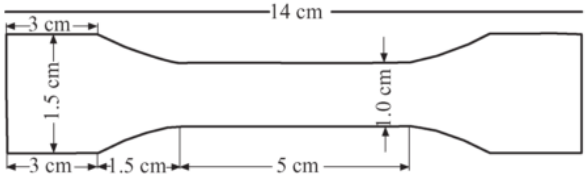

Figure B.2: Tensile test specimens, thickness 0.94 to 2.34mm (Yu et al., 2008)

In 2009, Shao et al. reported a linear relationship between tensile strength and fibre content for Moso bamboo [78]: $f_t = 562.69 \cdot V_f + 19.04$ which results in a tensile strength of $f_t = 562.69 \cdot 0.4 + 19.04 = 244\ N/mm^2$ for 40% fibre content.

In 2010, Shao et al. investigated the effect of nodes on tensile, bending, parallel shear and parallel and transverse compression strength of Moso bamboo. For all properties except tensile strength, the effects of nodes was positive. The effect on parallel compressive strength however, was very small (increase of 6%). Tensile strength of specimens with nodes dropped to on 67% of those without nodes [77].

Property	$\tilde{x}$	s	COV [%]	without node / node
Tensile strength without node [MPa]	154.24	13.92	9.00	
Tensile strength with node [MPa]	102.70	15.81	15.40	1:0.67
Compr. strength without node [MPa]	56.40	4.97	8.80	
Compr. strength with node [MPa]	59.80	5.65	9.50	1:1.06

Table B.4: Influence of nodes on tensile and compression strength of *Phyllostachys pubescens (Moso)* (Shao, 2010)

In 2014, Chen et al. reported a linear relationship between tensile strength and fibre content for 4-year old Moso bamboo with a moisture content of about 9.7% [10]: $f_t = 617.789 \cdot V_f + 6.936$ which results in a tensile strength of $f_t = 617.789 \cdot 0.4 + 6.936 = 254\ N/mm^2$ for 40% fibre content.

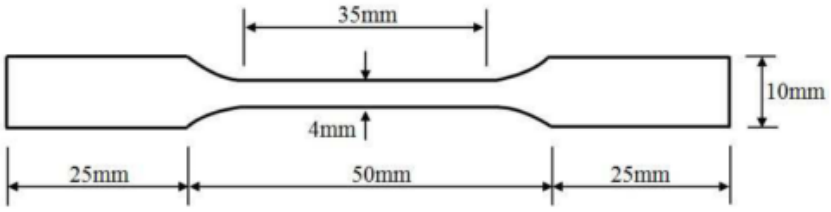

Figure B.3: Tensile test specimens, thickness 10mm (Chen et al., 2014)

Comparing the different results to each other, Shao's findings of 2010 produce the lowest values for specimens with nodes. Therefore a mean tensile strength of 100 N/mm^2 is a safe estimate and will be assumed in this thesis for *Phyllostachys pubescens (Moso)* with and without nodes.

Appendix C

Test Results

C.0.3 Dynamic Modulus of Elasticity

The following results were obtained for 14 culms of Moso and 7 culms Guadua bamboo respectively (f_{nat} natural frequency, D_0 outside culm diameter, t wall thickness, m mass, l_{culm} length of culm, ρ density, E_{dyn} Dynamic Modulus of Elasticity):

Table C.1: Dynamic Modulus of Elasticity for *Phyllostachys pubescens* (Moso)

Culm No.	f_{nat} [Hz]	D_0 [cm]	t [cm]	m [kg]	l_{culm} [cm]	no. nodes	ρ [kg/m^3]	E_{dyn} [MPa]
1	1647	8.65	0.9	1.84	125.0	6	689	11982
2	1254	9.88	1.1	3.00	157.0	9	614	9770
3	1808	10.38	1.0	1.92	109.0	5	583	9291
4	1806	10.45	1.0	2.98	112.0	6	870	14667
5	1752	10.00	1.3	2.54	112.5	7	642	10210
6	1996	11.13	1.2	2.70	109.5	6	666	13074
7	1723	10.33	0.9	2.12	121.0	5	640	11431
8	1635	11.08	1.2	2.48	113.5	6	573	8085
9	1755	10.43	1.0	2.64	119.0	5	732	13072
10	1827	9.58	0.8	1.68	113.5	5	652	11544
11	1847	10.73	1.0	2.52	120.5	5	699	14203
12	1859	10.90	1.2	2.42	109.0	6	614	10352
13	1801	10.10	1.0	2.06	116.0	5	634	11353
14	1960	10.40	0.9	1.84	104.5	4	640	11000
mean $\overline{x}$	1762	10.29	1.0	2.34	117.3	6	660	11431
SD σ	177.48	0.65	0.14	0.43	12.73	1.20	74.02	1865.63

Table C.2: Dynamic Modulus of Elasticity for *Guadua angustifolia*

Culm No.	f_{nat} [Hz]	D_0 [cm]	t [cm]	m [kg]	l_{culm} [cm]	no. nodes	ρ [kg/m^3]	E_{dyn} [MPa]
1	1732	14.50	1.2	5.58	157.5	5	682	21032
2	2176	15.03	1.6	5.64	117.0	3	719	19047
3	1532	11.75	1.2	5.30	165.0	5	787	20642
4	1488	13.70	1.5	7.08	185.0	5	671	20788
5	1645	10.00	1.3	5.46	147.5	6	1050	25369
6	1342	12.25	1.5	5.50	183.5	9	573	14352
7	1575	13.13	1.6	6.18	152.0	7	699	16537
mean $\overline{x}$	1641	12.91	1.4	5.82	158.2	6	740	19681
SD σ	265.70	1.73	0.16	0.62	23.29	1.89	150.77	3535.96

C.0.4 Compression Strength and Stiffness

The following test results were obtained for compression tests of *Phyllostachys pubescens* (Moso) and *Guadua angustifolia*, for a culm diameter D_0, wall thickness t, specimen height h, surface area A, specimen density ρ[1], maximum reached compressive force $F_{c,max}$, ultimate compressive strength f_c, compressive Modulus of Elasticity E_c. GX denotes specimens taken from short culm pieces for which E_{dyn} and ρ_{culm} were not determined. The moisture content was 13.58% for *Guadua angustifolia* and 11.30% for *Phyllostachys pubescens* (Moso).

Table C.3: Compression results for *Phyllostachys pubescens* (Moso)

Culm No.	D_0 [mm]	t [mm]	h [mm]	A [mm^2]	Node y/n	ρ [kg/m^3]	$F_{c,max}$ [kN]	f_c [MPa]	E_c [MPa]
M02	96	10.5	150	2804	n	564	117.1	41.76	6034
M02	97	11.5	166	3071	y	610	123.4	40.19	4787
M01	89	7.5	151	1920	y	768	95.8	49.86	8212
M06	112	10.0	150	3189	y	751	162.4	50.93	4715
M10	92	6.5	153	1746	y	801	90.5	51.85	8517
M01	88	7.5	150	1885	y	771	93.5	49.59	9126
M01	90	7.5	153	1944	y	783	100.4	51.64	8644
M05	109	12.5	155	3790	y	633	145.4	38.37	3719
M10	93	6.5	151	1756	n	778	93.8	53.43	8420
M10	97	6.5	150	1838	n	810	102.4	55.72	8784
M10	90	6.5	150	1695	n	754	88.5	52.21	8266
M13	103	8.5	150	2510	n	663	119.9	47.78	7016
M13	103	8.5	153	2510	n	693	122.2	48.68	7954
$\overline{x}$	96.5	8.5	152.5			721.5		48.62	7246
$\overline{x}_{clear}$	96.5	7.8	150.7			710.6		49.93	7745
$\overline{x}_{node}$	96.5	9.0	154.0			730.8		47.49	6817
σ	7.7	2.0	4.4			80		5.31	1820

[1]The height of the diaphragm was taken as 5 mm for *Guadua angustifolia* and 3 mm for *Phyllostachys pubescens*

Table C.4: Compression results for *Guadua angustifolia*

Culm No.	D_0 [mm]	t [mm]	h [mm]	A [mm^2]	Node y/n	ρ [kg/m^3]	$F_{c,max}$ [kN]	f_c [MPa]	E_c [MPa]
GXX[2]	127	12.5	144	4477	n	855	318	71.06	9249
G07	131	16.0	153	5781	y	691	245	42.31	6179
G07	133	13.5	151	5047	n	744	229	45.31	7883
G03	114	10.5	151	3414	y	935	258	75.44	11982
G03	114	10.5	151	3398	n	854	255	74.93	13560
G03	119	10.5	150	3563	n	856	263	73.84	12676
G03	116	10.5	153	3464	y	936	255	73.53	12856
G07	131	14.5	154	5284	y	733	237	44.91	6549
G07	132	15.5	151	5649	n	688	236	41.74	6783
G03	117	10.5	150	3497	n	859	269	77.00	13985
G07	132	15.5	152	5649	y	693	246	43.64	7274
G03	115	11.5	151	3721	n	766	239	64.23	8750
GXX[2]	127	12.5	142	4477	n	693	250	55.89	7847
G07	134	14.5	152	5421	n	711	231	42.59	7872
G03	118	11.0	152	3680	y	918	264	71.60	9651
$\overline{x}$	124	12.6	150			796		59.87	9540
$\overline{x}_{clear}$	124	12.4	149			781		60.73	9845
$\overline{x}_{node}$	123	13.0	153			818		58.57	8968
σ	7.9	2.1	3.2			95		14.83	2736

C.0.5 Bolt Shear Test

Table C.5 displays the following test results: Bolt shape round(○) or square (□), culm average outer diameter (D_0), culm average thickness (t), height of the specimen (h – of little importance for this test), edge distance from bottom of bolt to bottom end of specimen (l_{edge}), node (yes/no), average specimen density ($/rho$), culm thickness at the point of the continuous crack (t_{cr}), bearing surface ($A_b = td$), crack opening or splitting surface ($A_{cr} = nt_{cr}l_{edge}$), maximum bolt force (F_b), bearing strength ($F_b/2A_b$), crack opening force at onset of final tensile splitting (F_{cr}) and splitting capacity ($f_{s_\parallel}$). The specimens with initial cracks are included in these results and it was found that bearing strength was not distinctly smaller than for intact specimens. Note that the tensile splitting capacity ($f_{s_\parallel}$) has the character of a hypothetical material property as the bolt force and crack surface cannot be directly translated into Mode I splitting capacity. For further reading this issue is discussed in detail by Mitch [62]. Comparing bearing stiffness E_b to compression stiffness E_c, we find that bolt bearing is a little softer than pure compression, especially for the square bolt. However, for bearing deformation capacity, the elastic part is of little interest and E_b is not further discussed.

[2]Indicates short specimen for which density and dynamic MOE of entire culm was not determined.

Table C.5: Bolt shear test results for *Phyllostachys pubescens* (Moso) round ○ and square □ bolts

Bolt shape	Culm No.	D_0 [mm]	t [mm]	h [mm]	l_{edge} [mm]	Node y/n	ρ [kg/m^3]	t_{cr} [mm]	A_b [mm^2]	A_{cr} [mm^2]	F_b [kN]	f_b [MPa]	E_b [MPa]	F_{cr} [kN]	$f_{s_\parallel}$ [MPa]
○	M14	107	8	200	92	n	660	8	128	736	13.44	52.50	6441	13.43	18.25
○	M11	108	9.5	200	93	n	659	9	144	837	17.12	59.43	6991	15.02	17.95
○	M07	98	8	202	93	n	671	9	144	837	15.16	52.64	5117	13.79	16.48
○	M11	110	10	200	95	n	637	9	144	855	17.03	59.14	6801	16.57	19.38
○	M14	101	8	200	90	n	658	8	128	720	13.65	53.30	6357	13.59	18.88
○	M06	109	9.75	203	100	y	762	10	160	1000	20.03	62.58	6646	19.88	19.88
○	M13	100	8	201	90	y	733	9	144	810	14.54	50.49	4882	14.06	17.36
○	M01	84	7.5	201	90	y	787	7	112	630	14.68	65.53	6091	15.59	24.75
○	M07	99	9	201	94	y	730	9	144	846	17.89	62.12	6994	17.44	20.61
○	M05	100	10	201	93	y	677	9	144	837	20.76	72.07	7070	18.30	21.86
$\overline{x}_{clear}$○		105	8.7		93		657	8.6	138	797	15.28	55.41	6341	14.48	18.18
$\overline{x}_{node}$○		98	8.9		93		738	8.8	141	825	17.58	62.56	6337	17.05	20.89
σ_{clear}○		5	0.9		2		12	0.5	9	63	1.77	3.56	732	1.33	1.11
σ_{node}○		9	1.1		4		41	1.1	18	132	2.91	7.83	900	2.28	2.71

Bolt shape	Culm No.	D_0 [mm]	t [mm]	h [mm]	l_{edge} [mm]	Node y/n	ρ [kg/m^3]	t_{cr} [mm]	A_b [mm^2]	A_{cr} [mm^2]	F_b [kN]	f_b [MPa]	E_b [MPa]
□	M10	84	7	201	100	n	828	8.5	136	850	10.16	37.35	4698
□	M11	95	8.5	201	102	n	800	9	144	918	17.75	61.62	4011
□	M07	114	9	200	100	n	517	8	128	800	15.74	61.47	6131
□	M11	102	9	202	100	n	635	9	144	900	16.42	57.00	6071
□	M14	103	8.5	201	102	n	648	8.5	136	867	12.48	45.87	5762
□	M07	98	9	201	102	y	676	8	128	816	15.38	60.07	4400
□	M07	101	8.75	250	82	y	590	9	144	738	15.63	54.28	3532
□	M05	84	11	205	102	y	855	11	176	1122	17.83	50.64	5159
□	M01	100	7.5	201	100	y	551	8	128	800	14.00	54.68	4011
□	M06	108	11	200	100	y	727	11	176	1100	18.24	51.83	4455
□	M05	97	10.25	201	102	y	751	10.5	168	1071	18.19	54.14	5698
$\overline{x}_{clear}$□		100	8.4		101		686	8.6	138		14.51	52.66	5335
$\overline{x}_{node}$□		98	9.6		98		692	9.6	153		16.54	54.27	4028
σ_{clear}□		11	0.8		1		128	0.4	7		3.11	10.69	938
σ_{node}□		8	1.4		8		111	1.4	23		1.78	3.26	781

Appendix D

Drawings

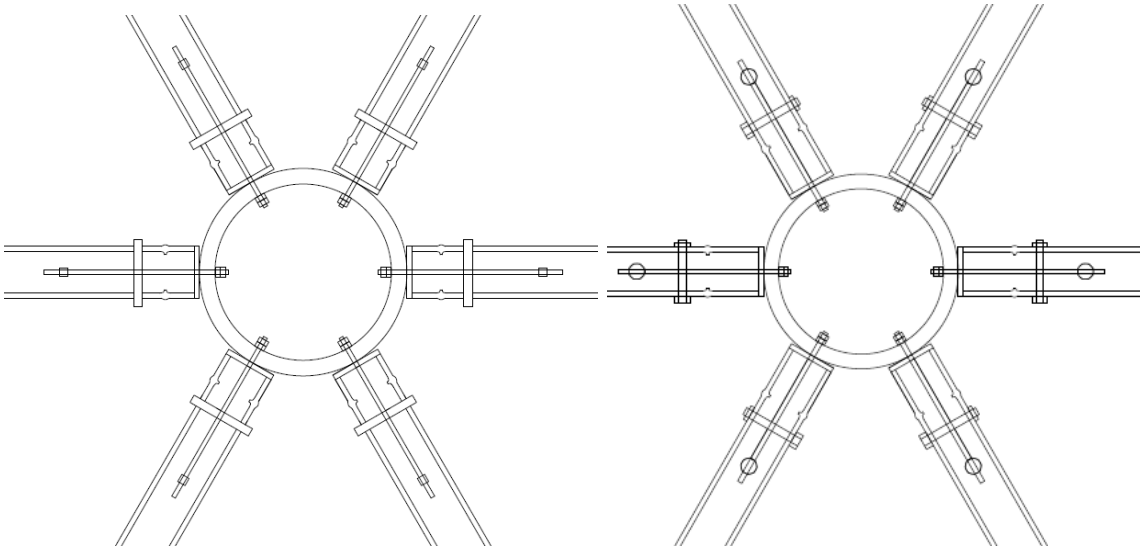

(a) Square cross dowels (b) Round cross dowels

Figure D.1: Dome Hubs

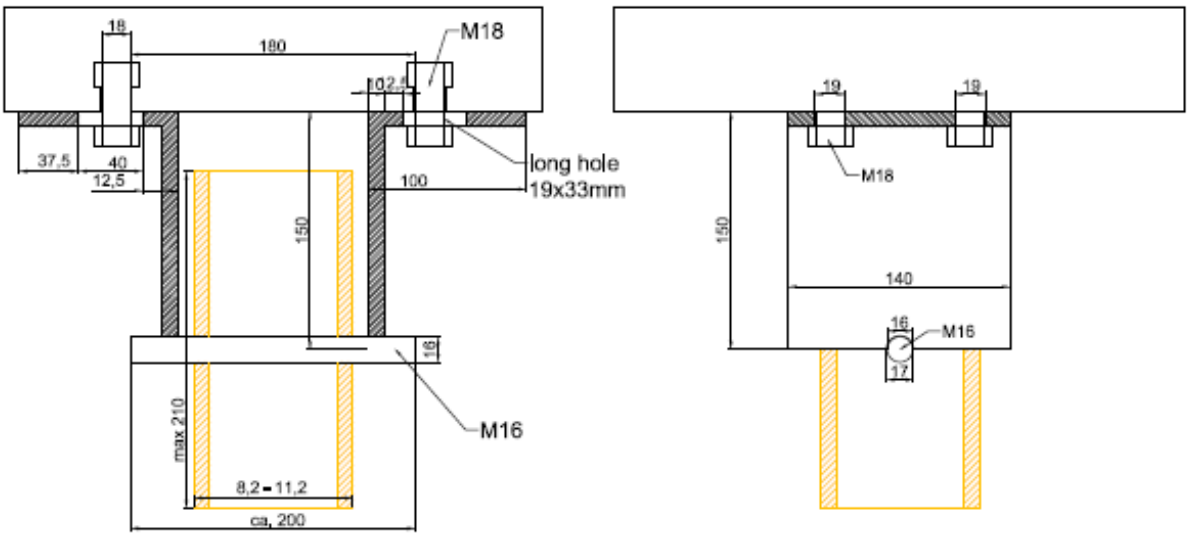

(a) Test set-up bolt shear test

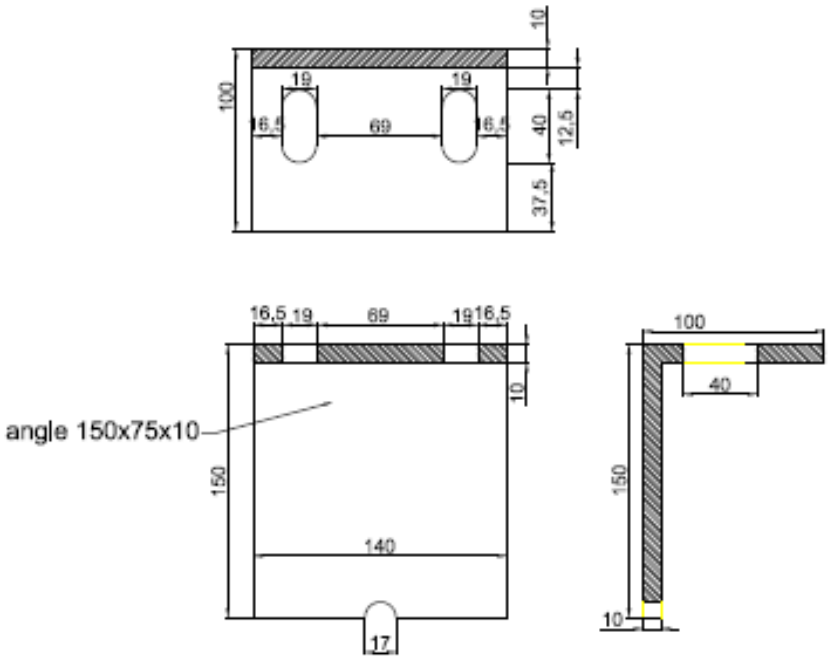

(b) Adjustable angle

Figure D.2: Bolt shear test set-up

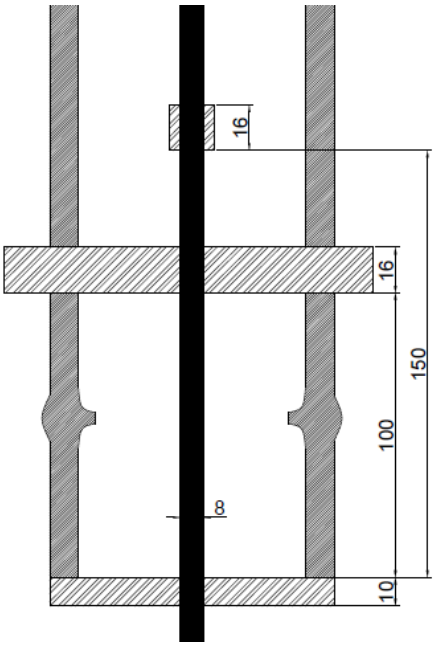

Figure D.3: Tensile connector